

Laser Based Mid-Infrared Spectroscopic Imaging – Exploring a Novel Method for Application in Cancer Diagnosis

Andrew McCrow

A thesis submitted to Imperial College London for the degree of PhD and
the Diploma of Imperial College London

Experimental Solid State Physics

The Blackett Laboratory

Imperial College London

London

SW7 2BW

United Kingdom

October 2011

Abstract

A number of biomedical studies have shown that mid-infrared spectroscopic images can provide both morphological and biochemical information that can be used for the diagnosis of cancer. Whilst this technique has shown great potential it has yet to be employed by the medical profession. By replacing the conventional broadband thermal source employed in modern FTIR spectrometers with high-brightness, broadly tuneable laser based sources (QCLs and OPGs) we aim to solve one of the main obstacles to the transfer of this technology to the medical arena; namely poor signal to noise ratios at high spatial resolutions and short image acquisition times. In this thesis we take the first steps towards developing the optimum experimental configuration, the data processing algorithms and the spectroscopic image contrast and enhancement methods needed to utilise these high intensity laser based sources. We show that a QCL system is better suited to providing numerical absorbance values (biochemical information) than an OPG system primarily due to the QCL pulse stability. We also discuss practical protocols for the application of spectroscopic imaging to cancer diagnosis and present our spectroscopic imaging results from our laser based spectroscopic imaging experiments of oesophageal cancer tissue.

Contents

<u>1.0 – Introduction</u>	1
<u>2.0 - Background to Research</u>	4
2.1 - Fundamental Drivers of the Research: Human Cost and Market Need	4
2.2 - The Inadequacy of the Gold Standard of Cancer Diagnosis: Histopathological Analysis	4
2.3 - Background to Infrared (IR) Spectroscopy	6
2.3.1 - The Use of IR Spectroscopy to Analyse Biological Samples and to Diagnose Cancer	7
2.3.2 - The Importance of the Collection of Microscopic Data and the Spatial Resolution of IR Spectroscopy	9
2.3.3 - Contribution to IR Spectra from Physical Properties of the Sample: Scattering	11
2.4 - Background to Chemical and Spectroscopic Imaging	12
2.4.1 - Chemical Imaging	13
2.4.2 - Spectroscopic Imaging	15
2.4.3 - Analysis of Large Data Sets: Multivariate Data Analysis	15
2.4.3.1 - Unsupervised Multivariate Algorithms	16
2.4.3.2 - Supervised Multivariate Algorithms	16
2.4.4 - Application of Spectroscopic Imaging to a Clinical Setting: Practical Protocols	16
2.5 - IR Spectroscopy and Spectroscopic Imaging Using Laser Sources	17
2.5.1 - Studies Using Synchrotron Sources	17
2.5.2 - Studies Using IR Lead-Salt Diode Lasers	19
2.5.3 - Studies Using QCLs	19

2.5.4 - Studies Using FELs	20
2.5.5 - Studies Using Non-Linear Lasers	20
2.6 - Alternative Technologies: Raman and Near IR spectroscopy	20
2.6.1 - Raman Spectroscopy	21
2.6.2 - Near IR Spectroscopy	23
<u>3.0 - Theory</u>	26
3.1 - IR Spectra	26
3.2 - Theory of Molecular Vibrations and IR Absorption	27
3.3 - Biochemical Significance of Spectral Data from Biological Samples	30
3.3.1 - Nucleic Acids: Phosphodiester Vibrations	31
3.3.2 - Proteins: Amide Vibrations	32
3.3.3 - Lipids	33
3.3.4 - Carbohydrates	33
3.4 - Quantitative Analysis of Spectra: Beer's Law	33
3.4.1 - Single-component Quantitative Analysis	34
3.4.2 - Multi-component Quantitative Analysis	34
3.5 - Instrumentation Used for the Collection of IR Spectra and Spectral Maps	36
3.5.1 - Dispersive IR Spectrometers	36
3.5.2 - FTIR Spectrometers	37
3.6 - Alternative Modes of IR Spectroscopy	38
3.6.1 - Transmission Mode Spectroscopy	38
3.6.2 - Reflection Mode Spectroscopy	38
3.6.3 - Transflection Mode Spectroscopy	39

3.6.4 - ATR Mode Spectroscopy	39
3.7 - IR Sources for IR Spectroscopy	40
3.7.1 - Brightness	40
3.7.2 - Brightness and Power of Thermal Sources	41
3.7.3 - Brightness and Power of Synchrotron and FEL Sources	42
3.7.4 - Brightness and Power of the OPG Imaging System	43
3.7.5 - Brightness and Power of the QCL Imaging System	44
3.8 - IR Detectors for IR Spectroscopy	45
3.8.1 - Responsivity and Spectral Responsivity	46
3.8.2 - Noise Equivalent Power	46
3.8.3 - Detectivity and Normalised Detectivity	47
3.9 - Instrumentation Figures of Merit and Noise	47
3.9.1 - Spatial Resolution and the Diffraction Limit	47
3.9.2 - Spectral Resolution	48
3.9.2.1 - Jasco FTIR Spectrometer Spectral Resolution	48
3.9.2.2 - OPG Imaging System Spectral Resolution	49
3.9.2.3 - QCL Imaging System Spectral Resolution	49
3.9.3 - Signal to Noise	49
3.9.3.1 - Noise	50
3.9.3.1.1 - Electronic Noise	50
3.9.3.1.2 - Environmental Noise	50
3.9.3.1.3 - Source Noise	51
3.9.3.1.3.1 - Source Noise from a Thermal Source	51

3.9.3.1.3.2 - Source Noise from an OPG Source	52
3.9.3.1.3.3 - Source Noise from a QCL Source	52
<u>4.0 - Experimental Set-up and Characterisation</u>	53
4.1 - Background to Samples	53
4.1.1 - Healthy Biological Tissue	53
4.1.1.1 - Connective Tissue	53
4.1.1.2 - Muscle Tissue	54
4.1.1.3 - Nervous Tissue	54
4.1.1.4 - Epithelial Tissue	54
4.1.2 - Cancer	55
4.1.2.1 - Medical Nomenclature for Cancer	55
4.1.3 - Samples	56
4.1.3.1 - Preparation of Samples	56
4.1.3.2 - Histopathological Classification of Tissue Samples	58
4.2 - Jasco FTIR Spectrometer	58
4.2.1 - Jasco FTIR Spectrometer Specifications	58
4.2.2 - Jasco FTIR Spectrometer Method of Operation	58
4.3 - Jasco IR Microscope	59
4.3.1 - Jasco IR Microscope Specifications	59
4.3.2 - Jasco IR Microscope Method of Operation	59
4.4 - The Mid-IR Optical Parametric Generator (OPG)	60
4.4.1 - OPG Output Characteristics	60
4.4.2 - OPG Beam Divergence	62

4.4.3 - OPG Method of Operation	64
4.5 - The Tuneable Quantum Cascade Laser (QCL)	67
4.5.1 - QCL Output Characteristics	67
4.6 - Cedip IR Camera	69
4.6.1 - Cedip Camera Specifications	69
4.6.2 - Cedip IR Camera Method of Operation	70
4.6.3 - Characterisation of IR Camera using a Black Body	70
4.6.3.1 - Energy Reaching IR Camera from a Black Body	70
4.6.3.2 - IR Camera Response to a Black Body	73
4.6.4 - Non Uniformity Correction (NUC)	74
4.6.4.1 - Linear Non Uniformity Correction (LNUC)	75
4.6.4.1.1 - Representative LNUC for Cedip IR Camera	77
4.6.4.2 - Non Linear Non Uniformity Correction (NLNUC)	79
4.6.4.2.1 - Representative NLNUC for Cedip IR Camera	80
4.6.4.3 - Patch Non Uniformity Correction (PNUC)	81
4.6.4.3.1 - Representative PNUC for Cedip IR Camera	83
4.6.4.4 - Assessment of the Quality of a NUC	83
4.6.5 - Bad Pixel Replacement (BPR)	84
4.6.6 - Resting Pixel Values on IR Camera and Analysis of Electronic and Environmental Noise	87
4.6.6.1 - Resting Pixel Values (RPVs) of IR Camera	88
4.6.6.2 - Electronic and Environmental Noise in IR Camera	89
4.7 - Imaging Optics (Overall Set-Up) for the OPG Imaging System	91

4.7.1 - Synchronisation of the IR Camera to the OPG	92
4.8 - Imaging Optics (Overall Set-Up) for the QCL Imaging System	92
4.8.1 - Synchronisation of the IR Camera to the QCL	93
4.9 - Optical Artefacts Caused by Coherent Sources	94
4.9.1 - Interference Fringes	95
4.9.2 - Speckle Patten	95
4.9.3 - Removal of Optical Artefacts Using a Diffuser	95
4.10 - OPG Pulse-to-Pulse Intensity Variations and Data Binning Algorithms	97
4.10.1 - Correlation between Array Detector in IR Camera and Reference Channel for OPG	97
4.10.2 - Detector Saturation by OPG: Moss Burstein Effect	99
4.10.3 - Detector Correlation and the Cedip Camera Time Constant	99
4.10.4 - OPG Data Binning Algorithms	100
4.10.4.1 - Time Constant Binning Algorithm	100
4.10.4.2 - Saturation Binning Algorithm	102
4.11 - QCL Pulse-to-Pulse Intensity Variations and the Variable Pulse Data Binning Algorithm	102
4.11.1 - Correlation between Array Detector in IR Camera and Reference Channel for QCL	103
4.11.2 - Detector Saturation by QCL	104
4.11.3 - Variable Pulse Data Binning Algorithm	104
4.12 - Characterisation of OPG Imaging System	106
4.12.1 - Experimental Measurement of the Spatial Resolution of the OPG Imaging System	106
4.12.2 - Analysis of the OPG Background and Analysis of OPG Total Noise	108

4.12.2.1 - OPG Background	108
4.12.2.2 - Total Noise from the OPG Imaging System	109
4.13 - Characterisation of QCL Imaging System	110
4.13.1 - Analysis of the QCL Background and Analysis of QCL Total Noise	110
4.13.1.1 - QCL Background	111
4.13.1.2 - Total Noise from the QCL Imaging System	111
<u>5.0 - Analysis of Spectral Maps from the FTIR</u>	114
5.1 - Selection of FTIR Instrument Measurement Parameters	114
5.1.1 - Spectral Resolution of the FTIR Spectrometer	115
5.1.2 - Spatial Resolution of the FTIR Spectrometer	116
5.1.3 - Signal-to-Noise Ratio, Measurement Time, Field of View and Data Set Measurement Time	117
5.2 - Pre-processing of IR Spectra	119
5.2.1 - Spectral Smoothing	119
5.2.1.1 - Boxcar Smoothing Algorithm	119
5.2.1.2 - Savitsky-Golay Smoothing Algorithm	120
5.2.2 - Spectral Subtraction	120
5.2.2.1 - Spectral Subtraction of BaF ₂ substrates	120
5.2.3 - Baseline Correction	121
5.2.3.1 - Pixel-to-Pixel Baseline Variations	122
5.2.4 - Data Compression	123
5.2.4.1 - Compression of Spectral Features into a Peak Area or Peak Height	123

5.2.4.1.1 - Biochemically Significant Spectral Features for Cancer Diagnosis	124
5.2.4.2 - Principal Component Analysis	126
5.3 - Tissue Classification Using IR Spectra	129
5.3.1 - Assessment of Tissue Classification Accuracy: Sensitivity and Specificity	129
5.3.2 - Tissue Classification Using Univariate Methods	129
5.3.2.1 - The F - Test	130
5.3.3 - Tissue Classification Using multivariate Methods	132
5.3.3.1 - Linear Discriminant Analysis	132
5.3.3.1.1 - Training Stage of LDA program	133
5.3.3.1.2 - Classification Stage of LDA program	134
5.3.3.2 - Case study: LDA	135
5.3.3.2.1 - Case study: Development of LDA model	135
5.3.3.2.2 - Case study: Results of LDA model	137
5.4 - Practical Protocols for Cancer diagnosis Using Spectral Mapping	138
<u>6.0 - Analysis of Spectral Maps from the OPG and QCL Imaging Systems</u>	141
6.1 - Analysis of OPG data	141
6.1.1 - Extracting Absorbance Values from OPG Imaging System Data	141
6.1.2 - The Uncertainty of Absorbance Data from the OPG Imaging System	142
6.1.2.1 - Estimation of Absorbance Uncertainty using Error Analysis	142
6.1.2.2 - Estimation of Absorbance Uncertainty using Repeated Measurements	145
6.1.3 - Comparison of Spectral Maps from OPG Imaging System and Jasco FTIR Spectrometer	146

6.1.4 - OPG Imaging System Images and their Application to Cancer Diagnosis	149
6.2 - Analysis of QCL data	152
6.2.1 - Extracting Absorbance Values from QCL Imaging System Data	153
6.2.2 - The Uncertainty of Absorbance Data from the QCL Imaging System	154
6.2.2.1 - Estimation of Absorbance Uncertainty using Error Analysis	154
6.2.2.2 - Estimation of Absorbance Uncertainty using Repeated Measurements	154
6.2.3 - Comparison of Spectral Maps from QCL Imaging System and Jasco FTIR Spectrometer	155
6.2.4 - QCL Imaging System Images and their Application to Cancer Diagnosis	160
<u>7.0 - Conclusions and Suggestions for Further Work</u>	166
7.1 - Overview of Thesis	166
7.2 - Suggestions for Further Work	167
<u>Appendix 1</u>	170
<u>Acknowledgements</u>	171

1.0 - Introduction

In this thesis the spectroscopic imaging of cancer biopsies using laser based IR sources - an optical parametric generator (OPG) and a quantum cascade laser (QCL) - is discussed. The originality of this work is a result of the described methodologies and protocols required for the extraction of biochemical information from spectroscopic images collected using laser based IR sources. To the best of the author's knowledge the few isolated studies published at this point in time [1-5] have not explored, in great detail, the critical issue of how quantitative information is obtained from a laser based spectroscopic imaging system and how this information can be used to inform a non-subjective diagnosis of cancer.

Dr Amrania's [1, 2] work deserves special mention at this point since his doctoral thesis (supervised by Prof C. C. Phillips), Ultrafast Mid-Infrared Spectroscopic Imaging with Biomedical Applications [6], provided the starting point for much of the work carried out in this thesis. Dr Amrania conducted several interesting experiments by coupling a homemade OPG to an IR camera array via an IR microscope. Using this experimental arrangement Dr Amrania was able to collect diffraction limited images of living cells undergoing mitosis and demonstrate the use of such a system for the analysis of histopathological tissue sections. The work in this thesis differs from Dr Amrania's exploration of OPG based spectroscopic imaging in several respects. Firstly, to generate spectroscopic images with fields of view that are comparable to those in conventional histopathology, the IR microscope (which provided a magnification of x16) used in Dr Amrania's experiments was replaced with a simple lens which provided much more modest magnifications (up to approximately x3). Secondly particular emphasis has been placed on the extraction of *numerical absorbance values* from the spectroscopic data sets which can be used to quantify the tissue classification process used by histopathologists when diagnosing cancer. Finally this thesis examines the use of a commercially available, tuneable, QCL (Block Engineering, Marlborough, USA) for the generation of spectroscopic images.

Chapter 2 provides the background of this work. The chapter begins with a brief discussion of the motivation for this work and then goes onto to explore the body of work that exists on the application of IR spectroscopy to cancer diagnosis. Next the use of IR sources (such as synchrotrons and QCLs) to collect spectroscopic images are discussed and finally the methods of Raman and Near IR spectroscopy are described.

In chapter 3 the theoretical considerations of this thesis are discussed. Firstly the theory of how specific molecular vibrations give rise to IR absorption, the vibrational modes of a biomolecule which are responsible for the characteristic shape of a typical biological IR spectrum, and quantitative

analysis of IR spectra are discussed. Next the operating principles and modalities (transmission and reflection) of IR spectrometers are discussed. Next it is demonstrated that the brightness of the OPG and QCL sources is what primarily distinguishes them from conventional thermal sources. Following this IR detectors are discussed and finally the theoretical limits of spatial resolution, spectral resolution, and signal to noise are explored.

Chapter 4 is the experimental section of the thesis. In this part of the thesis the samples, IR spectrometer, IR microscope, IR camera, OPG and QCL sources used for the collection of the data in this thesis are explained in more detail. In section 4.6 on the Cedip IR camera some important algorithms developed to improve image quality, such as the Non-Linear Non Uniformity Correction (NLNUC), and the Bad Pixel Replacement (BPR) are explained. Other important parts in this chapter include an experimental determination of the electronic/environmental noise, the elimination of optical artefacts caused by the coherent nature of the OPG and QCL sources, the use of a reference channel to account for pulse-to-pulse variability of the OPG source, and the experimental characterisation of the OPG and QCL imaging systems.

The purpose of chapter 5 is to describe to discuss the methodologies and protocols that are used when applying conventional IR spectroscopy to cancer diagnosis. Firstly the measurement parameters (spectral resolution, spatial resolution and SNR) required for the collection of meaningful, quantitative data are described. Secondly the methods of processing spectra, such as smoothing, baseline correction and data compression, are discussed. Thirdly the biochemically significant spectral features used for cancer diagnosis and sophisticated multivariate techniques (such as LDA) are described. The chapter ends with a discussion of the practical application of IR spectroscopy to a clinical environment and concludes that a critical success factor for this is the fast generation of reliable absorbance data; an issue that this thesis aims to solve.

Chapter 6 presents the spectral maps collected with the OPG and QCL imaging systems. It is shown that the SNR for a chemical image (with units of absorbance) collected with the OPG and QCL imaging systems is 2 and 30 respectively. The poor SNR (caused by the large intensity variation from pulse-to-pulse) from the OPG imaging system limits the usefulness of this system as a diagnostic tool. However the proof-of-principle studies performed with the QCL imaging system indicate that this system may be capable of extracting quantitative biochemical information with a system that is robust and cost effective (when compared to the OPG imaging system).

Chapter 7 concludes the thesis by summarising what has been covered in the previous chapters and suggesting possible directions for further work in the future.

As a final consideration the author would like to apologise in advance for any confusion caused by the choice of spectral units which will change from wavenumber (cm^{-1}) to micrometers (μm) at various times throughout the text. For convenience please refer to equation 1.1 to convert between these units.

$$\text{micrometers } (\mu\text{m}) = \frac{10^4}{\text{wavenumber } (\text{cm}^{-1})} \quad (1.1)$$

1. Amrania, H., A. McCrow, and C.C. Phillips, *A Benchtop, Ultrafast Infrared Spectroscopic Imaging System for Biomedical Applications* Review of Scientific Instruments, 2009. **80**(12): p. 123702-1 to 123702-6.
2. Amrania, H., et al., *Ultrafast Infrared Chemical Imaging of Live Cells*. Chemical Science, 2010. **2**(1): p. 107-111.
3. Baily, J.A., et al., *High Spatial Resolution for IR Imaging Using an IR Diode Laser*. Applied Spectroscopy, 2000. **54**(2): p. 159-163.
4. Guo, B., et al., *Multi-Wavelength Mid-Infrared Micro-Spectral Imaging using Semiconductor Lasers* Applied Spectroscopy Issue 2003. **57**(7): p. 811-822.
5. Guo, B., et al., *Laser-Based Mid-Infrared Reflectance Imaging of Biological Tissues*. Medical and Biological Imaging, 2004. **12**(1): p. 208-219.
6. Amrania, H., *Ultrafast Mid-Infrared Spectroscopic Imaging with Biomedical Applications*, in *Experimental Solid State Physics*. 2009, Imperial College: London.

2.0 - Background to Research

The purpose of this chapter is to describe the problems being addressed in this thesis and to place the work within the scientific landscape. To begin with the fundamental drivers of this research are briefly discussed; namely the human cost of cancer and the growing market opportunity for reliable cancer diagnostics. Next the traditional gold standard of cancer diagnosis is described and the shortcomings of this method are highlighted. Following this the methods of IR spectroscopy and spectroscopic imaging are discussed as potential tools for cancer diagnostics. Finally the chapter ends with a description of two alternative biomedical optical technologies; Raman spectroscopy and near infrared spectroscopy.

2.1 - Fundamental Drivers of the Research: Human Cost and Market Need

One in three people will develop some form of cancer in their lifetime[1] and, according to the World Health Organization, approximately 12.5% of all deaths in 2002 were caused by cancers[2]. These alarming statistics demonstrate the gravity of a problem which shows little sign of slowing in the future. Whilst many advances have been made into the prevention, diagnosis and treatment of the condition, 21st century issues, such as the increasing elderly population, mean that we can expect the death and suffering associated with cancer to continue.

In addition to the human cost of cancer there is a market opportunity created by the *need* for improved cancer care. The cancer diagnostics market can be segmented into the in-vivo and in-vitro diagnostics markets. The research in this thesis will primarily pertain to in-vitro diagnostics but there is potential for the technology to break into in-vivo diagnostics as well. In 2008 the European cancer in-vitro diagnostics (IVD) market was estimated to generate revenues of \$623 million and by 2015 this figure is expected to rise to \$1.5 billion[3]. The growth of the market is driven by an increasing elderly population and unhealthy lifestyle habits in western countries. In addition to this, governments and health care providers are realising the advantages of early detection of cancer; reduced recovery times means less of a strain of healthcare resources and manpower[4].

2.2 - The Inadequacy of the Gold Standard of Cancer Diagnosis: Histopathological Analysis

Depending on the type of cancer a different battery of tests may be employed. For example, bowel cancer may involve the analysis of a stool sample whereas a brain tumour sufferer may be subject to MRI and CT scans[1]. However for the vast majority of cancers the gold standard is a biopsy followed by a histopathological examination. For a histopathological examination a thin section (approximately 3 - 10 μ m thickness) of a tissue biopsy is taken and, since biological tissue does not have much useful contrast in normal microscopy, the section is stained with natural dyes

(haematoxylin and eosin or “H & E” stain) (Figure 1). A haematoxylin & eosin stain colours protein-rich regions of the tissue pink and nucleic acid-rich regions of the tissue blue. A histopathologist will then make a *subjective* diagnosis based on the tissue morphology and his/her past experience examining H & E stains. A more complete discussion of the tissue processing and classification stages is discussed in section 4.1.

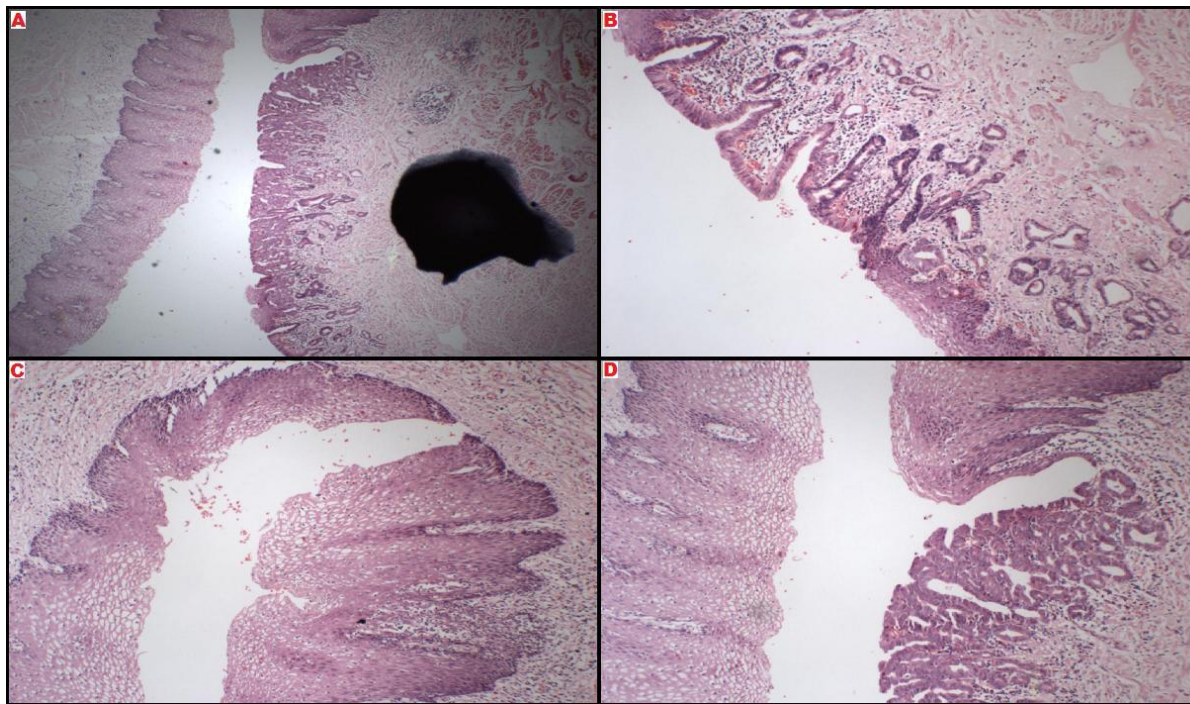


Figure 1. H & E stained tissue sections of oesophagus tissue. A) Squamous epithelium and high grade tissue. The black spot is a blot of ink used as a reference point B) Squamous epithelium and low grade tissue. C) Squamous epithelium tissue. D) Squamous epithelium and high grade tissue.

Various studies[5, 6] have indicated that a more rigorous gold standard is required as there is a poor level of inter-observer agreement between histopathologists which is largely due to the subjective nature of the diagnosis. Work carried out by Kendall et al analysed the agreement between three independent gastrointestinal histopathologists using Kappa statistics[7]. Kappa statistics are thought to be more robust than a simple percentage agreement calculation since Kappa statistics take into account agreement occurring by chance (whereas a simple % agreement does not). Kendall’s study indicates there is considerable variation (Kappa value of 0.49 between all three histopathologists which indicates only a moderate level of agreement) between pathologists in the grading of oesophageal pathology. Furthermore no consensus agreement was reached on the classification of any pre-cancerous conditions such as “low-grade dysplasia”. The reliable detection of pre-cancerous conditions is especially important since it is well established that early detection of cancer, before systemic invasion sets in, greatly increases the chance of a full recovery for the patient.

The ideal diagnostic test would provide rapid, non-invasive, non-subjective diagnosis at the point-of-care with no prior tissue processing required. IR spectroscopy and spectroscopic imaging, which will be discussed in sections 2.3-2.4, have the potential to fulfil many of these criteria but have yet to realise their full potential as diagnostic tools.

2.3 - Background to Infrared (IR) Spectroscopy

IR spectroscopy is a technique used to identify chemical species within a sample. IR radiation is absorbed resonantly (at specific frequencies) by molecular bonds and therefore an IR spectrum (Figure 2) can be correlated with chemical content. IR spectroscopy was originally carried out using dispersive IR spectrometers (section 3.5.1) however dispersive instruments have been supplanted by Fourier Transform Infrared (FTIR) spectrometers (section 3.5.2) for the majority of applications. FTIR spectrometers offer significant advantages over dispersive instruments, such as improved signal-to-noise and data acquisition rates[8], and in 1969 the first commercial FTIR unit appeared on the market[9]. IR spectroscopy has found applications in a variety of fields from explosive residue identification[10] to analysing archaeological artefacts[11]. A particularly active area of research for IR spectroscopy is biomedical analysis. Over the past two or three decades numerous studies have been conducted which demonstrate that IR spectroscopy of cells or tissues contain sufficient spectral information to differentiate between different cell types and tissue structures and even to detect pathological changes. Specific examples of these types of studies include multiple sclerosis[12] and prion-infected tissue[13] as well as cancers of the lung[14], skin[15], liver [16], and many other types of cancer[17]

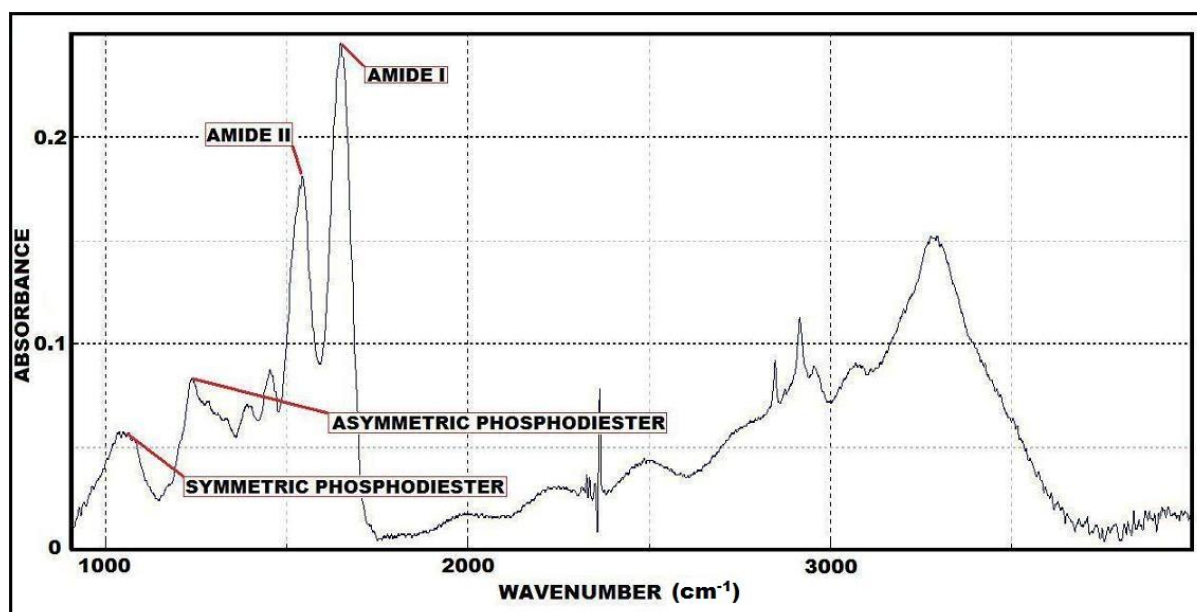


Figure 2. Example spectrum (taken with an aperture size of 50 μ m by 50 μ m, spectral resolution of 4 cm^{-1} , 50 spectra co-added) taken from a biological (human oesophagus, 5 μ m thickness) tissue section using a single channel Jasco FTIR spectrometer - The amide and phosphodiester peaks have been labelled and the spike at 2350 cm^{-1} is due to CO_2 in the atmosphere. The spectrum has been baseline corrected.

2.3.1 - The Use of IR Spectroscopy to Analyse Biological Samples and to Diagnose Cancer

The rationale for the use of IR spectroscopy in cancer detection is that the various states of the disease are accompanied by a change in the biochemistry of the tissue which is detectable spectroscopically. Particularly relevant to the research in this thesis is a publication by Maziak et al regarding the spectroscopic differences between healthy and cancerous human oesophagus tissue[18]. Maziak's publication reports that specific changes, frequency shifts (Figure 3) and changes in absorption intensity (Figure 4), were observed in the FTIR spectral features of oesophageal cancer when compared to normal tissue. After identifying the spectroscopic differences between malignant and healthy tissue Mazik then goes on to correlate these spectroscopic differences to the biochemistry of healthy and malignant tissue (thereby establishing spectroscopic criteria for the diagnosis of cancer). Some of the biochemical differences between malignant and healthy tissue include an increase in the nuclei-to-cytoplasm ratio, an increase in the amount of DNA relative to RNA, decrease in the glycogen level and a decrease in the overall CH_3 -to- CH_2 ratio. Maziak's publication is an exploratory study (involving 40 healthy samples and 40 malignant samples taken from 10 patients) which demonstrates the potential of IR spectroscopy as a tool for cancer diagnosis. However, clearly larger patient populations (clinical trials) would be required to establish IR spectroscopy as a practical diagnostic technique to be used in a clinical environment. Finally Maziak's study does not indicate the spatial resolution that spectra were collected at which makes it difficult to assess the quality of the results, particularly because other published articles[16] stress

that IR spectra collected from large sample areas give spectra which are the averages of several different tissue types.

Frequency (cm^{-1}) and assignment of the major bands in the infrared spectra of normal and malignant esophagus tissues		
Normal (cm^{-1})	Malignant (cm^{-1})	Vibrational mode and main contribution
933	923	—
964	967	$\nu_s\text{PO}_4^{2-}$ of phosphorylated proteins and nucleic acid
995	999	$\nu_s\text{PO}_4^{2-}$ of RNA
1024	1021	$\nu\text{C}-\text{O} + \delta\text{C}-\text{O}$ of glycogen
1049	1057	$\nu\text{C}-\text{O} + \delta\text{C}-\text{O}$ of glycogen
1080	1086	$\nu_s\text{PO}_2^-$ of nucleic acids
1155	1171	$\nu\text{C}-\text{O}$ of side chain groups in proteins
1237	1239	$\nu_{as}\text{PO}_2^-$ of nucleic acids
1301	1303	—
1340	1341	—
1399	1398	$\delta_s\text{CH}_3$ of proteins and lipids and $\nu_s\text{COO}^-$ of fatty acids
1453	1455	$\delta_{as}\text{CH}_3$ of proteins and lipids
1465	1466	δCH_2 of lipids
1545	1544	Amide II of proteins
1653	1656	Amide I of proteins
1741	1740	$\nu\text{C}=\text{O}$ of lipids
2853	2853	$\nu_s\text{CH}_2$ of lipids
2927	2924	$\nu_{as}\text{CH}_2$ of lipids
2957	2957	$\nu_{as}\text{CH}_3$ of lipids, nucleic acids and proteins
3291	3294	Amide A of proteins and $\nu\text{O}-\text{H}$ of carbohydrates

Figure 3. Table showing spectroscopic differences (frequency shifts) between normal and cancerous (malignant) oesophagus tissue sections. A notable omission from this table is the amide III peak at 1240cm^{-1} which may interfere with the asymmetric phosphodiester stretch of DNA. [Maziak, D.E., et al., Fourier-Transform Infrared Spectroscopic Study of Characteristic Molecular Structure in Cancer Cells of Oesophagus: An Exploratory Study. Cancer Detection and Prevention, 2007. 31(3): p. 244-53.]

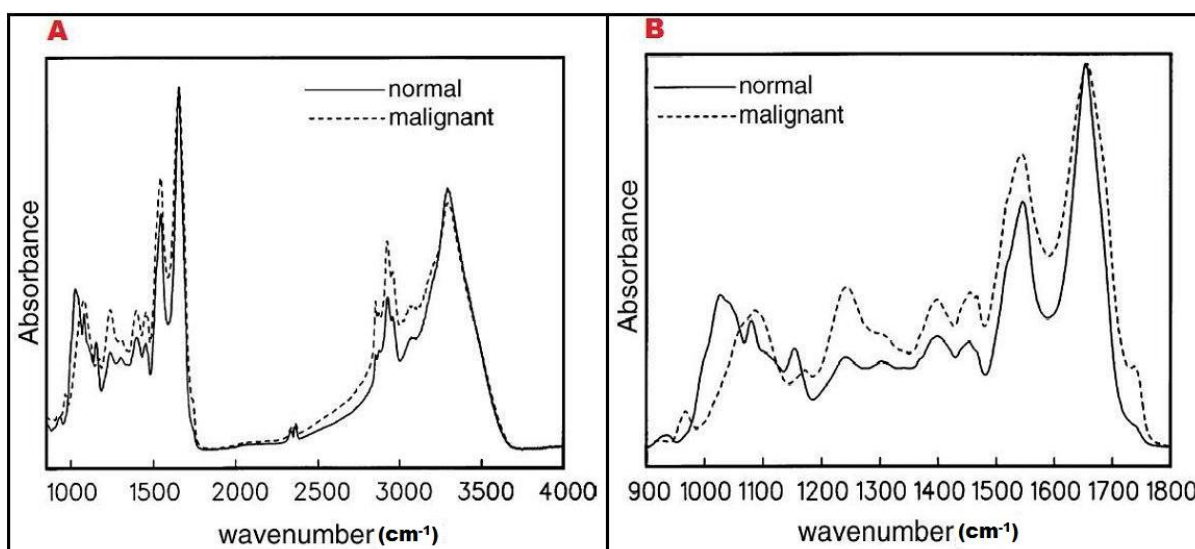


Figure 4. A) IR spectra in the frequency region of 900-4000 cm^{-1} for normal and malignant oesophageal tissue. B) IR spectra in the frequency region of 900-1800 cm^{-1} for normal and malignant oesophageal tissue. [Maziak, D.E., et al., Fourier-Transform Infrared Spectroscopic Study of Characteristic Molecular Structure in Cancer Cells of Oesophagus: An Exploratory Study. *Cancer Detection and Prevention*, 2007. 31(3): p. 244-53.]

2.3.2 - The Importance of the Collection of Microscopic Data and the Spatial Resolution of IR Spectroscopy

Work carried out by Diem et al on the correlation of IR spectroscopy to histopathology of liver tissue [16] pays particular attention to the importance of the collection of *microscopic* infrared spectra for the diagnosis of disease. It seems obvious enough that macroscopic spectral results will not contain anatomical information and will reduce the information content by averaging the spectral signatures of various tissue types.

Since the collection of microscopic data is of paramount importance it is critical to understand the spatial resolution limitations of IR spectroscopy. The spatial resolution of IR spectrometers is ultimately determined by the diffraction limit (discussed in section 3.9.1) although in practice spatial resolution is somewhat worse than the diffraction limit due to aberrations in the optical setup. As a rough estimate the diffraction limited spatial resolution is approximately equal to the wavelength of illuminating light being used which, in the case of IR, is between 3-15 μm . Diffraction limited resolution is determined theoretically from the Airy illumination pattern of a point source. In the Airy illumination pattern 84% of the energy associated with the original source is contained in a central Airy disk and the remaining 16% of energy is distributed into concentric bright rings around the Airy disk[19]. Incidentally these concentric “Airy disks” may confound faithful image generation and introduce optical artefacts into an image with diffraction limited spatial resolution. The problem of optical artefacts at diffraction limited spatial resolution is nicely demonstrated in Dumas’ [20]

recent (2009) publication where he demonstrates that spectral information regarding the lipid distribution throughout a human hair is not faithfully revealed in certain (non-confocal) optical arrangements (Figure 5). One possible method which addresses this difficulty has been suggested by Carr et al where a sophisticated mathematical treatment involving a point spread function deconvolution is applied[21].

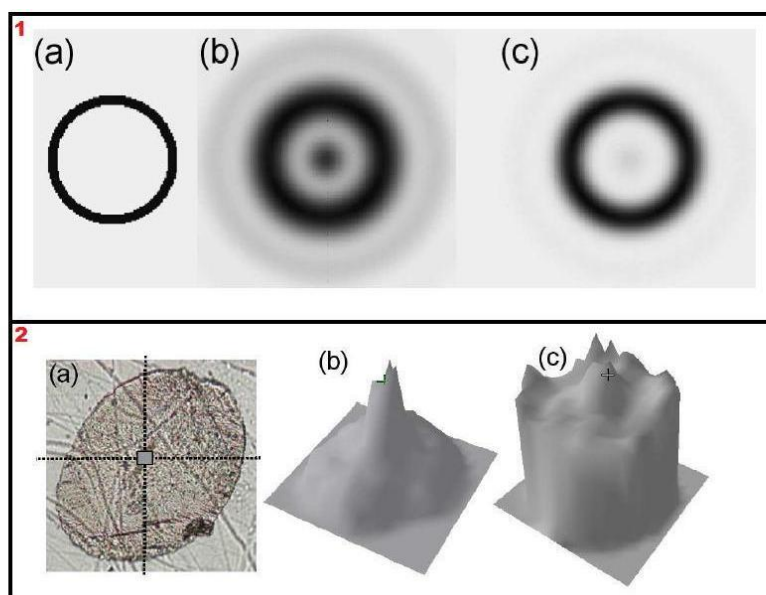


Figure 5. Optical artefacts in images close to the limits of spatial resolution;

1) a) Ring-shaped test pattern with 14 μ m diameter and a thickness of 2 μ m. b) Chemical image collected at 6 μ m for a single aperture (non-confocal geometry) c) Two apertures (confocal geometry). It is very clear that, for the non-confocal geometry, one may conclude that there is a chemical component with a characteristic frequency at 6 μ m at the center.

2) a) Visible image of human hair b) Chemical image of lipids, at 2920cm⁻¹ using a microscope an internal source and an array detector c) A confocal synchrotron IR microscope. Marked differences between the two images can be observed. First, the lipids content appears to be much higher with the conventional microscope equipped with array detector. Second, and more importantly, the presence of lipids in the outside layer of the hair section, the cuticle, is not revealed with a non-confocal arrangement.

[Dumas, P., L. Miller, and M.J. Tobin, Challenges in Biology and Medicine with Synchrotron Infrared Light. ACTA Physics Polonica A, 2009. 115(2): p. 446-454.]

For single channel detection systems spatial resolution is obtained by constraining (aperturing) the illuminated region, the region being detected, or both. A confocal optical arrangement (both illumination and detection aperturing) is shown to give around a 30% improvement in spatial resolution over a single aperture arrangement and if only one aperture is to be employed the best option is to use an aperture before the sample (illuminating region)[22]. Spatial resolution beyond the normal diffraction limit can be obtained by increasing the (numerical aperture) NA of the system, as in the (attenuated total reflection) ATR method (section 3.6.4) [23] or by using near-field techniques.

2.3.3 - Contribution to IR Spectra from Physical Properties of the Sample: Scattering

A final consideration regarding the application of IR spectroscopy to determine the biochemistry of biological tissue is the identification of spectral features which are not caused by the sample composition. Simple scattering, for example, can distort an absorption measurement and is usually manifested as a sloping baseline on an IR spectrum (this effect can be nullified by an appropriate background subtraction)[8]. Another example of scattering is “Mie scattering” which occurs in cellular structures when the interrogating light has a wavelength which is comparable (or less than) the size of the scattering particle (such as the nucleus). The result of Mie scattering on an IR spectrum is the superposition of broad undulating features across the baseline. A recent (March 2009) publication by Bassan et al [24] demonstrated Mie scattering by examining different sized isolated polymethyl methacrylate (PMMA) spheres and showing that they produce strikingly different IR spectra from each other as well when the spheres are packed closely together or when PMMA is analysed as a thin film (Figure 6). Resonant Mie Scattering occurs when there is simultaneous absorption as well as Mie scattering and it causes a sharp decrease in the intensity on the high wavenumber side of absorption bands (this corruption of the absorption bands is also referred to as “the dispersion artefact”). The phenomena of scattering, Mie scattering and resonant Mie scattering contaminate the “true” absorbance values and obviously need to be corrected for in order to utilise IR spectroscopy as a non-subjective indicator of disease. To correct for these physical artefacts computer algorithms are being developed which can operate on the IR spectra and recover the true absorption spectra[25, 26].

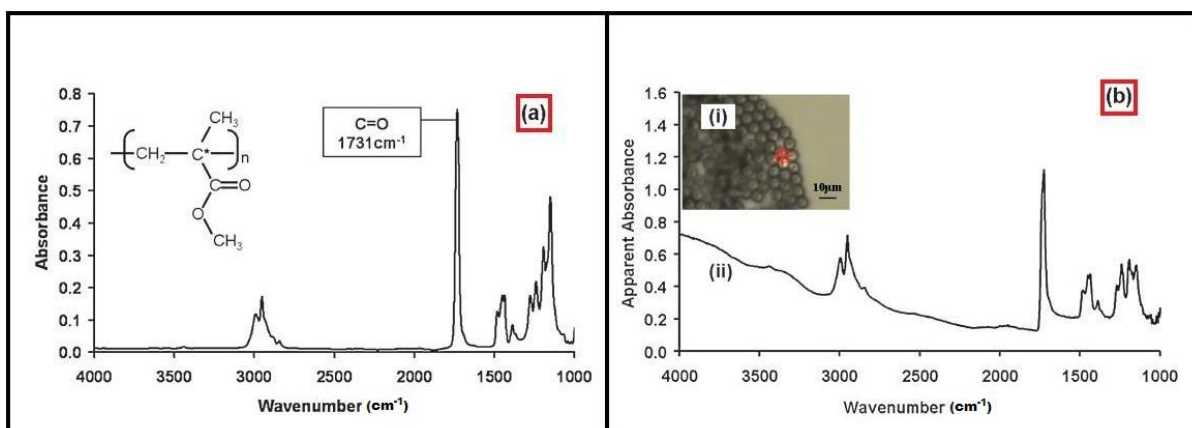


Figure 6. (a) The infrared transmission spectrum of a thin film of PMMA deposited on CaF_2 ; (b)(i) an optical image of 5.5mm diameter PMMA microspheres deposited on CaF_2 , and (b)(ii) the infrared transmission spectrum taken from a region where the PMMA spheres are close packed as indicated by the red box in (i). [Bassan, P., et al., *Resonant Mie Scattering in Infrared Spectroscopy of Biological Materials - Understanding the 'Dispersion Artefact'*. Analyst, 2009. 134: p. 1586-1593.]

2.4 - Background to Chemical and Spectroscopic Imaging

Single point collection of spectra from biological samples has shown potential for the identification of cancerous tissue. However, by point mapping (single detector), raster scanning (line of detectors) or imaging (array detector) spectral maps can be generated which add morphological information to the biochemical information provided by IR spectra. This is especially important for biological specimens since they are heterogeneous and bulk spectroscopic methods would either give variable spectra (depending on the region of tissue which is being analysed) or average out inhomogeneous parts of the sample.

In 1980 the first example of spectral mapping was published by Wells et al.[27] This publication was concerned with astronomical applications and it was not until 1990 that spectral mapping began to be carried out on biological tissue. Following these spectral mapping publications the first commercial spectral imaging (using array detectors) instrument was introduced in 1995[9]. This instrument contained an InSb detector and consequently had spectroscopic limitations since the detector wavelength cut-off is at $5\mu\text{m}$. In response to this limitation Digilab produced a MCT-based spectral mapping instrument in 1997[9]. With the availability of these spectral mapping instruments numerous studies have been carried out on biological tissue with promising results. Examples of these studies include spectral mapping of human colon carcinoma[28], lung tissue[29] and brain tumours[30].

Spectral maps contain vast amounts of data and an intuitive representation of this information is important especially if spectroscopic techniques are to be applied in the medical field. However one serious flaw spectral mapping suffers from when applied in a clinical setting is that histopathologists

are not trained in IR spectroscopy and will have difficulty interpreting spectroscopic data. This consideration has been crucial in this research and successful coding of the spectroscopic information into a format which clinicians can appreciate, and ultimately adopt, is seen as a critical success factor for this work. The use of chemical imaging (which reduces spectral maps by selecting only one significant spectral feature), or more generally, spectroscopic imaging (which combines several spectral features per spectrum in a spectral map) are highly visual and intuitive ways to represent spectral mapping data. Furthermore spectroscopic images are readily comparable to the conventional stains of samples which allows for familiar interpretation by clinicians. As such spectroscopic imaging could be used as an adjunct tool in the tissue classification process and, since extra (semi-quantitative) biochemical information is contained within these pictures, confidence in these tissue classifications can be expected to improve significantly.

2.4.1 - Chemical Imaging

To construct a chemical image first some feature of the IR spectra (such as peak height or absorbance area) is selected (usually based on the spectroscopist's pre-knowledge of the biochemistry of the sample being studied) which is then represented by a colour scale at each pixel. The spectroscopist may choose, for example, the amide I (1650cm^{-1}) absorbance height and let the minimum height correspond to blue and let the maximum height correspond to red. Then each pixel in the image is assigned its corresponding colour and chemical image is generated (Figure 7). A comparison of an H and E stain and a chemical image is shown in Figure 8.

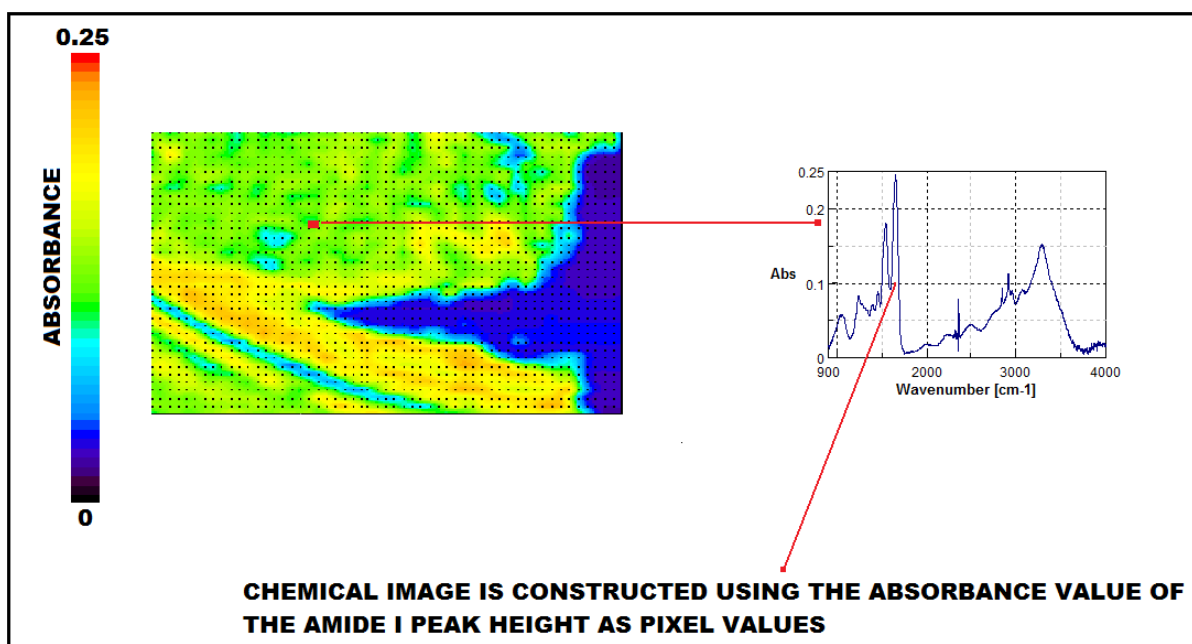


Figure 7. Example of a chemical image constructed from a spectral map using the height of the amide I peak as the pixel value. Individual spectra were collected with a single channel Jasco FTIR spectrometer using an aperture size of $50\mu\text{m}$ by $50\mu\text{m}$, a spectral resolution of 16cm^{-1} , and 50 spectra were co-added per pixel. The chemical image is made up of 55 by 36 pixels.

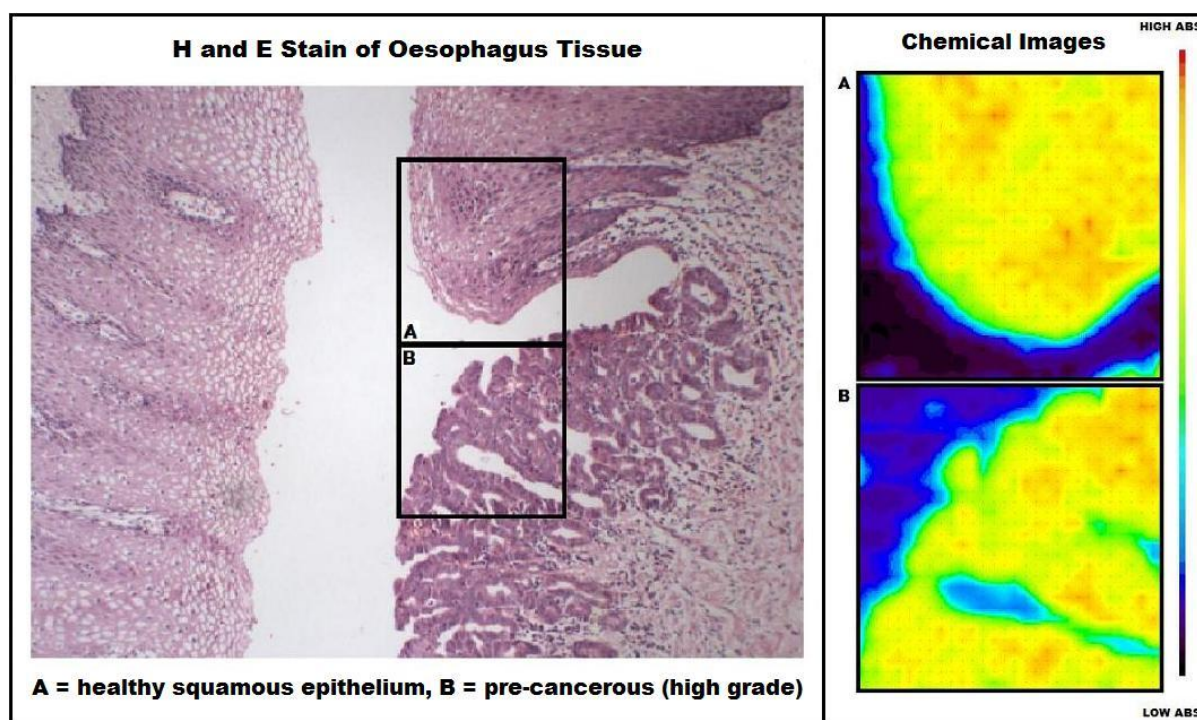


Figure 8. An example of chemical imaging from an oesophagus tissue sample containing both pre-cancerous (high grade) tissue and healthy squamous epithelium tissue. The chemical images were taken with a single channel Jasco FTIR spectrometer at an aperture size of $10\mu\text{m}$ by $10\mu\text{m}$, a spectral resolution of 16cm^{-1} and at the amide I peak (1650cm^{-1}). Both chemical images have a field of view of $300\mu\text{m}$ by $300\mu\text{m}$. Box A contains healthy squamous epithelium tissue and box B contains the pre-cancerous (high grade) tissue.

2.4.2 - Spectroscopic Imaging

Chemical images contain limited biochemical information since they are constructed using only one spectral feature. By combining several spectral features from each spectrum in a spectral map spectroscopic images can be generated which have greater biochemical content and therefore will be more accurate in the tissue classification process than chemical imaging. One of the simplest examples of spectroscopic imaging is using the ratio of two spectral features to represent the pixel value (Figure 9). However a myriad of different ways to combine the spectral information contained in a spectrum can be conceived and multivariate statistical methods can be useful to pick the optimum combination of spectral information for the purposes of tissue classification.

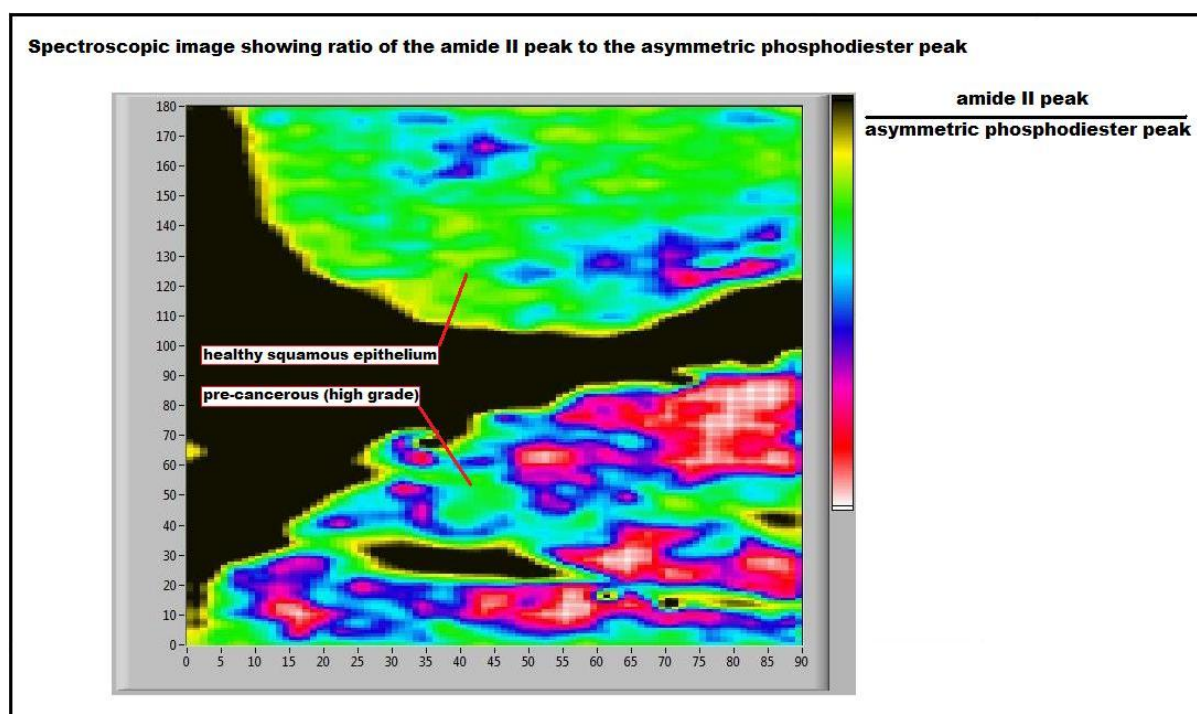


Figure 9. Example of a spectroscopic image from an oesophagus tissue sample containing both pre-cancerous (high grade) and healthy squamous epithelium tissue. The spectra were collected using a single channel Jasco FTIR spectrometer at an aperture size of $10\mu\text{m}$ by $10\mu\text{m}$ and a spectral resolution of 16cm^{-1} . The field of view of the image is $300\mu\text{m}$ by $600\mu\text{m}$. The spectroscopic image was constructed by taking the ratio of the amide II peak to the asymmetric phosphodiester peak.

2.4.3 - Analysis of Large Data Sets: Multivariate Data Analysis

The coupling of array infrared detectors to FTIR spectrometers facilitates the collection of extremely large data sets: For example, a 128 by 128 array infrared detector will collect 16384 spectra in a single measurement. In some instances it may be desirable to examine the data set pixel by pixel and to compare these spectra with libraries of known spectra. However this approach is generally impractical and multivariate statistical techniques are being increasingly employed to analyse large

sets of spectra[15, 31]. Multivariate techniques applied to these data sets are either unsupervised or supervised.

2.4.3.1 - Unsupervised Multivariate Algorithms

Unsupervised multivariate algorithms, such as “cluster analysis[15]”, take a set of unknown spectra and organise them into groups (clusters) based on the degree of spectral similarity between them. However since each spectrum in the spectral map will contain approximately 1000 data points the spectra will usually be compressed (subjectively by a human user) before it is passed onto the unsupervised algorithm. Consequently, even an “unsupervised” approach has some input from a human user regarding the biochemical origin of the spectral features. One problem with the practical application of unsupervised multivariate techniques in a clinical environment is that each data set (spectral map from a patient’s tissue biopsy) is analysed independently and the large body of pre-collected, pre-analysed spectra from similar patient biopsies are ignored in the analysis. Multivariate statistical techniques which can leverage the pre-existing libraries of spectra which exist (supervised multivariate algorithms) would probably be more readily integrated into a clinical environment.

2.4.3.2 - Supervised Multivariate Algorithms

Supervised pattern recognition methods, such as “linear discriminant analysis (LDA)[31]” require the user to train the program using pre-existing spectra collected from various tissue classifications. During this “training stage” the user will instruct the program to recognize particular spectral features (or combinations of spectral features) in the spectra that are characteristic of the various tissue classifications. The human user’s input of the spectral features represents the subjective part of the program where the user will need to supply the program with those *biochemically significant* variables (spectral features) which provide the optimum discrimination between tissue types. Once the LDA program is trained it can be used to partition the unknown spectra into the (pre-defined) tissue classifications. A particular study using LDA by Mansfield et al [31] carries out work which involves the non-subjective analysis of spectral data sets. Their strategy uses a three step process to analyse these data sets. First a genetic algorithm-guided optimal wavelength selection process, secondly a classification of spectra using a trained linear discriminant analysis program and finally a visual representation of the data in the form of chemical images.

2.4.4 - Application of Spectroscopic Imaging to a Clinical Setting: Practical Protocols

With the ability to collect spectroscopic data sets which contain morphological, as well as chemical, information considerable interest is being directed towards applying spectroscopic imaging in a

clinical setting. In this respect a significant problem is that the many excellent reports to date study a variety of organs using different instrumentation, utilising a variety of processing techniques and applying different decision making algorithms. In his 2007 paper Rohit Bhargava [4] describes practical protocols for spectroscopic imaging in a clinical environment. Bhargava describes how adjunct computer-based pattern recognition algorithms can be applied, optimised and validated with respect to conventional staining methods. The key technological developments detailed in this paper for the transfer of spectroscopic imaging from the research lab to clinical environments are; large sample sizes, robust classification which is interpretable by non-experts in spectroscopy and high fidelity FTIR imaging instrumentation. It seems obvious enough that a large number of tissue samples are necessary for statistical confidence. There does however still appear to be some disagreement regarding the best method of analysing spectroscopic data sets. In Rohit Bhargava's study a multivariate, supervised classification in which the input variables (wavelengths) are derived by performing a data reduction step on *manually* selected spectral features is preferred. The third key development described is high fidelity FTIR instrumentation. The primary concern here is for high spatial resolution (diffraction limited) spectral maps accomplished with high SNR and fast data acquisition times (on the time scale of minutes). The limiting feature of conventional FTIR instrumentation is the thermal IR source (globar) which provides a brightness (defined as photon flux or power emitted per source area and solid angle) which can be improved upon with the use of other IR sources. Brighter sources such as synchrotrons and non-linear lasers provide orders of magnitude improvement in brightness and will be discussed in section 2.5.

2.5 - IR Spectroscopy and Spectroscopic Imaging Using Laser Sources

As previously discussed, one feature of FTIR instrumentation which limits its performance is the source of IR radiation used. Thermal sources (usually a globar) have a brightness which typically provides low SNR at the high (diffraction limited $\approx 10\mu\text{m}$) spatial resolutions required for the examination of biological specimens. An alternative approach to this problem is to use a high brightness laser sources which provide improved SNR all the way down to the diffraction limit[32]. Furthermore higher brightness provides higher throughput which allows for shorter data acquisition times. IR spectroscopic studies have been reported with various laser sources such as synchrotrons[33], IR lead-salt diode lasers[34] and quantum cascade lasers (QCLs)[35].

2.5.1 - Studies Using Synchrotron Sources

Synchrotron sources have been the subject of considerable interest since they not only offer a brightness advantage over thermal sources (two to three orders of magnitude greater) they also

possess other useful features; they are continuum sources with a spectral range from far-IR through X-rays, they are pulsed (on the scale of ps) and possesses well defined polarisation states[21]. Conventional thermal sources illuminate light onto an area of approximately 100 μm whereas synchrotrons typically fill an area of 10-20 μm [36] hence the brightness advantage does not mean that synchrotrons produce more power but it is because the light is emitted from synchrotrons into a narrower range of angles than from thermal sources. A comparison of the brightness between a thermal and synchrotron source has been made by Miller et al by measuring the signal received on an IR detector as an aperture size is increased (Figure 10). In Figure 10 it is seen that because of the small synchrotron illumination area (10-20 μm) synchrotrons only offer improved performance (over single channel FTIR spectrometers) for aperture sizes less than 70 μm [33, 36]. Therefore synchrotrons are best suited to diffraction limited studies (using confocal arrangement) of small sample areas and for studies only requiring moderate spatial resolutions (greater than 50 μm) thermal sources (in single channel FTIR spectrometers) offer an equivalent SNR to a synchrotron source. The majority of synchrotron studies collect point spectra from samples and images are built up by mapping a single detector. However very recently work has been completed on coupling array detectors to multiple synchrotron beams thereby facilitating wide-field detection using high-brightness synchrotron light [37].

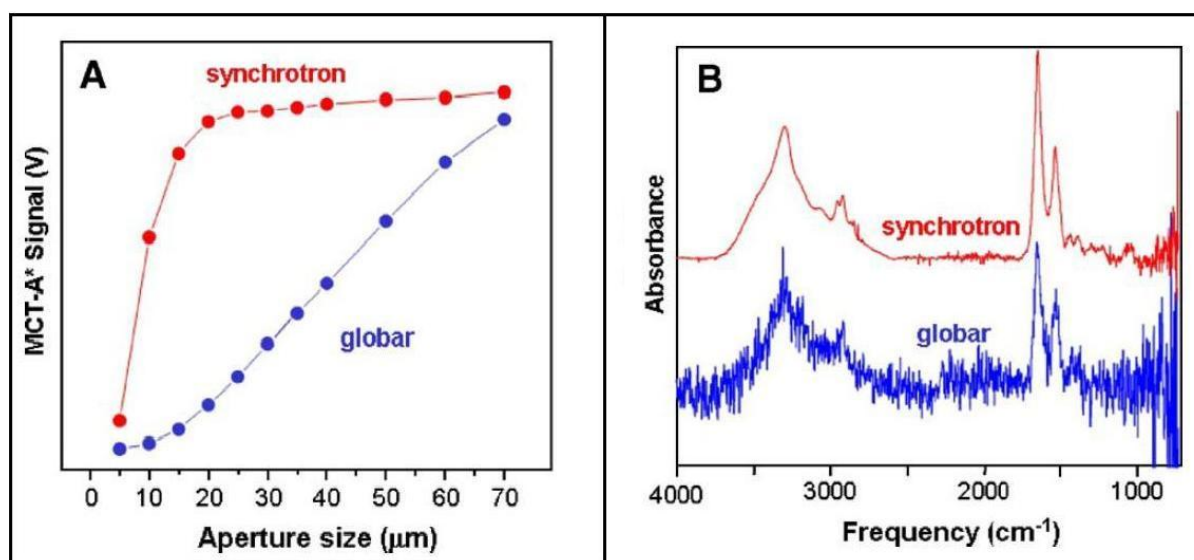


Figure 10. (A) Infrared signal through various aperture sizes using a synchrotron versus globar source. A confocal IR microscope was used with a single-point detector. (B) Infrared spectra of a single red blood cell collected with a synchrotron versus globar source. [Miller, L. and R.J. Smith, Synchrotrons Versus Globars, Point-Detectors Versus Focal Plane Arrays: Selecting the Best Source and Detector for Specific Infrared Microspectroscopy and Imaging Applications. *Vibrational Spectroscopy*, 2005. 38(1-2): p. 237-240.]

2.5.2 - Studies Using IR Lead-Salt Diode Lasers

IR lead-salt diode lasers have been utilised for spectroscopic imaging and reported by Bailey et al[34]. These laser sources (able to focus to spot size of $50\mu\text{m}$, tuneable from 1530cm^{-1} to 1620cm^{-1} , linewidth of 0.25cm^{-1} , and a power on the order of 1mW) offer a brightness advantage (unfortunately Bailey does not quantify this advantage) over thermal sources but have received less attention than other sources (synchrotrons and QCLs) since they don't give broadband irradiance and have limited tuneability over the mid-IR region. Unlike thermal and synchrotron sources, lead-salt laser diodes are monochromatic so a pre-knowledge of the spectral characteristics of the sample under study is useful so that images can be collected at the most relevant wavenumbers. The monochromatic feature of lasers is probably not much of an issue since a typical IR spectrum contains lots of superfluous information: For example if chemical images are generated using only ten wavenumbers from spectra containing 1000 data points each then 99% of the spectral data collected by a broadband source is actually redundant. In Bailey's publication he describes that images were generated with 31 by 51 (1581) pixels at wavenumber of 1568cm^{-1} and 1530cm^{-1} taking a total of 5 hours (2.5 hours for each wavenumber). A similar image (with equivalent S/N, spatial resolution and field of view) collected with a single channel FTIR spectrometer would take 1 month to generate[34], although the FTIR data set would be hyperspectral (contain images at several wavenumbers across spectral range).

2.5.3 - Studies Using QCLs

QCLs have also been reported in spectroscopic imaging [35, 38-40] and offer some attractive features. Compared to thermal sources QCLs provide up to 5 orders of magnitude improvement in the diffraction limited optical power that can be used to illuminate an object (up to 10mW average power) and also offer orders of magnitude improvement in power and brightness over lead-salt diode lasers[38]. Commercially produced QCL lasers are available in most wavelengths spanning the mid-IR spectral region and typically have tuning ranges that are approximately 10% of the central wavelength[35]. However, very recently, a widely tuneable mid-IR source has appeared on the market (Block Engineering, Marlborough, USA) which offers a tuning range of $1670\text{cm}^{-1} - 830\text{cm}^{-1}$ ($6 - 12\mu\text{m}$) which is ideally suited to IR imaging of biological tissue. Work by Guo et al evaluates the system engineering merit of laser based spectral imaging with QCLs. In Guo's paper QCLs are compared to thermal sources and are shown to offer excellent SNR ($>20\text{dB}$, or $\text{SNR} > 100$, at the diffraction limit) due to both the high brightness and the low "relative intensity noise (RIN)" of the beam (the RIN describes the instability in the power level of the beam). The RIN for QCLs is around 120dB/Hz ($\text{SNR} = 10^{12}$) compared to the RIN for a thermal source which is approximately 80dB/Hz

($\text{SNR} = 10^8$) [38]. In principle the RIN can be mitigated by normalising the laser signal to that of a 2nd reference detector that monitors the illuminating beam (see section 4.10 for a description of this kind of ratioing procedure). In a separate publication Guo demonstrates the advantages of using laser based systems for reflectance mode imaging[39].

2.5.4 - Studies Using FELs

Another IR laser source which can provides monochromatic light in the mid IR is the free electron laser (FEL). In his 2002 paper, the source issue in infrared micospectroscopy[41], Smith discusses the limitations of thermal sources and theoretically shows; firstly that synchrotrons are an excellent source for spatial resolutions on the order of the illumination wavelength and, secondly that FELs can provide better sources still for sub wavelength resolution. This is because FELs offer an even higher brightness (up to 7 orders of magnitude for a 1W FEL compared to a 2000K blackbody), at a specific wavelength, than synchrotrons (see section 3.7.3 for more details). To the best of the author's knowledge no (mid-IR) chemical imaging studies have been performed on biological samples using FEL technology.

2.5.5 - Studies Using Non-Linear Lasers

A seemingly underemployed IR source for biomedical spectroscopic studies is non-linear lasers. This is quite surprising since lasers operating with non-linear crystals offer broadly tuneable sources over the mid-IR with an even higher brightness than synchrotrons[41]. Whilst work has been carried out using non-linear laser sources in conjunction with solid immersion lenses [42] and chemical imaging of hydrocarbon contaminants on metallic surfaces[43] the possibility of biomedical chemical imaging has been largely neglected. To help bridge this deficiency the work carried out in this thesis involves chemical imaging of biological samples using a home-made, tuneable mid-IR optical parametric generator (OPG) source (section 4.4) coupled to an array detector. This system has already been shown capable of diffraction-limited spatial resolution, at a spectral resolution of $12\text{-}20\text{cm}^{-1}$, with an excellent temporal resolution of 100ps[44]. The imaging system has also been applied to the in vitro study of human ovarian cancer cells[45]. This thesis aims to apply this novel spectroscopic imaging system to the problem of cancer diagnosis.

2.6 - Alternative Technologies: Raman and Near IR spectroscopy

In addition to IR spectroscopy other optical techniques exist which are capable of extracting biochemical information from a sample and have the potential to be used as diagnostic tools, two such techniques are Raman spectroscopy and near-IR spectroscopy. It should be noted that these

techniques are better viewed as complementary rather than competitors to IR spectroscopy as they provide different information on sample composition. This fact has been exploited with the commercial introduction of integrated confocal laser Raman and FTIR microscope systems[46].

2.6.1 - Raman Spectroscopy

Raman spectroscopy is capable of giving “spectroscopic fingerprints” which are similar but complementary to those from IR spectroscopy[47] (Figure 11). As with IR spectroscopy a relationship can be established between peak intensities and molecular composition allowing for quantitative analysis. Raman spectroscopy utilizes a laser source and relies on inelastic scattering, or Raman scattering, in the visible to near infrared part of the electromagnetic spectrum. For inelastic scattering an incident laser beam interacts with phonons or other excitations in the system and, as a result, the energies of the laser photons are either shifted up or down. Measurement of the inelastically scattered light is then used to generate a Raman spectrum of the sample. Raman spectral imaging systems have extremely high achievable spatial resolution (due to the illumination source being a laser and the short wavelength of the interrogating light) coupled with excellent chemical specificity. However the use of a laser source means the interrogation of large fields of view (FOV) becomes problematic since going to larger spot sizes decreases the laser power density as a function of spot size; For example changing all linear dimensions by a factor of 10 requires 100 times the laser power to maintain equivalent Raman scattering. Therefore the coupling of Raman spectroscopy to array detectors is not as straightforward as it is with IR spectroscopy. The first steps towards realising the diagnostic value of spectroscopic techniques is demonstrated by an in vivo Raman spectroscopy clinical trial of oesophageal cancer, dysplasia (pre-cancer) and chronic inflammation caused by acid reflux[48]. These trials have been investigated by statistical analyses and have sensitivities and specificities of about 95%.

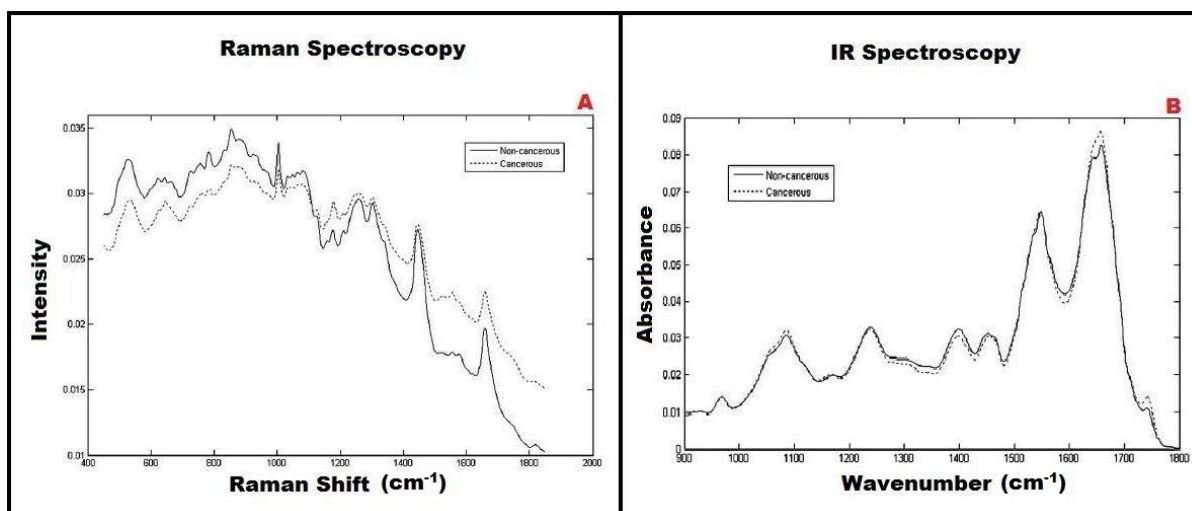


Figure 11. Comparison of spectra from Raman and IR spectroscopy A) Mean Raman spectra from non-cancerous and cancerous lymph nodes and B) Normalized FTIR mean spectra from non-cancerous and cancerous lymph nodes. [Isabelle, M., et al., Lymph Node Pathology Using Optical Spectroscopy in Cancer Diagnostics Spectroscopy, 2008. 22: p. 97-104.]

The primary disadvantage of Raman when compared to IR spectroscopy is that Raman scattering is an infrequent process (typically 10^{-9} to 10^{-6} of the large elastic scattered light)[49]. Hence the main difficulty of Raman spectroscopy is separating the weak inelastically scattered light from the intense Rayleigh scattered laser light. The low Raman efficiency means that high intensity illuminating lasers are required for the collection of spectra which can lead to photo-toxicity issues[50]. Various modifications of the Raman process enable enhancement of the Raman spectra such as coherent anti-Stokes Raman scattering (CARS) and surface enhanced Raman scattering (SERS). In addition to the weak Raman scattering cross section the Raman signal must be differentiated from the phenomenon of fluorescence which also gives signals with energies less than that of the incident photons.

The main advantages of Raman spectroscopy are that it benefits from using light sources and detectors that function in the much more technically established visible/near IR spectral region. Furthermore the shorter wavelengths used have a lower diffraction limit than mid IR and are weak scatters of water and CO₂ which do not dominate the spectra as they do with IR spectroscopy. For this reason purging is unnecessary and no special accessories are needed for measuring aqueous solutions. Also little or no sample preparation is required with Raman spectroscopy whereas with IR spectroscopy (with the exception of the ATR mode) samples are typically required to be a processed to an optimal thickness. This feature of Raman spectroscopy coupled with Raman compatible fibre optics make endoscopic studies particularly attractive.

2.6.2 - Near IR Spectroscopy

Near-IR Spectroscopy uses a region of the electromagnetic spectrum in the range of approximately 0.7 μm to 2.5 μm . IR in this region has absorptions arising from overtones and combination bands in the sample and spectra can be obtained using near-IR in a similar fashion to that of conventional IR spectroscopy.

The main disadvantage of Near-IR Spectroscopy is that the spectral features for overtone and combination bands tend to be broad and overlapped which makes assignment more difficult than in IR spectroscopy (Figure 12).

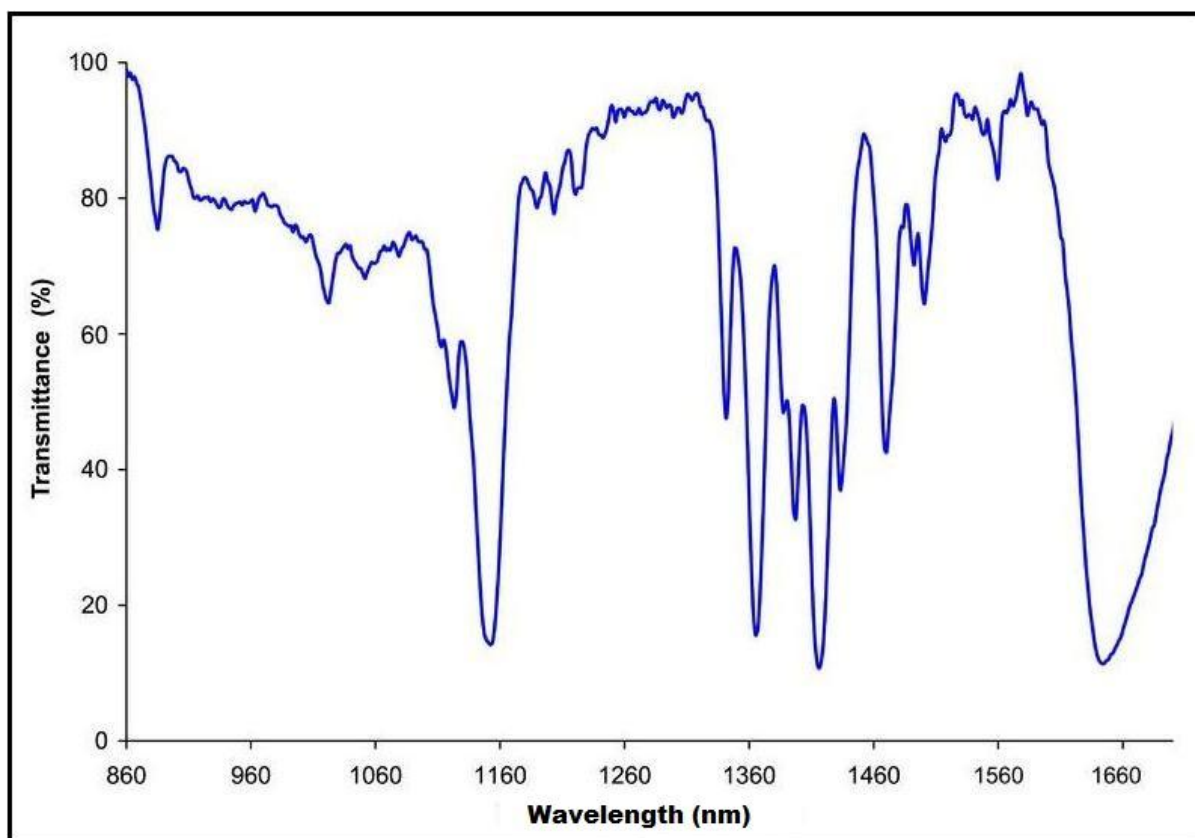


Figure 12. Near IR absorption spectrum of dichloromethane showing complicated overlapping overtones of mid IR absorption features

Near-IR radiation exhibits absorption that is one to two orders of magnitude less than mid-IR radiation. This feature of Near-IR spectroscopy eliminates the need for extensive sample preparation and makes it possible to analyze samples thicker than 5 μm . One major problem with IR micro-spectroscopy is the large bandwidth (>10 μm) it is necessary to operate with. Whilst the all-reflective optics in IR microscopes are designed to eliminate aberrations there is evidence that chromatic

aberrations persist in the optical set-up: Usually samples are placed between IR transparent substrates for inspection however the substrates are typically dispersive and introduce chromatic aberrations[51]. Near-IR spectroscopy operates over a much smaller bandwidth (<2 μ m) and so chromatic aberrations introduced from dispersive elements in an optical arrangement are minimized.

1. Cancer Research UK. Available from: <http://www.cancerresearchuk.org/cancerstats>.
2. World Health Statistics 2010. Available from: <http://www.who.int/whosis/whostat/2010/en/index.html>.
3. European Cancer IVD Market. Frost and Sullivan, 2008. Available from: <http://www.frost.com/prod/servlet/report-toc.pag?repid=M2EC-01-00-00-00>
4. Bhargava, R., Towards a Practical Fourier Transform Infrared Chemical Imaging Protocol for Cancer Histopathology. Anal Bioanal Chem, 2007. **389**(4): p. 1155-1169.
5. Jensen, P., M.R. Krogsgaard, and J. Christiansen, Observer Viability in the Assessment of Type and Dysplasia of Colorectal Adenomas, Analysed using Kappa Statistics. Dis Colon Rectum, 1995. **38**: p. 195-198.
6. Melville, D.M., J.R. Jass, and D.M. Morson, Observer Study of the Grading of Dysplasia in Ulcerative Colitis. Human Pathology, 1989. **20**: p. 1008 - 1014.
7. Kendall, C., et al., Ramen spectroscopy, A Potential Tool for the Objective Identification and Classification of Neoplasia in Barrett's Oesophagus. Journal of Pathology, 2003(5): p. 602-9.
8. Smith, B.C., Fundamentals of Fourier Transform Infrared Spectroscopy. 1996, CRC Press. p. 6.
9. Wright, N.A. and E.V. Misco, Developing a Chemical-Imaging Camera. The Industrial Physicist, 2003. **9**(5).
10. Bukowski, E.J., J.A. Monti, and S.M. Richard, Fourier Transform Infra-Red (FTIR) Spectroscopy for the Identification of Explosives. Forensic Magazine, 2006 Available from: <http://www.forensicmag.com/article/fourier-transform-infra-red-ftir-spectroscopy-identification-explosives>
11. Salvado', N., et al., Advantages of the Use of SR-FT-IR Microspectroscopy: Applications to Cultural Heritage. Analytical Chemistry, 2005. **77**(11): p. 3444-3451.
12. LeVine, S.M. and D.L. Wetzel, Chemical Analysis of Multiple Sclerosis Lesions by FT-IR Microspectroscopy. Free Radical Biology and Medicine, 1998. **25**(1): p. 33-41.
13. Kneipp, J., et al., In Situ Identification of Protein Structural Changes in Prion-Infected Tissue. Biochimica and Biophysica Acta, 2003. **1639**(3): p. 152-8.
14. Benedetti, E., et al., A New Approach to the Study of Human Solid Tumor Cells by Means of FT-IR Microspectroscopy. Society for Applied Spectroscopy, 1990. **44**(8): p. 1276-1280.
15. McIntosh, L.M., et al., Analysis and Interpretation of Infrared Microscopic Maps: Visualisation and Classification of Skin Components by Digital Staining and Multivariate Analysis. Biospectroscopy, 1999. **5**(5): p. 265-275.
16. Chiriboga, L., H. Yee, and M. Diem, Infrared Spectroscopy of Human Cells and Tissue. Part VI: A Comparative Study of Histopathology and Infrared Microspectroscopy of Normal, Cirrhotic, and Cancerous Liver Tissue. Applied Spectroscopy, 2000. **54**(1): p. 1-8.
17. Diem, M., P.R. Griffiths, and J.M. Chalmers, Vibrational Spectroscopy for Medical Diagnosis. 2008: John Wiley & Sons.
18. Maziak, D.E., et al., Fourier-Transform Infrared Spectroscopic Study of Characteristic Molecular Structure in Cancer Cells of Oesophagus: An Exploratory Study. Cancer Detection and Prevention, 2007. **31**(3): p. 244-53.
19. Hecht, E., Optics. 2001, Addison Wesley. p. 471.
20. Dumas, P., L. Miller, and M.J. Tobin, Challenges in Biology and Medicine with Synchrotron Infrared Light. ACTA Physics Polonica A, 2009. **115**(2): p. 446-454.
21. Bhargava, R. and I.W. Levin, Spectrochemical Analysis Using Infrared Multichannel Detectors. 2005, Blackwell Publishing. p. 78-80.
22. Carr, G.L., Resolution Limits for Infrared Microspectroscopy Explored with Synchrotron Radiation. Review of Scientific Instruments 2000. **72**(3): p. 1613- 1619.
23. Kazarian, S.G. and A. Chan, Micro- and Macro- Attenuated Total Reflection Fourier Transform Infrared Spectroscopic Imaging in 5th International Conference on Advanced Vibrational Spectroscopy. 2010, Applied Spectroscopy: Melbourne, Australia. **64**(5): p. 135A-152A.
24. Bassan, P., et al., Resonant Mie Scattering in Infrared Spectroscopy of Biological Materials - Understanding the 'Dispersion Artefact'. Analyst, 2009. **134**: p. 1586-1593.
25. Romeo, M. and M. Diem, Correction of Dispersive Line Shape Artifact Observed in Diffuse Reflection Infrared Spectroscopy and Absorption/Reflection (Transflection) Infrared Micro-Spectroscopy. Vibrational Spectroscopy, 2004. **38**(1-2): p. 129-132.
26. Bassan, P., et al., Resonant Mie Scattering (RMieS) Correction of Infrared Spectra from Highly Scattering Biological Samples. Analyst, 2009. **135**: p. 268-277.
27. Wells, W., A.E. Potter, and T.H. Morgan, Near-Infrared Spectral Imaging Michelson Interferometer for Astronomical Applications. Infrared Imaging Systems Technology, 1980(226).
28. Lasch, P., et al. Imaging of Human Colon Carcinoma Thin Sections by FT-IR Microspectrometry in Conference on Infrared Spectroscopy - New Tools in Medicine. 1998. San Jose, CA.

29. Krafft, C., et al., *Raman and FTIR Imaging of Lung Tissue: Methodology for Control Samples* Vibrational Spectroscopy, 2007. **46**(2): p. 141-149.
30. Krafft, C., et al., *Identification of primary tumors of brain metastases by infrared spectroscopic imaging and linear discriminant analysis*. Technology in Cancer Research and Treatment 2006. **5**(3): p. 291-8.
31. Mansfield, J.R., et al., *LDA-Guided Search Engine for the Nonsubjective Analysis of Infrared Microscopic Maps*. Applied Spectroscopy, 1999. **53**(11): p. 1323-1330.
32. Dumas, P. and L. Miller, *The Use of Synchrotron Infrared Microspectroscopy in Biological and Biomedical Investigations*. Vibrational Spectroscopy, 2003. **32**: p. 3-21.
33. Diem, M., et al., *Comparison of Fourier transform Infrared (FTIR) Spectra of Individual Cells Acquired Using Synchrotron and Conventional Sources*. Infrared Physics & Technology, 2004. **45**: p. 331-338.
34. Baily, J.A., et al., *High Spatial Resolution for IR Imaging Using an IR Diode Laser*. Applied Spectroscopy, 2000. **54**(2): p. 159-163.
35. Phillips, M.C. and N. Ho, *Infrared Hyperspectral Imaging Using a Broadly Tunable External Cavity Quantum Cascade Laser and Microbolometer Focal Plane Array* Optics Express, 2008. **16** (3): p. 1836-45.
36. Miller, L. and R.J. Smith, *Synchrotrons Versus Globars, Point-Detectors Versus Focal Plane Arrays: Selecting the Best Source and Detector for Specific Infrared Microspectroscopy and Imaging Applications*. Vibrational Spectroscopy, 2005. **38**(1-2): p. 237-240.
37. Nasse, M.J., et al., *High-Resolution Fourier-Transform Infrared Chemical Imaging with Multiple Synchrotron Beams*. Nature Methods, 2011. **8**: p. 413-416.
38. Guo, B., et al., *Multi-Wavelength Mid-Infrared Micro-Spectral Imaging using Semiconductor Lasers* Applied Spectroscopy Issue 2003. **57**(7): p. 811-822.
39. Guo, B., et al., *Laser-Based Mid-Infrared Reflectance Imaging of Biological Tissues*. Medical and Biological Imaging, 2004. **12**(1): p. 208-219.
40. Le, H.Q. and Y. Wang, *Semiconductor Laser Multi-Spectral Sensing and Imaging*. Sensors, 2010. **10**(1): p. 544-583.
41. Smith, T.I., *The Source Issue in Infrared Microspectroscopy*. Nuclear Instruments and Methods In Physics Research, 2002. **483**: p. 565-570.
42. Michaels, C.A., *Mid-Infrared Imaging with a Solid Immersion Lens and Broadband Laser Source*. Applied Physics Letters, 2007. **90**: p. 121131-3.
43. Ludowise, P.D., et al., *A PPLN Laser-Based System for Chemical Imaging*, in *Imaging Spectrometry. Conference No5, Denver CO*. 1999, Society of Photo-Optical Instrumentation Engineers.
44. Amrania, H., A. McCrow, and C.C. Phillips, *A Benchtop, Ultrafast Infrared Spectroscopic Imaging System for Biomedical Applications* Review of Scientific Instruments, 2009. **80**(12): p123702-1 to 123702-6
45. Amrania, H., et al., *Ultrafast Infrared Chemical Imaging of Live Cells*. Chemical Science, 2010. **2**(1): p. 107-111.
46. Isabelle, M., et al., *Lymph Node Pathology Using Optical Spectroscopy in Cancer Diagnostics* Spectroscopy, 2008. **22**: p. 97-104.
47. Krafft, C., et al., *Raman and FTIR Microscopic Imaging of Colon Tissue: A Comparative Study*. Journal of Biophotonics, 2008. **2**: p. 154-169.
48. Puppels, G.J., *In Vivo Raman Spectroscopy*, in *Institute of Physics Conference Series 165: Symposium 1*, D.B. Williams and R. Shimuzu, Editors. 2000.
49. Kendall, C., et al., *Vibrational Spectroscopy: A Clinical Tool for Cancer Diagnostics*. The Royal Society of Chemistry, 2009. **134**: p. 1029-1045.
50. Uzunbajakava, N., et al., *Non-Resonant Raman Imaging of Protein Distributions in Single Human Cells*. Biopolymers, 2002. **72**: p. 1-9.
51. Lasch, P. and J. Kneipp, *Biomedical Vibrational Spectroscopy*. 2008, Wiley-Interscience, p. 42.

3.0 - Theory

In this chapter the important theoretical concepts regarding the research conducted in this thesis will be discussed. Firstly the theory of IR absorption and quantitative analysis will be covered. Then the instrumentation will be considered (imaging modes, IR sources and IR detectors). Finally the important concepts of spatial resolution, spectral resolution and noise will be discussed in terms of what is practically achievable with a spectroscopic imaging system.

3.1 - IR Spectra

Infrared radiation is absorbed by matter and converted into energy of molecular vibration. If a sample is illuminated with a range of wavenumbers (667cm^{-1} - 5000cm^{-1}) then an IR spectrum can be generated by determining the % absorption, %transmission or absorbance at each wavelength. By comparing an unknown sample spectrum with libraries of known spectra from pre-analysed samples the unknown sample can be identified. An example of an IR spectrum (from a biological sample) is displayed in Figure 1.

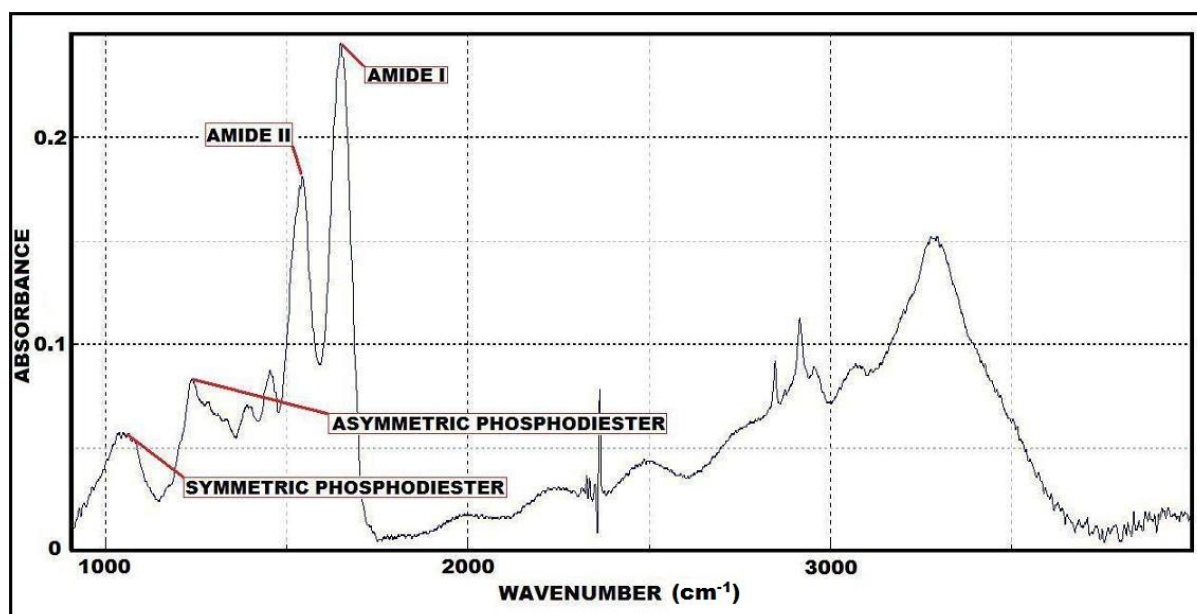


Figure 1. Example spectrum (taken with an aperture size of $50\mu\text{m}$ by $50\mu\text{m}$, spectral resolution of 4cm^{-1} , 50 spectra co-added) taken from a biological (human oesophagus, $5\mu\text{m}$ thickness) tissue section using a single channel Jasco FTIR spectrometer - The amide and phosphodiester peaks have been labelled and the spike at 2350cm^{-1} is due to CO_2 in the atmosphere. The spectrum has been baseline corrected.

Typically wavenumber (or wavelength) is plotted on the x axis and a variable describing the sample absorption properties (such as % transmission (%T), % absorption (%A) or absorbance (A)) is plotted on the y axis. %transmission, %absorption and absorbance are related by equations 3.0-3.3.

$$\%T = \frac{\text{sample spectrum}}{\text{background spectrum}} \times 100 \quad (3.0)$$

$$\%A = 100 - \%T \quad (3.1)$$

$$A = -\log_{10} \left[\frac{\text{sample spectrum}}{\text{background spectrum}} \right] = \log_{10} \left(\frac{1}{T} \right) \quad (3.2)$$

Where;

$$T = \frac{\%T}{100} \quad (3.3)$$

The positions of peaks (or troughs) in a spectrum can be correlated with molecular bonds within the sample and the height (or area) of the peaks gives an indication of the amount of chemical species present.

3.2 - Theory of Molecular Vibrations and IR Absorption

A caveat of the molecular vibration/absorption rule is that for absorption to occur a molecular vibration must change the dipole moment of a molecule. The reason why a dipole moment change must occur for IR radiation to be absorbed involves the mechanism by which infrared photons transfer their energy to a molecule. In general; the larger the dipole change the stronger the intensity of the corresponding peak in the IR spectrum.

There are two types of molecular vibration; stretching or bending. To illustrate the theory of molecular vibration consider the molecular vibrations of CO₂ (Figure 2). CO₂ is a linear molecule and has four fundamental vibrations. The asymmetrical stretch of gives a strong absorption at 2350cm⁻¹ (this band is often recorded on sample spectra due to the presence of CO₂ in the atmosphere). The two scissoring (or bending) vibrations are equivalent and therefore have the same frequency appearing in an IR spectrum at 666cm⁻¹. Finally the symmetrical stretch of CO₂ does not absorb infrared radiation because this vibration causes no change in the dipole moment of the molecule.

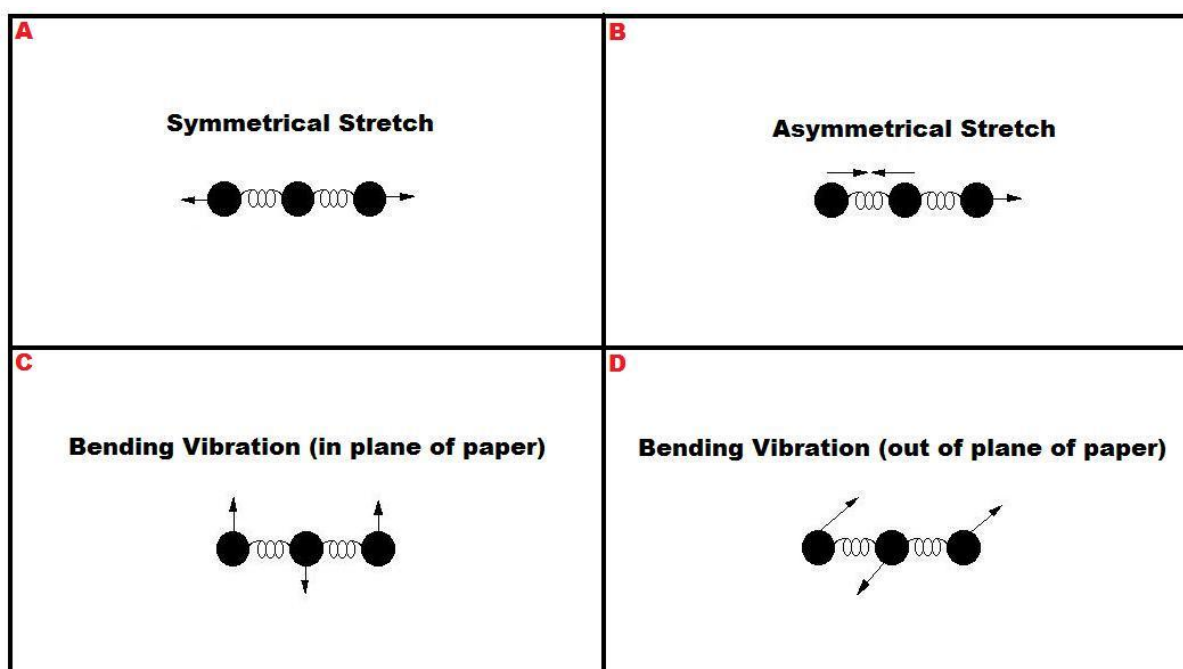


Figure 2. Diagram showing the fundamental vibrational modes of a CO₂ molecule. A) Symmetrical stretch. This mode is IR inactive since it does not change the dipole moment of the molecule. B) Asymmetrical stretch observed at 2350cm⁻¹ of an IR spectrum. C) Bending vibration (in plane of page) observed at 666cm⁻¹. D) Bending vibration (perpendicular to plane of page) also observed at 666cm⁻¹ (both bending vibrations are degenerate).

As a simple example consider the stretching vibration of a diatomic molecule. Assuming the diatomic molecule behaves like a simple harmonic oscillator analogous to two masses (m_1 and m_2) connected by a spring obeying Hooke's law. A classical analysis of this system using Newton's and Hooke's law gives the following results;

$$E = \frac{1}{2}kx^2 \quad (3.4)$$

Where;

E = Potential energy of system

k = Spring constant

x = displacement

$$\omega = \sqrt{\frac{k}{\mu}} \quad (3.5)$$

Where;

ω = angular frequency of vibration

μ = reduced mass

$$\mu = \frac{m_1 m_2}{m_1 + m_2} \quad (3.6)$$

However a quantum mechanical treatment using Schrodinger's Equation of the same problem indicates that the energy of the system is quantised.

$$E_v = \omega_e \left(v + \frac{1}{2} \right) \quad (3.7)$$

Where;

E_v = Quantised energy levels

v = vibrational quantum number (= 0,1,2,3,.....)

ω_e = spectroscopic constant

$$\omega_e = \frac{\omega}{2\pi c} \quad (3.8)$$

Where;

c = speed of light

In this simple (quantum) model energy is absorbed in equal discrete units and the diatomic molecule will undergo transitions up and down a ladder of energy levels. Transitions of two or more levels at once correspond to bands called overtones in the IR spectrum (used in near-IR spectroscopy, section 2.6.2). In order to make the model more realistic the harmonic potential can be replaced with an anharmonic potential to account for the physical properties of a diatomic molecule such as dissociation at high energies (Figure 3).

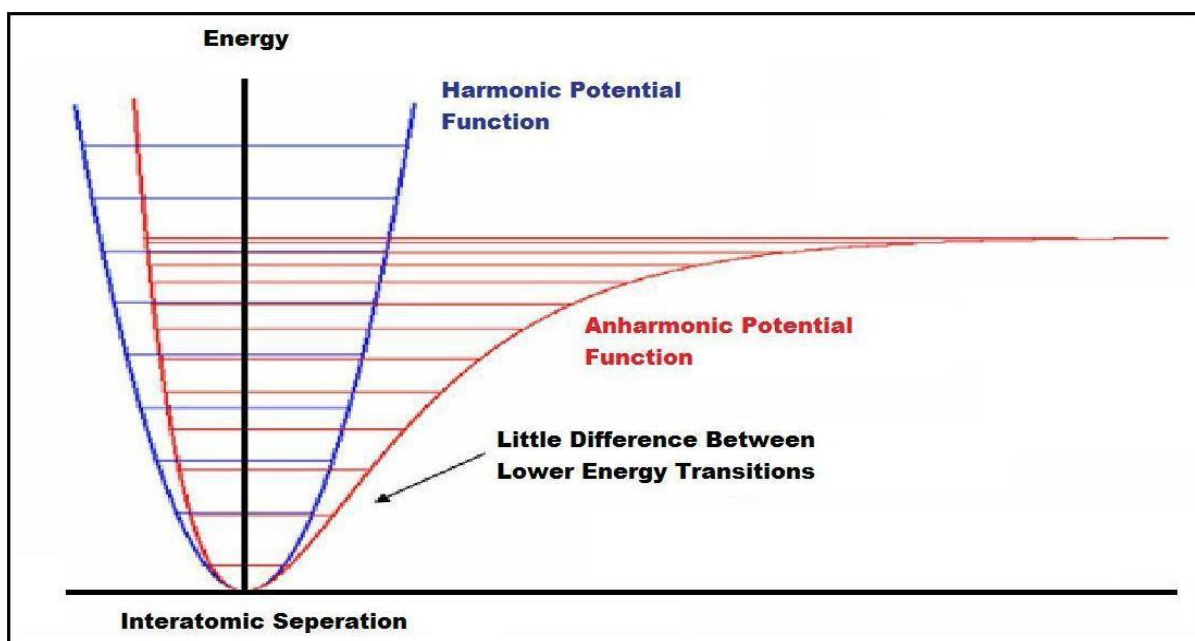


Figure 3. Comparison of harmonic and anharmonic potentials for a diatomic molecule

To account for the anharmonicity the potential function equation 3.7 can be generalised to;

$$E_v = \omega_e \left(v + \frac{1}{2} \right) - \omega_e x_e \left(v + \frac{1}{2} \right)^2 \quad (3.9)$$

Compared to the harmonic potential the anharmonic potential perturbs the lower energy levels of the harmonic model only very slightly. However as the interatomic distance increases the energy levels become more closely spaced and transitions require less energy.

3.3 - Biochemical Significance of Spectral Data from Biological Samples

When applied to biological tissue IR spectroscopy produces complex spectra with overlapping and broad spectral features across the entire spectral range. There may be significant contributions to individual spectral features from several different chemical components as well as structural (secondary protein structure and conformation of nucleic acid structure have been demonstrated to affect spectral features [1] and interaction factors (a solid sample spectrum may have broader spectral features than a gaseous sample spectrum of the same chemical species). For example the so called “asymmetric phosphodiester” spectral feature at 1240cm^{-1} has significant contributions from protein, glycoprotein and DNA (Figure 4). Therefore one should not always assume that a spectral feature is entirely the product of a single chemical species within a sample. Since these spectra have some dependence on the sample composition it is useful to examine the biochemical makeup of a typical sample of biological tissue. Biological tissue is primarily composed of (excluding water)

nucleic acids (DNA and RNA), proteins, lipids and carbohydrates. A complete library of the spectra of individual biochemical components can be found in the appendix of Diem, Griffiths and Chalmers book; Vibrational Spectroscopy for Medical Diagnosis[2].

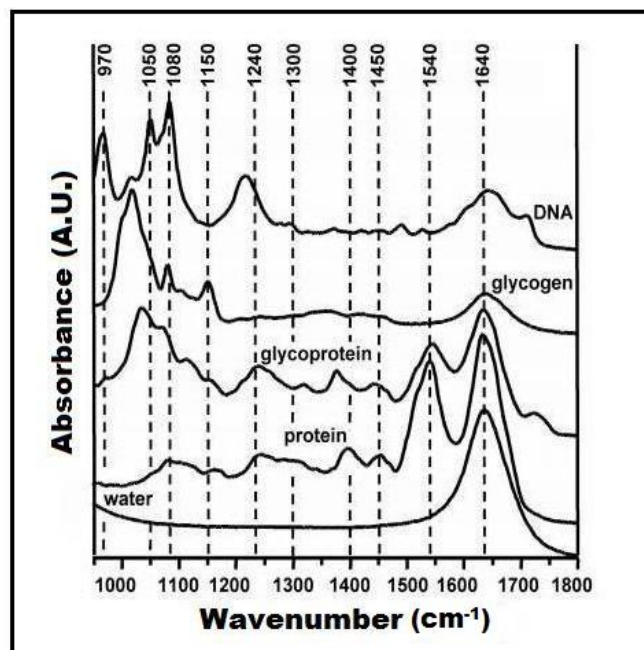


Figure 4. IR Spectra of individual bio molecules. Spectra were acquired in ATR mode from dehydrated films of pure DNA, protein, glycogen and glycoprotein. It can be seen that certain spectral features (such as the amide I peak at 1640cm^{-1}) have contributions from several biochemical components. [Wang, T.D., et al., Detection of Endogenous Biomolecules in Barrett's Esophagus by Fourier Transform Infrared Spectroscopy. PNAS, 2007. 104(40): p. 15864-15869.]

3.3.1 - Nucleic Acids: Phosphodiester Vibrations

Nucleic acids are polymers constructed from individual units (monomers) called nucleotides. Nucleic acids in biological entities exist in two main types; RNA and DNA. DNA contains the genetic instructions used in the development of living organisms. When proteins are manufactured within a cell first DNA is transcribed into (messenger) RNA and then RNA is translated into protein. RNA is then vital in the protein synthesis phase but it also fulfils other functions in the cell (such as “transfer RNA” and “ribosomal RNA” which both help facilitate the process of translation of RNA into proteins). There are only five different nucleotides which compose the “building blocks” for DNA and RNA polymers (Figure 5). During spectroscopic analysis reference is made to the symmetric phosphodiester stretch (1080cm^{-1}) and the asymmetric phosphodiester stretch (1238cm^{-1}). The phosphodiester vibrations are vibrational modes which are associated with the phosphodiester bond (shown in Figure 5) which is found in both RNA and DNA.

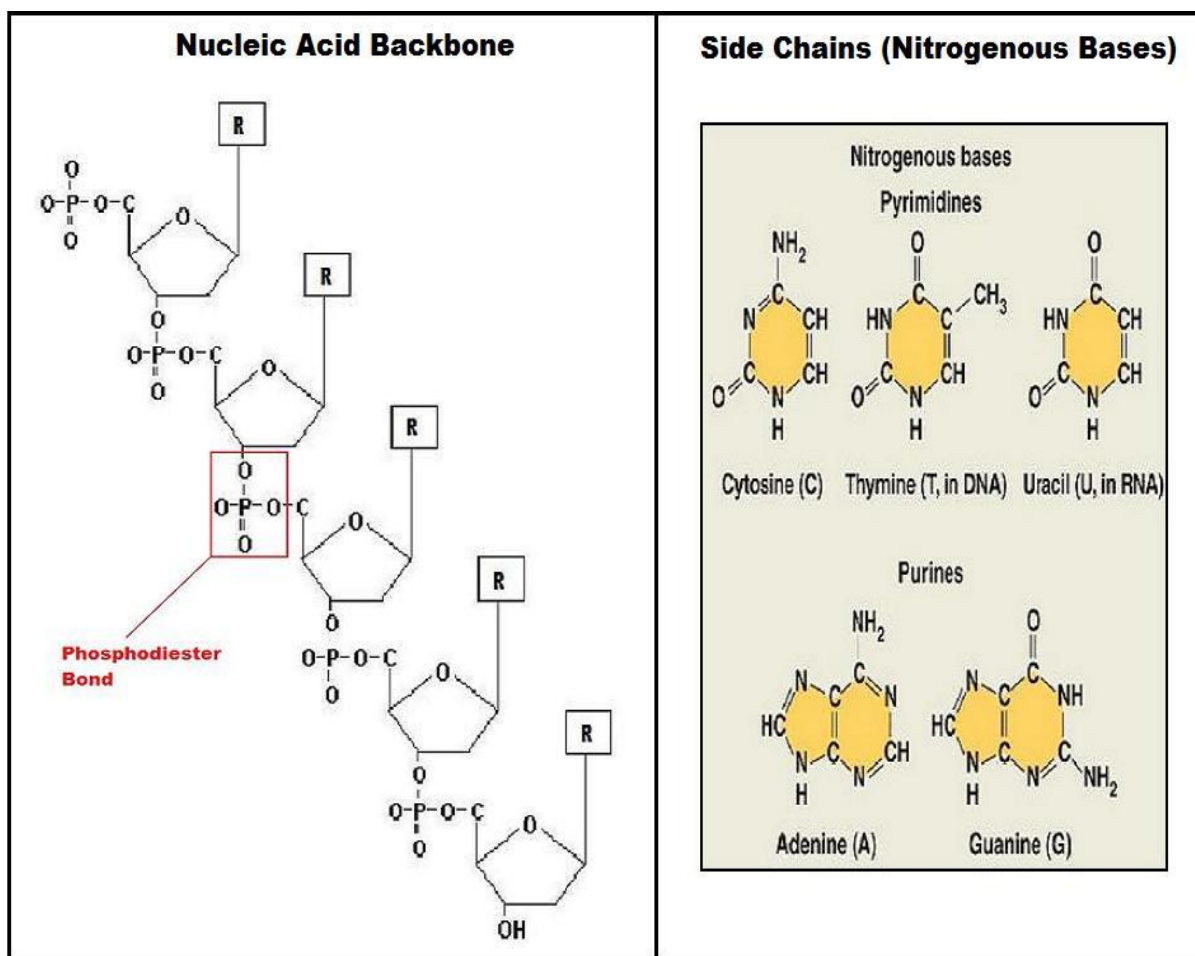


Figure 5. Nucleic acid structure - The DNA / RNA backbone is shown on the left. Nitrogenous bases (shown on the right) connect to the backbone at positions labelled R. The nitrogenous bases labelled C, A and G are found in both DNA and RNA whilst the nitrogenous bases labelled T and U are only found in DNA and RNA respectively. An example of the phosphodiester bond is also labelled on the diagram.

3.3.2 - Proteins: Amide Vibrations

Proteins fulfil a variety of functions in biological organisms including cell structure, cell signalling and immune response. Proteins are polymers composed of 20 amino acids (Figure 6). Amino acids form chains during the translation process in protein manufacture and these chains have a repeating backbone structure. Proteins come in a huge variety and their diversity is made possible by the interactions of the side chains with themselves and their external environment. Proteins provide the main contribution to some of the most salient features in a biological spectrum including the amide I (1650cm^{-1}) and amide II (1550cm^{-1}) peaks.

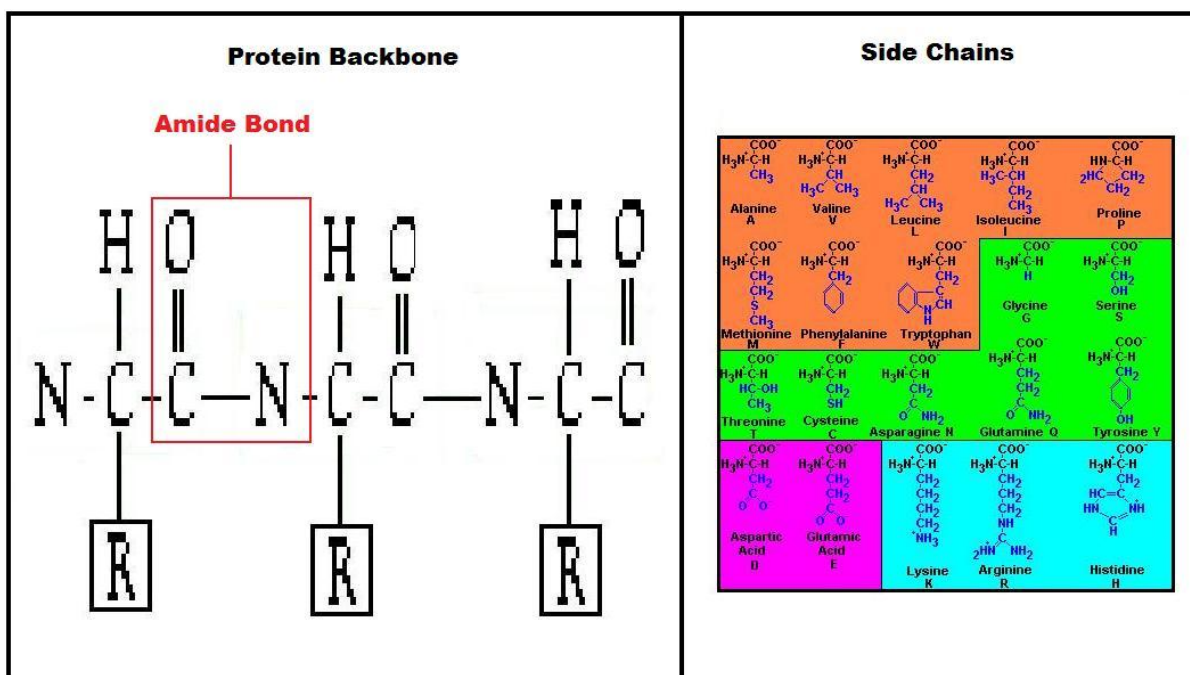


Figure 6. Protein structure: The protein backbone is shown on the left and the side chains (shown on the right) connect at the positions labelled R. Side chains in the orange area are non-polar and hydrophobic, those in green are polar and hydrophobic, those in magenta are acidic and those in blue are basic. The amide bond has been labelled on the backbone of the protein chain.

3.3.3 - Lipids

Lipids are a broad class of biological molecule (such as fats) which exhibit some hydrophobic tendencies. Lipids hydrophobic properties make them especially useful for cell membranes and they commonly exist as lipid bilayers. In addition to this lipids are used in energy storage and cell signalling. The hydrophobic part of a lipid consists of a long hydrocarbon tail which contains several CH_2 bonds which are spectroscopically active (2850cm^{-1} and 2959cm^{-1}).

3.3.4 - Carbohydrates

Carbohydrates are primarily used for energy storage. Examples of carbohydrates include glucose, fructose and glycogen. Glycogen consists of a core protein, glycogenin, surrounded by approximately 30,000 glucose units. Glycogen provides the main contribution to peaks in biological spectra at 1025cm^{-1} and 1155cm^{-1} .

3.4 - Quantitative Analysis of Spectra: Beer's Law

Infrared spectroscopy can not only be used to identify the presence of a chemical species it can also be used to quantify the concentration of a chemical in a sample. In this section both single component and multi-component samples are discussed.

3.4.1 - Single-component Quantitative Analysis

For a single component sample the height (or area) of a peak in the absorbance spectrum is directly proportional to the quantity of chemical species in the Infrared beam. The fundamental result used to extract chemical concentrations from absorbance data (measured in terms of height) is Beer's law;

$$A = \epsilon lc \quad (3.10)$$

Where;

A = Absorbance (measured as a height)

ϵ = Absorptivity (m^2/mol)

l = Path-length (m)

c = Concentration (mol/m^3)

The absorptivity is a fundamental property of a particular molecular species and provides the link between absorbance and concentration. The absorptivity depends of the type of molecule and has a wavelength dependence ($\epsilon = \epsilon(\lambda)$). The absorbance is measured as a peak height or peak area from a spectrum. Care must be taken in the application of Beer's law as it is not always valid: The derivation of Beer's law assumes that every absorbing particle behaves independently and errors are introduced when particles are lying along the same optical path such that some particles are in the "shadow" of others. Therefore intense absorbance bands are not to be used to perform quantitative analysis since at high chemical concentrations molecular interactions become significant.

3.4.2 - Multi-component Quantitative Analysis

Most samples of interest, such as biological specimens, are composed of several different chemical components (such as proteins and nucleic acids) and it is often desirable to determine the concentrations of several components at once. If the absorbance at a particular wavelength is assumed to be the sum of all the absorbances of all the sample components then quantitative analysis can be performed by assuming the additivity of Beer's law. The introduction of additional absorptive components into the analysis increases the mathematical complexity of the model and there are several representations to choose from. Multi-component methods typically involve the analysis of individual sample components (in the case of bio-molecules this includes the analysis of isolated DNA and protein) to create the model. One study by Wang et al[3] has gathered spectra from individual cellular components (Figure 4) and derived the tissue concentrations of components

based on extinction coefficients derived from dry powder spectra (Figure 7). Using these individual bio-component spectra and tissue concentrations a linear model was applied and the predicted spectra for various oesophagus tissue classifications (squamous, Barrett's non-dysplasia, Barrett's dysplasia and gastric) were compared with the models predictions (Figure 8). The multi-component model employed by Wang et al provides an excellent fit to the measured spectra with a relative error < 0.1%

Tissue	DNA, %	Protein, %	Glycogen, %	Glycoprotein, %	Rel err, %
Squamous (n = 38)	5 ± 3	78 ± 8	15 ± 7	2 ± 2	0.08 ± 0.06
Barrett's (n = 38)	6 ± 4	88 ± 8	3 ± 3	3 ± 4	0.09 ± 0.07
Gastric (n = 22)	9 ± 3	75 ± 6	4 ± 3	12 ± 4	0.05 ± 0.03
Pathologist #1, Barrett's					
Nondysplastic (n = 23)	4 ± 3	91 ± 5	3 ± 3	2 ± 3	0.10 ± 0.09
Dysplastic (n = 15)	9 ± 4	83 ± 8	3 ± 3	5 ± 5	0.09 ± 0.07
Pathologist #2, Barrett's					
Nondysplastic (n = 20)	3 ± 3	92 ± 5	2 ± 2	2 ± 3	0.12 ± 0.10
Dysplastic (n = 18)	8 ± 4	83 ± 7	3 ± 3	5 ± 4	0.09 ± 0.07

Figure 7. Table showing tissue concentration of DNA, protein, glycogen and glycoprotein from various biological tissue (human oesophagus) classifications (squamous, Barrett's (non-dysplasia and dysplasia) and gastric mucosal derived from a model based on the extinction coefficients of dry powder spectra. In this study two independent pathologists graded the Barrett's tissue as either non-dysplasia or non-dysplasia. [Wang, T.D., et al., Detection of Endogenous Biomolecules in Barrett's Esophagus by Fourier Transform Infrared Spectroscopy. PNAS, 2007. 104(40): p. 15864-15869.]

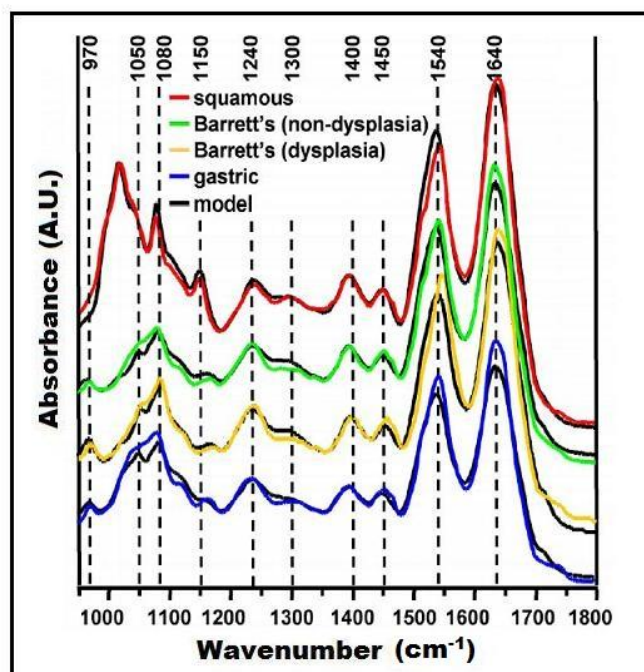


Figure 8. Comparison of a quantitative model results (black spectra) to representative measured spectra of various biological tissue (human oesophagus) classifications (squamous, Barrett's (non-dysplasia and dysplasia) and gastric mucosal derived from a model based on the extinction coefficients of dry powder spectra. [Wang, T.D., et al., Detection of Endogenous Biomolecules in Barrett's Esophagus by Fourier Transform Infrared Spectroscopy. PNAS, 2007. 104(40): p. 15864-15869.]

3.5 - Instrumentation Used for the Collection of IR Spectra and Spectral Maps

In this section the conventional instrumentation used to collect IR Spectra and spectral maps (dispersive and FTIR spectrometers) is described.

3.5.1 - Dispersive IR Spectrometer

The first IR spectrometers were dispersive instruments which utilised a diffraction grating to select individual wavelengths. By selecting several wavelengths (one after another) across the spectral range an entire IR spectrum can be generated. For each wavelength the beam of monochromatic infrared light is divided into two separate beams. One is passed through the sample, the other passed through a reference which replicates the conditions the sample exists in. Both beams then pass through a beam splitter which quickly alternates which of the two beams (sample or reference) enters a detector. Alternately a broadband beam can be passed through the sample and reference, chopped and then reflected off a diffraction grating to select individual wavelengths (Figure 9). The two signals (the background and sample) are then used in equations 3.0 -3.3 and an absorbance spectrum is obtained.

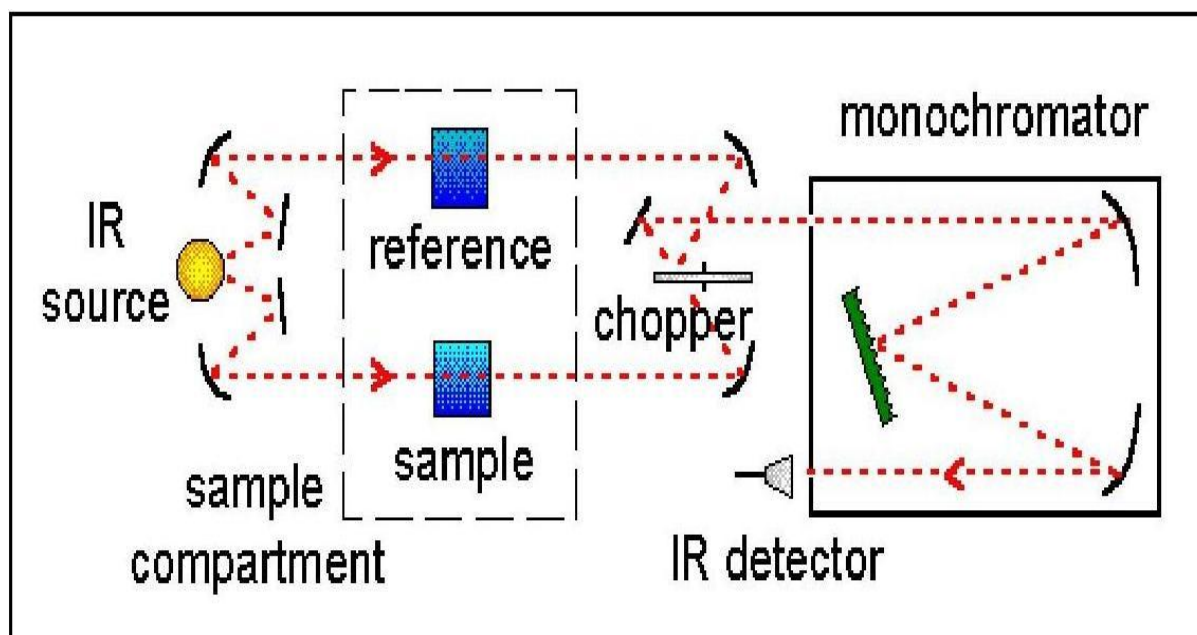


Figure 9. Diagram showing the operation of a dispersive IR spectrometer [<http://elchem.kaist.ac.kr/vt/chem-ed/spec/vib/ir-instr.htm>]

3.5.2 - FT-IR Spectrometer

For most applications dispersive IR spectrometers have been supplanted by Fourier transform infrared (FTIR) spectrometers which give significant advantages (reduced data acquisition time, higher S/N ratio and increased throughput) over dispersive IR spectrometers. FTIR spectroscopy provides an alternative method of collecting spectra: By utilizing an interferometer a continuum of frequencies can be measured simultaneously. The measured signal is an interferogram which can be Fourier transformed to give a spectrum (Figure 10).

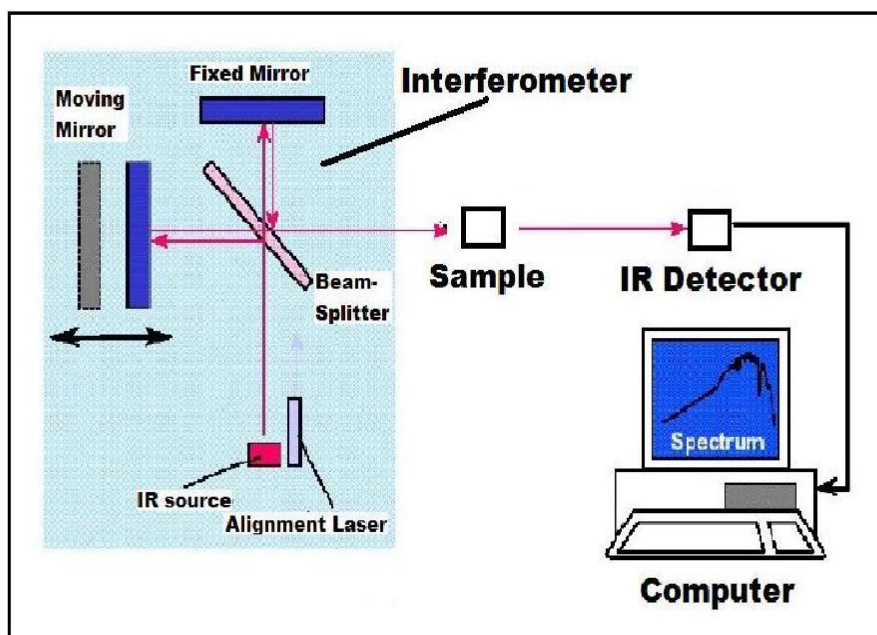


Figure 10. FTIR Spectrometer. By using an interferometer a continuum of frequencies can be measured simultaneously. The measured signal is then an interferogram which can be Fourier transformed to give a spectrum.

3.6 - Alternative Modes of IR Spectroscopy

IR spectra can be collected by operating an IR spectrometer in transmission, reflectance, transfection or ATR mode. In the following sections (3.6.1 - 3.6.4) the salient features of each mode and their respective strengths and weaknesses are discussed.

3.6.1 - Transmission Mode Spectroscopy

For the transmission sampling technique the infrared radiation is passed through the sample and an IR detector detects the portion of the beam that is transmitted.

To avoid complete absorption biological samples must be processed to a thickness of about $5\mu\text{m}$. For the case of biological tissue this typically involves fixation, waxing and the use of a microtome. Transmission mode not only provides the highest SNR than any other mode it is also useful since transmission spectra are amenable to quantitative analysis using Beer's law.

3.6.2 - Reflectance Mode Spectroscopy

For reflectance mode spectroscopy the IR light is incident on the sample through an objective and reflected light is then collected by the same objective and sent to the detector.

Reflectance mode IR spectroscopy achieves much lower SNRs compared to transmission mode (since most of the illuminating IR radiation is absorbed). The main advantage of reflectance mode spectroscopy is that spectra can be obtained from the surface of unprepared or thick specimens.

3.6.3 - Transflection Mode Spectroscopy

A popular method for acquiring IR spectra is the so called “transflection” mode. In this mode special slides are used which are composed of glass that is coated with a thin layer of Ag/SnO₂. These slides are transparent to visible light and chemically inert but are completely reflective in the infrared. To collect an IR spectrum the IR beam is transmitted through the sample, reflected off the coating, and then transmitted through the sample again. Since the radiation traverses the sample twice the sample must be half as thick (typically 3μm) as it is in the normal transmission mode.

The major advantage of the Transflection mode is that of cost. A Transflection slide is approximately \$2 a slide (low e slide, Kevley Technologies, Chesterfield, OH) and an IR substrate such as BaF₂ is around \$200 a slide (however if BaF₂ slides were bulk manufactured the cost can be expected to fall significantly). Clearly if IR spectroscopy is to be applied in a clinical setting then it is imperative that the technique be made as cost-effective as possible so transflection slides offer a major commercial advantage.

3.6.4 - Attenuated Total Reflection (ATR) Spectroscopy

In ATR mode an infrared beam is directed into a crystal with a high refractive index at a certain angle such that total internal reflection occurs (Figure 11). An evanescent wave is created that extends beyond the surface of the crystal into the sample. This evanescent wave penetrates the sample surface by a few microns (0.5μm - 5μm). Consequently, there must be good contact between the sample and the crystal surface. In regions of the infrared spectrum where the sample is absorptive the evanescent wave will be attenuated. The emerging IR beam is modified by the evanescent wave and is passed to the detector in the IR spectrometer.

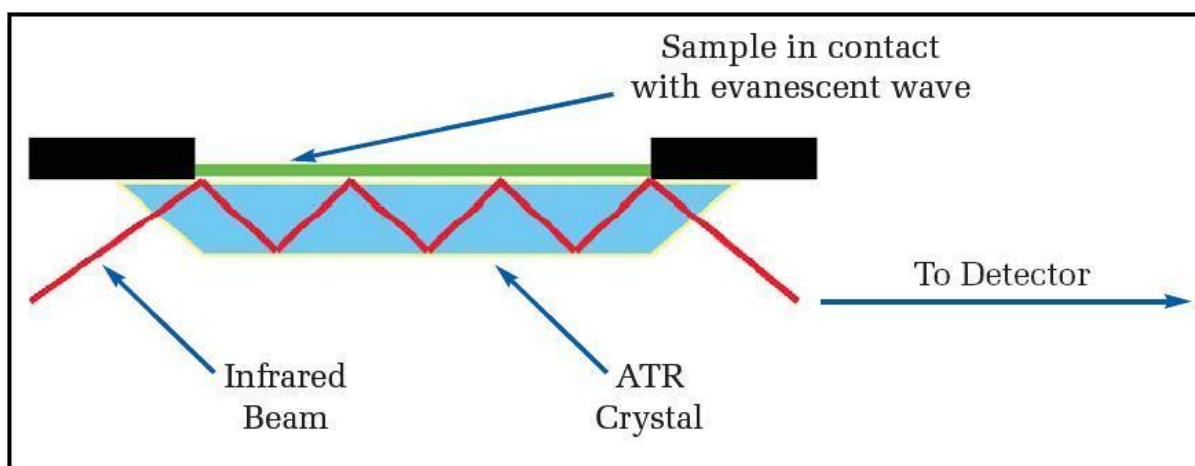


Figure 11. Beam path through ATR crystal.

ATR mode IR spectroscopy enables collection of IR spectra at high spatial resolution by immersing the sample in a material of high refractive index. Furthermore the use of a hemispherical internal reflection element also increases the numerical aperture (NA) of the system (and hence the spatial resolution) by increasing the outer ray angle of incidence. In addition to offering improved spatial resolution the ATR mode also allows for analysis of highly absorbing samples or samples in aqueous environments and hence is very well suited to the analysis of the surface of unprepared biological samples[4]. A recent publication by Kuimova et al at Imperial College[5] demonstrated the ability of ATIR-FT-IR micospectroscopy to resolve sub-cellular components such as the nucleus and the endoplasmic reticulum (ER) of live cells. The study then proceeded to examine the in situ response of live cells to changing the cell medium from a normal environment to one containing PBS thereby demonstrating the ability to study cell dynamics. Other work has demonstrated the endoscopic use of IR spectroscopy by coupling IR fibre-optics to ATR-FT-IR spectroscopy to demonstrate the in situ detection of colorectal cancer[6]. Unfortunately to collect spectra in the ATR mode the crystal and sample must be in direct contact. This can be problematic with hard and brittle specimens. Furthermore wet samples can produce bubbles at the crystal/sample interface that can interfere with the spectra.

3.7 - IR Sources for IR Spectroscopy

In section 3.7 the brightness and power of various sources of IR radiation will be examined.

3.7.1 - Brightness

The key metric for comparing different IR sources is the brightness (sometimes also called radiance) which is defined as the power per unit solid angle per unit area of emitting surface ($Wsr^{-1}m^{-2}$).

Brightness characterizes total emission, while a quantity called spectral brightness characterizes the emission of light at a single wavelength (or frequency). The brightness is equal to the sum (or integral) of all the spectral brightness' from a surface.

3.7.2 - Brightness and Power of Thermal Sources

Commercially available FTIR spectrometers use a thermal source as their source of IR radiation. Normally a “globar” is used which is a silicon carbide rod electrically heated to somewhere in between 1000K – 2000K[7]. A thermal source produces unpolarised, incoherent radiation across a wide spectral range and can be approximated as a black body source in thermal equilibrium. The spectral brightness (units of $\text{Wsr}^{-1}\text{m}^{-2}\text{Hz}^{-1}$) of an ideal black body source of temperature T is given by Planck's law;

$$B(f, T) = \frac{2h}{c^2} \frac{f^3}{e^{\frac{hf}{kT}} - 1} \quad (3.11)$$

Where;

h = Planck' constant

c = Speed of light

K = Boltzmann's constant

f = Temporal frequency of radiation (Hz)

The spectral brightness for a spectral range of frequency (f to f + Δf) is given by;

$$B(f, \Delta f, T) = \int_f^{f+\Delta f} df \frac{2h}{c^2} \frac{f^3}{e^{\frac{hf}{kT}} - 1} \quad (3.12)$$

Or for small bandwidths;

$$B(f, \Delta f, T) \cong \frac{2h}{c^2} \frac{f^3 \Delta f}{e^{\frac{hf}{kT}} - 1} \quad (3.13)$$

Using equation 3.13 we can calculate the maximum optical power ($P_{\text{BB MAX}}$) that can be delivered to a diffraction limited spot (area = λ^2) placed a distance d from a black body with an emitting surface of area A_{BB} by using the following relation;

$$P_{BB \text{ MAX}} = \frac{B\lambda^2 A_{BB}}{d} \quad (3.14)$$

Where;

λ = wavelength of radiation

3.7.3 - Brightness and Power of Synchrotron and FEL Sources

Accelerator based sources, such as synchrotrons and FELs, utilise a relativistic electron beam to generate laser light (unlike conventional laser sources which rely on bound atomic or molecular states to create laser light). The main distinction between synchrotron and FEL radiation is that synchrotrons emanate broadband radiation whilst FELs emits monochromatic radiation of higher brightness than synchrotrons. The use of synchrotron sources in IR spectroscopy has been well documented in the literature[8] and has already been discussed in the background section 2.5.1.

Figure 12 and Figure 13 are taken from the publication, The Source Issue in Infrared Microspectroscopy[9], and they compare the power and brightness respectively of synchrotrons and FELs to a blackbody source. It can be seen from figure 13 that FELs provide the highest brightness across the spectral range, followed by synchrotrons and then thermal sources.

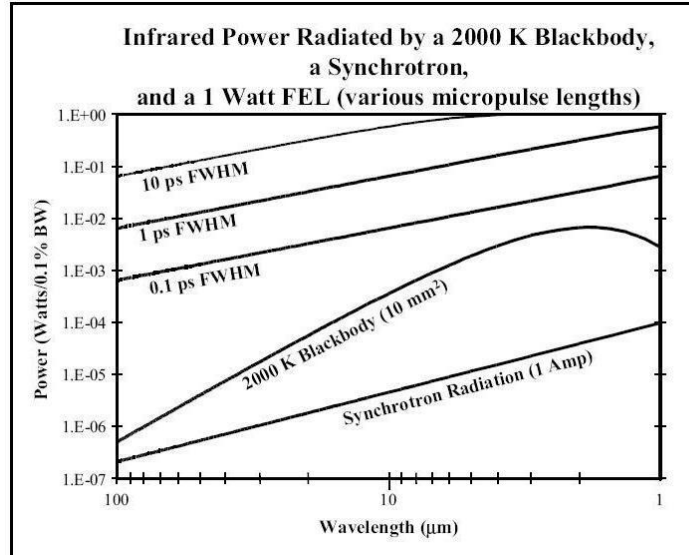


Figure 12. Comparison of the infrared power in a 0.1% bandwidth emitted by a FEL with that from a 1A synchrotron and that from a 10mm² blackbody. The FEL power is shown for micropulse lengths of 0.1, 1.0 and 10 ps. [Smith, T.L., The Source Issue in Infrared Microspectroscopy. Nuclear Instruments and Methods In Physics Research, 2002. 483: p. 565-570.]

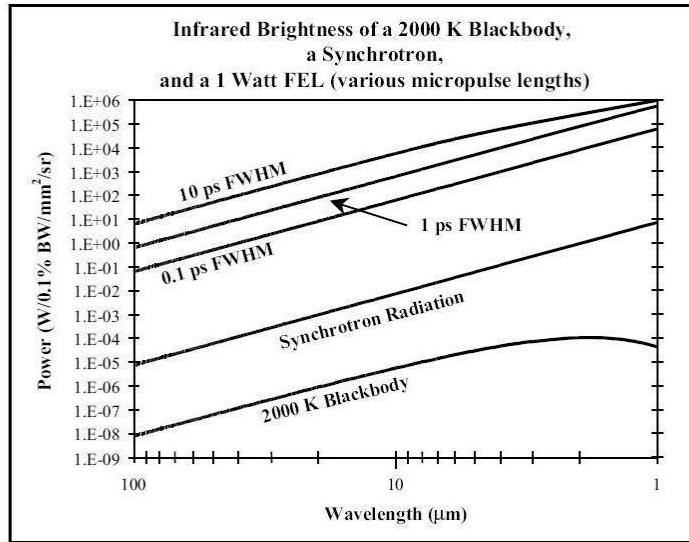


Figure 13. Comparison of the infrared brightness in a 0.1% bandwidth of a FEL with that of a 1A synchrotron and that of a 10mm² blackbody. The FEL brightness is shown for micropulse lengths of 0.1, 1.0 and 10 ps. [Smith, T.I., The Source Issue in Infrared Microspectroscopy. Nuclear Instruments and Methods In Physics Research, 2002. 483: p. 565-570.]

3.7.4 - Brightness and Power of the OPG Imaging System

The OPG delivers an extremely high irradiance (I_{OPG}) of 10^{13} Wm^{-2} and has an ultra short pulse duration (100ps). If we assume that all of the OPG light is collected by lenses (and ignore any attenuation of the beam by the optics) then the maximum optical power that can be delivered by the OPG at wavelength (λ) in a diffraction limited area ($P_{OPG \text{ MAX}}$) given by;

$$P_{OPG \text{ MAX}} = I_{OPG} \lambda^2 \quad (3.15)$$

However, since the OPG is a pulsed source, in order to make a valid comparison to a black body which emits continuously the diffraction limited power of the OPG must be multiplied by a corrective factor to account for the repetition rate and pulse length. For example, for a 100ps pulse length, and a rep-rate of 3Hz, the OPG is only delivering energy for 300ps per second which means the energy delivered is reduced by a factor of 3×10^{-10} relative to a continuous beam with the same irradiance. It should be noted here however that whilst the short pulse length means that an OPG delivers less energy than a continuous source in does provide the advantage of the possibility of real-time imaging. Figure 14 compares various blackbody sources (with emitting surface areas of 10mm² and placed 1m from the sample) with 2 hypothetical OPG systems operating with 10μJ pulse energies (across entire mid-IR region) but with different rep-rates (3, 100Hz). Figure 15 shows a more realistic comparison for the home-made OPG laser (described in section 4.4) used in this research using pulse energies from Figure 4 (chapter 4) and demonstrates that the OPG delivers a

more than 6 orders of magnitude improvement in diffraction limited optical power compared to a thermal source.

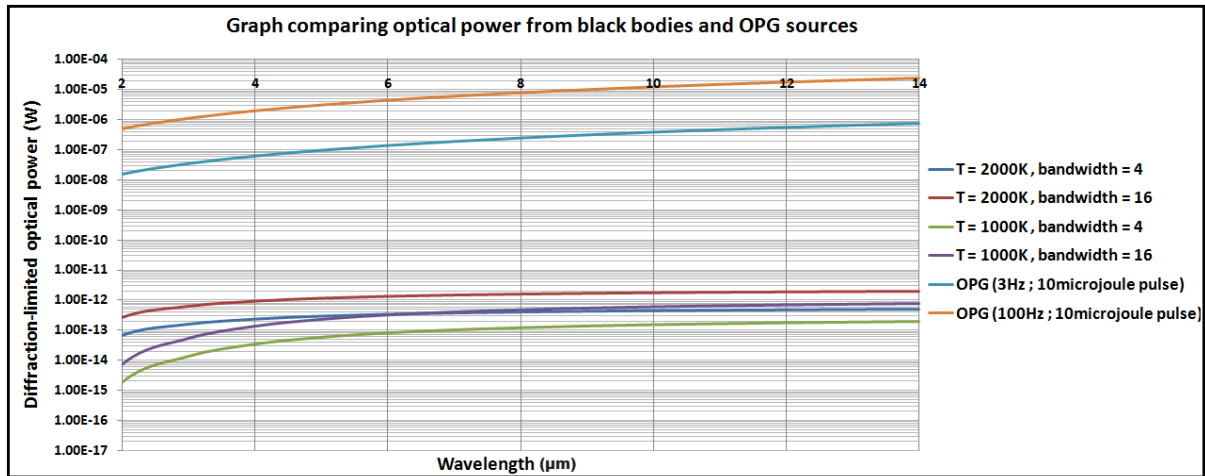


Figure 14. Graph comparing optical power delivered to a diffraction limited area from various different temperature blackbodies (with emitting surface area of 10mm^2 and placed 1m from the sample) and two hypothetical OPG sources operating with a $10\mu\text{J}$ pulse energy and rep-rates of 3Hz and 100Hz.

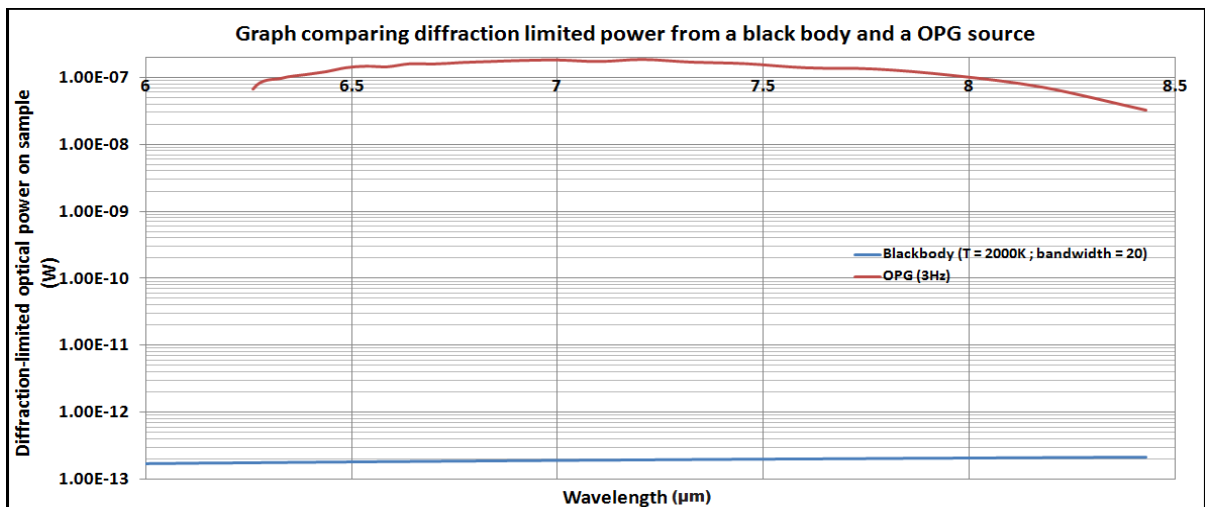


Figure 15. Graph comparing diffraction limited power from a black body (with emitting surface area of 10mm^2 and placed 1m from the sample) and the home-made OPG source used in the OPG imaging system. The OPG source delivers an irradiance of 1013Wm^{-2} in a pulse duration of 100ps and rep-rate of 3Hz.

3.7.5 - Brightness and Power of the QCL Imaging System

The Comparison of the diffraction limited optical power delivered by a QCL proceeds as it did with the OPG calculation in section 3.7.4 For a QCL with an irradiance of (I_{QCL}) of 10^4Wm^{-2} , a pulse duration of 200ns and a rep-rate of 200kHz the maximum optical power that can be delivered by the QCL at wavelength (λ) in a diffraction limited area ($P_{\text{OPG QCL}}$) given by;

$$P_{QCL\ MAX} = I_{QCL}\lambda^2 \quad (3.16)$$

As before, we assume that all of the QCL light is collected by lenses and ignore any attenuation of the beam by the optics. The correction factor which accounts for the rep rate and pulse length is 0.04. Figure 16 compares various blackbody sources (with emitting surface areas of 10mm² and placed 1m from the sample) with a hypothetical OPG and QCL source.

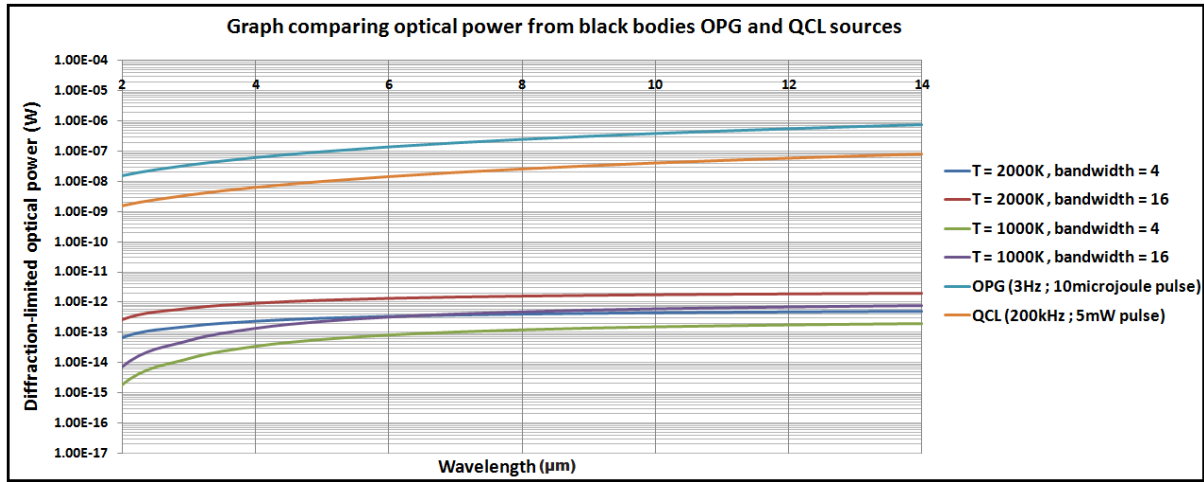


Figure 16. Graph comparing optical power delivered to a diffraction limited area from various different temperature blackbodies (with emitting surface area of 10mm² and placed 1m from the sample), a hypothetical OPG source operating with a 10μJ pulse energy and rep-rates of 3Hz and a QCL with a rep rate of 200kHz and a pulse power of 5mW.

3.8 - IR Detectors for IR spectroscopy

IR detectors can be classified into two categories; thermal detectors and photon detectors. For thermal detectors the thermal effects of incident IR radiation cause some property of the detector to vary in a measurable way. Examples of thermal IR detectors include the thermometer and pyroelectric detector. Photon detectors contain an active element which absorbs IR photons and converts them into an electron-hole pair or a photoelectron. Due to nature of semiconductor material of which they are comprised they only count the effective number of quanta absorbed (those with energy greater than the band gap energy). An example of a photon detector is an HgCdTe (MCT) detector. Since the thermal detection mechanism requires absorbed radiation to change the temperature of the active element for a thermal detector the response time (>ms) is typically slower than photo-detectors (<ns), for which the absorption process is accompanied by an electron-hole pair generation.

Some of the figures of merit commonly used for IR detectors are the following;

3.8.1 - Responsivity and Spectral Responsivity

$$R = \frac{Q}{P} \quad (3.17)$$

Where;

Q = the output quantity supplied by the detector (e.g. current, voltage or any other physical quantity).

P = incident power

The above definition may be considered somewhat ambiguous since the output of an IR detector also depends on the incident wavelength, λ , and the modulation frequency, f , of the incident radiation. The spectral quality of the incident power is especially significant for photon detectors since they exhibit a cut-off frequency below which the responsivity is 0. When the definition of the responsivity is extended to include spectral and modulation frequency dependence it is termed the spectral responsivity, $R(\lambda, f)$.

3.8.2 - Noise Equivalent Power

For two detectors with equal responsivity, the detector with the smallest (root mean square) output noise, Q_n , on the useful signal is the most sensitive. The noise equivalent power is defined as the ratio of output noise to responsivity:

$$NEP = \frac{Q_n}{R} \quad (3.18)$$

The NEP can be interpreted as the input power that gives a unity signal to noise ratio at the output. Hence the smaller the NEP the better the detector performance is. Since NEP depends on R it also depends on the photon wavelength as well as the modulation frequency of the IR power and therefore should be regarded as $NEP(\lambda, f)$.

3.8.3 - Detectivity and Normalised Detectivity

A figure of merit that is directly proportional to the detector performance is more convenient than NEP. For this reason the inverse of NEP is defined as the detectivity, D .

$$D = \frac{1}{NEP} \quad (3.19)$$

By taking into account the detector absorbing active area, A , and the signal bandwidth, B , we can define the specific (normalised) detectivity, D^* as;

$$D^* = \frac{\sqrt{AB}}{NEP} \quad (3.20)$$

The units of D^* are defined as $(\text{cm} \cdot \text{Hz}^{1/2} / \text{W}) = \text{Jones}$. D^* is then the detector output S/N ratio at 1 Watt of input of IR radiation normalised to a detector with unit active area and a unit bandwidth. In general photon detectors typically have D^* values of around $\sim 10^{11}$ Jones and thermal detectors $\sim 10^{10}$ Jones. Photon detectors are therefore typically more sensitive than thermal detectors.

3.9 - Instrumentation Figures of Merit and Noise

In section 3.9 the spatial and spectral resolution are discussed and the noise present in spectroscopic measurements is described.

3.9.1 - Spatial Resolution and the Diffraction Limit

Spatial resolution quantifies how close points can be to each other and still be visibly resolved. The fundamental maximum spatial resolution obtainable by a microscope is defined by the diffraction limit. This means that even if there were no imperfections in the optical arrangement there would still be a limit on the spatial resolution obtained from a particular optical set-up. The Rayleigh criterion gives an equation which can be used to estimate the minimum distance that two adjacent points can still be resolved (r);

$$r = \frac{0.61\lambda}{NA} \quad (3.21)$$

Where;

λ = Wavelength

NA = Numerical aperture

$$NA = n \sin \theta \quad (3.22)$$

n = refractive index of the imaging medium

θ = half angle of the maximum cone of light which can enter or exit the objective

For example, if a 5cm diameter lens is placed 7cm from a sample (therefore $\theta = 20^\circ$) and is illuminated with light with a wavelength of $4.2\mu\text{m}$ the diffraction-limited spatial resolution would be $5.5\mu\text{m}$. In practice however optical aberrations and detector size often limit the spatial resolution of an optical system somewhat higher than the diffraction limit.

When the pixel size at the sample plane (native pixel size divided by magnification) is larger than the diffraction limit the system is said to be 'pixel size-limited'. For example, in the case of an optical arrangement given above, if we imagine that the optical arrangement is providing a X2 magnification with a camera pixel size of $30\mu\text{m}^2$ the system would be pixel limited at $15\mu\text{m}$ (not $5.5\mu\text{m}$). On the other hand a magnification of X15 would give a pixel size of $2\mu\text{m}$ but since the spatial resolution is already limited by diffraction the spatial resolution would be $5.5\mu\text{m}$ (so the system is said to be 'diffraction limited'). When the pixel size at the sample plane is smaller than the diffraction limit pixels are being wasted and it would be more fruitful to decrease the magnification, thereby increasing the field of view and still achieving the same spatial resolution.

3.9.2 - Spectral Resolution

Spectral resolution describes how well an instrument can distinguish closely spaced spectral features. A 4cm^{-1} spectral resolution, for example, can distinguish spectral features only 4cm^{-1} apart. The spectral resolution is determined by the instrument being used and the following sections (3.9.2.1 -3.9.2.3) describe how the spectral resolution is determined for an FTIR spectrometer, the OPG imaging system and the QCL imaging system used in this research.

3.9.2.1 - Jasco FTIR Spectrometer Spectral Resolution

In the case of a FTIR spectrometer the spectral resolution is dependent on the optical path difference (OPD) introduced by the moving mirror (or the distance the moving mirror travels) in the Michelson interferometer. The spectral resolution is simply given by the inverse of the achievable OPD. For example if an interferometer introduces a 2cm OPD then the spectrometer can achieve a spectral resolution of 0.5cm^{-1} . High spectral resolution spectra are acquired from an FTIR at the expense of longer data acquisition times (because it takes the moving mirror longer to scan larger OPDs) and lower signal to noise (since the detectors are exposed to the environment for longer).

3.9.2.2 - OPG Imaging System Spectral Resolution

The spectral resolution obtainable with the OPG is determined by the OPG linewidth (Fig 4, chapter 4). This means the spectral resolution is around 20cm^{-1} which may not be high enough to detect the finer spectral features of an IR spectrum from a biological tissue sample. However the salient features, such as the Amide II which has a full width half maximum (FWHM) of 50cm^{-1} , are still resolvable.

3.9.2.3 - QCL Imaging System Spectral Resolution

The spectral resolution obtainable with the QCL is determined by the QCL linewidth (approximately 1cm^{-1}). This means the spectral resolution is around 1cm^{-1} which is high enough to resolve all spectral features of interest in a biological spectrum.

3.9.3 - Signal to Noise

The signal-to-noise ratio (often abbreviated SNR or S/N) is a measure used to quantify how much a signal has been corrupted by noise. It is defined as the ratio of signal power to the noise power corrupting the signal. A SNR higher than 1 indicates more signal than noise. In this research the following equations will be used;

$$SNR = \frac{P_{signal}}{P_{noise}} \quad (3.23)$$

Or alternatively to calculate the SNR of a pixel in an image which is the average of N images;

$$SNR = \frac{\mu}{\sigma} \quad (3.24)$$

Where;

μ = pixel mean

σ = standard error of pixel

Where;

$$\sigma = \frac{\text{standard deviation}}{\sqrt{N}} \quad (3.25)$$

N = number of images averaged

3.9.3.1 - Noise

A typical signal detected by an IR detector from an IR source will have noise which can be considered to be from three sources; electronic, environmental and source noise.

3.9.3.1.1 - Electronic Noise

This is noise associated with the IR detector itself and due to random fluctuations in the detector electronics (see section 4.6.6.2 for an experimental measurement of the electronic noise from the Cedip IR camera).

3.9.3.1.2 - Environmental Noise

This is noise arising from IR radiation in the ambient surroundings and is proportional to the data acquisition time. A theoretical estimation of the contribution from the environmental noise can be made by: Firstly approximating the surroundings as a blackbody at a temperature of 300K and integrating Planck's formula (equation 3.11) over the sensitive spectral range of the IR detector and then estimating the energy contribution from the environment by integrating over the area of interest and the data acquisition time of the IR detector. A description of the process of integrating a blackbody ($T = 300K$) over the spectral range of the Cedip IR camera (section 4.6) is provided in Dr Hemmel Amrania's thesis[10] and the result is;

$$\int_{\nu_2}^{\nu_1} d\nu' B(\nu', T) = A(x_1) - A(x_2) \quad (3.26)$$

Where;

$B(\nu', T)$ = Planck's blackbody formula

ν_1 = lower spectral cut-off frequency of camera

ν_2 = upper spectral cut-off frequency of camera

And

$$A(x) = \frac{2k^4 T^4}{h^3 c^2} \sum_{n=1}^{\infty} \left[\frac{x^3}{n} + \frac{3x^2}{n^2} + \frac{6x}{n^3} + \frac{6}{n^4} \right] e^{-nx} \quad (3.27)$$

Where;

$$x = \frac{100hcv}{kT} \quad (3.28)$$

It should be noted however that the analysis performed by Dr Hemel Amrania does not account for the spectral response of the Cedip camera (Fig 14, chapter 4) which is shown to have a maximum of 90% (at 3μm) and fall off rapidly after 8μm. A more complete discussion, which accounts for the spectral response, of the energy reaching the Cedip IR camera from a blackbody (and therefore the environmental noise can be determined by considering a blackbody at room temperature) can be found in section 4.6.3.

3.9.3.1.3 - Source Noise

The source noise will obviously depend on the source being used. Practically the source noise can be characterised by measuring the fluctuations in the source power over a long period of time (relative intensity noise, RIN). In this section (3.9.3.1.3) the source noise from a thermal, OPG and QCL source will be considered.

3.9.3.1.3.1 - Source noise from a Thermal Source

The thermal source used in an IR spectrometer is typically a silicon carbide rod (electrically heated to approximately 1500°C) which can be approximated as a blackbody radiator. For a thermal source the IR radiation is generated by the movement of molecules within the material. If we consider that each molecule in the material is emitting IR radiation independently, and the average number of emissions per second from the material is ψ , then the probability of x emissions per second from the material, $P(x)$, will be described by the Poisson distribution.

$$P(x) = \frac{e^{-\psi} \psi^x}{x!} \quad (3.29)$$

In a Poisson distribution the parameter ψ is not only the average number of emissions it also characterises the variance of the distribution. If we also assume that the power of a thermal source is proportional to the average number of emissions then the SNR of a thermal source is given by;

$$SNR_{THERMAL\ SOURCE} = \frac{\psi}{\sqrt{\psi}} = \sqrt{\psi} \quad (3.30)$$

If we consider a 1cm^3 sample of silicon carbide there are approximately 10^{21} molecules in the sample. Since the average number of emissions per second from such a large number of molecules can be expected to be rather large the SNR of a thermal source can be expected to be very large too. In a publication by Guo[7] the relative intensity noise (which described the SNR of a thermal source) is given as 80dB ($\text{SNR}_{\text{THERMAL}} \approx 10^8$).

3.9.3.1.3.2 - Source Noise from an OPG Source

The source noise from the OPG can be generated by several sources such as cavity vibration, fluctuations in the laser gain medium or from transferred noise from the pump source. The RIN (also referred to as pulse-to-pulse variability) of the OPG source has been characterised experimentally (shown to be $\text{SNR}_{\text{OPG SOURCE}} \approx 3.3$) and will be discussed further in section 4.4.1. This pulse-to-pulse variability will be accounted for by the use of a reference channel and rationing procedures to normalise each pulse. This method will be discussed further in section 4.10 where it will be seen that the practical issue of being unable to install a highly correlated reference channel means that the OPG source noise is very difficult to entirely eliminate.

3.9.3.1.3.3 - Source Noise from a QCL Source

The QCL is a very stable source (compared to the OPG, Figure 13, chapter 4) and the source noise (RIN) from the QCL used in this research is characterised experimentally to be $\text{SNR}_{\text{QCL SOURCE}} \approx 650$ in section 4.8.1.

1. Lasch, P. and J. Kneipp, *Biomedical Vibrational Spectroscopy*. 2008, Wiley-Interscience. p. 2.
2. Diem, M., P.R. Griffiths, and J.M. Chalmers, *Vibrational Spectroscopy for Medical Diagnosis*. 2008: John Wiley & Sons.
3. Wang, T.D., et al., *Detection of Endogenous Biomolecules in Barrett's Esophagus by Fourier Transform Infrared Spectroscopy*. PNAS, 2007. **104**(40): p. 15864-15869.
4. Colley, C.S., et al., *Spectroscopic Imaging of Arteries and Atherosclerotic Plaques*. Biopolymers, 2004. **74**: p. 328-335.
5. Kuimova, M.K., A. Chan, and S.G. Kazarian, *Chemical Imaging of Live Cancer Cells in the Natural Aqueous Environment*. Applied Spectroscopy, 2009. **63**(2): p. 164-171.
6. Li, Q., et al., *In Vivo and in Situ Detection of Colorectal Cancer Using Fourier Transform Infrared Spectroscopy*. World J Gastroenterol, 2005. **11**(3): p. 327-330.
7. Guo, B., et al., *Multi-Wavelength Mid-Infrared Micro-Spectral Imaging using Semiconductor Lasers Applied Spectroscopy Issue* 2003. **57**(7): p. 811-822.
8. Bhargava, R. and I.W. Levin, *Spectrochemical Analysis Using Infrared Multichannel Detectors*. 2005, Blackwell Publishing. p. 56-83.
9. Smith, T.I., *The Source Issue in Infrared Microspectroscopy*. Nuclear Instruments and Methods In Physics Research, 2002. **483**: p. 565-570.
10. Amrania, H., *Ultrafast Mid-Infrared Spectroscopic Imaging with Biomedical Applications*, in *Experimental Solid State Physics*. 2009, Imperial College: London.

4.0 - Experimental Set-up and Characterisation

In this chapter the experimental equipment used in this research will be described and characterised. In the first half of the chapter (sections 4.1 - 4.8) the samples, Jasco FTIR spectrometer, IR microscope, OPG, QCL, and Cedip IR camera will be described. In the second half of the chapter (sections 4.9 - 4.11) some important considerations for using OPG and QCL sources to collect spectroscopic data will be explained such as optical artefacts caused by coherent sources and detector saturation. Finally the OPG and QCL imaging system will be characterised so that their practical limitations can be identified (sections 4.12 - 4.13).

4.1 - Background to Samples

In the following sections (4.1.1 – 4.1.3.2) firstly healthy and cancerous biological tissue is discussed. Then the preparation and histopathological grading of the biological (human oesophagus) tissue samples used in the research is described.

4.1.1 - Healthy Biological Tissue

Animal tissues can be grouped into four basic types: connective, muscle, nervous, and epithelial.

4.1.1.1 - Connective Tissue

Connective tissues are fibrous tissues which give shape to organs and hold them in place. They are made up of cells separated by non-living material, which is called extracellular matrix. Stroma tissue (Figure 1) is a kind of connective tissue which acts as a supportive framework for tissues and organs.

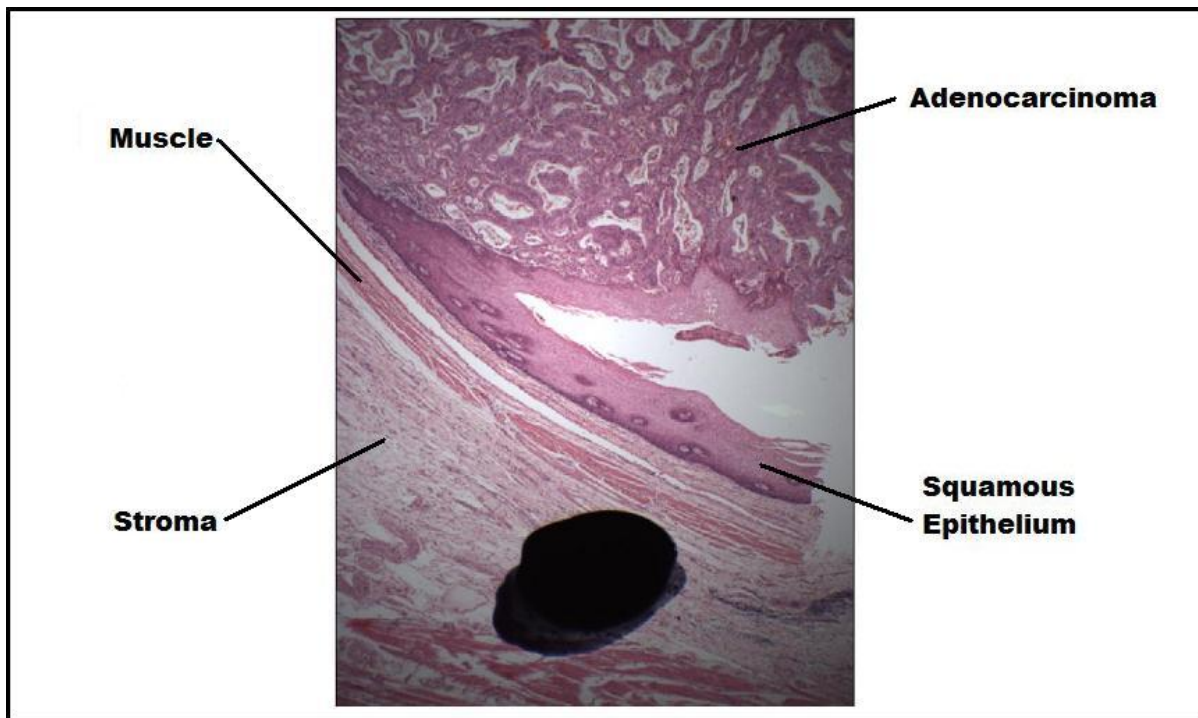


Figure 1. H and E stain of biological tissue (human oesophagus) section which has regions of healthy tissue (squamous epithelium, muscle and stroma) and regions of adenocarcinoma. The black spot is a blot of ink used as a reference point.

4.1.1.2 - Muscle Tissue

Muscle tissue (Figure 1) functions to produce force and cause motion, either locomotion or movement within internal organs. Muscle tissue is separated into three distinct categories: visceral or smooth muscle, which is found in the inner linings of organs; skeletal muscle, in which is found attached to bone providing for gross movement; and cardiac muscle which is found in the heart, allowing it to contract and pump blood throughout an organism.

4.1.1.3 - Nervous Tissue

Cells comprising the central nervous system and peripheral nervous system are classified as neural tissue. In the central nervous system, neural tissue forms the brain and spinal cord and, in the peripheral nervous system forms the cranial nerves and spinal nerves.

4.1.1.4 - Epithelial Tissue

The epithelial tissues are formed by cells that cover organ surfaces such as the surface of the skin, the airways, the reproductive tract, and the inner lining of the digestive tract (including the oesophagus). Epithelial tissues perform a protective function and may also be specialized to function

in secretion and absorption. Epithelium tissue can be further classified by their appearance into classes such as cuboidal epithelium (cuboidal in shape with spherical nuclei), columnar epithelium (elongated column shape) or squamous epithelium (thin, flat cells with oval shaped nuclei).

4.1.2 - Cancer

Cancer can be loosely defined as a class of diseases in which a group of cells exhibit uncontrolled growth, invasion of adjacent tissues, and sometimes, metastasis (spread to other locations in the body via blood or lymph). The property which distinguishes malignant tumours from benign tumours is that benign tumours are self-limited and do not invade or metastasize. It is estimated that cancer is responsible for about 13% of all deaths[1] and the American Cancer Society estimated that 7.6 million people died from cancer during 2007[2].

4.1.2.1 - Medical Nomenclature for Cancer

Various terms are often used interchangeably to describe cancer. The following closely related terms may be used to designate abnormal growths:

- Metaplasia: Is the reversible replacement of one mature differentiated cell type with a different type of mature differentiated cell type. Cells are influenced by their environments and metaplasia is usually a response to some abnormal stimulus. Once the stimulus that causes metaplasia is removed the cells return to their normal configuration. An example of metaplasia is Barrett's oesophagus. In Barrett's oesophagus the normal cells (called "squamous epithelium") of the lower end of the oesophagus are replaced by different cells (usually the "columnar epithelium" cells found in lower parts of the oesophagus) under the influence of acid reflux from the stomach.
- Dysplasia: Refers to an abnormality in maturation of cells within a tissue. In this condition cells revert to an immature state and accelerated division occurs.
- Neoplasm: The scientific term to describe an abnormal proliferation of genetically altered cells. Neoplasms are divided into two classes; benign or malignant. A malignant neoplasm (malignant tumour) is synonymous with cancer. A benign neoplasm or benign tumour is a tumour that does not invade other tissues and does not form metastases.
- Tumour: In general terms a tumour can be taken to mean any abnormal swelling, lump or mass. The more common interpretation of the word tumour is synonymous with solid neoplasm. Most cancers form a tumour but some, like leukaemia, do not.

- Carcinoma: Malignant tumours which originate from epithelial cells. This sub group of cancers represents the most common form of cancer. Carcinomas include breast, prostate, lung and, particularly relevant to this research, oesophagus cancer.
- Adenocarcinoma: A cancer of the epithelium tissue which originated in glandular tissue.

4.1.3 - Samples

Research in this thesis has been conducted with oesophagus tissue samples (biopsies) provided by Dr Bill Otto and Sir Nick Wright at Cancer Research UK (CRUK). Adjacent sections (one section was taken and the second section was taken directly above / below the plane of the first section) were divided into two groups; one group was mounted onto glass slides and stained with natural dyes, haematoxylin and eosin (H & E) (Figure 1), for examination by a histopathologist with a light microscope and the other group was mounted onto BaF₂ slides for IR chemical imaging. The use of adjacent sections is not an ideal situation since there is the possibility of small tissue changes between adjacent sections. A better arrangement would have been to examine a tissue section spectroscopically and subsequently stain the *same* tissue sections for histopathological analysis. However since the primary objective of these experiments was to demonstrate the advantages of using laser based sources over thermal sources for spectroscopic imaging rather than to demonstrate the use of spectroscopic imaging as a diagnostic tool this was not a major concern.

4.1.3.1 - Preparation of Samples

In the experiments conducted in this thesis the samples were fixed, embedded in wax and sliced with a microtome. The tissue processing stages used for this research were as follows;

- Biopsy: Firstly the tissue samples were removed from the patients by surgery
- Fixation: Immediately after the tissue is removed it underwent a process called fixation to preserve the tissue from degradation and to maintain the internal structure of the cells. Fixation involves bathing the samples in a fixative, in this research the fixative used was 4% formaldehyde in PBS. Subsequently Fixatives preserve tissues or cells by irreversibly "fixing" proteins in the shape that they're in. This process can denature the proteins and obviously destroys the biological functionality. Work by Gazi et al[3] demonstrates that the fixative 4% formaldehyde in PBS does not contribute to the IR spectrum of fixed cells (this was accomplished by comparing the IR spectra of fixed and unfixed cells).
- Paraffin Processing: To prepare the biological tissue for the embedding process specimens were soaked in several baths of progressively more concentrated ethanol (1 bath of 80% ethanol, 2 baths of 95% ethanol and 2 baths of 100% ethanol). The purpose of this stage is to

dehydrate (remove the water) the tissue. Following dehydration by ethanol xylene was used to remove the alcohol.

- Embedding: For the paraffin wax embedding stage the tissue samples were placed into moulds and molten paraffin wax was poured over them. Once the wax had cooled the tissue samples were ready to be sectioned. Paraffin is used because its IR absorption features do not greatly interfere with the spectrum of the sample. The most relevant absorption features of paraffin are limited to the C-H stretch region (2800 - 3000 cm^{-1} or 3.6 - 3.3 μm) (Figure 2) but there are also weaker C-C stretching modes which fall near 1465 cm^{-1} (6.8 μm) which may interfere with the spectrum[4].

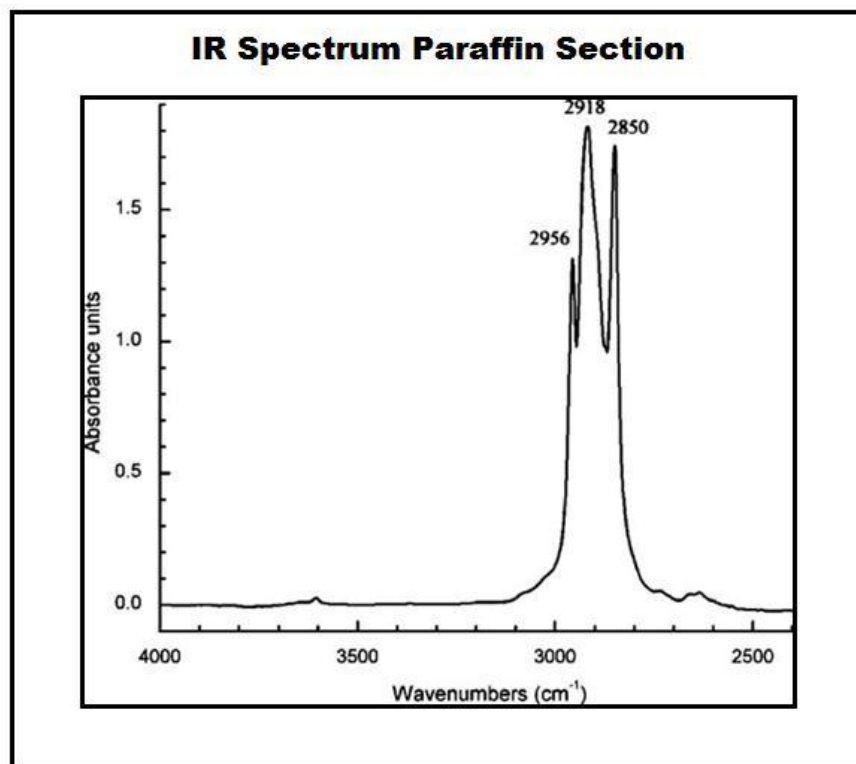


Figure 2. IR Absorbance Spectrum of a Paraffin Section. [Meuse, C.W. and P.E. Barker, Quantitative Infrared Spectroscopy of Formalin-fixed, Paraffin-embedded Tissue Specimens: Paraffin Wax Removal with Organic Solvents. *Applied Immunohistochemistry & Molecular Morphology*, 2009. 17(6): p. 547-552.]

- Sectioning: The tissue was then sliced into thin (5 μm thick) sections using a microtome. One group of sectioned samples was stained for microscopic examination and the other was de-waxed for IR examination.
- Staining: The tissue sections used for visual inspection were mounted onto glass slides and stained with an H&E stain. Haematoxylin colours structures containing nucleic acids, such as

ribosomes and the chromatin-rich nuclei blue. Eosin colours protein-rich structures, such as the cytoplasm, pink. Staining is necessary for visual contrast of the tissue.

- De-waxing: Since the paraffin wax would interfere with the IR absorption spectra (Figure 2) it was necessary to remove as much of it as possible before chemical images are collected. This was achieved by washing the tissue sections three times in clean xylene.
- Mounting on IR substrates: The samples to be examined spectroscopically were mounted on (mid-IR transparent) BaF₂ substrates.

4.1.3.2 - Histopathological Grading of Tissue Samples

A CRUK Histopathologist (Dr Bill Otto) classified tissue sections in terms of how abnormal the cells appeared by using a grading system. The grading system used at CRUK is descriptive (e.g., "high grade" or "low grade") and the grade refers to how much the tumour cells resemble or differ from the normal cells of the same tissue type. The different grades of tissue are as follows;

- Healthy: No sign of abnormality.
- Low grade: Cells are generally well differentiated with some indication of immature cells or poor differentiation.
- High grade: Cells exhibiting very poor differentiation.
- Carcinoma: Cells exhibiting very poor differentiation, indication of immature cells and no resemblance to normal cells.

4.2 - Jasco FTIR Spectrometer

In sections 4.2.1-4.2.2 the Jasco FTIR spectrometer specifications and method of operation for the Jasco FTIR instrument used in the experiments in this research is discussed.

4.2.1 - Jasco FTIR Spectrometer Specifications

The FTIR spectrometer utilised for chemical mapping was a JASCO FTIR 600plus. The instrument was capable of collecting spectra at a spectral resolution from 16cm⁻¹ to 1cm⁻¹. The source of radiation used in the JASCO FTIR spectrometer is a "globar" electrically heated to approximately 1500K.

4.2.2 - Jasco FTIR Spectrometer Method of Operation

A brief outline of the operating principles of a FTIR spectrometer is outlined in the theory section 3.5.2.

4.3 - Jasco IR Microscope

In sections 4.3.1-4.3.2 the Jasco IR microscope specifications and method of operation for the Jasco IR microscope used in the experiments in this research is discussed.

4.3.1 - Jasco IR Microscope Specifications

The IR microscope utilised is a *JASCO IRT-30 IR* microscope. The microscope is a commercial instrument sold as an accessory to the FTIR 600plus Jasco product line. The microscope functions in either transmission or reflection mode. The objective can be switched between a 16X Cassegrainian, 32X Cassegrainian or ATR mode. The sampling area is defined by an aperture between the objective and IR detector. The minimum sampling area is 3 μm (using 32X Cassegrainian) and therefore diffraction limited imaging is obtainable. The microscope includes a 100 μm by 100 μm single channel MCT detector used for measurements in mapping mode. The numerical aperture (NA) of the upper and lower objectives in the IR microscope is 0.65[5]. Additional features of the microscope include a precision, automated X-Y-Z sample stage with software facilities for IR mapping and a CCD camera for the visible.

4.3.2 - Jasco IR Microscope Method of Operation

IR microscopes are similar to optical microscopes but special care must be taken in their physical construction since they are required to operate over a significantly broader range of wavelengths; Mid-IR radiation covers a wavelength range $>10\mu\text{m}$ whilst visible microscopes are only required to operate within a wavelength range of $<0.5\mu\text{m}$. Furthermore the glass optics used within visible microscopes are opaque at wavelengths longer than (approximately) 4.5 μm . For operation over a broad range of wavelengths reflecting optics and Cassegrainian configurations are preferred to refractive arrangements because they eliminate chromatic aberrations.

The beam path is illustrated below (Figure 3). Light is directed into the microscope from the FTIR spectrometer and, depending on if the microscope is being operated in reflection or transmission mode, two paths are possible. For transmission mode spectra the flipping mirror directs the light downwards so that it comes from underneath the sample stage. First the light passes through the lower condensing Cassegrainian and illuminates the sample. The upper Cassegrainian objective provides the magnification. After the light has passed through objective it passes through the aperture. The aperture can be adjusted via a PC interface to define the sampling area of the specimen being examined. The physical aperture size is given by the objective magnification and the sample area selected. For example a physical aperture size of 640 μm by 640 μm with a magnification

of x16 would provide a sampling area of $40\mu\text{m}$ by $40\mu\text{m}$. Following the aperture the light is finally passed to the detector.

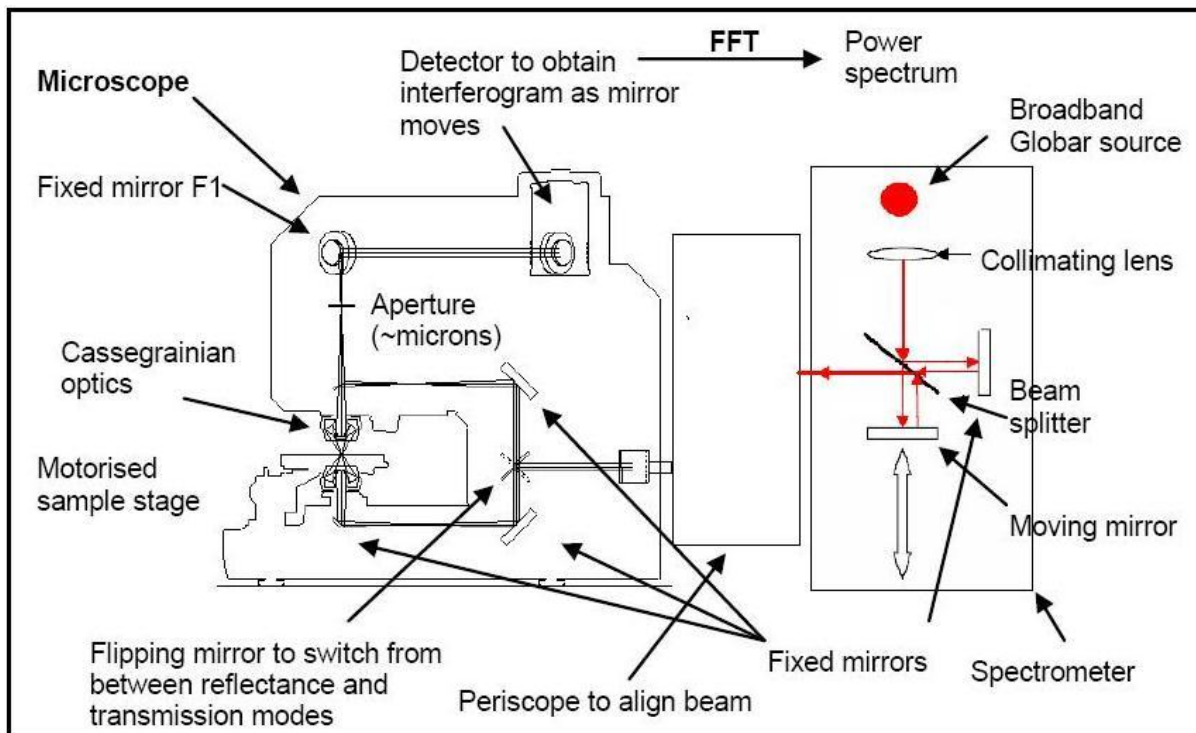


Figure 3. Schematics to show operation of the JASCO IRT-30 Infrared Microscope. The detector in the microscope is a $100\mu\text{m}$ by $100\mu\text{m}$ MCT detector. For transmission mode the flipping mirror directs the light downwards so that it comes from underneath the sample stage passes through the lower condensing Cassegrainian, illuminates the sample then onto the upper Cassegrainian. For reflection mode the flipping mirror directs the IR light upwards and the upper Cassegrainian is used as both the condenser and objective.

For reflection mode the flipping mirror directs the IR light upwards and the upper Cassegrainian is used as both the condenser and objective. Once the light returns back up the Cassegrainian it passes to the aperture and then finally to the detector.

4.4 - The Mid-IR Optical Parametric Generator (OPG)

In sections 4.4.1-4.4.3 the OPG output characteristics and method of operation are discussed.

4.4.1 - OPG Output Characteristics

The mid-IR light source utilised in this research was a home-made Er:Cr:YSGG pumped OPG. The output wavelengths (for a ZnGeP_2 crystal) are continuously tuneable over the ranges $4\mu\text{m}$ - $5\mu\text{m}$ (signal) and $6.4\mu\text{m}$ - $8.6\mu\text{m}$ (idler). The idler pulse is vertically polarised (same polarisation as the pump) and the signal pulse is horizontally polarised. Typical line-widths of the output are $10\text{-}20\text{cm}^{-1}$ (Figure 4). The output is pulsed at a frequency of 3Hz and has a pulse length of approximately 100ps.

The idler pulse energy varies from 1 μ J -10 μ J (Figure 5) and is a maximum (around 10 μ J) at 7.2 μ m. However the pulse-to-pulse stability can vary as much as 30% from the mean average (Figure 6). Figure 6 shows the energy output variation for both the pump energy and the ZnGeP₂ idler energy. The beam could be focused to a \approx 100 μ m diameter spot. The irradiance of the OPG can attain 10³MWcm⁻² (however the short pulse length means that the fluence is low enough not to cause any damage to a biological sample).

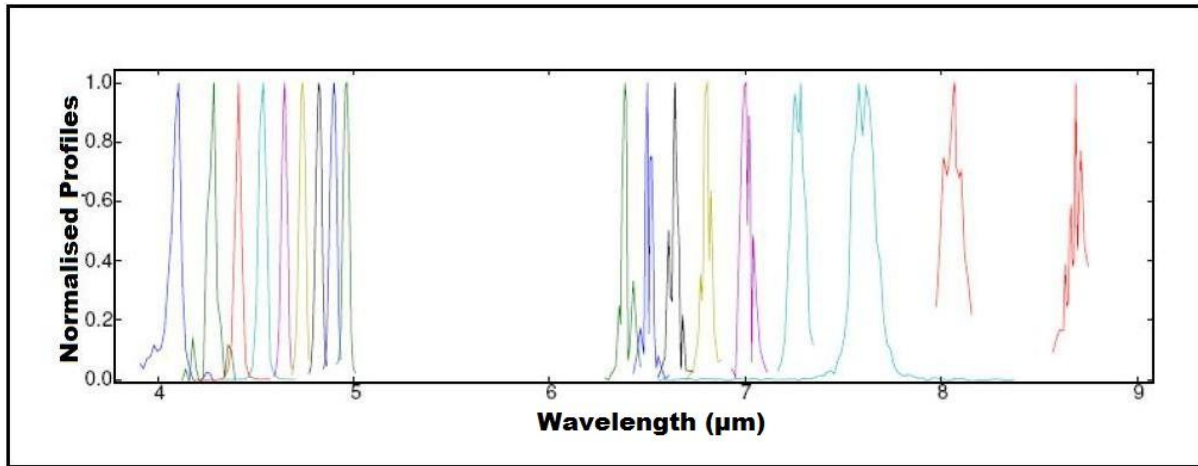


Figure 4. Diagram showing the line widths of the home-made OPG pulses (for ZnGeP₂ at various wavelengths across its spectral range. [Steed, R.J., Saturation of Intersubband Transitions in P-type and N-type III-V Quantum Wells., Thesis in Physics. 2008, Imperial College: London.]

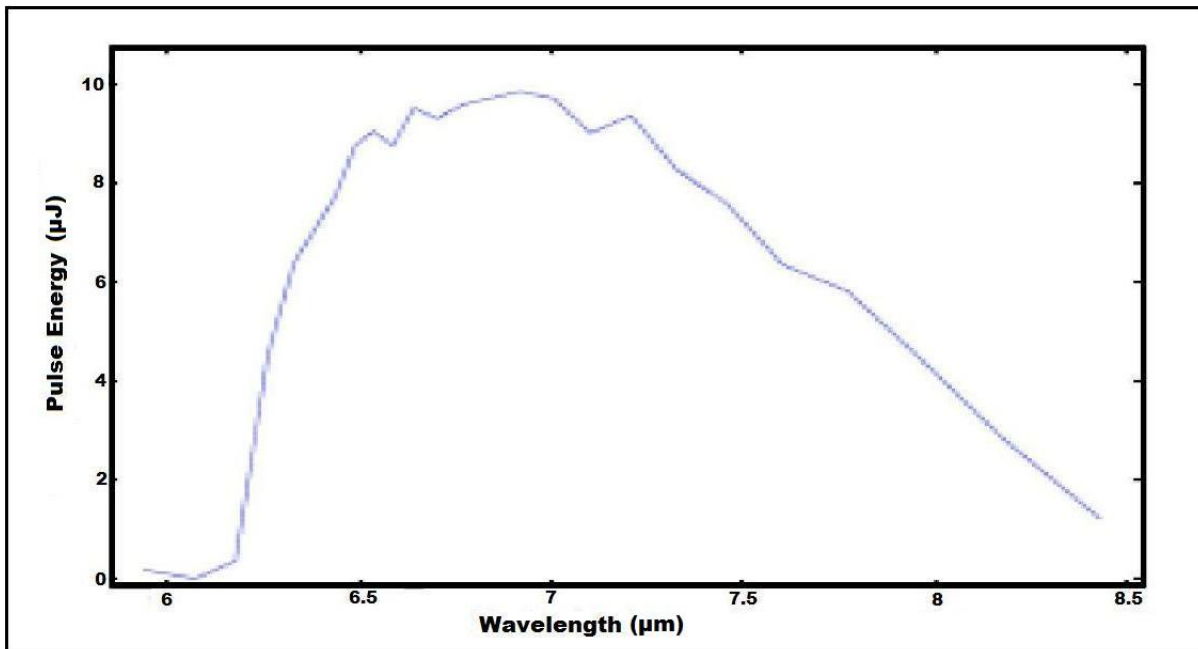


Figure 5. OPG idler energy characteristics for ZnGeP₂. [Steed, R.J., Saturation of Intersubband Transitions in P-type and N-type III-V Quantum Wells., Thesis in Physics. 2008, Imperial College: London.]

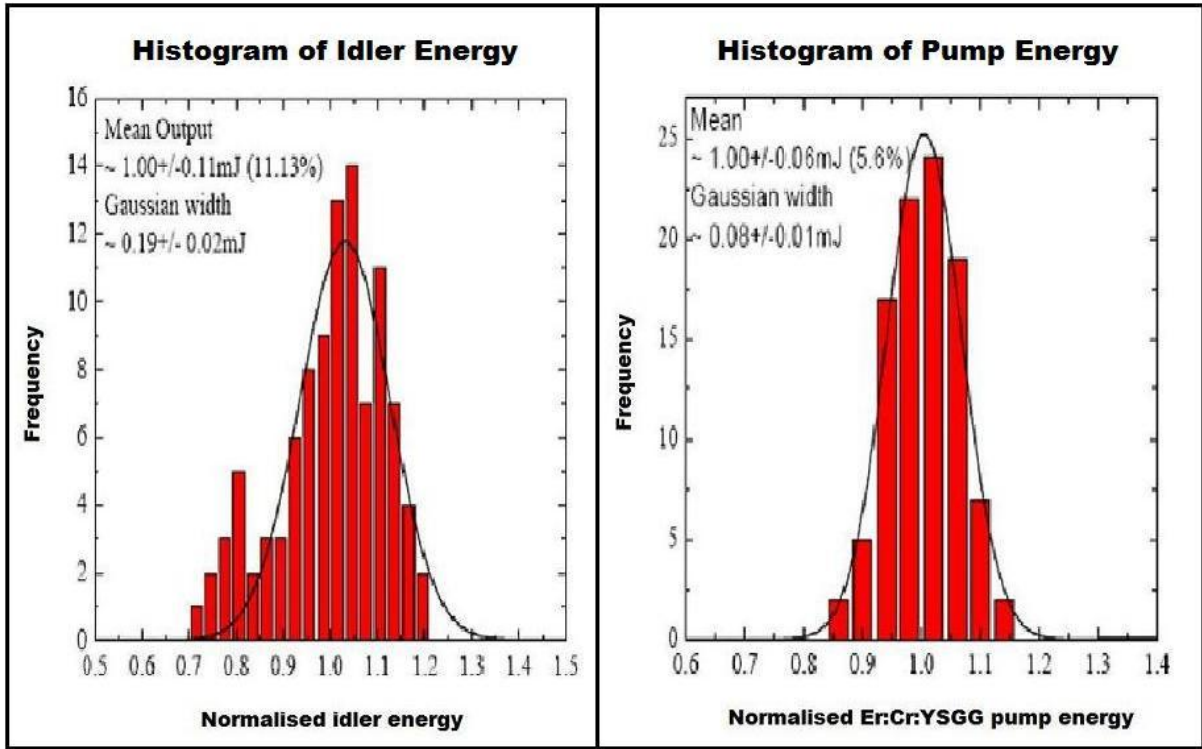


Figure 6. Histograms showing the normalised energy distribution of the pump and idler pulses for the home made OPG. The pump wavelength is $2.79\mu\text{m}$ and the idler wavelength used here is $7.2\mu\text{m}$ (however distribution is largely independent of wavelength). The average pulse energy of the pump is 3mJ and the average pulse energy of the idler (at $7.2\mu\text{m}$) is $10\mu\text{J}$. [Steed, R.J., Saturation of Intersubband Transitions in P-type and N-type III-V Quantum Wells., Thesis in Physics, 2008, Imperial College: London.]

4.4.2 - OPG Beam Divergence

The cross sectional and axial profile of the home made OPG beam has been determined experimentally by Dr Robert Steed by measuring the response of a MCT detector from the OPG with a movable aperture in the beam path. The intensity distribution was discovered to be Gaussian in cross section and Lorentzian in the z direction (direction of propagation)[6]. The cross sectional and axial profile of the intensity of the OPG beam can be described theoretically by the following equations (in cylindrical polar coordinates);

$$I(r, z) = I(z)e^{-\left[\frac{r^2}{w^2(z)}\right]} \quad (4.0)$$

$$I(z) = \frac{1}{1 + \left(\frac{z}{z_R}\right)^2} \quad (4.1)$$

$$w^2(z) = w_0^2 \left[1 + \left(\frac{z}{z_R} \right)^2 \right] \quad (4.2)$$

$$z_R = \frac{\pi w_0^2}{\lambda} \quad (4.3)$$

Where;

w = beam diameter

w_0 = beam diameter at focus

z_R = Rayleigh range = distance from the focus where the cross sectional area has doubled from focus

λ = wavelength of OPG

The Rayleigh range for a wavelength of $7\mu\text{m}$ and a beam waist at the focus of $100\mu\text{m}$ is 4.5mm .

Using equations 4.0-4.3 a relationship for the divergence can be derived;

$$Z_N = \sqrt{(N - 1)Z_R} \quad (4.4)$$

Where;

N = factor increase in cross sectional area

Z_N = distance from focus where cross sectional area has increased by a factor of N

Figure 7 shows how the cross sectional area of the beam varies as the distance from the focus is increased for a wavelength of $7\mu\text{m}$ and a beam waist at the focus of $100\mu\text{m}$. It can be seen from this figure that after approximately 1m the beam cross section has increased by a factor of $40,000$; from 10^{-4}cm^2 to around 4cm^2 .

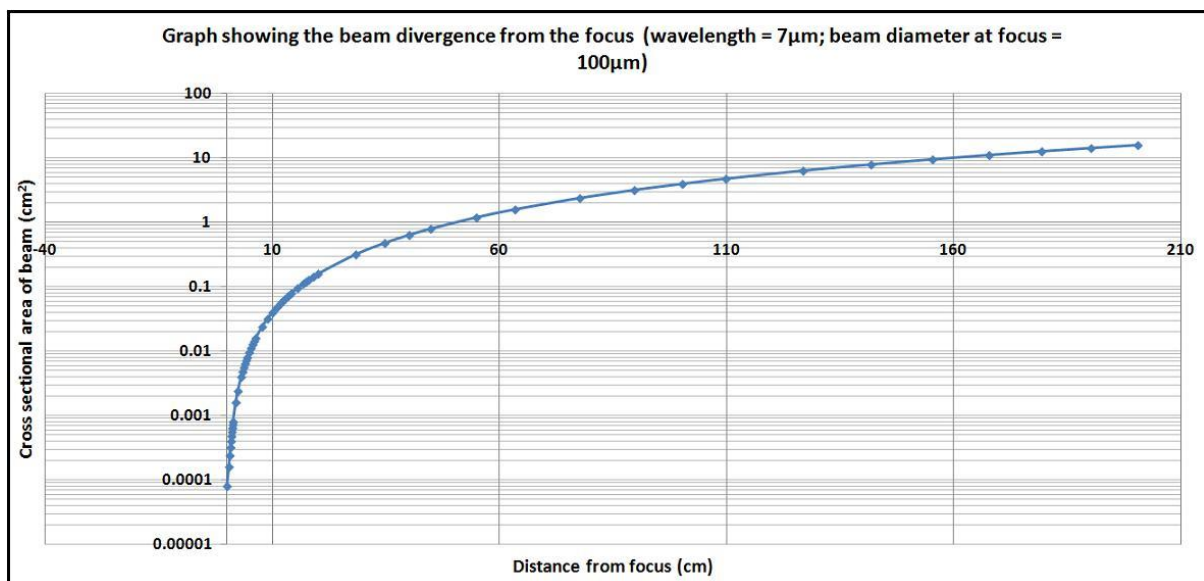


Figure 7. Graph showing the beam divergence from the focus (wavelength = $7\mu\text{m}$; beam diameter at focus = $100\mu\text{m}$)

4.4.3 - OPG Method of Operation

In this section a brief description of the laser operation is described. For a more in depth discussion describing the electro-optical components and parametric down-conversion theory please refer to Dr Robert Steed's Thesis[7].

A schematic of the initial stage of the pump laser is shown in Figure 8. The active element is an $\text{Er}^{3+}:\text{Cr}^{3+}:\text{YSGG}$ Rod. The active element is placed between two mirrors (laser cavity) in a flash lamp. A Q-switch, modelocker and cavity dumper is also contained within the cavity. The flash lamp pulses produce a population inversion which generates IR radiation of $2.79\mu\text{m}$.

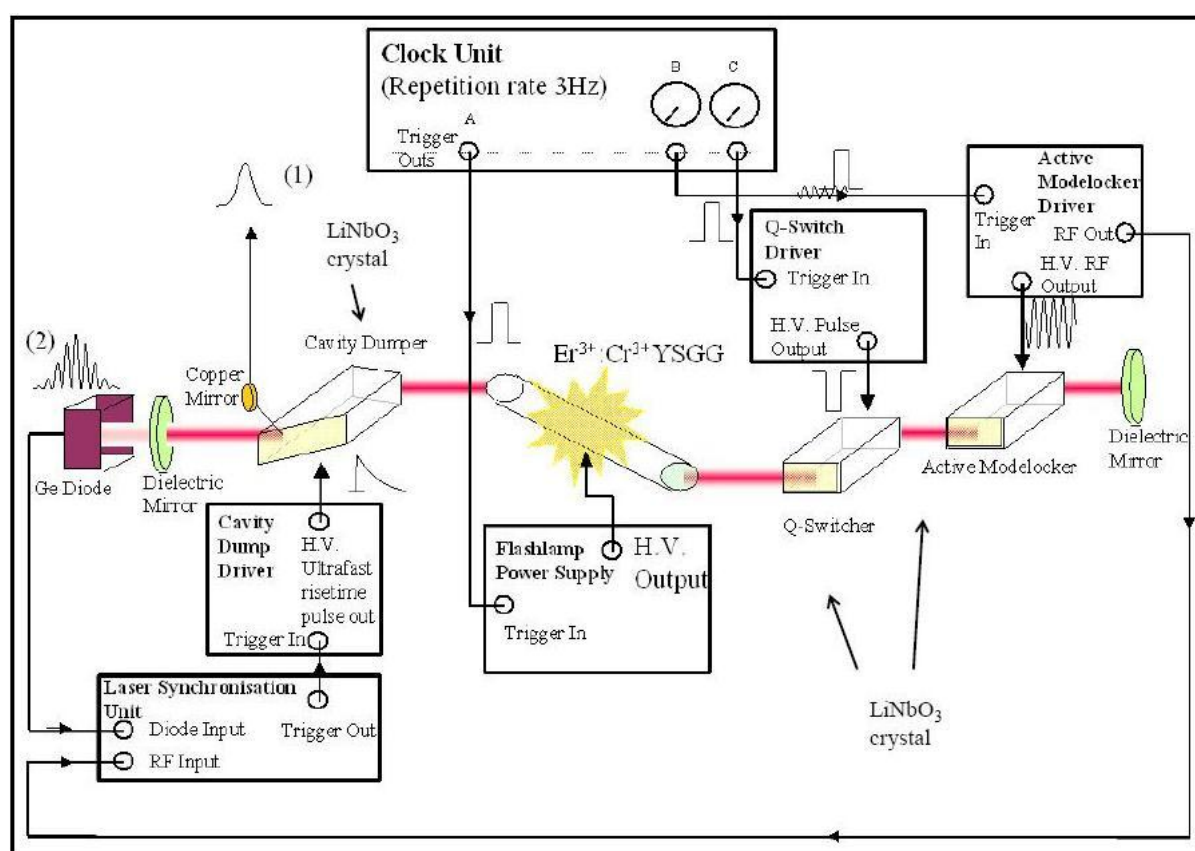


Figure 8. Schematic of the pump laser and associated driving electronics. It consists of an Er:Cr:YSGG active element and three electro-optic LiNbO₃ crystal modulators namely a Q-switcher, an active mode-locker and a cavity dumper. The Germanium (Ge) diode monitors the cavity output via second harmonic generation (SHG) in the LiNbO₃ crystals by the 2.79 μ m radiation (2). The final laser output (1) is a 2.79 μ m, 0.70mJ, 100ps laser pulse. All elements inside the cavity have Brewster polished facets and are placed at the Brewster angle to eliminate Fresnel and mode selection effects. [Steed, R.J., Saturation of Intersubband Transitions in P-type and N-type III-V Quantum Wells., Thesis in Physics, 2008, Imperial College: London.]

The Q-switch, modelocker and cavity dump are electro-optical elements made from lithium niobate (LiNbO_3) crystals. The Q-switch and modelocker facilitated the production of high intensity 100ps

length pulses. The cavity dump diverts the pulses out of the cavity and into a 4-pass amplifier (Figure 9).

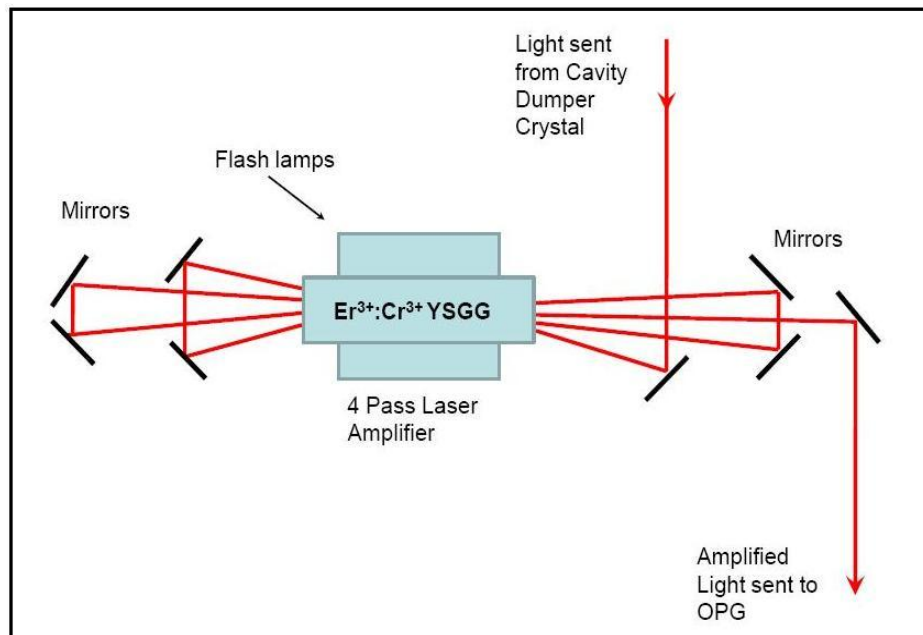


Figure 9. 4 pass laser amplifier: Light from the cavity dumper crystal is sent via various copper mirrors through an $\text{Er}^{3+}:\text{Cr}^{3+}$ YSGG gain medium crystal. The output amplified light is then sent to the OPG

After the amplifier stage the laser pulse (pump) is then passed through a non-linear optical crystal such as ZnGeP_2 (Figure 10). Here the laser light undergoes a non linear process and is split into two beams (signal and idler). By rotating the OPG crystal the signal and idler beams can be tuned to different wavelengths in the mid-IR region (an example of a tuning curve is shown in Figure 11). A dichroic mirror is used to filter out the pump from the emerging beam and subsequent polarisers and filters can be used to select either the signal or idler beams.

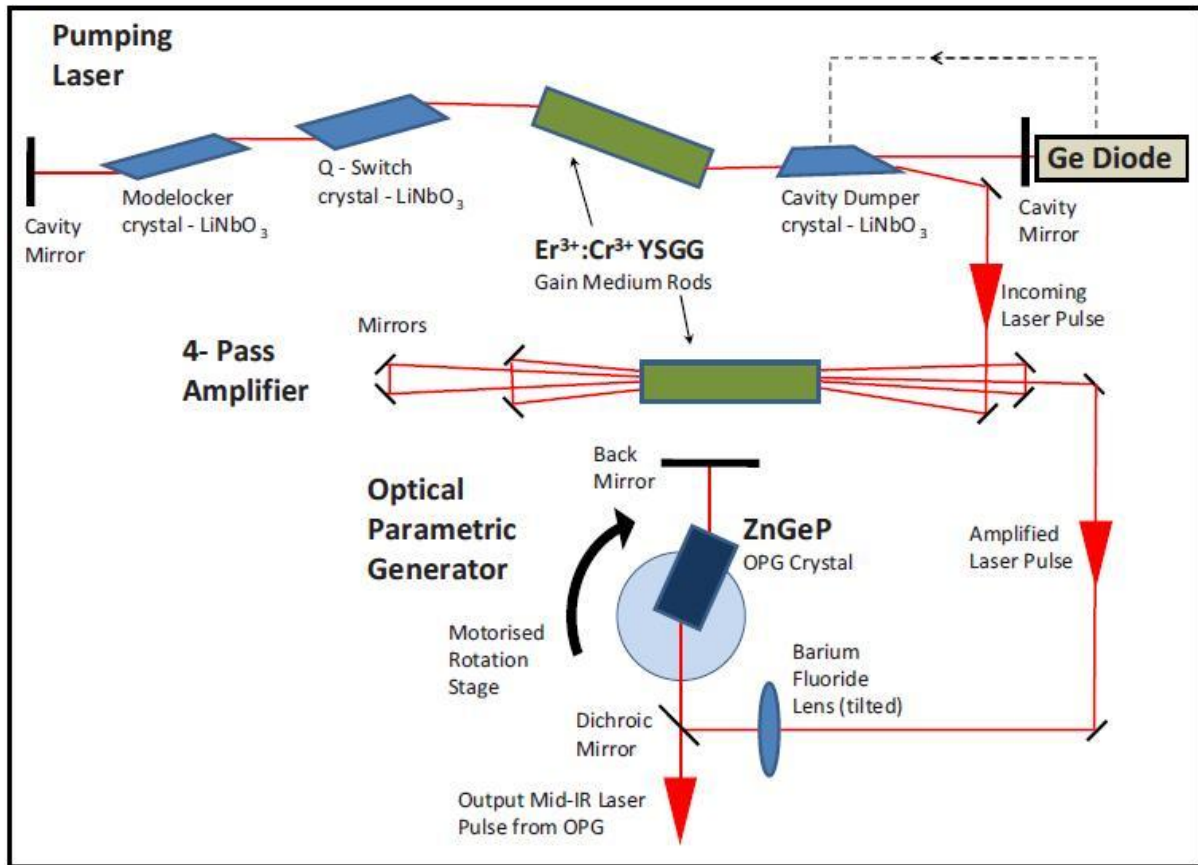


Figure 10. Schematic of the entire OPG optical set-up. The first two parts are the pumping laser and 4-pass amplifier and the last stage is the OPG. The OPG crystal is a ZnGeP₂ crystal and the emitted light can be tuned by rotating the OPG crystal.

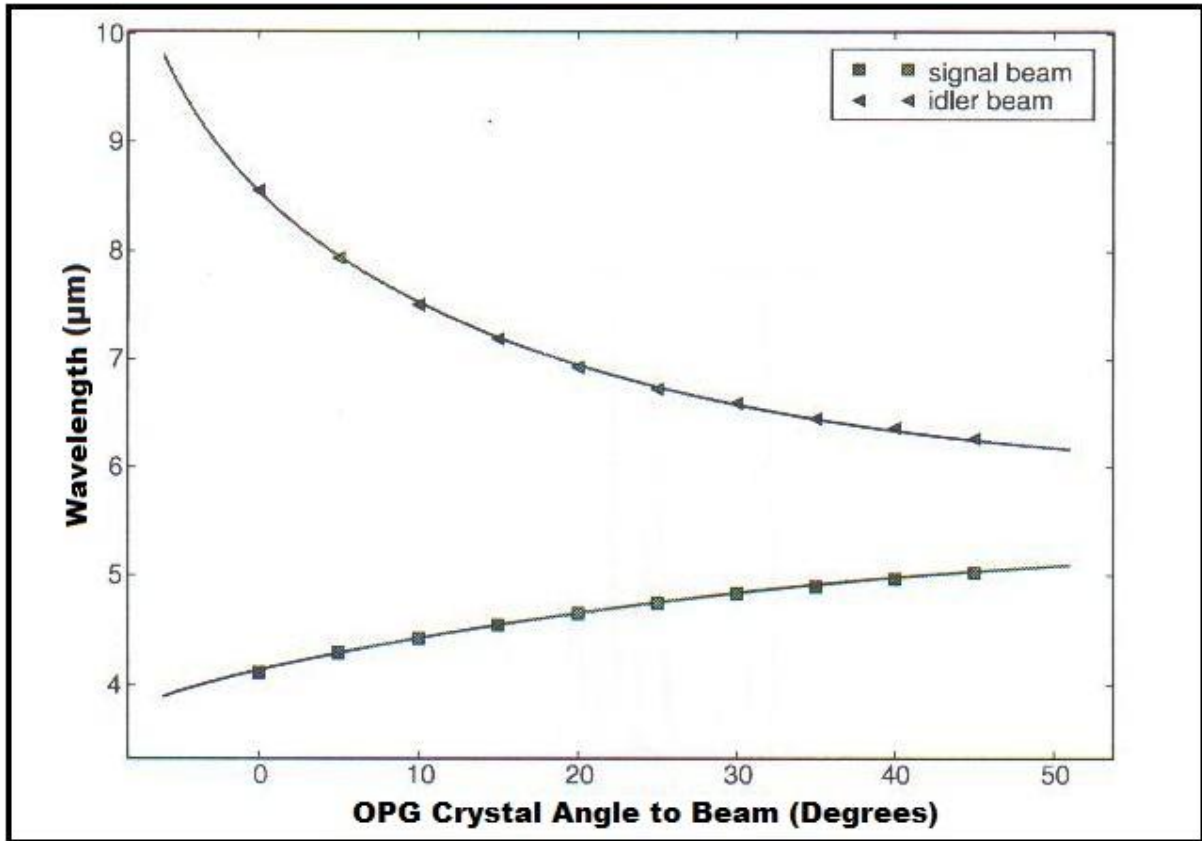


Figure 11. Wavelengths of OPG output (signal and idler beams) for ZnGeP₂ plotted as a function of angle of incidence (angle between incident beam and normal with respect to front facet of crystal. Uncertainty for wavelength measurements is estimated to be $\sim \pm 0.02 \mu\text{m}$. [Steed, R.J., Saturation of Intersubband Transitions in P-type and N-type III-V Quantum Wells., Thesis in Physics. 2008, Imperial College: London.]

4.5 - The Tuneable Quantum Cascade Laser (QCL)

In sections 4.5.1 the QCL output characteristics are discussed. The QCL is available commercially under the brand name LaserTune™ from Block Engineering, Marlborough, USA.

4.5.1 - QCL Output Characteristics

The output wavelengths of the QCL are continuously tuneable over the range of approximately 6.0-9.5 μm . The output is pulsed at a frequency of 200kHz and has a pulse length of approximately 200ns. The pulse energies have a minimum and maximum average power of 0.5mW (at 1000 cm^{-1}) and 12mW (at approx 1075 cm^{-1}) respectively as the QCL is tuned across the spectral range (Figure 12). The pulse energy at a particular wavelength is very stable (with a noise of approximately 0.2%) (Figure 13). The beam has a diameter of approximately 5mm at the point it leaves the QCL and has a divergence on the order of 2mrad. The linewidth is estimated to be approximately 1 cm^{-1} .

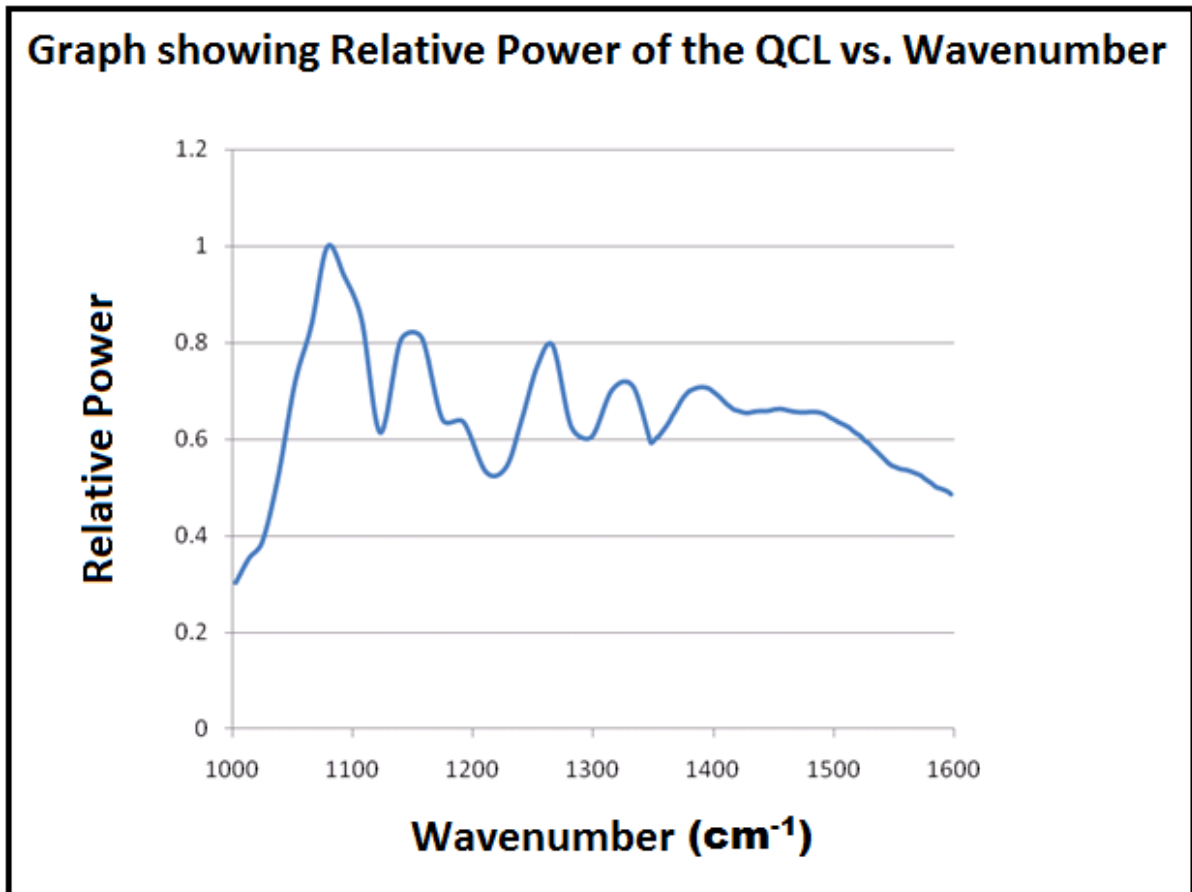


Figure 12. QCL Power Spectrum. The maximum average power is approximately 12mW.

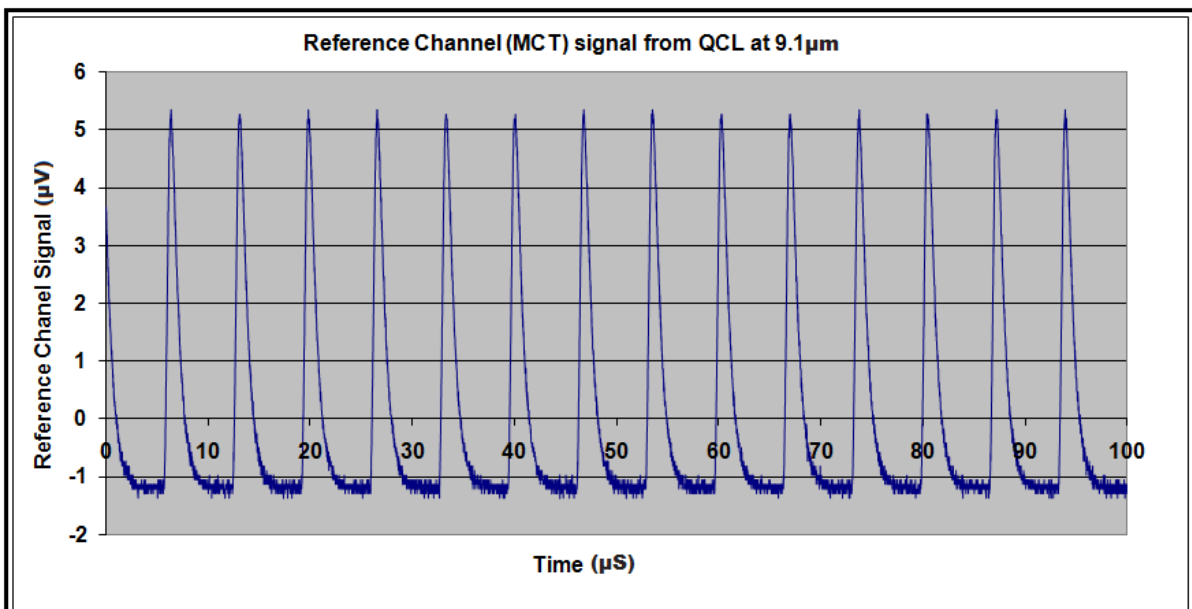


Figure 13. QCL pulse energy measured at 9.μm for 14 individual shots. It can be seen that the QCL source is very stable with a noise level less than 1%

4.6 - Cedip IR Camera

In section 4.6 the Cedip IR camera specifications and method of operation for the Cedip IR camera used in the experiments in this research is discussed. Furthermore in section 4.6.6 the “resting pixel values” (pixel values when camera is on but is not in the OPG beam path) of the Cedip IR camera and electronic/environmental noise is analysed in detail.

4.6.1 - Cedip Camera Specifications

The camera utilised was a CEDIP Jade IR camera. The camera contains a 320 x 240 focal plane array (FPA) MCT detector (Mars LW K508 FPA manufactured by Sofradir). The detector array size is 9mm by 6mm and each pixel has dimensions of approximately 30 μ m by 30 μ m. The integration time (period of time shutter of camera is open for) of the camera can be varied from 2 μ s to 10ms and the camera can capture up to 2000 frames per second. The time constant of the camera is on the order of 1s (section 4.10.3). The pixel bit depth of the camera is 14 (up to 16384 greyscale value per pixel). The detector temperature is maintained at 77K using a Stirling engine microcooler. The cold filter has been removed to enable a greater range of wavelengths to be detected; the detector is active from $\lambda \approx 2\mu$ m -10 μ m (Figure 14 shows the spectral response of the camera). The camera operates in “true snap-shot mode” so that each pixel in the FPA is read simultaneously as opposed to a sequential pixel sampling algorithm (where one pixel is sampled at a time).

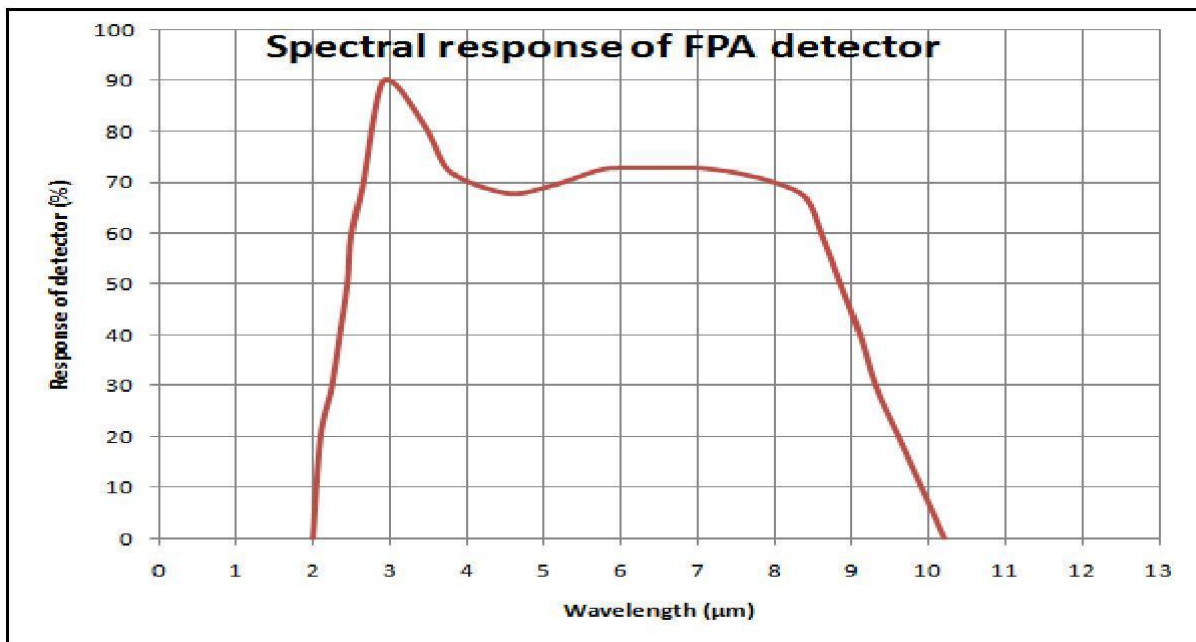


Figure 14. Spectral response of CEDIP Jade IR camera. Note this graph takes into account the transmission properties of the detector window, anti reflection coating and quantum efficiency of the detector.

4.6.2 - Cedip IR Camera Method of Operation

The absorption of an IR photon by the MCT sensitive material generates an electron hole pair. The electron is in the conduction band and the hole is in the valence band of the semiconductor. The charges created by the absorption of IR photons are stored by a capacitor in the Read out Integrated Circuit (ROIC). Once the integration period has finished, the charge stored in the capacitor is transferred to a charge-voltage conversion amplifier. The signals from the charge-voltage conversion amplifier are then transferred to multiplexers (80 to 1).

4.6.3 - Characterisation of IR Camera using a Black Body

To better understand the operation of the IR camera it is useful to characterise its detector response to a black body. An experiment was performed (in collaboration with Mr Laurence Drummond) using a hot plate (with a black metal sheet mounted on it) at various different temperatures with various different exposure times (integration times) of the IR camera. To ensure that a uniform irradiance reached the detector array in the camera the hot plate was allowed to reach thermal equilibrium before each measurement. The hot plate (with a surface area of 0.0196m^2) was placed approximately 15cm from the detector array in the camera. The temperature of the hotplate was measured using a standard laboratory thermocouple.

4.6.3.1 - Energy Reaching IR Camera from a Black Body

The spectral brightness ($\text{Wsr}^{-1}\text{m}^{-2}\text{Hz}^{-1}$) of a black body is described by Plank's law (equation 3.11). To determine the energy (E) reaching the IR detector array (in a given time interval) the spectral brightness calculated from Plank's law must be corrected for the black body area, the amount of time the camera is exposed to the black body (integration time), the solid angle subtended by the camera detector from the black body source and the range of frequencies (or wavelengths) of interest.

To correct for the black body area the spectral brightness is simply multiplied by the area of the black body (A_B).

To correct for the amount of time the detector is exposed to the radiation from the black body the spectral brightness is multiplied by the integration time (t) of the IR camera.

To correct for the solid angle the spectral brightness will have to be multiplied by a constant to account for the solid angle subtended by the detector array from the black body. The solid angle (Ω) can be estimated using equation 4.5.

$$\Omega = A_D/r^2 \quad (4.5)$$

Where;

$r \approx$ Distance of detector array from black body

$A_D \approx$ Area of detector array

For example, if the distance of the array from the black body is 15cm and the detector array area is 54mm² then the solid angle is 0.0024Sr.

Finally, to account for the spectral response of the IR detector array, Plank's formula is convoluted with the IR detector response function $f(\lambda)$ (shown graphically in Figure 14) over the sensitive range of the IR detector array. Therefore the spectral brightness received by the IR camera ($B_{IR\ CAM}$) is given by;

$$B_{IR\ CAM} = \int_{\lambda_1}^{\lambda_2} B(\lambda, T) f(\lambda) d\lambda \quad (4.6)$$

Where;

$\lambda_1 =$ Lower cut-off wavelength of IR camera $\approx 2\mu\text{m}$

$\lambda_2 =$ Upper cut-off wavelength of IR camera $\approx 10.2\mu\text{m}$

$B(\lambda, T) =$ Plank's formula for spectral brightness (as a function of λ and T);

$$B(\lambda, T) = \frac{2hc^2}{\lambda^5} \frac{1}{e^{\frac{hc}{\lambda kT}} - 1} \quad (4.7)$$

Equation 4.6 has been solved numerically for temperatures from 0 to 1500K and is shown in Figure 15.

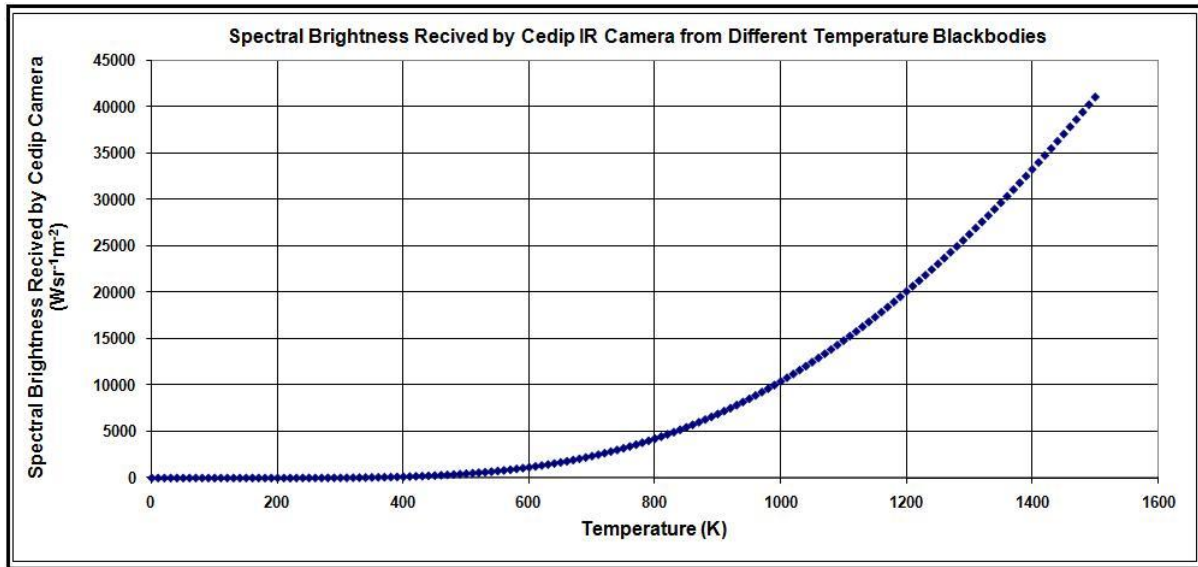


Figure 15. Spectral Brightness Received by Cedip IR Camera from Different Temperature Blackbodies with temperatures from 0 -1500K. The spectral brightness was calculated by convoluting Plank's formula with the Cedip IR camera spectral response function across the sensitive range of the Cedip IR camera

By performing a polynomial fit (using LABVIEW) to the curve in Figure 15 an expression can be generated relating the spectral brightness received by the IR camera to the temperature of the black body, hence;

$$B_{IR\ CAM} = \int_{\lambda_1}^{\lambda_2} B(\lambda, T) f(\lambda) d\lambda = B_{IR\ CAM}(T) \quad (4.8)$$

Consequently the energy reaching the IR detector (E) is calculated as follows;

$$E = t\Omega A_B B_{IR\ CAM}(T) \quad (4.9)$$

Therefore for the given experimental set-up ($t = 2\mu s$; $\Omega = 0.0024\text{Sr}$; $A_B = 0.0196\text{m}^2$) the energy deposited (in Joules) onto the IR detector array in a $2\mu s$ time interval (for blackbodies with temperatures between 300-600K) is given (approximately) by equation 4.10.

$$E = (-3.44 \times 10^{-13}) + (2.72 \times 10^{-11})T - (1.37 \times 10^{-13})T^2 - (1.83 \times 10^{-16})T^3 + (1.40 \times 10^{-18})T^4 \quad (4.10)$$

4.6.3.2 - IR Camera Response to a Black Body

Figure 16 shows the experimental results obtained by exposing the detector array in the Cedip IR camera to a hot plate at several different temperatures at several different integration times. The graphs in Figure 16 were created by averaging the detector response (across the entire array) and plotting the results against the energy reaching the detector array given by equation 4.10 By normalising all the measurements taken at different integration times to an integration time of $2\mu\text{s}$ it can be seen that the detector array response is saturating at lower average pixel values for lower integration times.

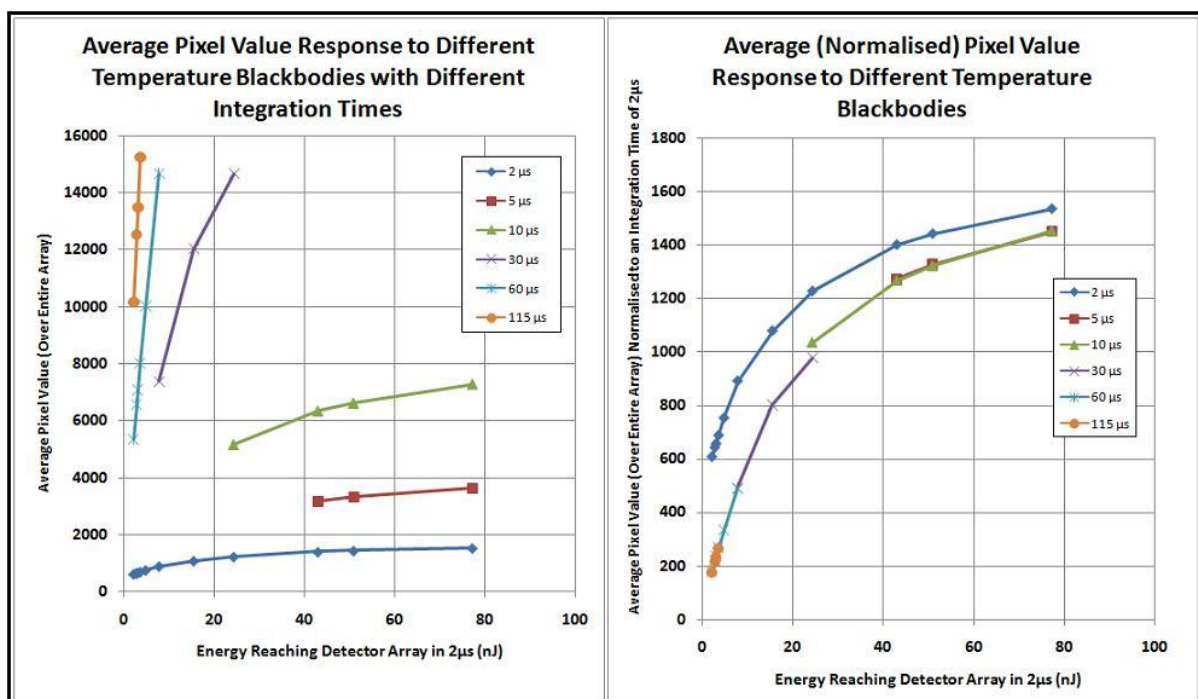


Figure 16. Average detector response of Cedip IR camera to a hotplate at different temperatures at different integration times. The graph on the left shows the average raw pixel value response to different integration times. The graph on the right shows all the measurements at different integration times normalised to an integration time of $2\mu\text{s}$.

It is evident from Figure 16 that the average detector response to an incident energy is, in general, non-linear. However at low incident energies the detector response behaves linearly which is demonstrated by Figure 17.

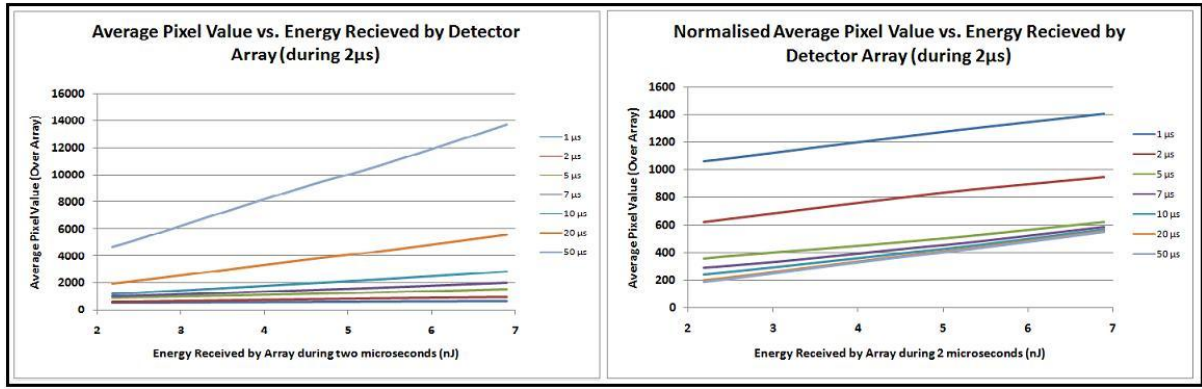


Figure 17. Average detector response of Cedip IR camera to a hotplate at different temperatures at different integration times. The graph on the left shows the average raw pixel value response to different integration times. The graph on the right shows all the measurements at different integration times normalised to an integration time of 2µs.

Therefore, in general, the (non-linear) relationship between detector response (Y_{ij}) for a given incident energy (X_{ij}) is;

$$Y_{ij} = f_{ij}(X_{ij}) \quad (4.11)$$

Where f_{ij} can be estimated by making a series of measurements whereby the detector array is uniformly illuminated with a black body of extensive surface area (so $X_{ij} = X(T)$).

However for low incident energies each detector in the array responds linearly to the amount of energy reaching it (in a given time interval) so each detector (with coordinates, ij) in the array can be assigned its own gain (m_{ij}) and offset (c_{ij}) parameters. Therefore the detector response (Y_{ij}) for a given (low) incident energy (X_{ij}) is;

$$Y_{ij} = m_{ij}X_{ij} + c_{ij} \quad (4.12)$$

4.6.4 - Non Uniformity Correction (NUC)

When using multichannel detectors a non uniformity correction is required to compensate for the differences in individual detector characteristics. In the following section (4.6.4) both a simple linear NUC, non-linear NUC and patch NUC are discussed.

4.6.4.1 - Linear Non Uniformity Correction (LNUC)

Figure 18 illustrates how the disparities between three individual detectors can give variable detector responses for a given incident energy.

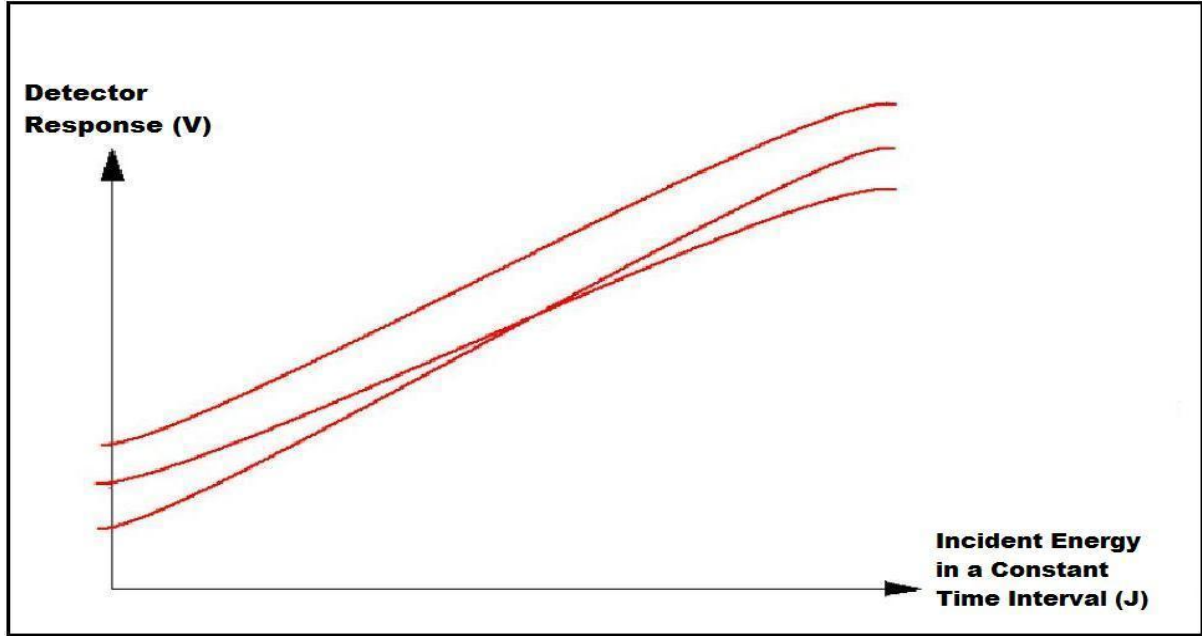


Figure 18. Graph showing disparate detector characteristics in an array of IR detectors. A non uniformity correction is required to compensate for these detector disparities.

The (linear) NUC is accomplished by performing the so called “two-point black body method”. The two-point method involves a uniform illumination of the array (to ensure an equal incident energy on each individual element in the array) with two reference energies (practically this is accomplished by using a black body with an extensive surface area at two reference temperatures, so $X_{ij} = X(T)$). Firstly the average detector responses (over the entire array) are calculated for reference temperature 1 (T_1) and reference temperature 2 (T_2). Secondly all the detectors in the array are brought into line with the average detector response (so that *at the reference energies* all detectors in the array have the same response).

The average detector response at T_1 and T_2 is given by equations 4.13 and 4.14 respectively;

$$\overline{Y(T_1)} = \frac{\sum_{ij} Y_{ij}(T_1)}{N} \quad (4.13)$$

$$\overline{Y(T_2)} = \frac{\sum_{ij} Y_{ij}(T_2)}{N} \quad (4.14)$$

Where;

N = Number of detector elements in array

Figure 19 illustrates how individual detector elements (in this case two detector elements with coordinates AB and CD) are brought into line with the average (over entire array) detector response for two reference measurements.

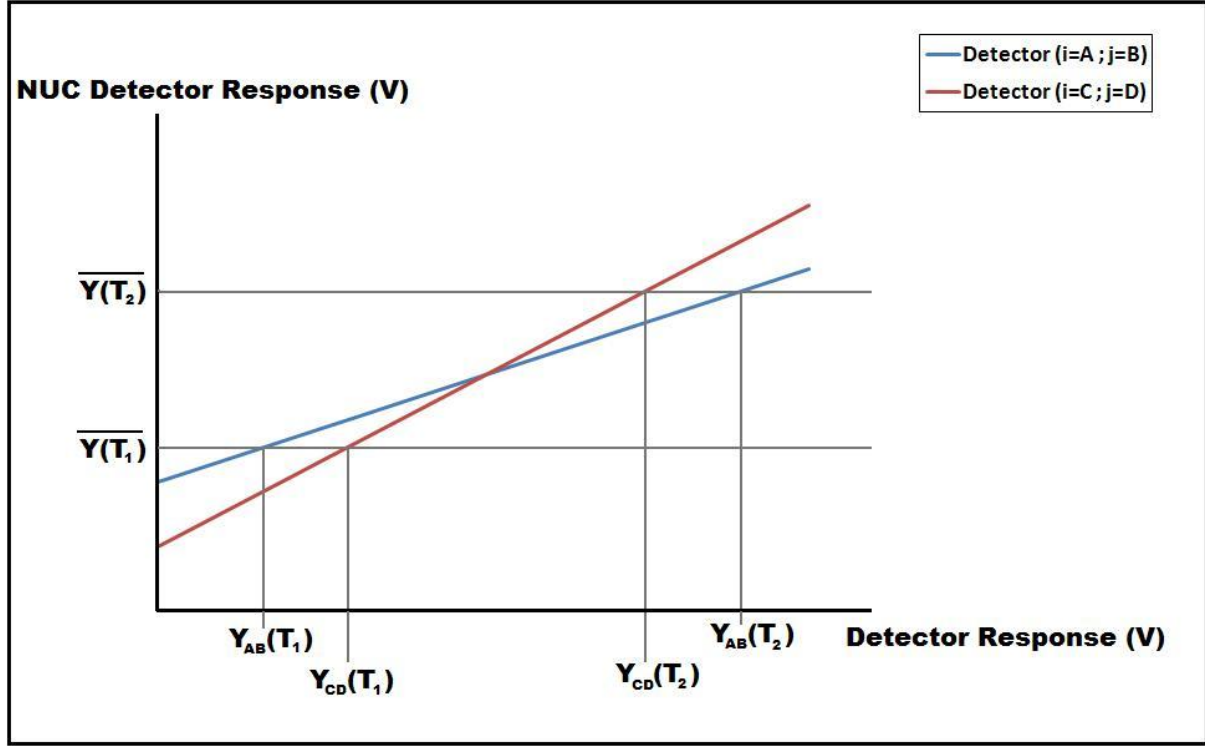


Figure 19. Non Uniformity Correction. Graph illustrating the method of bringing individual detectors in an IR array into line with the average (over entire array) detector response for two reference measurements.

The slopes and y-intercepts of the straight lines in Figure 19 are labelled as α_{ij} and β_{ij} respectively.

$$\alpha_{ij} = \frac{\overline{Y(T_2)} - \overline{Y(T_1)}}{Y_{ij}(T_2) - Y_{ij}(T_1)} \quad (4.15)$$

$$\beta_{ij} = \overline{Y(T_1)} - \alpha_{ij}Y_{ij}(T_1) = \overline{Y(T_2)} - \alpha_{ij}Y_{ij}(T_2) \quad (4.16)$$

The NUC detector responses (Y_{ij}^{NUC}) are then given by;

$$Y_{ij}^{NUC} = \alpha_{ij}Y_{ij} + \beta_{ij} \quad (4.17)$$

It should be noted that the α_{ij} and β_{ij} values will (by definition) ensure that the values of Y_{ij}^{NUC} at the reference temperatures T_1 and T_2 are $\overline{Y}(T_1)$ and $\overline{Y}(T_2)$ respectively. However for temperatures (or more generally incident energies) which are not equal to the reference measurements there may still be some disparity between individual detector elements due to the individual detectors deviations from a linear response.

4.6.4.1.1 - Representative LNUC for Cedip IR Camera

The calibration method for the two-point blackbody LNUC performed for the research in this thesis is described in detail elsewhere[8]. To illustrate the LNUC method a flat black book was used for the lower reference temperature and a hotplate (painted black) in thermal equilibrium was used for the upper temperature. Both the hotplate and the black book were placed as close as possible to the detector array and no lenses were used. Figure 20 and Figure 21 show the distribution of the α_{ij} and β_{ij} values respectively.

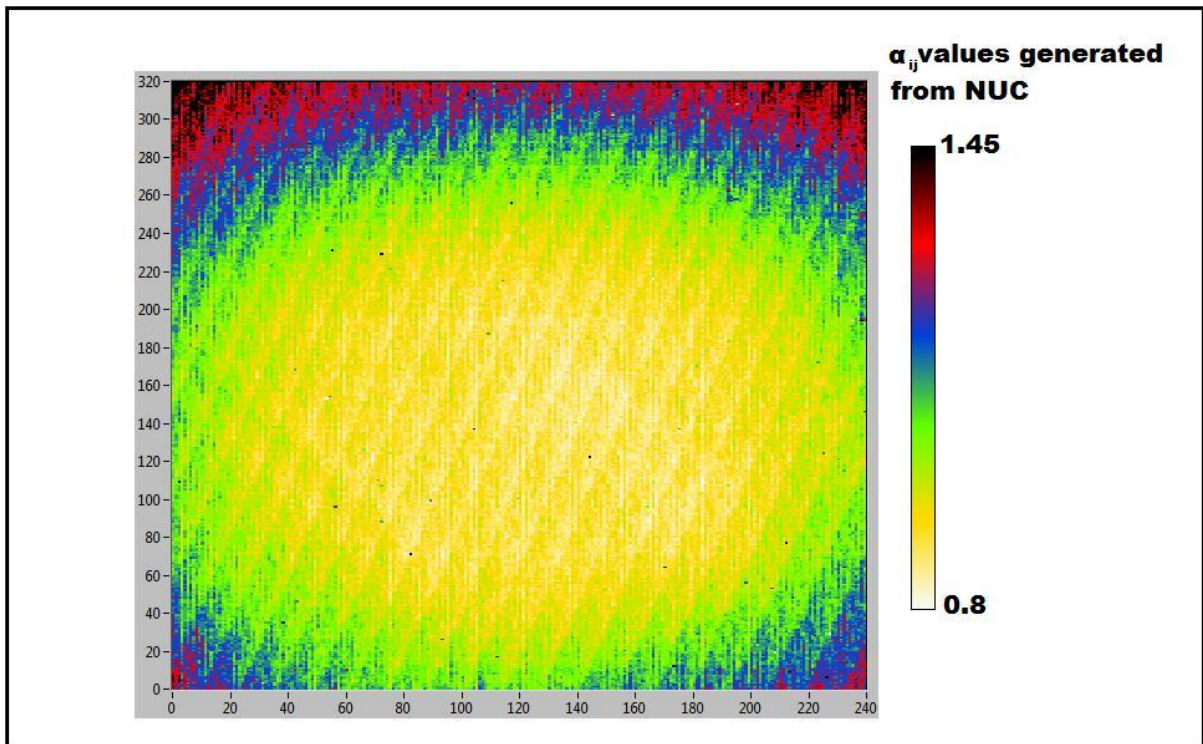


Figure 20. Alpha values of array generated from a typical non uniformity correction. The alpha values have a range of 0.1 to 2 with 99.34% of the alpha values in the range 0.8 to 1.45. A bad pixel replacement algorithm has been applied limiting the pixel value between 0.8 and 1.45. The distribution of alpha values indicates that the detector elements on the edge of the array have the largest alpha values.

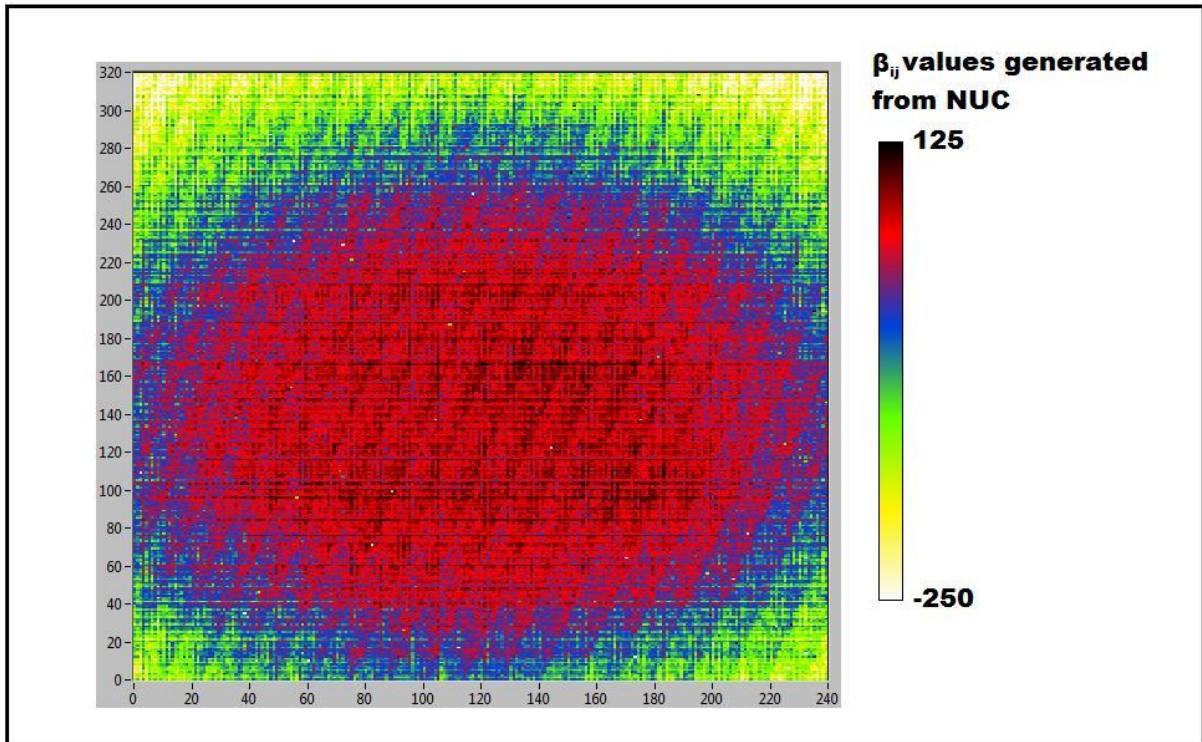


Figure 21. Beta values of array generated from a typical non uniformity correction. The beta values have a range of -957 to 530 with 99.41% of the beta values in the range -250 to 125. A bad pixel replacement algorithm has been applied limiting the pixel value between -250 and 125. The distribution of beta values indicates that the detector elements on the edge of the array have the smallest beta values.

An example of the pixel values from the IR camera when it has been exposed to a hotplate (at 55°C) before and after a LNUC is shown in Figure 22. The raw data (without any NUC) shows similar detector characteristics in horizontal lines which is most likely a consequence of the construction method of the detector array. After the LNUC has been performed (using the α_{ij} and β_{ij} values shown in Figures 20 and 21 respectively) the illumination pattern is still non-uniform which is a symptom of the inadequacy of the LNUC to account for the *non-linear* response characteristics of the individual detectors in the array. Figure 23 shows the detector response characteristics (with a LNUC applied) for several different uniform illuminations using a hotplate at several different temperatures.

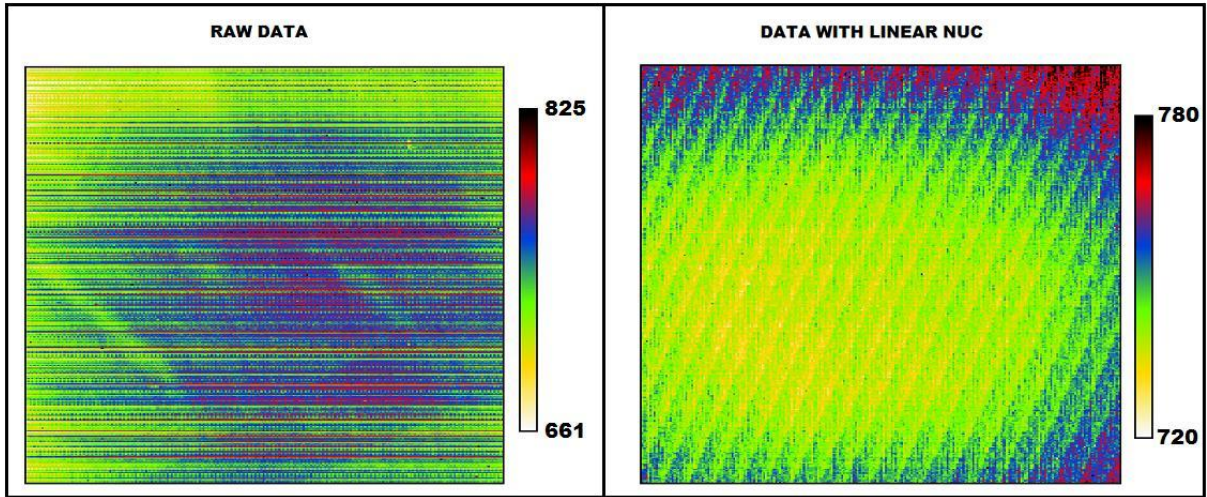


Figure 22. Pixel values recorded on the Cedip IR camera from a hotplate at 55 degrees Celsius with and without linear NUC (integration time of camera = $2\mu\text{s}$; Solid angle subtended by detector from the hotplate = 0.0024Sr ; Surface area of the blackbody = 0.0196m^2) . There are 99.88% of the pixel values in the ranges 661-825 and 720-780 for the raw data and the linear NUC data respectively.

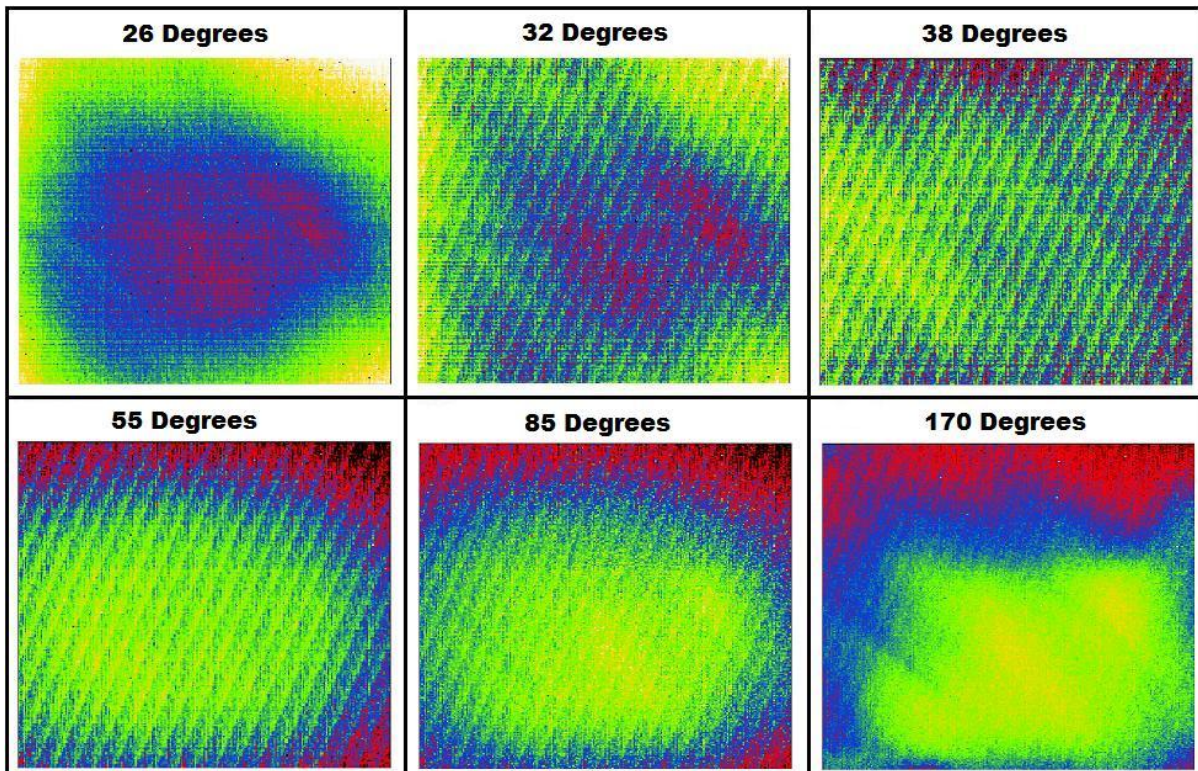


Figure 23. Response (with linear NUC applied) of the detector array in the Cedip IR camera when illuminated with a hot plate (an approximation to a blackbody with extensive surface area) at several different temperatures.

4.6.4.2 - Non Linear Non Uniformity Correction (NLNUC)

The average detector response at temperature T_k is given by;

$$\overline{f(T_k)} = \frac{\sum_{ij} f_{ij}(T_k)}{N} \quad (4.18)$$

So to perform a NLNUC, by analogy with the LNUC method, curves are plotted for each individual detector element with the average detector response on the y-axis and the individual detector responses on the x-axis. The resulting curves can then be fitted to polynomial functions (of order n) to generate non-linear NUC detector response functions (Y_{ij}^{NLNUC}) of the form;

$$Y_{ij}^{NLNUC} = \alpha_{ij} + \beta_{ij}Y_{ij} + \gamma_{ij}Y_{ij}^2 + \dots + \delta_{ij}Y_{ij}^n \quad (4.19)$$

4.6.4.2.1 - Representative NLNUC for Cedip IR Camera

To illustrate the NLNUC method a hot plate was placed 15cm from the detector array and the array detector response was recorded for several different temperatures. By calculating the average detector response across the entire array for the different blackbody temperatures (using equations 4.18) the 4th order NLNUC detector response functions were determined. Figure 24 shows the detector response characteristics (with a 4th order NLNUC applied) for several different uniform illuminations using a hotplate at several different temperatures.

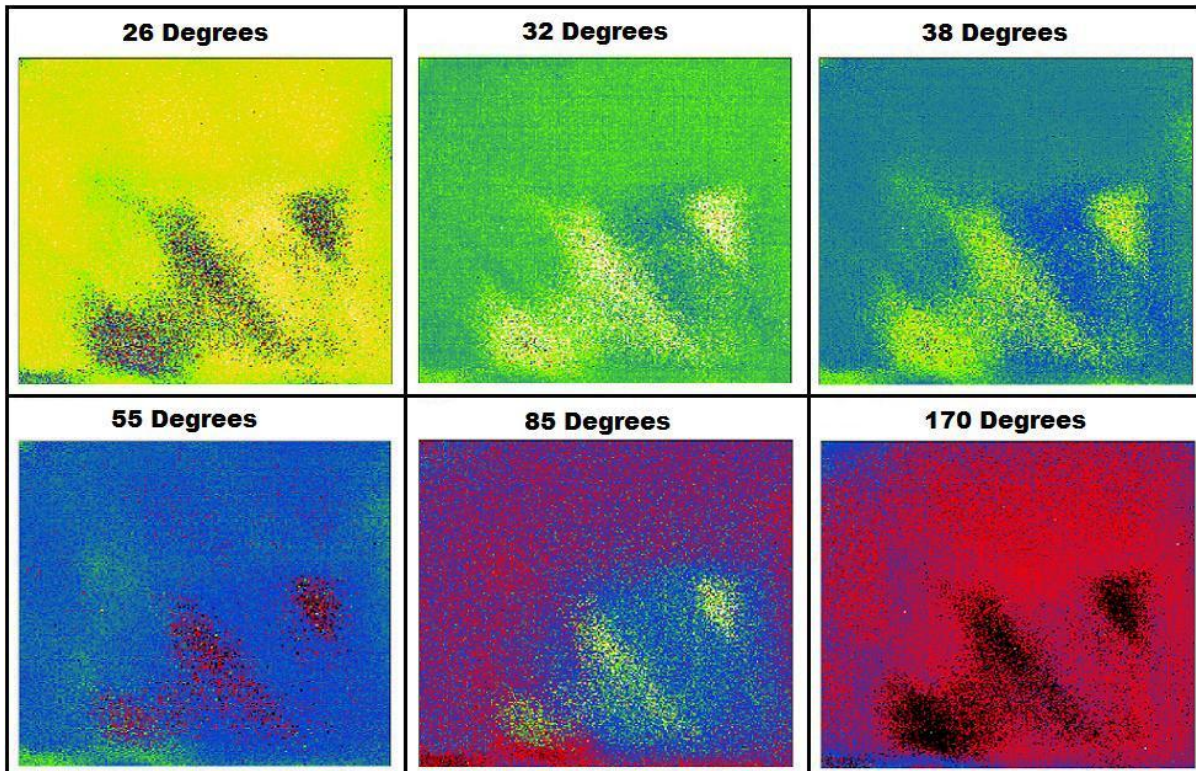


Figure 24. Response (with non-linear NUC applied) of the detector array in the Cedip IR camera when illuminated with a hot plate (an approximation to a blackbody with extensive surface area) at several different temperatures.

By comparing figure 24 with Figure 23 it is obvious that a NLNUC provides a superior method of compensating for individual detector disparities compared to a LNUC.

4.6.4.3 - Patch Non Uniformity Correction (PNUC)

The purpose of a conventional NUC (both linear and non-linear) is to account for the differences in the individual pixel response characteristics of a detector array to a uniform irradiance of incident energy. However the NUC can only be expected to behave reliably when the NUC is used on a data set that was collected with a similar incident energy that the NUC was developed with. In other words, if an NUC is calculated using a blackbody with an incident energy range of 2-7nJ, for example, then the NUC cannot be expected to account for detector disparities present at 30nJ. Therefore a conventional NUC has a scope (range over which the NUC can be faithfully applied) which suggests that NUCs (both linear and non-linear) developed with a blackbody may be inadequate to account for individual detector disparities when the camera array is illuminated with the high intensity OPG or QCL source. The PNUC was developed (in collaboration with Mr Laurence Drummond) to address this issue of detector disparities present at intensities obtained with laser sources.

The PNUC uses images collected by illuminating the Cedip camera detector array with a laser source to calculate a correction for the individual detector disparities (at high intensities) of the array. The

PNUC works by bringing the individual detector responses into line with the average detector responses of a surrounding small area (patch) of pixels. The key assumption is that the illumination is approximately uniform over this small patch. The size of the “small patch” can be estimated (for the OPG) from Figure 25 which shows the detector array response (with a LNUC applied) when a single shot from the OPG illuminates the array. It can be seen that a patch size of 3 by 3 pixels is probably small enough that the illumination over this patch is approximately uniform (whereas for a patch of 33 by 33 pixels the illumination is certainly not uniform).

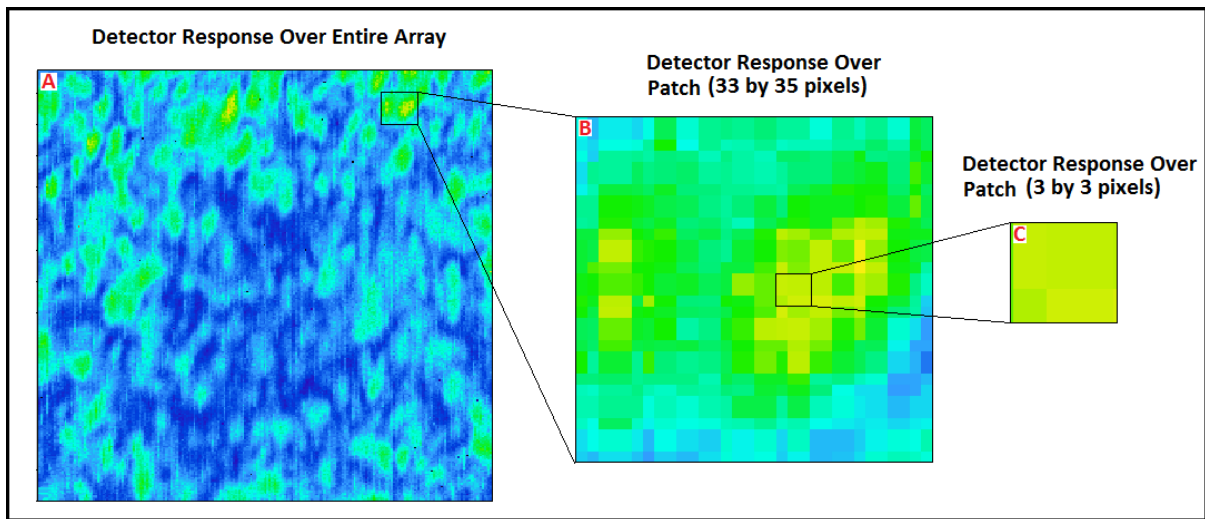


Figure 25. Estimation of the size of a patch needed to apply the PNUC to data collected with the OPG. The images were taken with all the optics set up as normal (except with no sample in the beam path). The camera was operated with a 2 point linear NUC and the resting pixel values (RPVs) were deducted. A) The detector response across the entire array. B) The detector response for a patch of pixels (33 by 35). C) The detector response for a patch of pixels (3 by 3). It can be seen that the illumination is approximately uniform over a patch of 3 by 3 pixels.

If we begin by considering a single detector element then, by analogy with equation 4.18, the average detector response over a patch of adjacent pixels for shot S_k is given by;

$$\overline{f(S_k)} = \frac{\sum_{patch} f_{ij}(S_k)}{N} \quad (4.20)$$

So to perform a PNUC several shots are taken with a laser source and curves are plotted for each individual detector element with the average detector response over the patch on the y-axis and the individual detector responses on the x-axis. The resulting curves can then be fitted to polynomial functions (of order n) to generate PNUC detector response functions (Y_{ij}^{PNUC}) of the form;

$$Y_{ij}^{PNUC} = \alpha_{ij} + \beta_{ij}Y_{ij} + \gamma_{ij}Y_{ij}^2 + \dots + \delta_{ij}Y_{ij}^n \quad (4.21)$$

4.6.4.3.1 - Representative PNUC for Cedip IR Camera

To illustrate the PNUC method 250 shots were collected with the OPG at 5 different wavelengths (6.5 μm , 6.75 μm , 6.9 μm , 7.0 μm and 7.9 μm ; 50 shots were collected at each wavelength). Each of these shots had the LNUC applied to them and they were corrected for the RPVs (pixel values when the camera was on but not being illuminated by the OPG, section 4.6.6.1). A patch size of 3by3 pixels was used and the PNUC detector response functions were generated using equations 4.20 and 4.21. Since it was observed that the PNUC detector response functions were linear only 1st order PNUC detector response functions were required. Once the 1st order PNUC detector response functions were generated a PNUC was applied to a representative single shot from the OPG source to illustrate the effect the PNUC has on a single image (Figure 26).

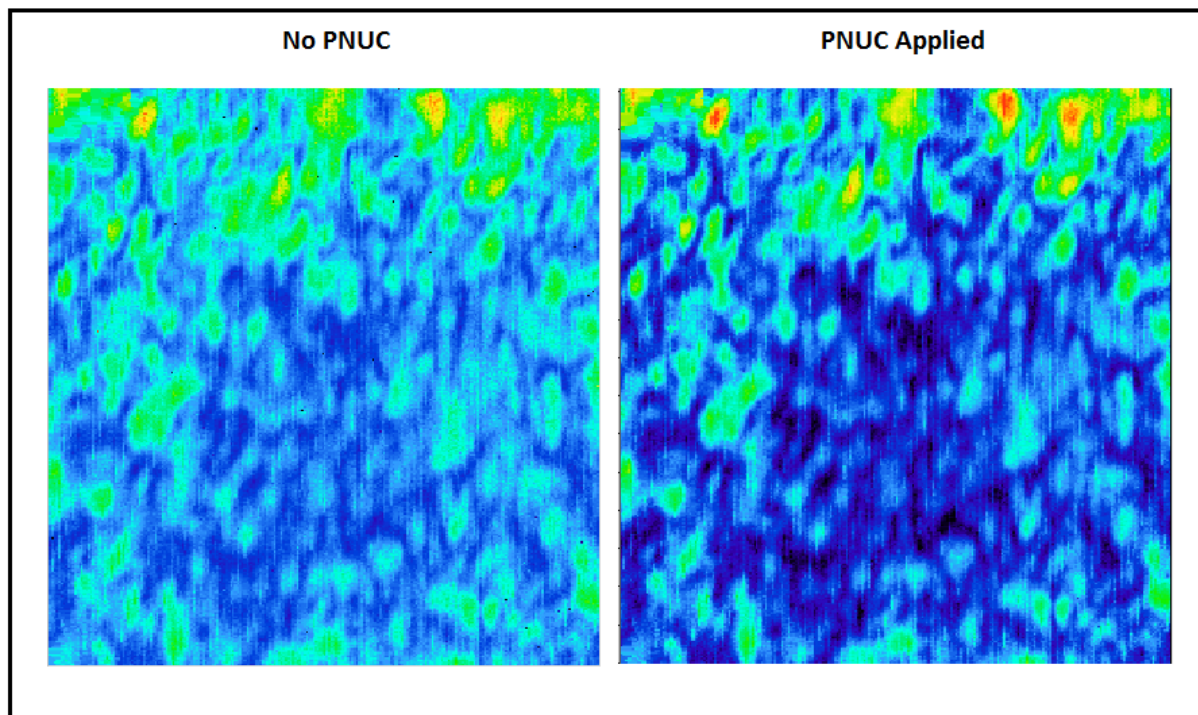


Figure 26. Comparison of images before and after a patch NUC has been applied for a single shot from the OPG. The patch size used was 3by3 pixels and the original image has a LNUC applied and the RPVs (the pixel values when the camera is on but it is not being illuminated by the OPG source) have been deducted.

4.6.4.4 - Assessment of the Quality of a NUC

In general an NUC (linear, non-linear or patch) attempts to fit functions to the curves generated by plotting the individual pixel responses on the x-axis and the average pixel response on the y-axis at several different uniform illuminations. The quality of the NUC is determined by how well the

generated NUC functions (Y_{ij}^{NUC}) approximate the actual curves (Y_{ij}^{Actual}) and can be assessed by calculating the residuals (R) of the NUC functions;

$$R(Y_{ij}) = Y_{ij}^{Actual}(Y_{ij}) - Y_{ij}^{NUC}(Y_{ij}) \quad (4.22)$$

Clearly if the NUC functions fit the actual curves very well the residual functions will be close to 0 and appear as just low level noise. However if there is a significant difference between the fitted and actual curves then the residual functions will show the values of Y_{ij} (and hence illumination energy) which are systematically different for the fitted and actual functions (Figure 27).

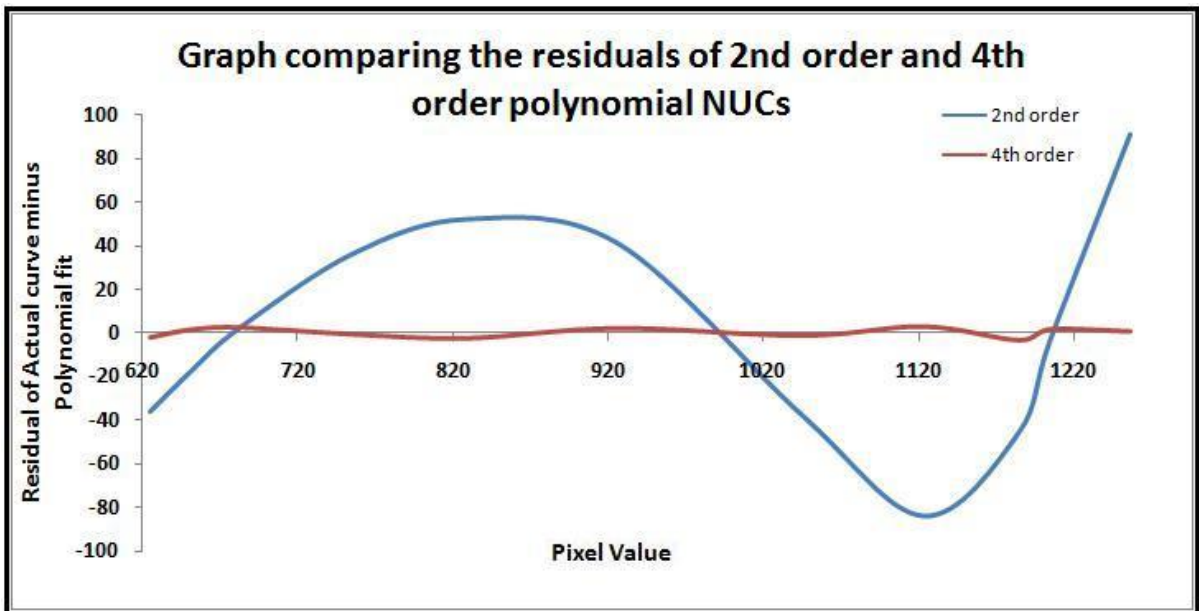


Figure 27. Graph comparing the 2nd order and 4th order residuals. The 4th order exhibits a much better fit to the observed data than the 2nd order evidenced by the fact that the residual is almost zero. The 2nd order residual shows that there are large deviations of the fitted 2nd order polynomial to the actual data especially at pixel values of 820 and 1820.

4.6.5 - Bad Pixel Replacement (BPR)

Some pixels, usually those operating outside the linear regime, appear as black or white coloured pixels on the image and can be eliminated by using a bad pixel replacement (BPR) algorithm. By setting boundary conditions, such as the “noisy BPR” which compares each pixel value to the average of its neighbours (8 adjacent pixels), “bad” pixels can be identified and replaced. In the case of the noisy BPR method the “bad” pixels are replaced with the average of their adjacent pixels. The algorithm for the noisy BPR is;

NOISY BPR

If;

$$mean - (A \times s.d) < pixel\ value < mean + (A \times s.d)$$

Where;

Mean = average of 8 adjacent pixels

s.d = standard deviation of 8 adjacent pixels

A = constant

Then leave the pixel alone otherwise replace pixel with the average of its adjacent pixels.

The noisy BPR (with A = 3) was applied automatically (by the propriety software of the Cedip IR camera) to all the images collected in this research. The noisy BPR is one example of a bad pixel replacement algorithm. Another BPR which will be used frequently in the analysis of the OPG imaging data is called the “threshold BPR”. The threshold BPR is used to replace pixels whose values are significantly different from the majority of the other pixels in an image. In other words the pixel values are limited to maximum and minimum (threshold) values. A few pixels with abnormally large (or small) values are problematic since image contrast will be compromised (Figure 28 and Figure 29). This is because the colour palette which represents the pixel value has a range defined by the maximum and minimum pixel values. Particular care must be taken in this situation however since post bad pixel replacement the maximum and minimum absorbance values can no longer be used for quantitative analysis. The algorithm for the threshold BPR is;

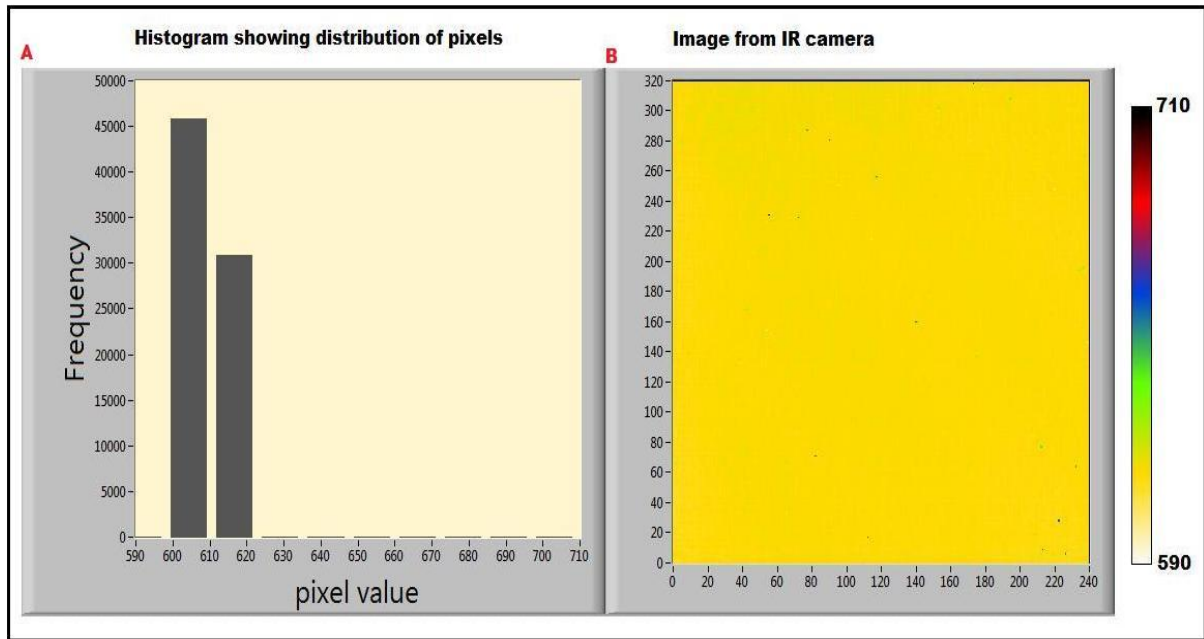


Figure 28. Threshold BPR algorithm. Original data; the histogram of all the pixels from the array shows that some of the pixels are significantly different from the majority of the other pixels (A) which compromises image contrast (B)

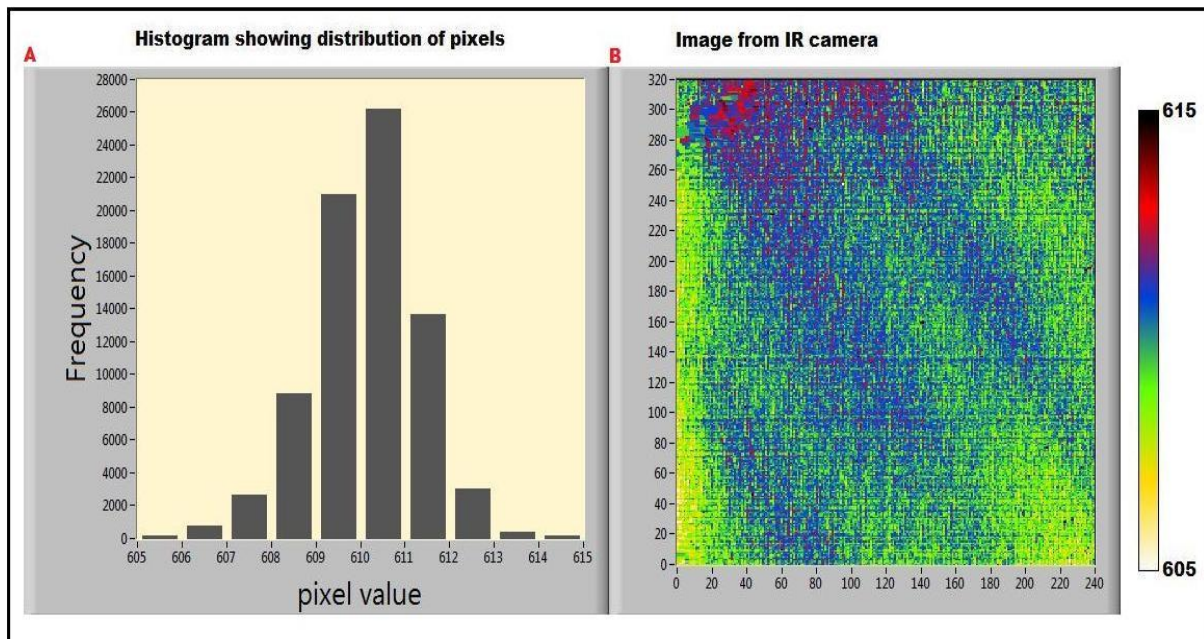
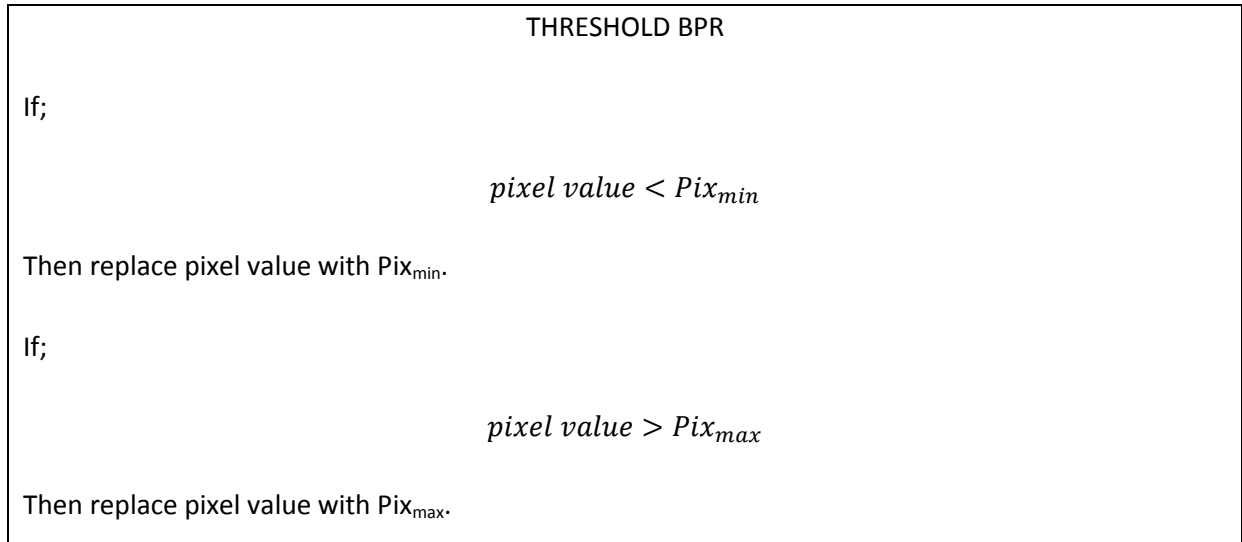


Figure 29. Threshold BPR algorithm. Corrected data - Minimum pixel value limited to 605 and maximum pixel value limited to 615; the histogram of all the pixels with the threshold BPR applied shows that most of the pixels are within the range 605-615 (A). Greater image contrast is observed once the threshold BPR is applied (B)



The upper (Pix_{max}) and lower (Pix_{min}) limits can either be set arbitrarily or defined by the following equations;

$$Pix_{max} = \sigma + (A \times s.d.)$$

$$Pix_{min} = \sigma - (A \times s.d.)$$

Where;

σ = mean pixel value of image

s.d. = standard deviation of pixels in image

A = constant

If the pixels in the image are assumed to have an approximately normal distribution then;

A = 1 will replace approximately 32% of the pixels

A = 2 will replace approximately 5% of the pixels

A = 3 will replace approximately 0.4% of the pixels

And so on.

4.6.6 - Resting Pixel Values on IR Camera and Analysis of Electronic and Environmental Noise

When the camera is turned on each detector in the IR array has a non-zero “resting pixel value (RPV)” which should be deducted from subsequent measurements so that each detector in the camera array is calibrated to zero. These RPVs fluctuate in time due to electronic noise (section 3.9.3.1.1) and/or environmental noise (section 3.9.3.1.2).

Figure 16 shows the average camera pixel values for various different values of integration time (time camera shutter is open) when the Cedip IR camera was exposed to a black body. The data points plotted at an energy of approximately 2.2nJ were collected when the blackbody was turned off and so represent electronic and environmental signals only. It is expected that the environmental signal component would have a strong dependence on the integration time and the electronic signal component would be independent of integration time. The relationship between average pixel value (P_{av}), electronic signal (S_{ele}) and the environmental signal (S_{env}) for $1\mu s$, for an integration time t (μs), can be expressed as;

$$P_{av} = S_{ele} + tS_{env} \quad (4.23)$$

The graph in Figure 16, which shows the normalised average pixel value for $2\mu s$ ($2P_{av}/t$), has an electronic signal component which decreases as the integration time increases (as $t \rightarrow \infty$; $S_{ele}/t \rightarrow 0$) since ;

$$\frac{P_{av}}{t} = \frac{S_{ele}}{t} + S_{env} \quad (4.24)$$

Hence at a large integration time the normalised average pixel value is essentially the environmental noise component (for $2\mu s$). Therefore, at an integration time of $2\mu s$ and with the LNUC applied, the RVPs are composed of approximately 400 pixel values from the electronic signal and 200 pixel values from the environmental signal. For an integration time of $50\mu s$ and with the LNUC applied the RVPs are composed of approximately 400 pixel values from the electronic signal and 5000 pixel values from the environmental signal.

To examine the nature of the RVPs and the electronic / environmental noise a data set was collected (the OPG imaging system was operated *without* the laser on) for 500 shots, at an integration time of $2\mu s$, with the LNUC applied.

4.6.6.1 - Resting Pixel Values (RVPs) of IR Camera

To estimate the RVPs of each detector in the IR camera each pixel in the image was averaged over all 500 shots and a “heat map” was generated to visualise the distribution of the mean pixel values. The heat map for the mean pixel values shows a resting pixel value range of 580 to 710 with the majority (99.84%) of the pixels in the range 605 to 615. As discussed in section 4.6.5 in order to visualise the pixel distribution a threshold BPR needs to be applied to replace abnormally large / small pixels.

Figure 30 shows the heat map for the mean pixel values with a threshold BPR applied to limit the pixel value between 605 and 615.

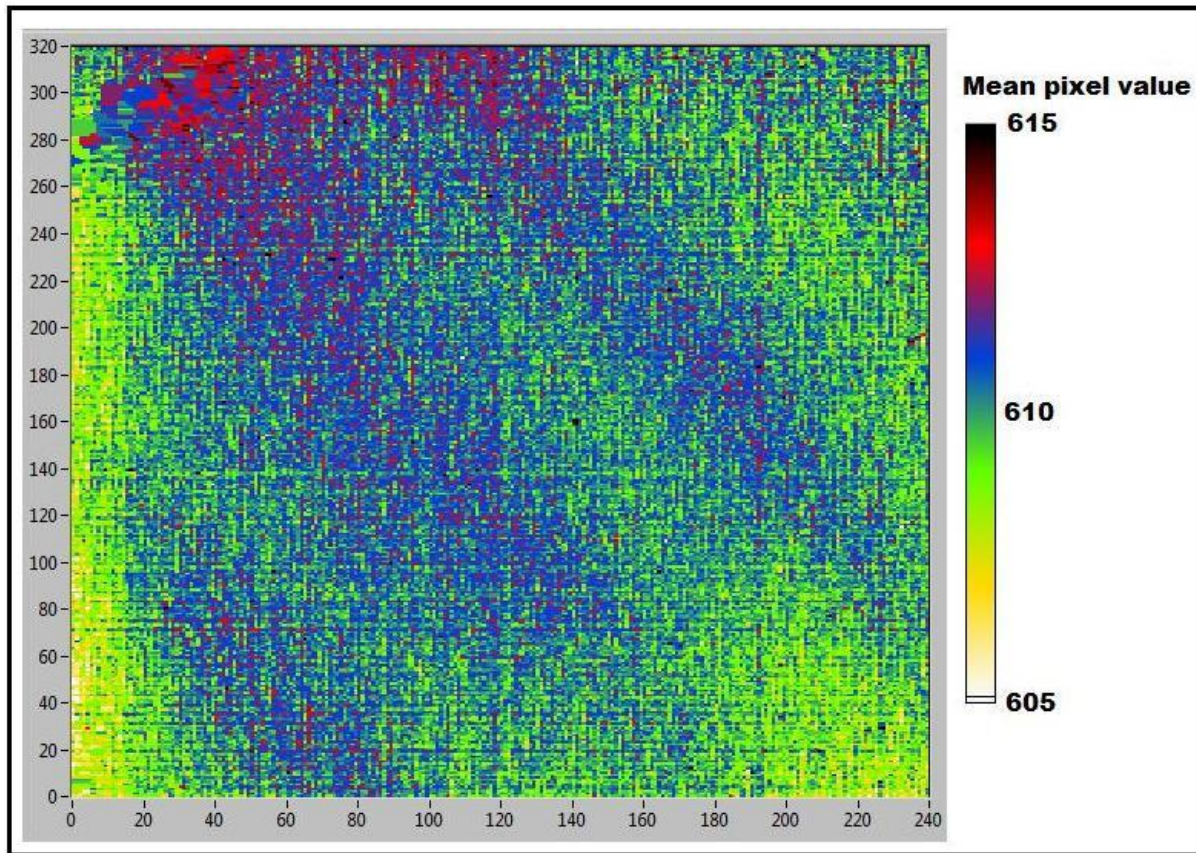


Figure 30. Mean values for the resting pixel values of the IR camera. The original pixel value range was 580 to 710 with the majority (99.84%) of the pixels in the range 605 to 615. A bad pixel replacement algorithm has been applied limiting the pixel values to the range 605 - 615.

4.6.6.2 - Electronic and Environmental Noise in IR Camera

To estimate the electronic and environmental noise the pixel uncertainties were calculated from the 500 shots using equation 4.25

$$\text{pixel uncertainty} = \frac{\text{s.d. in pixel value from } N \text{ shots}}{\sqrt{N}} \quad (4.25)$$

Where;

s.d. = Standard deviation

N = Number of shots (500 in this case)

The pixel uncertainties have a range 0.01 to 0.4 and with 98.72% of the values between 0.08 and 0.16. Figure 31 shows the heat map for the pixel uncertainties (threshold BPR applied limiting the

pixel range between 0.08 and 0.16). The heat map for the uncertainties in the resting pixel values shows that the uncertainties for the central pixels are somewhat less than those on the periphery indicating that the central pixels give the most reliable values. However the highest pixel uncertainty is only 0.4 pixel values so all the resting pixel values can be measured to a high level of confidence. The distribution of the RPV uncertainties can be understood by comparing Figure 31 to Figure 20. It can be seen that the central pixels have the smallest gain values (α_{ij}) which means that for a given “detector response range” the “LNUC detector response range” in the centre of the array is less than the “LNUC detector response range” on the edge of the array. Therefore if the electronic/environmental noise across the array is approximately constant then the LNUC will generate the uncertainty distribution seen in Figure 31. Figure 31 Characterises the electronic/environmental noise from the detector array in the IR camera and shows that it is less than a pixel value (and in the central region of array practically zero) when 500 shots are taken and averaged.

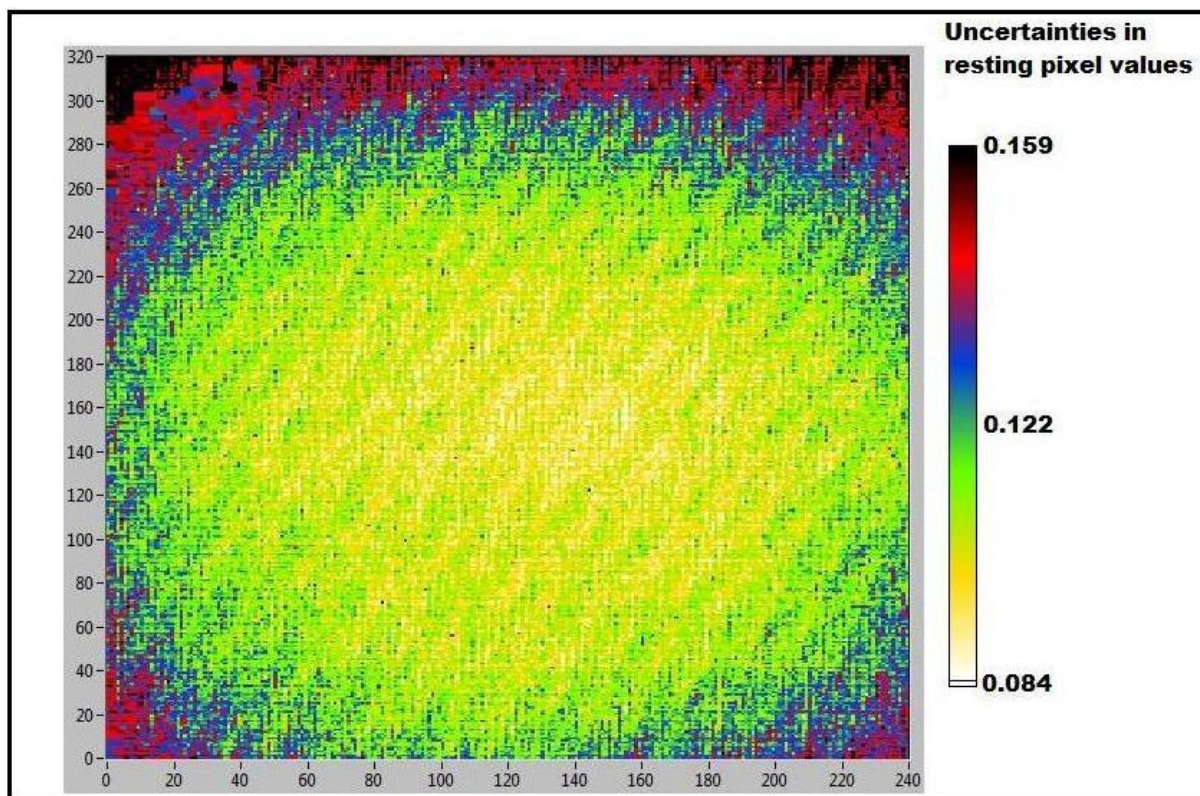


Figure 31. Uncertainties in the resting pixel values of the IR camera characterising the electronic noise in the IR camera. The pixel uncertainties have a range 0.01 to 0.4 and with 98.72% of the values between 0.08 and 0.16. A bad pixel replacement algorithm has been applied limiting the pixel values to the range 0.084 - 0.159.

4.7 - Imaging Optics (Overall Set-Up) for the OPG Imaging System

The basic set-up for the OPG imaging system is shown in Figure 32. The sample, objective lens and reference lens were mounted on movable mounts which allowed for precise translation in the x-y-z directions. The reference channel was placed into the optical setup to correct for the pulse-to-pulse variations from the OPG and will be discussed in more detail in section 4.10. A diffuser was used to eliminate optical artefacts caused by the coherence of the OPG light (section 4.9). The filter was used to eliminate the pump beam and the polariser was used to select either the (vertically polarised) idler or (horizontally polarised) signal beam. A condenser lens was experimented with before the sample but it was found that it introduced optical artefacts into the image and so was omitted.

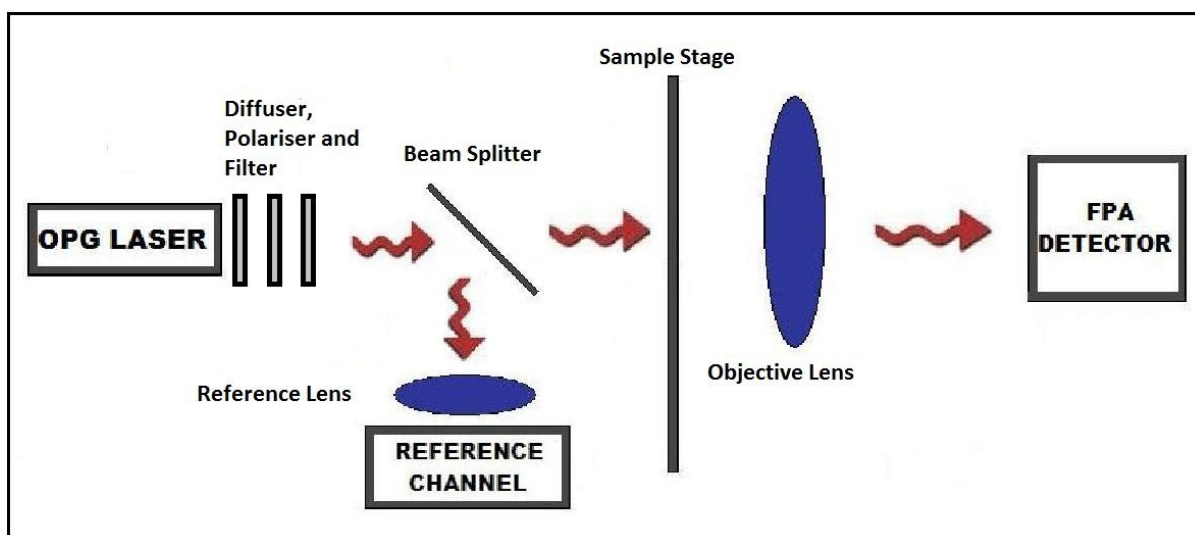


Figure 32. Imaging optics for OPG and camera

A chemical image with absorbance pixel values (A_{OPG}) can be collected from the OPG imaging system by collecting images of the sample, the “OPG background” (section 4.12.2.1) and the resting pixel values (RPV) (section 4.6.6.1) and using equation 4.26.

$$A_{OPG}(x, y) = -\log_{10} \left[\frac{Sample(x, y) - RPV(x, y)}{OPG \text{ Background } (x, y) - RPV(x, y)} \right] \quad (4.26)$$

Where x and y are the co-ordinates of the pixels in the IR detector array.

The measurement of the RPVs (Figure 30) is discussed in section 4.6.6.1. In general it is best to measure the RPVs frequently (before every chemical image is collected) since the RPVs on the IR

camera tend to drift after about a day. The OPG background is measured by running the OPG imaging system without the sample in the sample stage and is discussed in section 4.12.2.1.

4.7.1 - Synchronisation of the IR Camera to the OPG

As described in section 4.4 the OPG has 100ps pulsed output at a rep rate of 3Hz. In order to minimise the amount of background signal received from the environment the integration time of the camera was set to a value of $2\mu\text{s}$. In order to ensure that each laser pulse arrived at the time when the IR camera shutter was open ($2\mu\text{s}$ window) it was necessary to synchronise the camera shutter with the OPG laser. To accomplish synchronisation an adjustable electronic delay box (built by Dr Hemmel Amrania) was connected from the timing electronics of the OPG source (controlling electro-optic components) to the trigger of the camera. Since the time delays between electronic TTL pulses and actual events was unknown and because of day-to-day drift (caused by electronic and thermal variations) in the timing an adjustable delay box was a necessity. A more complete discussion of the details of the camera-OPG synchronisation can be found in Dr Hemmel Amrania's thesis[8].

4.8 - Imaging Optics (Overall Set-Up) for the QCL Imaging System

The basic set-up for the QCL imaging system is shown in Figure 33. The optical components used were the same as for the OPG imaging system (section 4.7) but a reference channel was not required since the QCL is a relatively stable source (section 4.5.1).

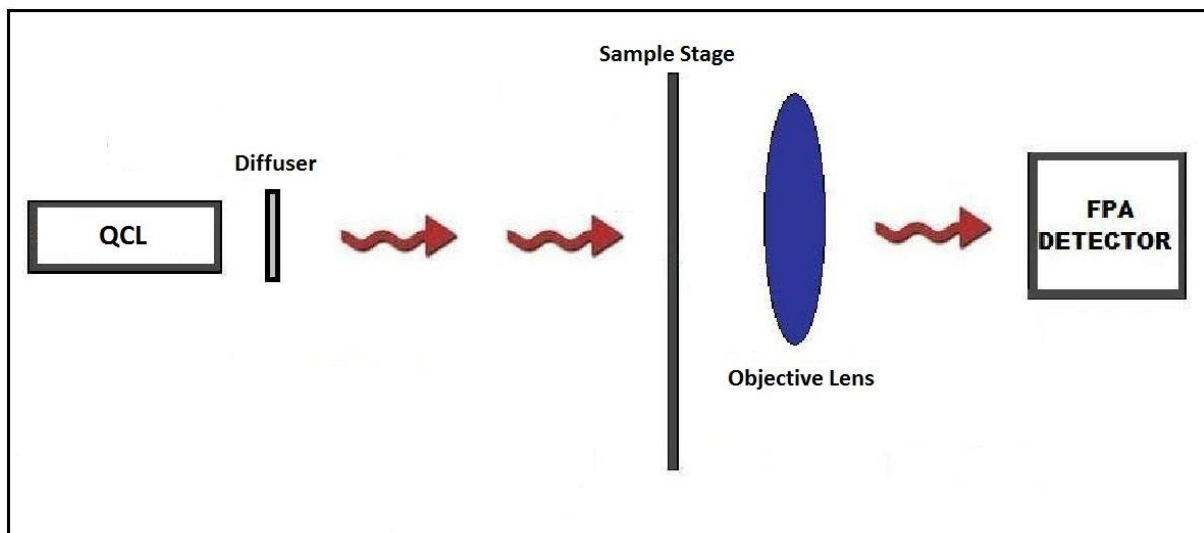


Figure 33. Imaging optics for QCL and camera

A chemical image with absorbance pixel values (A_{QCL}) can be collected from the QCL imaging system by collecting images of the sample, the “QCL background” (section 4.13.1.1) and the resting pixel values (RPVs) (section 4.6.6.1) and using equation 4.27.

$$A_{QCL}(x, y) = -\log_{10} \left[\frac{Sample(x, y) - RPV(x, y)}{QCL\ Background(x, y) - RPV(x, y)} \right] \quad (4.27)$$

Where x and y are the co-ordinates of the pixels in the IR detector array.

4.8.1 - Synchronisation of the IR Camera to the QCL

As described in section 4.5 the QCL is a pulsed source with an approximate pulse length of 0.2µs and a rep rate of 200kHz (one pulse every 5µs). Unlike the OPG the QCL timing electronics cannot be accessed which make it impossible to synchronise the camera shutter to a single QCL pulse (as it was with the OPG). Furthermore the higher rep rate of the QCL relative to the OPG means that several shots can be captured within one integration time which provides higher signal to noise ratios. However, at integration times greater than approximately 70µs some camera pixel values begin to saturate (at their maxim pixel value of 16,000) due to the high environmental signal (approximately 10,000 pixel values) and the signal from the QCL. It was found that the optimum configuration for the QCL imaging system was with the camera integration time as long as possible without any of the pixels saturating; found to be approximately 60µs. During an integration time of 60µs the camera receives somewhere between 11-12 shots from the QCL depending on when the camera shutter opens relative to the QCL pulses. Figure 34 shows the average (over the entire array) pixel value of the camera vs. the shot number for a 100 images taken with the camera and clearly illustrates the change in camera signal as the camera receives 11 or 12 shots.

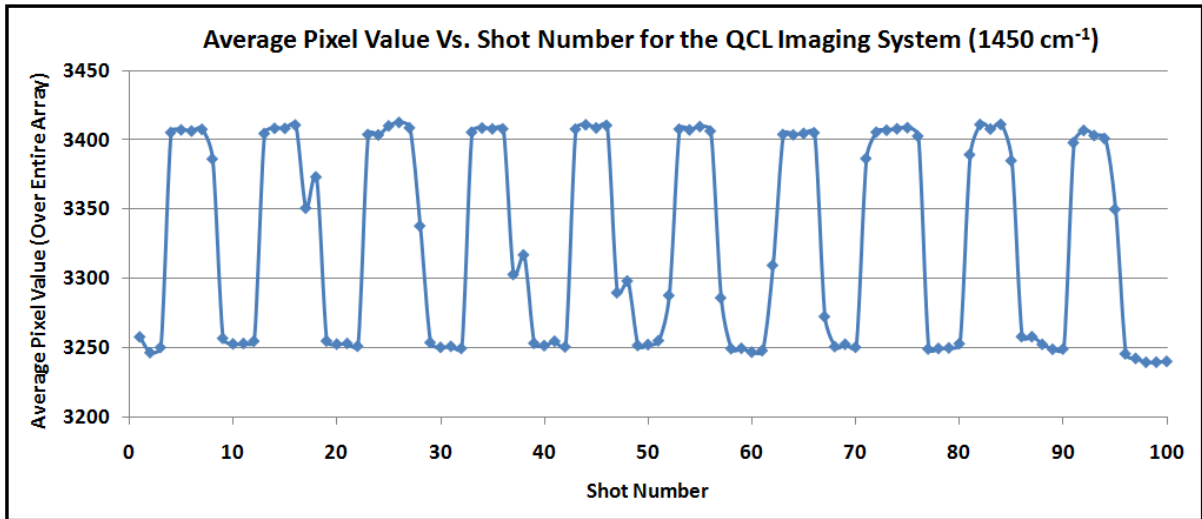


Figure 34. Synchronisation of the IR camera to the QCL without the diffuser. The camera integration time was 60 μ s meaning that the camera receives somewhere between 11-12 shots from the QCL depending on when the camera shutter opens relative to the QCL pulses.

An algorithm has been developed to reduce the “noise” contribution arising from the variable number of QCL pulses received by the camera and is discussed in section 4.11.3. The total noise will be discussed in more detail in section 4.13.1.2.

4.9 - Optical Artefacts Caused by Coherent Sources

The advantages of laser light over light from thermal sources for spectral imaging has been discussed in this thesis (section 3.7). However there are some problems associated with the coherent nature of light emitted from OPG and QCL sources. These problems – interference effects and speckle effect – generate optical artefacts which need to be corrected for before the images collected with a laser based imaging system can be used for quantitative analysis.

Coherence effects can be divided into two classifications: temporal coherence and spatial coherence. Temporal coherence relates to the finite bandwidth of the source and spatial coherence relates to a light sources finite extent in space[9]. The coherence length, Δl_c , (the length in space over which a waves phase can be predicted reliably) is calculated from the line-width, $\Delta\sigma$, of the source using equation 4.28.

$$\Delta l_c = \frac{1}{\Delta\sigma} \quad (4.28)$$

For example, the OPG the linewidth is approximately 20cm⁻¹ and hence the coherence length is calculated to be 5m.

4.9.1 - Interference Fringes

Regions of constructive and destructive interference can readily be observed when using a coherent source and Figure 35 shows a 1951 USAF resolution test chart illuminated by the OPG system.

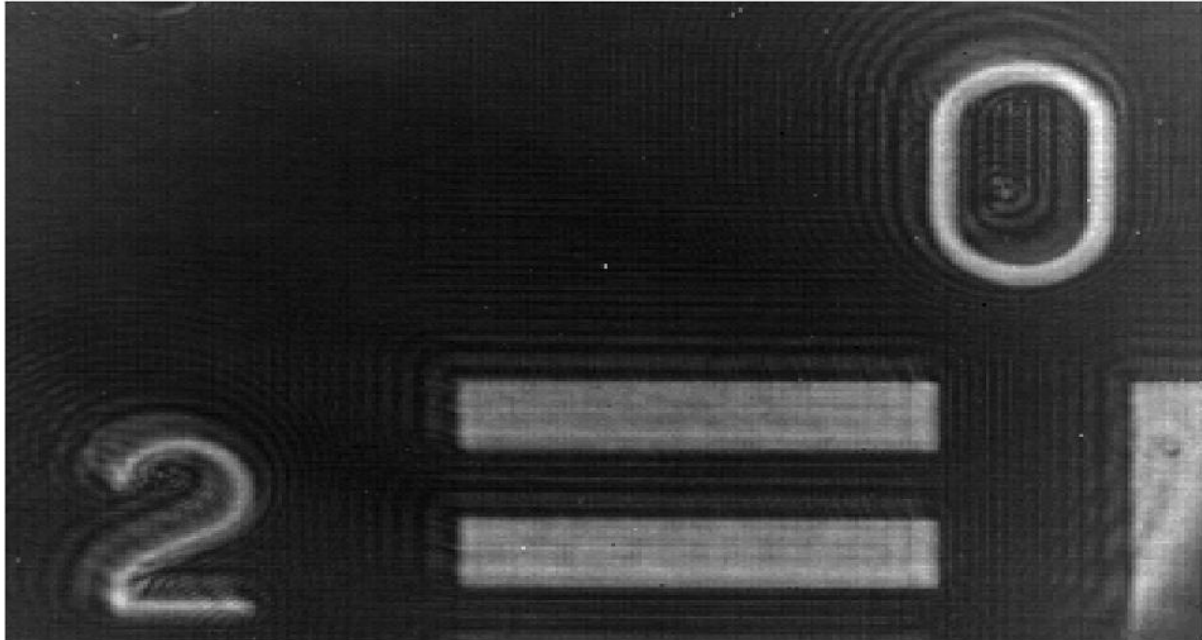


Figure 35. Example of interference effects caused by coherence of OPG light on the 1951 USAF resolution test chart

4.9.2 - Speckle Pattern

Speckle pattern is another manifestation of the phenomenon of interference. The pattern is created when coherent light is scattered from a rough surface (in this case the sample) and the many scattered waves, having different phases, add together to give a resultant whose amplitude (and therefore intensity) varies randomly. The result of speckle pattern is observed as “graininess” in the images.

4.9.3 - Removal of Optical Artefacts Using a Diffuser

Both interference fringes and speckle pattern are caused by the coherent nature of the OPG and QCL sources[10]. Therefore to eliminate these effects an optical component, a diffuser, was introduced into the experimental set-up which will destroy the coherence of the source. In our case a mechanically rotating diffuser (BaF₂ disc with roughened surface) was placed into the optical path of the beam and multiple shots were averaged. The diffuser was rotated using a stepper motor so that each pulse of the laser passed through a different part of the diffuser. Figure 36 illustrates the

removal of interference fringes by the use of a diffuser and Figure 37 shows the elimination of speckle pattern.

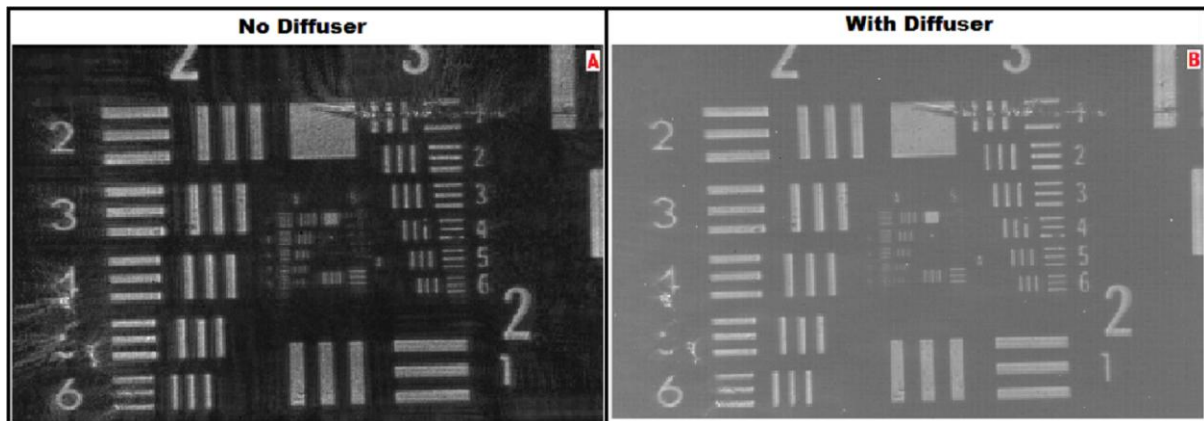


Figure 36. Removal of interference fringes using diffuser. A) no diffuser (with interference fringes). B) with diffuser (no interference fringes). Both pictures are the average of 150 shots taken at $2.79\mu\text{m}$.

Note: picture B also demonstrates the spatial resolution of the OPG Imaging system. The optics are arranged so there is a magnification of approximately X2, using the pump radiation with a wavelength of $2.79\mu\text{m}$, and a numerical aperture of approximately 0.4. In this case the spatial resolution is pixel limited at approximately $15\mu\text{m}$ (since the diffraction limit is approximately $4\mu\text{m}$). The smallest feature resolvable on the USAF target is 28.50 line-pairs/mm giving a measured resolution of approximately $17.5\mu\text{m}$.

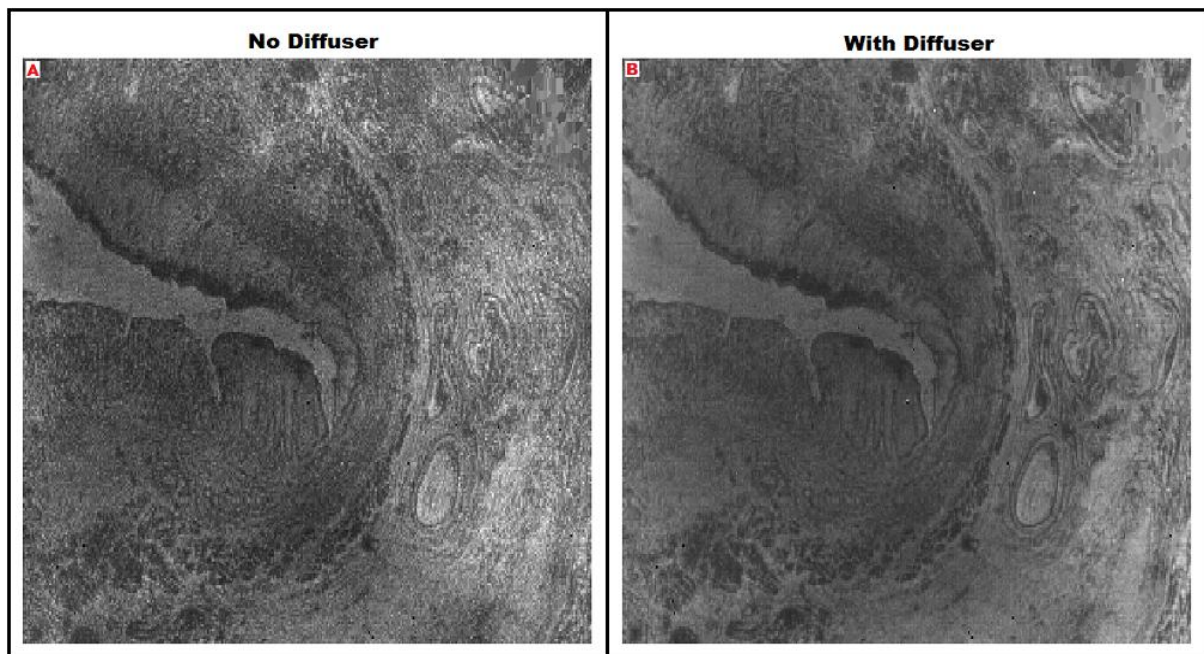


Figure 37. Removal of speckle pattern (caused by coherence of OPG source) using diffuser. A) no diffuser. B) with diffuser. Both pictures are the average of 150 shots taken at 2.79 microns.

4.10 - OPG Pulse-to-Pulse Intensity Variations and Data Binning Algorithms

In section 4.10 the use of the reference channel will be explained as a method of improving the total noise present in an image collected from the OPG imaging system. The reference channel measurement will allow each individual shot from the OPG to be normalised by using the reference channel as an independent measurement of the intensity of each individual OPG pulse. To obtain a reference channel measurement from the OPG imaging system a beam splitter was placed into the optical path to divert off a portion of the beam into a reference detector (section 4.7). In this case an MCT was used along with focusing optics (BaF₂ lens). To account for spatial variations in the beam profile particular attention was paid to focusing the entire beam onto the reference detector. The intensity of each pulse was recorded on an oscilloscope and an intensity value was extracted (Figure 38). This information was then used in subsequent calculations to account for the pulse-to-pulse variability of the OPG and to generate quantitative spectroscopic data. In section 4.10.4 data binning algorithms have been developed to account for saturation of the Cedip IR camera by the OPG source and to correct for the long time constant (approximately 1s) of the Cedip IR camera.

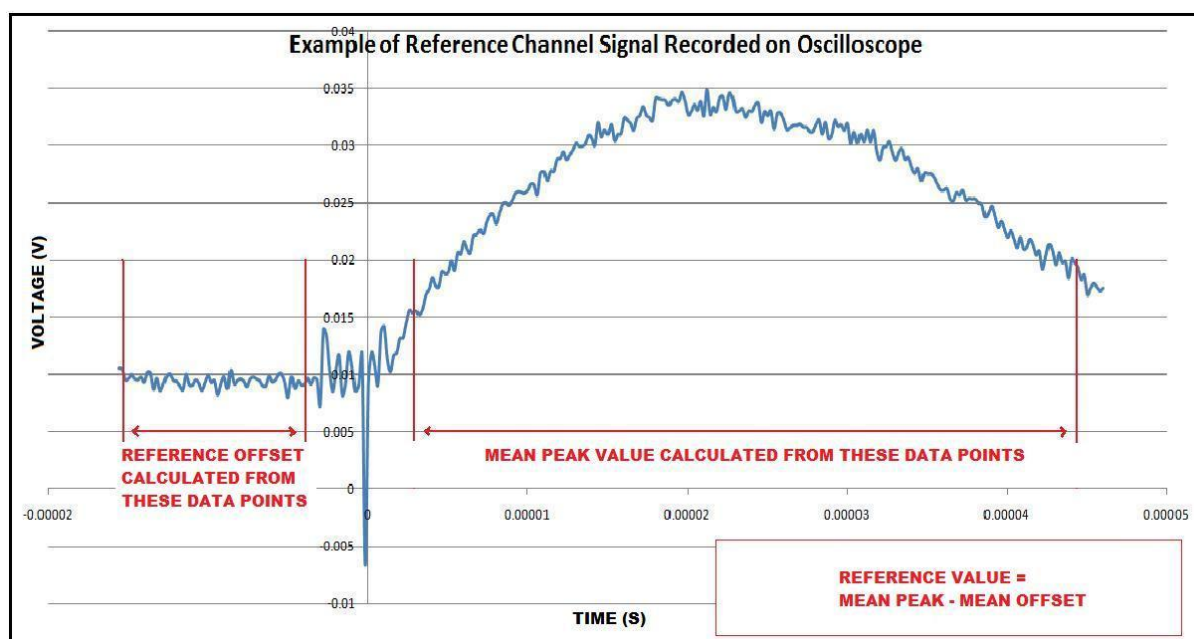


Figure 38. Picture to illustrate reference channel calculation. Windows are selected for the reference offset and the mean peak calculations to remove the spike at the origin which is generated by interference from the OPG laser electronics

4.10.1 - Correlation between Array Detector in IR Camera and Reference Channel for OPG

Since the reference channel intensity will be used to normalise each laser pulse it is useful to characterise the relationship between the FPA detector in the camera and the reference channel.

With all optics set up as normal for the OPG imaging system (except no sample in the sample holder) data was collected from the camera and reference channel for various different values of beam attenuation. The beam was attenuated with the use of attenuation filters in the beam path which varied between 4% and 91% transmission. Figure 39 shows an example of a correlation plot (taken at $7\mu\text{m}$) collected by plotting the reference signal versus the average (over entire array) camera pixel value for each shot (450 shots, 50 shots at each attenuation value). It can be seen from this plot that there is a good correlation (indicated by the $0.85 R^2$ value) with the exception of a few “bad” data points which do not lie particularly close to the best fit line (probably due to the time constant problem described in section 4.10.3). Furthermore it should be noted that the y-intercept of the correlation graph gives an indication of the average value of the resting pixel values (section 4.6.6.1) from the Cedip camera. Similar correlation plots were collected for several wavelengths across the spectral range of the OPG and have been discussed elsewhere[8]. A correlation plot is also shown for $4.3\mu\text{m}$ which shows good correlation at low laser intensities but saturation effects at high intensities (Figure 40). This saturation effect will be discussed in more detail in section 4.10.2. Finally the correlation between a single pixel on the FPA and the reference channel can be analysed. It is expected that the correlation for a single pixel should be somewhat lower than that of the entire array due to spatial variations in the intensity of the beam profile. Indeed examination of the correlation between 10 individual pixels chosen at random gave an average R^2 value of 0.69 supporting the hypothesis for lower correlation of individual pixels compared to the average array ($0.85 R^2$ value).

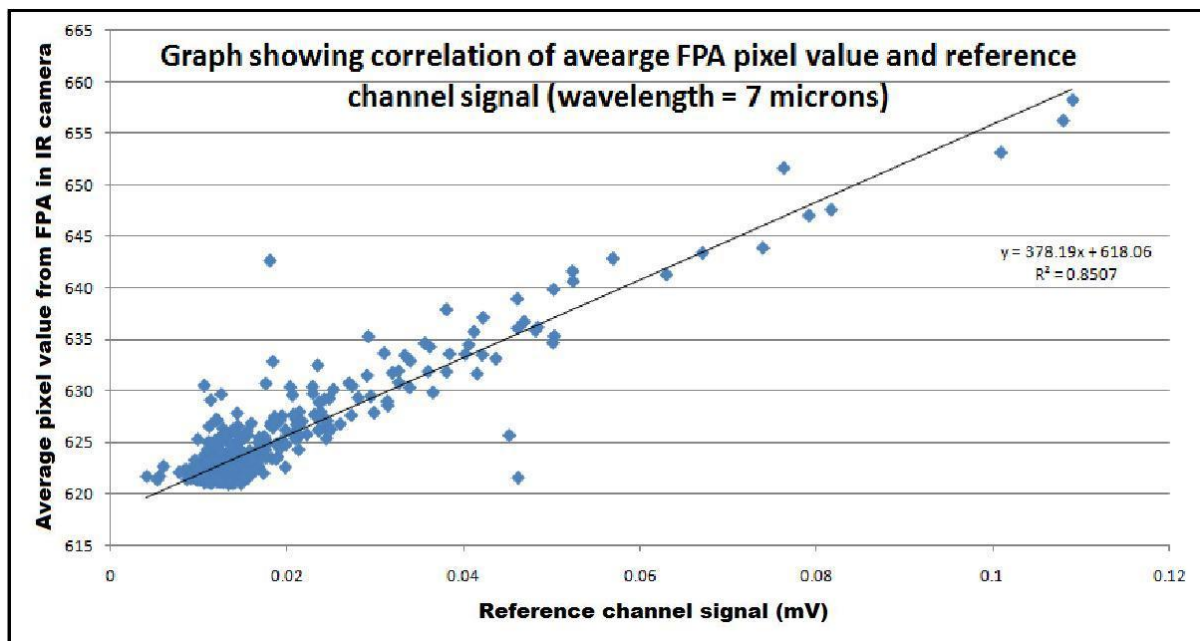


Figure 39. Correlation of camera and ref channel ($7\mu\text{m}$)

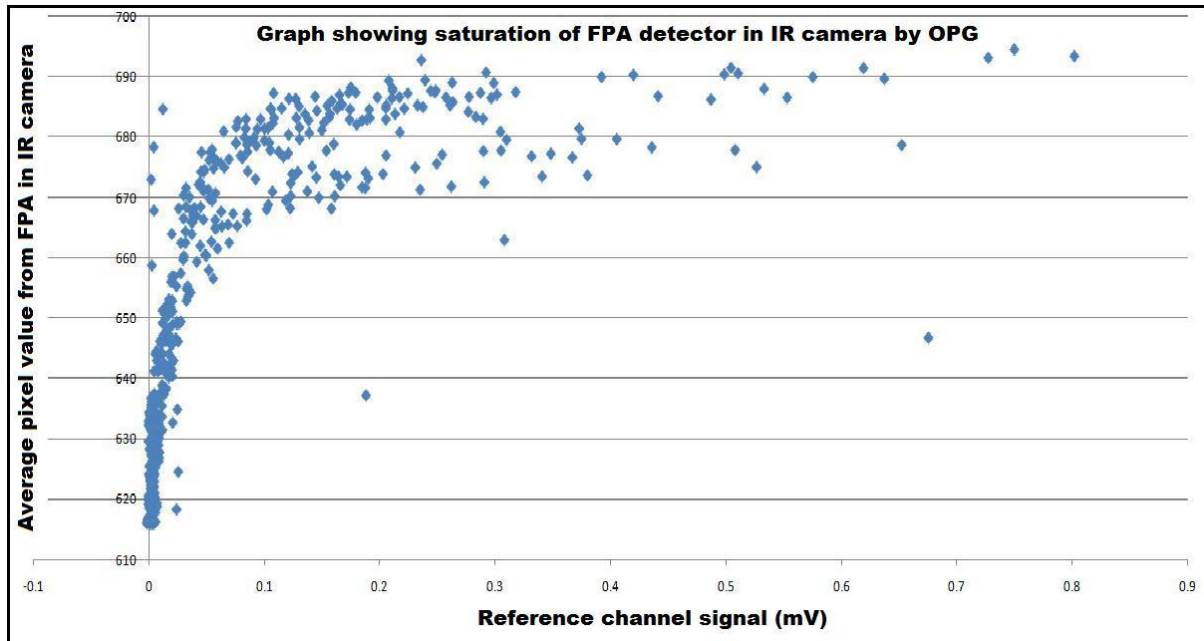


Figure 40. Graph showing correlation (with saturation) of average signal on FPA in camera to reference channel (4.3 microns). 450 shots.

4.10.2 - Detector Saturation by OPG: Moss Burstein Effect

Fig 40 shows that at high pulse intensities the average pixel value of the FPA begins to saturate. This means that a linear correlation between the reference channel and camera no longer exists and special care must be taken during the interpretation of this data for quantitative analysis. A possible explanation for the detector saturation mechanism is discussed in Dr Hemmel Amrania's thesis[8]. This mechanism, the Moss Burstein effect, is due to the recombination time of the quantum detector being comparable to the pulse length of the laser (100ps). It is also asserted that the saturation point appears at lower intensities for longer wavelengths due to the curvature of the conduction band in the semiconductor material of the detector.

4.10.3 - Detector Correlation and the Cedip Camera Time Constant

Figure 41 shows plots of the average camera pixel value recorded by the Cedip camera vs. shot number and the reference channel signal (using a single channel MCT detector) vs. shot number recorded from the OPG pulses (operating at 3Hz). It can be seen that the time constant of the reference channel is less than 0.33s and the time constant of the Cedip camera is on the order of 1s (by comparing individual shots such as shot 95). The time constant of the Cedip IR camera was not expected to be this long because it is operating with fast response MCT detectors whose time constant is determined by the recombination time of electron-hole pair in the semiconductor (typically <ns). Therefore the relatively long time constant of the Cedip camera is probably

determined by the read out electronics of the camera. The effect of the difference in time constant between the reference channel and the Cedip camera is to corrupt the correlation curves (Figure 39 and figure 40) and introduce additional noise into the subsequent absorbance measurements. Consequently a data binning algorithm has been developed to account for this problem (section 4.10.4.1)

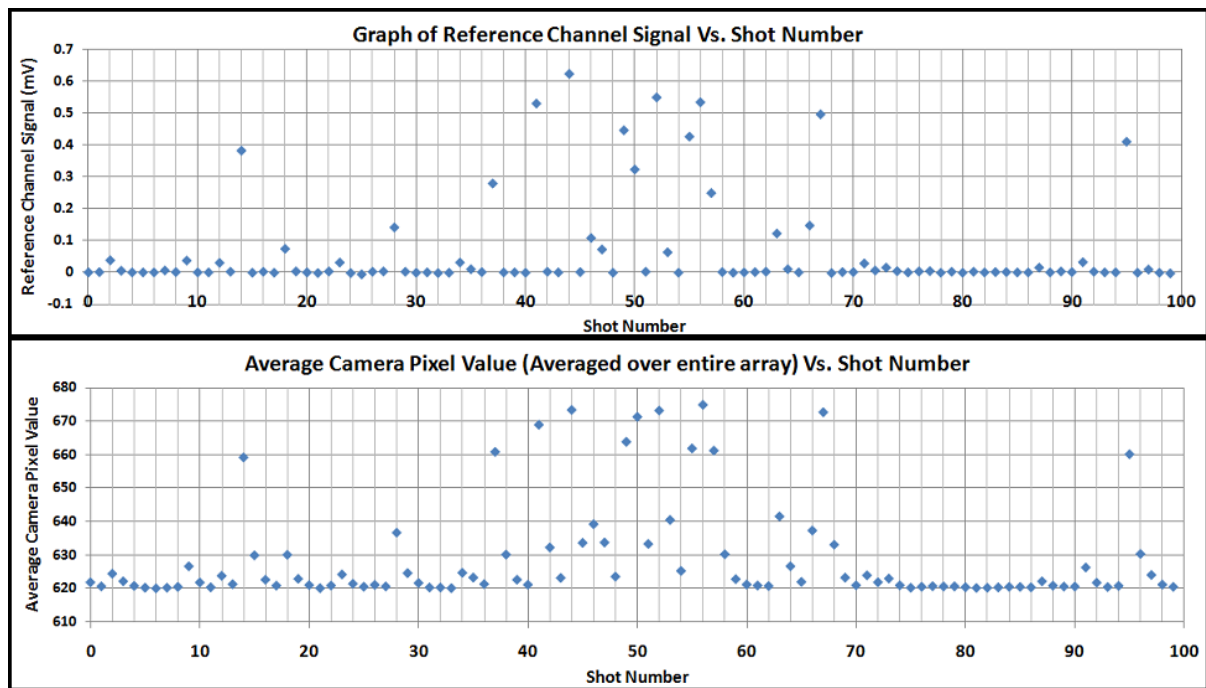


Figure 41. Plots showing the average camera pixel value recorded on the Cedip camera and the reference channel signal (using a single channel MCT detector) recorded from the OPG pulses when the OPG is operating at 3Hz. It can be seen that the time constant of the reference channel is less than 0.33s and the time constant of the Cedip camera is on the order of 1s (by comparing individual shots such as shot 95)

4.10.4 - OPG Data Binning Algorithms

In order to account for the effects of the long time constant of the Cedip camera and detector saturation by the OPG two data binning algorithms were developed - The Time Constant Binning Algorithm and The Saturation Binning Algorithm – which will be discussed in the following sections (4.10.4.1 – 4.10.4.2).

4.10.4.1 - Time Constant Binning Algorithm

The difference in the time constant between the Cedip camera and the reference channel conspires to reduce the detector correlation since there are certain shots collected by the Cedip camera whose signal is primarily composed of the decaying signal from the previous shot. For instance consider shot 96 shown on Fig 41 collected by the Cedip camera. The reference channel indicates that there

was essentially no power emitted from the OPG at this point in time but a signal was still recorded on the Cedip camera which was a result of the decaying signal from shot 95. In the case of a correlation plot of average camera signal vs. reference channel signal this residual signal will reduce the correlation somewhat and reduce the ability of the reference channel to compensate for the pulse-to-pulse variability of the OPG source. Furthermore the problem is even more severe when several shots from the OPG are received by the Cedip camera consecutively. For example shot 49 is measured to have a greater signal than shot 50 by the reference channel but the Cedip camera records shot 50 as having a greater signal than shot 49 (since shot 50 is the sum of shot 50 and the decaying shot 49). To account for this problem (for data collected at a rep rate 3Hz with the OPG) the Time Constant Binning Algorithm was developed. The Time Constant Binning Algorithm works as follows;

- 1) The average camera pixel base line is measured (in the case of Figure 41 it is approximately 621 pixel values)
- 2) Only those shots whose average pixel value are above the base line and where the previous shot is along the baseline (to within an acceptable error margin) are retained.

Figure 42 shows graphically which shots would be retained (boxed in red) once the Time Constant Binning Algorithm has been applied.

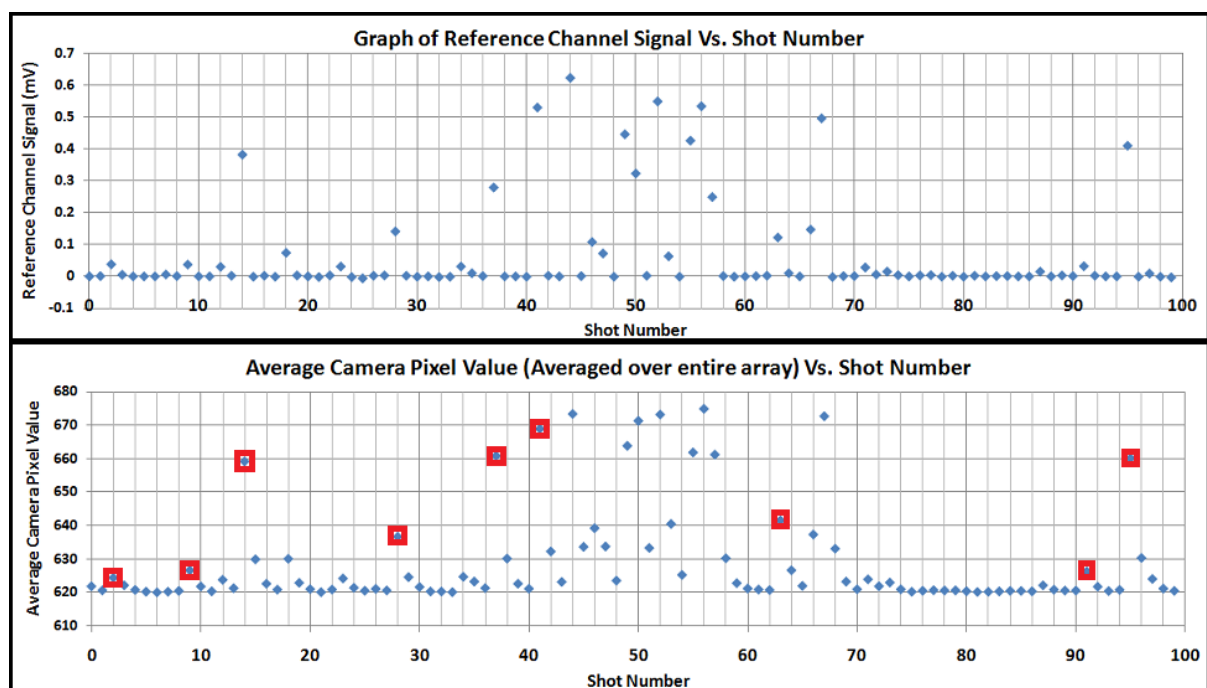


Figure 42. Time Constant Binning Algorithm. The algorithm only retains (boxed in red) those shots whose average pixel value are above the base line and where the previous shot is along the baseline (to within an acceptable error margin).

4.10.4.2 - Saturation Binning Algorithm

As already mentioned at high OPG pulse intensities (corresponding to reference channel signals above approximately 0.1mv) the FPA in the Cedip camera begins to saturate. Furthermore at low (or even zero) intensities very poor contrast is observed in the images generated by the OPG source. These observations suggest the need for a “saturation binning algorithm” which will reject those OPG shots which have their intensity (as measured by the reference channel) above or below a certain range. This does have the unfortunate effect of increasing the data acquisition time for the collection of a data set but ensures that the data may be used for quantitative analysis. To accomplish this data binning a LABVIEW code was written which can remove the “bad” shots from the data set by examining the correlation plots for the average pixel value versus the reference channel (Figure 43). Incidentally the “low intensity shots” (particularly those corresponding to zero signal on the reference channel) can be used to estimate the resting pixel values (RPVs) of the Cedip camera.

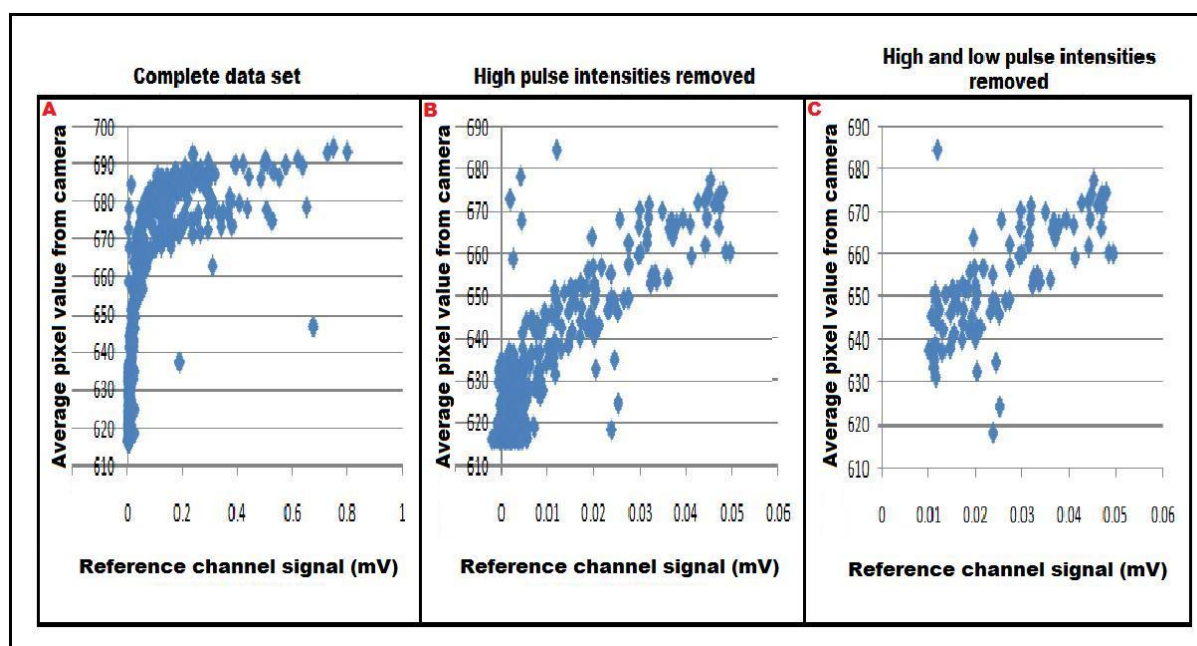


Figure 43. Data binning algorithm: A) Complete data set. B) Data set with high pulse intensities (saturated data points) removed. C) Data set with high and low pulse intensities removed.

4.11 - QCL Pulse-to-Pulse Intensity Variations and the Variable Pulse Data Binning Algorithm

In section 4.11.1 and 4.11.2 the issue of detector saturation with the QCL is explored. In section 4.11.3 the “variable pulse data binning algorithm” is described for correcting for the QCL – Cedip camera synchronisation problem described in section 4.8.1.

4.11.1 - Correlation between Array Detector in IR Camera and Reference Channel for QCL

One major advantage of the QCL imaging system compared to the OPG imaging system is the temporal stability of the output of the QCL. However it is still important to characterise the camera pixel response to changes in the intensity of the QCL beam since the camera pixel values will be used to calculate numerical absorbance values. The critical point is to operate the QCL at a beam intensity region which gives a linear response between beam intensity and camera pixel value. To identify the linear response region for the QCL imaging system correlation curves were generated for several wavelengths across the spectral range. As with the correlation experiments between the OPG and a reference channel (section 4.10.1) a similar analysis was performed with the QCL imaging system. All the optics set up as normal for the QCL imaging system except with a beam splitter (made from BaF₂) in the beam path which diverts off a fraction of the beam into a MCT detector reference channel. A lens (made from BaF₂ and with a focal length of 5cm) was used to collect the diverted light into the reference channel and there was no sample placed in the sample holder. With the use of attenuation filters (varying between 4% and 91% transmission) data was collected from the camera and reference channel for various different values of beam attenuation. To generate the correlation plots 100 images were collected and averaged (over the entire array and all shots) for the camera and, for the reference channel, the pulses received were averaged over a time of 60μs (since the camera integration time was 60μs). Figure 44 shows two representative correlation plots generated for the QCL imaging system (for wavenumbers of 1000cm⁻¹ and 1300cm⁻¹). In these representative plots it can be seen that some wave numbers (1000cm⁻¹) behave linearly and some (1300cm⁻¹) do not behave linearly. In the case of the 1300cm⁻¹ wavenumber the QCL must be attenuated so that the camera pixel response is linear.

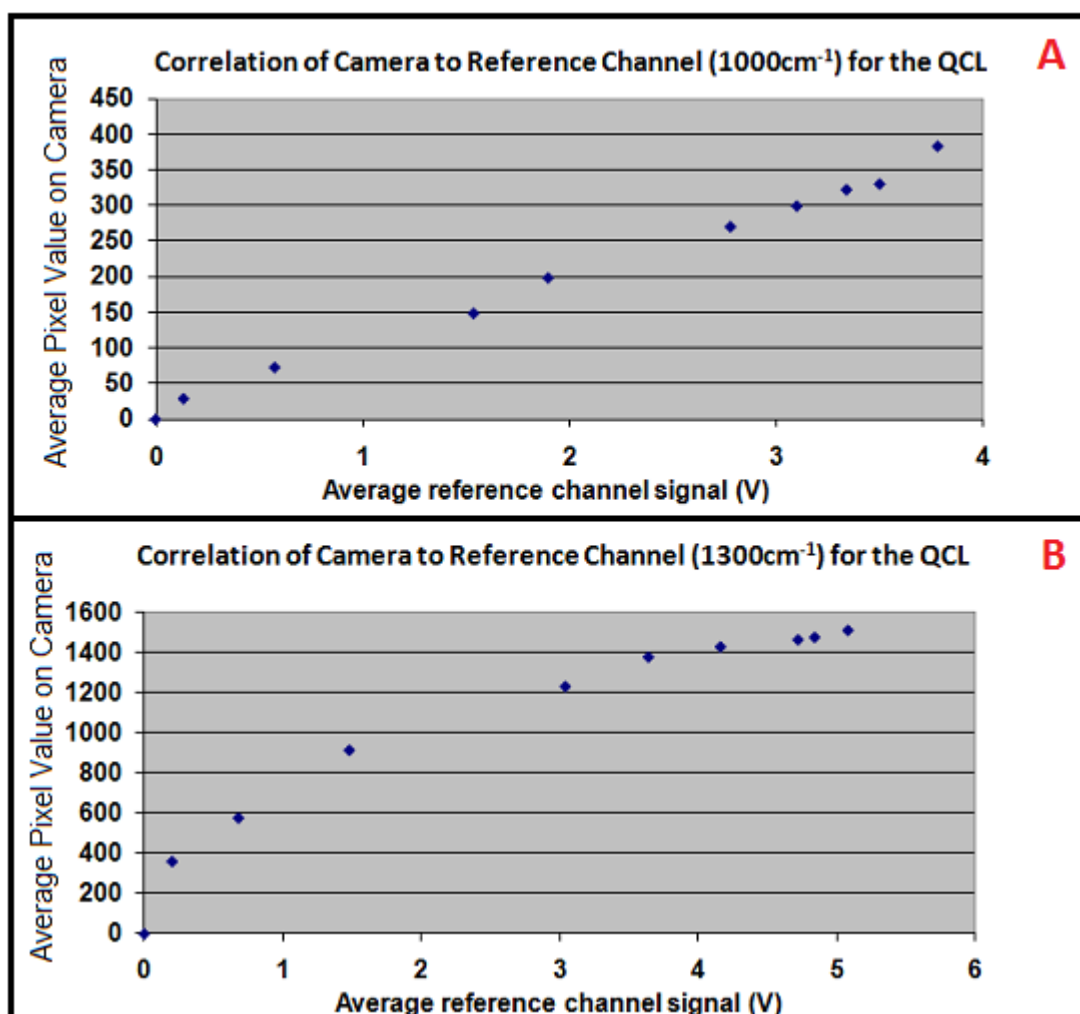


Figure 44. Correlation plots for the QCL imaging system. For the camera, 100 images were collected and averaged (over the entire array and all shots) and, for the reference channel, pulses were averaged over a time of 60 μ s (since the camera integration time was 60 μ s) to generate the correlation plots.

4.11.2 - Detector Saturation by QCL

In general it is observed that the Cedip camera saturates at QCL pulse intensities which are recorded approximately greater than 4V on the reference channel. Furthermore it can be seen from Figure 44 that the Cedip camera response to the QCL source is approximately linear between 1-4V. The fact that the camera response is approximately linear in this region suggests that an attenuator should be placed in the beam path to limit the beam intensity which reaches the Cedip camera. In order to keep the beam intensity in a valid range a 40% beam attenuator was placed in the beam path for all the data collected from the QCL imaging system.

4.11.3 - Variable Pulse Data Binning Algorithm

In section 4.8.1 it was shown that the Cedip camera signal varies systematically in response to the number of QCL pulses received in one integration time of the Cedip camera. The total noise present

by averaging 100 shots (from the camera) can be shown to be around 0.6% (by using the mean and standard error of all 100 shots) but this level of noise could be improved by removing all the camera images that received 11 QCL pulses and only retaining those shots which receive 12 QCL pulses. The situation is made a little more complicated by the use of the diffuser which acts to randomise the QCL pulse energy received by the Cedip camera (Figure 45). The variable pulse data binning algorithm works by calculating the average of all shots and removing all shots below the average (Figure 46). Once the variable pulse data binning algorithm has been applied the total noise is reduced to approximately 0.3%

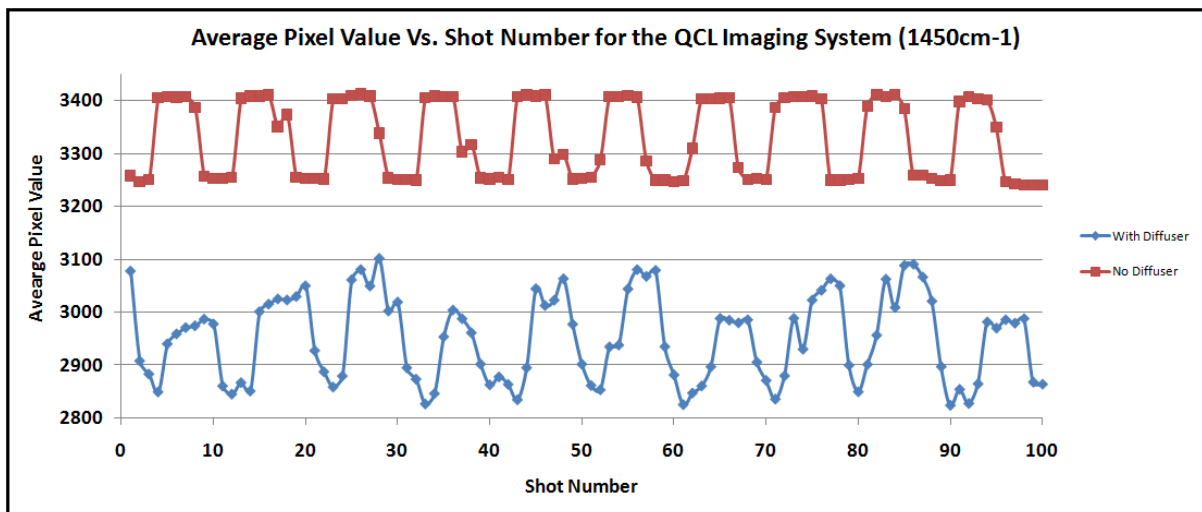


Figure 45. Graph illustrating the average pixel value received by the Cedip camera for 100 consecutive shots from the QCL (with and without a diffuser present). The camera integration time was $60\mu\text{s}$ meaning that the camera receives somewhere between 11-12 shots from the QCL depending on when the camera shutter opens relative to the QCL pulses.

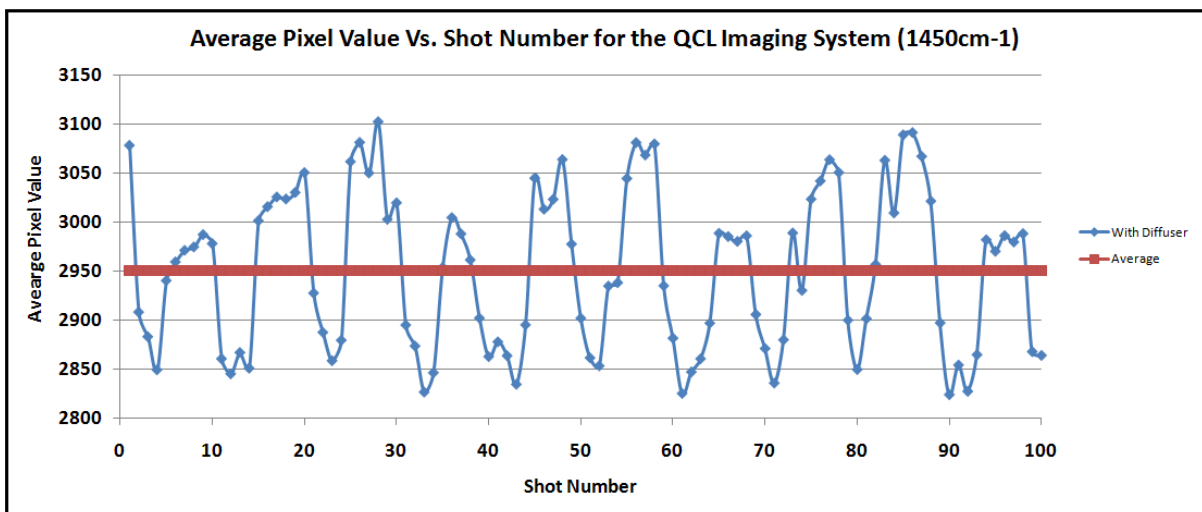


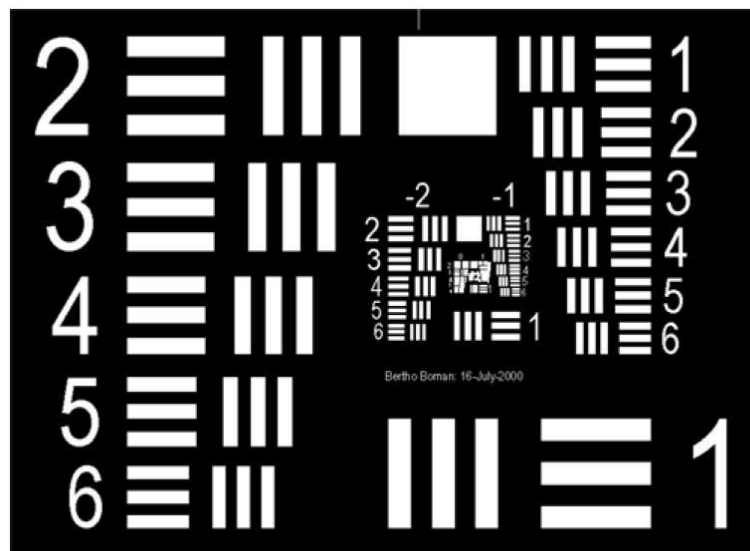
Figure 46. Variable Pulse Data Binning Algorithm. The algorithm works by removing all shots below the average value of all shots (red line).

4.12 - Characterisation of OPG Imaging System

In section 4.12 characterisation experiments to examine the spatial resolution, the OPG background, and the total noise from an image for the OPG Imaging system are described.

4.12.1 - Experimental Measurement of the Spatial Resolution of the OPG Imaging System

A practical method of testing the spatial resolution of an optical arrangement is the use of USAF 1951 resolution test. The test consists of a number of slits and lines with known dimensions etched onto a polyethylene sheet (Figure 47 and Figure 48). By measuring the smallest pair of slits that the system is able to spatially resolve the spatial resolution can be determined experimentally.



Levenson, Martin, Advanced Light Source Division, Infrared Physics & Technology 49 (2006) 45-52

Figure 47. USAF 1951 Resolution test target

Number of Line Pairs / mm in USAF Resolving Power Test Target 1951												
Group Number												
Element	-2	-1	0	1	2	3	4	5	6	7	8	9
1	0.250	0.500	1.00	2.00	4.00	8.00	16.00	32.0	64.0	128.0	256.0	512.0
2	0.280	0.561	1.12	2.24	4.49	8.98	17.95	36.0	71.8	144.0	287.0	575.0
3	0.315	0.630	1.26	2.52	5.04	10.10	20.16	40.3	80.6	161.0	323.0	645.0
4	0.353	0.707	1.41	2.83	5.66	11.30	22.62	45.3	90.5	181.0	362.0	-----
5	0.397	0.793	1.59	3.17	6.35	12.70	25.39	50.8	102.0	203.0	406.0	-----
6	0.445	0.891	1.78	3.56	7.13	14.30	28.50	57.0	114.0	228.0	456.0	-----

Figure 48. USAF Resolution test - table of scales and dimensions accompanying the resolution test target

The results of a measurement carried out with the OPG imaging system (with a magnification of X1, using the pump radiation with a wavelength of 2.79 μ m and a numerical aperture of 0.4) is shown in Figure 49. As can be seen from Figure 49 That the lines on the target at 14.30 line-pairs/mm are still

resolvable corresponding to one line pair per $70\mu\text{m}$. Since this line pair is still resolvable it can be concluded the spatial resolution is approximately $70\mu\text{m}$. Since the magnification was X1 and the native pixel size is $30\mu\text{m}$ the system is *pixel limited* at $30\mu\text{m}$. It should also be noted here that images in Figure 49 were taken without the use of a diffuser (hence the presence of interference fringes seen clearly in the 1.12 line-pairs/mm picture). This is not an ideal situation since these fringes may lead to a misinterpretation of the position of certain slits. Figure 37 demonstrates the spatial resolution measurement of the OPG Imaging system (with and without a diffuser) with the optics arranged so there is a magnification of approximately X2, using the pump radiation with a wavelength of $2.79\mu\text{m}$, and a numerical aperture of approximately 0.4. In this case the system is pixel limited at approximately $15\mu\text{m}$. The smallest feature resolvable on the USAF target in Figure 36 is the 28.50 line-pairs/mm which corresponds to one line-pair every $35\mu\text{m}$ giving a measured spatial resolution of approximately $35\mu\text{m}$.

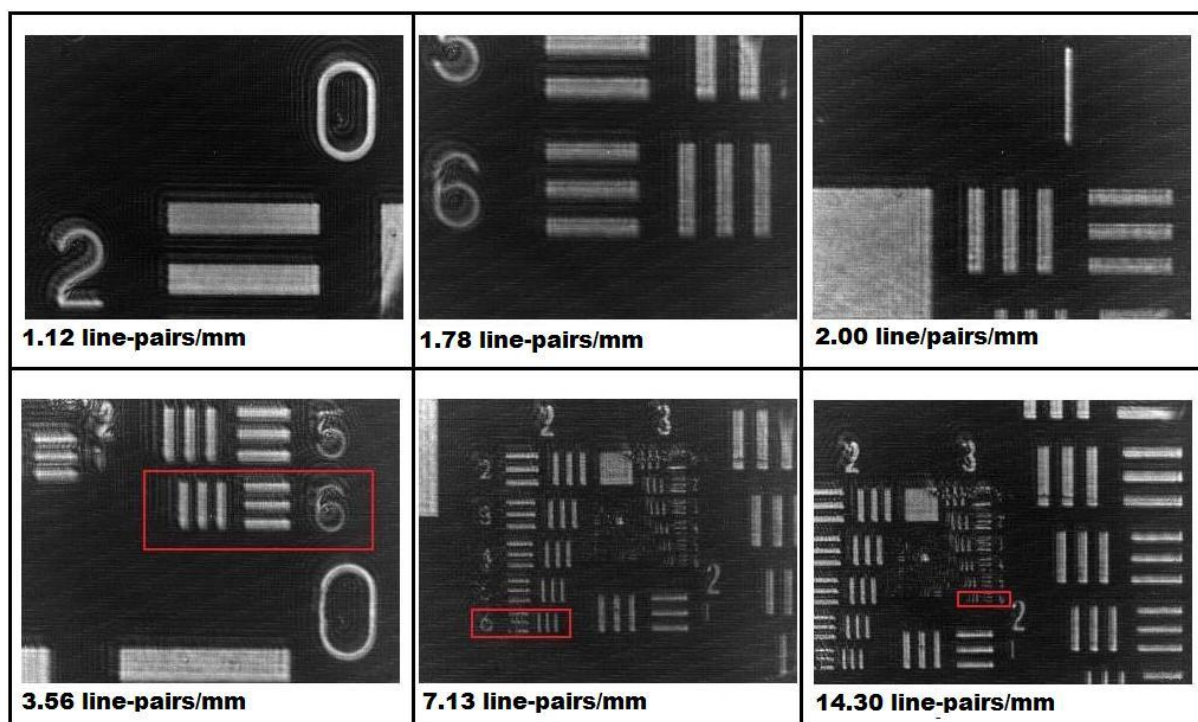


Figure 49. Experimental results from the OPG imaging system (with a magnification of X1, using the pump radiation with a wavelength of $2.79\mu\text{m}$ and a numerical aperture of 0.4) using the USAF resolution test target. The spatial resolution for this optical arrangement is pixel limited at $30\mu\text{m}$ (diffraction limit is approximately $4\mu\text{m}$). Spatial resolution is determined experimentally to be approximately 14.30 line-pairs/mm ($35\mu\text{m}$).

4.12.2 - Analysis of the OPG Background and Analysis of OPG Total Noise

In order to extract absorbance data from the OPG imaging system an “OPG background” has to be collected for each chemical image and used in equation 4.26. Empirically it is observed that the OPG background images vary from pulse-to-pulse and this variation is attributed to environmental, electronic and source noise (section 3.9.3.1). To examine the nature of the OPG background (and total noise) data sets were collected for 21 wavelengths (ranging from 6.5 μm to 8.4 μm), at an integration time of 2 μs , with an LNUC applied and with 500 shots per wavelength. All the optics set up as normal (including the diffuser) but with no sample in the beam path. The raw data was then processed using the data binning algorithms (time constant and saturation), corrected for the RPVs and each shot was divided by its corresponding reference value.

4.12.2.1 - OPG background

To calculate the OPG background the mean pixel values were determined from this data set. One representative “heat map” is shown for 6.6 μm in Figure 50. The range of mean pixel values is -385 to 280. By using the threshold BPR with limits of 100 to 225 (replacing 0.5% of pixels) the mean pixel distribution can be better visualised.

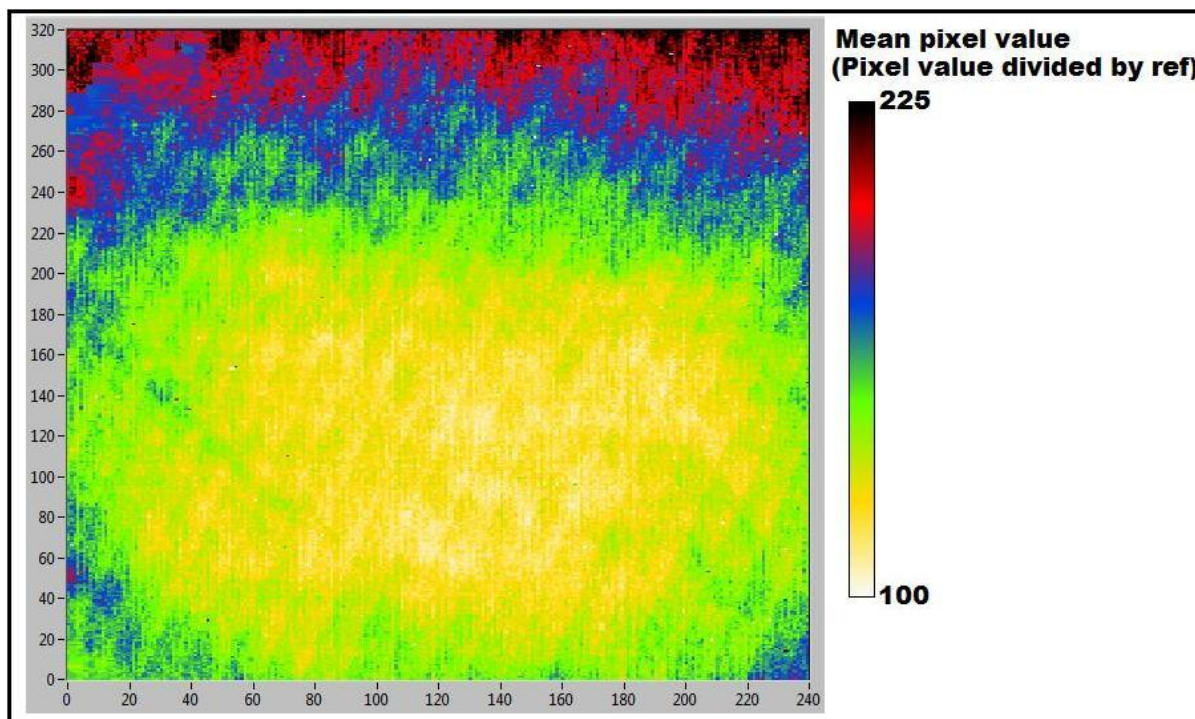


Figure 50. Example of the OPG background: The OPG was tuned to 6.6 μm and fired directly into the IR camera (with no sample in the optical path). A threshold bad pixel replacement algorithm has been used limiting the pixel values between 100 and 225 (replacing 0.5% of pixels).

4.12.2.2 - Total Noise from the OPG Imaging System

The uncertainty in the pixel values (calculated using equation 4.25) of this data set gives an indication of the (total) noise present in an image taken with the OPG imaging system. The representative data set (taken at $6.6\mu\text{m}$) has an uncertainty range of 0.4 to 32. By setting the pixel limits to the range 4 to 13 (replacing 0.08% of the pixels with the threshold BPR) the majority of the pixel uncertainty values are seen to be between 4 and 13. An analysis of the % uncertainty in the pixel values indicated a range of uncertainties between -560% and 33%. By utilising the threshold BPR (limits 3.5% and 6.3%; replacing 0.07% of the pixels) the majority of the % uncertainty pixel values can be seen to be between 3.5% and 6.3% (Figure 51). Finally the % uncertainty was averaged over the entire array for every wavelength and graph of average % uncertainty vs. wavelength was created (Figure 52). Figure 52 indicates that – as a rough estimate – the % uncertainty for any given pixel and any wavelength is around 5%. Using relation 4.29 the SNR of the OPG background image ($\text{SNR}_{\text{OPG TOTAL}} = 20$) can be calculated.

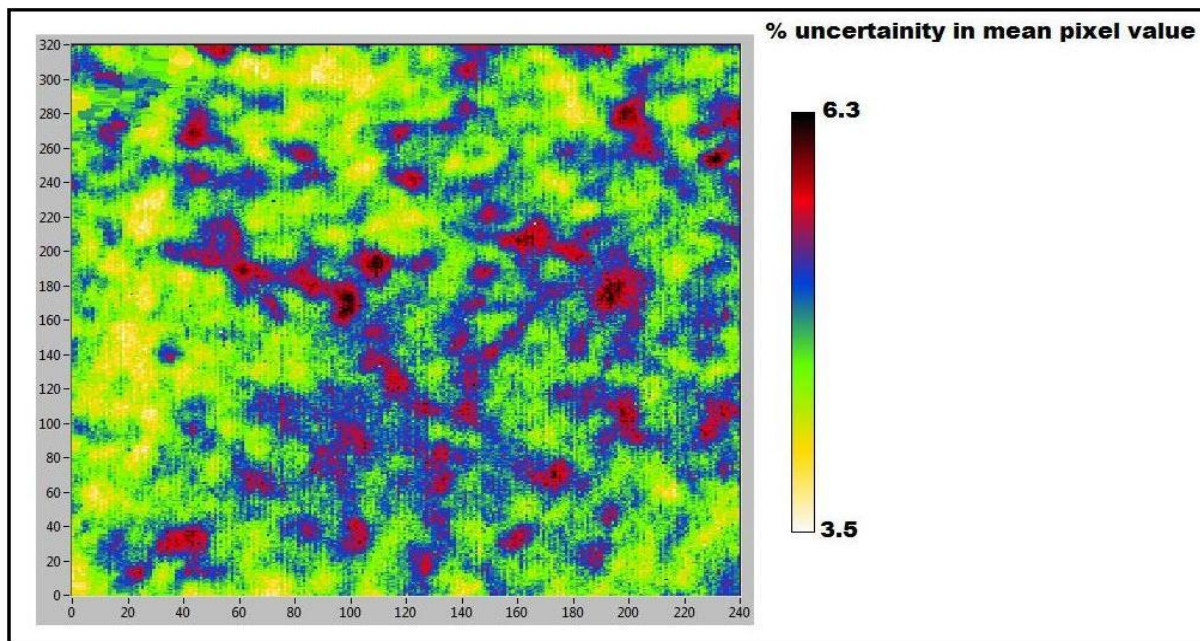


Figure 51. Percent uncertainty in the mean pixel value for the background (using OPG imaging system) - $6.6\mu\text{m}$. A threshold BPR (limits 3.5% and 6.3%; replacing 0.07% of the pixels) has been used

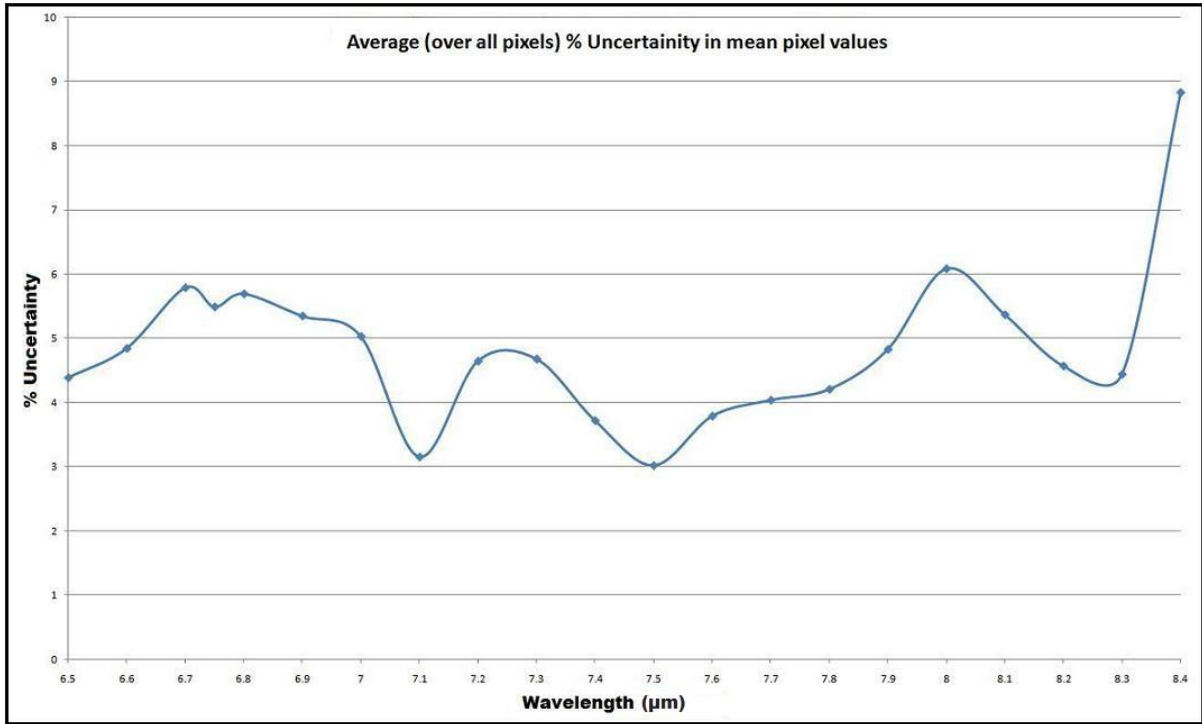


Figure 52. Average % Uncertainty (over entire array) for background across spectral range of idler beam for the OPG imaging system

$$SNR = \frac{100}{\% \text{ uncertainty}} \quad (4.29)$$

Since the electronic and environmental noise have been shown to be very small (section 4.6.6.2) it follows that the source noise is the primary contribution to the overall noise in an image collected from the OPG imaging system.

4.13 - Characterisation of QCL Imaging System

In sections 4.13.1 – 4.13.3 characterisation experiments to examine the QCL background and the QCL source noise are described.

4.13.1 - Analysis of the QCL Background and Analysis of QCL Total Noise

In order to extract absorbance data from the QCL imaging system an *average* “QCL background” has to be collected for each chemical image and used in equation 4.27 To examine the nature of the QCL background (and total noise) data sets were collected for 36 wavelengths (ranging from 7.4μm to 10μm), the integration time of the Cedip camera was set to 60μs, a NLNUC and PNUC was applied, and 100 shots per wavelength were collected. The variable pulse data binning algorithm (4.11.3) was

then applied to the data leaving around 50 shots per wavelength. All the optics were set up as normal (including the diffuser) but with no sample in the beam path. The raw data was then corrected for the environmental and electronic signals (RPVs, section 4.6.6.1).

4.13.1.1 - QCL Background

To calculate the QCL background the mean pixel values for each wavelength were determined from this data set. One representative “heat map” is shown for 8.7 μm in Figure 53 where the range of mean pixel values is 879 to 4966. By using the threshold BPR with limits of 1571 to 3839 (replacing 3.8% of pixels) the mean pixel distribution can be better visualised.

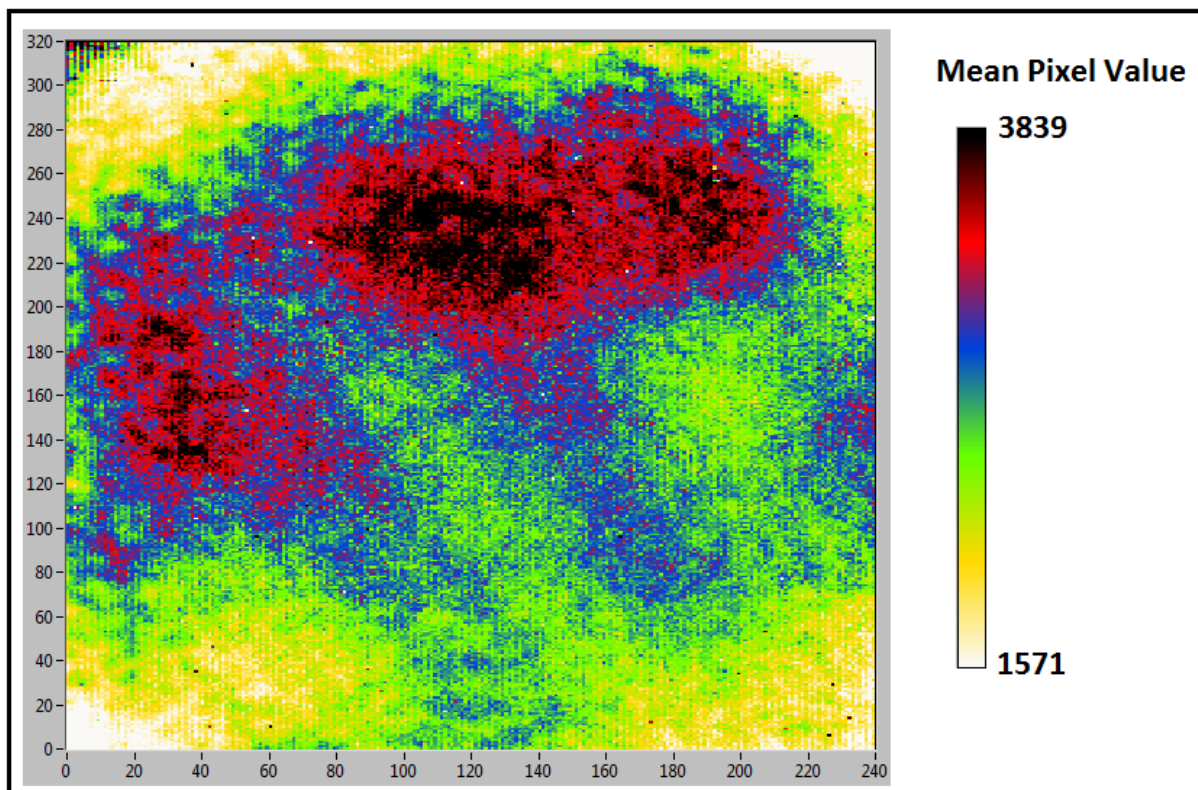


Figure 53. Example of the QCL background: The QCL was tuned to 8.7 μm and fired directly into the IR camera (with no sample in the optical path). A threshold bad pixel replacement algorithm has been used limiting the pixel values between 1571 and 3839 (replacing 3.8% of pixels).

4.13.1.2 - Total Noise from the QCL Imaging System

The uncertainty in the pixel values (calculated using equation 4.25) for each wavelength of this data set gives an indication of the total noise present in each average OPG background image. The representative data set (taken at 8.7 μm) has an uncertainty range of 4.0 to 21.6. An analysis of the % uncertainty in the pixel values indicated a range of uncertainties between 0.11% and 0.67%. By utilising the threshold BPR (limits 0.14% and 0.56%; replacing 0.9% of the pixels) the majority of the

% uncertainty pixel values can be seen to be between 0.14% and 0.56% (Figure 54). Finally the % uncertainty was averaged over the entire array for every wavelength and graph of average % uncertainty vs. wavelength was created (Figure 55). Figure 55 indicates that – as a rough estimate – the % uncertainty for any given pixel and any wavelength is around 0.3%. Using relation 4.29 the SNR of a background QCL image ($SNR_{QCL\ TOTAL} = 333$) can be calculated.

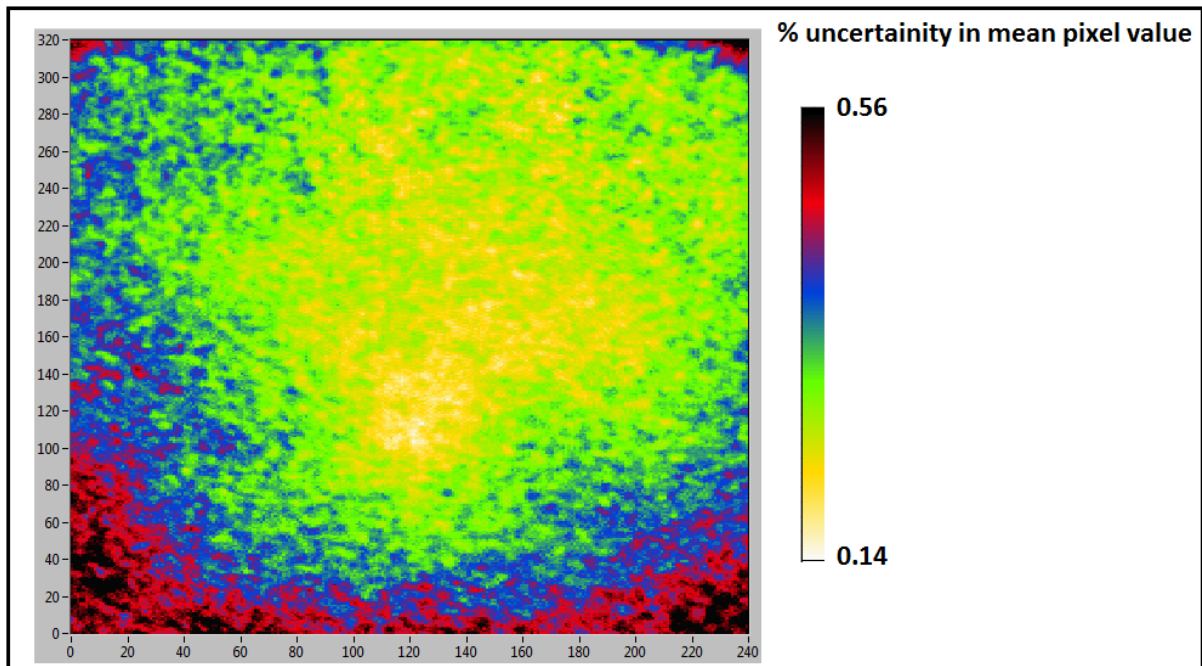


Figure 54. Pixel % uncertainty values for representative QCL background image taken at $8.7\mu m$. The original pixel values ranged from 0.19% to 0.67% but a threshold BPR was applied limiting the pixel range from 0.14% to 0.56% (replacing 0.9% of the pixels).

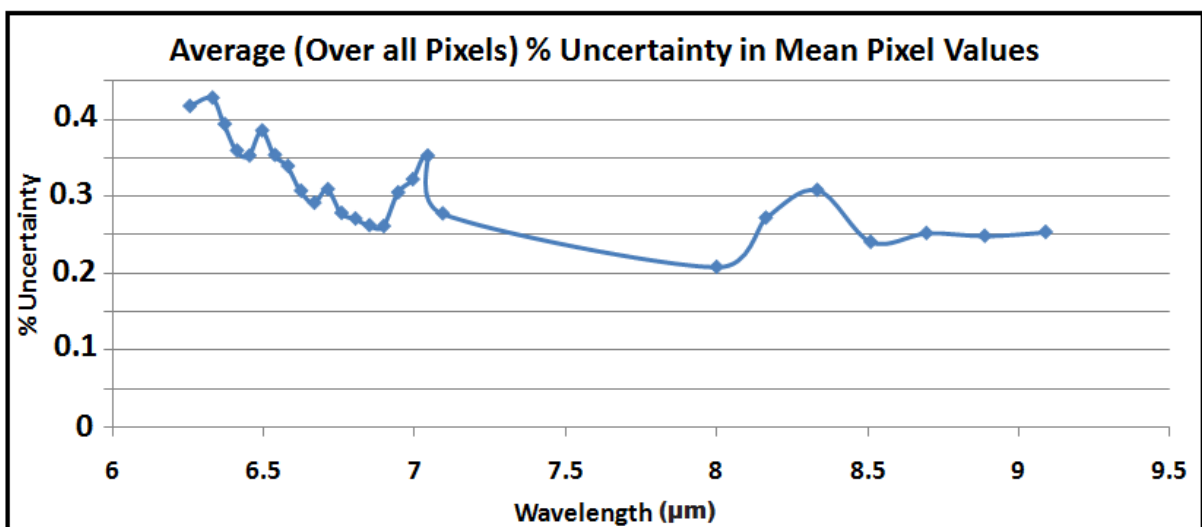


Figure 55. Average % Uncertainty (over entire array) for background across spectral range for the QCL imaging system

1. *Cancer Research UK*. Available from: <http://www.cancerresearchuk.org/cancerstats>.
2. *American Cancer Society*. Available from: <http://www.cancer.org/>.
3. Gazi, E., et al., *Fixation Protocols for Subcellular Imaging by Synchrotron-Based Fourier Transform Infrared Spectroscopy*. Biopolymers, 2005. **77**: p. 18-30.
4. Miller, L. and P. Dumas, *Chemical Imaging of Biological Tissue with Synchrotron Infrared Light*. Biochimica et Biophysica, 2006. **1758**(7): p. 846-57.
5. Amrania, H., A. McCrow, and C. Phillips, *A Benchtop, Ultrafast Infrared Spectroscopic Imaging System for Biomedical Applications* Review of scientific instruments, 2009. **80**.
6. Frogley, M., *Er:Cr:YSGG Pumped Dual Optical Parametric Generator (OPG) Laser*, C.C. Phillips, Editor. 2004: EXSS Physics Dept, Imperial College.
7. Steed, R.J., *Saturation of Intersubband Transitions in P-type and N-type III-V Quantum Wells.*, in *Physics*. 2008, Imperial College of Science, Technology and Medicine: London.
8. Amrania, H., *Ultrafast Mid-Infrared Spectroscopic Imaging with Biomedical Applications*, in *Experimental Solid State Physics*. 2009, Imperial College: London.
9. Hecht, E., *Optics*. 2001, Addison Wesley. p. 560.
10. Hard, R., R. Zeh, and R. Allen, *Phase-Randomised Laser Illumination for Microscopy*. Journal of Cell Science, 1977. **23**: p. 335-343.

5.0 - Analysis of Spectral Maps from FTIR

The purpose of the work described in this chapter is to explore the capabilities (and shortcomings) of the current spectral mapping technology and to describe the complete process of using IR spectroscopy for cancer diagnosis. This process is the following: Collection of high quality spectra; Pre-processing of spectra to correct for spectral artefacts which are not related to the biochemistry of the sample; Robust and reproducible classification of spectra into tissue classifications (such as cancerous and healthy).

To begin with, the selection of the FTIR spectrometer measurement parameters and processing of IR spectra will be explained. Following this an analysis of the biochemical origin of important spectral features and statistical methods used to analyse spectral data will be examined. Finally the application of spectral mapping to cancer diagnosis in a clinical setting and the multivariate technique of linear discriminant analysis (LDA) will be presented.

5.1 - Selection of FTIR Instrument Measurement Parameters

When collecting spectral maps with a FTIR spectrometer a number of measurement parameters (such as spectral resolution, measurement time and SNR) must be decided. Incorrect selection of FTIR measurement parameters can render large quantities of data unusable in the subsequent analysis. However, with careful consideration, time can be saved in the data collection stage and the efficiency of the data analysis can be improved. The so-called “FTIR trading rules” which give the relationships between measurement parameters for the collection of point spectra (for a given spectral feature) are given below[1].

$$SNR \propto \sqrt{\text{measurement time}} \quad (5.0)$$

$$SNR \propto \text{spectral resolution} \quad (5.1)$$

$$\text{measurement time} \propto \frac{1}{\text{spectral resolution}} \quad (5.2)$$

$$SNR \propto \text{spatial resolution} \quad (5.3)$$

In addition to the FTIR trading rules a particular instrument may have inherent limitations. The FTIR spectrometer instrument used to collect the spectral maps is discussed in detail in section 4.2 and consists of a FTIR spectrometer coupled to an IR microscope equipped with a single channel MCT detector. Single channel detection schemes require images to be built up one pixel at a time which can be very time-consuming (an image consisting of 55 by 36 pixels, with an aperture size of 50µm by 50µm, and a spectral resolution of 4cm⁻¹ took 18 hours to acquire with the Jasco instrument). A

multichannel detection scheme (array detector coupled to a FTIR spectrometer), such as the Bruker Hyperion 3000, would allow for far superior data collection rates (a 64 by 64 pixel image can be collected in a few minutes).

Ideally spectra would have a spectral resolution high enough to resolve all the relevant spectral features of interest (section 5.1.1), a signal-to-noise ratio which allows quantitative data to be extracted from the data with some confidence (section 5.1.2) and a measurement time which is as short as possible. Unfortunately it can be seen from the FTIR trading rules that certain desirable features, such as high signal-to-noise ratio and measurement time, are proportional. Since compromises must be made it is useful to consider the context in which these spectra will be used and establish which criteria are the most critical for collecting meaningful information.

5.1.1 - Spectral Resolution of the FTIR Spectrometer

High spectral resolution spectra are acquired from a FTIR spectrometer at the expense of longer data acquisition times and low signal to noise (equations 5.2 – 5.3). In addition to this high spectral resolution may produce superfluous data which will cause the greater use of computational power in the subsequent data analysis. For these reasons it is desirable to collect spectra at a spectral resolution which retains all the relevant features of a biological IR spectrum without compromising the data fidelity. Figure 1 shows the IR spectra of several important isolated bio-molecules (collected by Wang et al[2]) with some approximate scales superimposed onto the figure to demonstrate the full width half maximum (FWHM) of some important spectral features. The spectral resolution required to resolve a spectral feature is on the order of the FWHM of the spectral feature that needs to be resolved (although the width of a spectral feature from an isolated bio-molecule is probably somewhat finer than the same feature in a biological sample due to less neighbouring interactions). Therefore a spectral resolution of 16cm^{-1} would be sufficient to resolve the broader spectral features (such as the amide I, amide II and the asymmetric phosphodiester peaks) but probably not enough to resolve the finer spectral features (such as the symmetric phosphodiester peak). A spectral resolution of 4cm^{-1} would be able to adequately resolve the finer features of an IR spectrum (such as the symmetric phosphodiester peak) and would probably be the optimum spectral resolution to use if those spectral features are required.

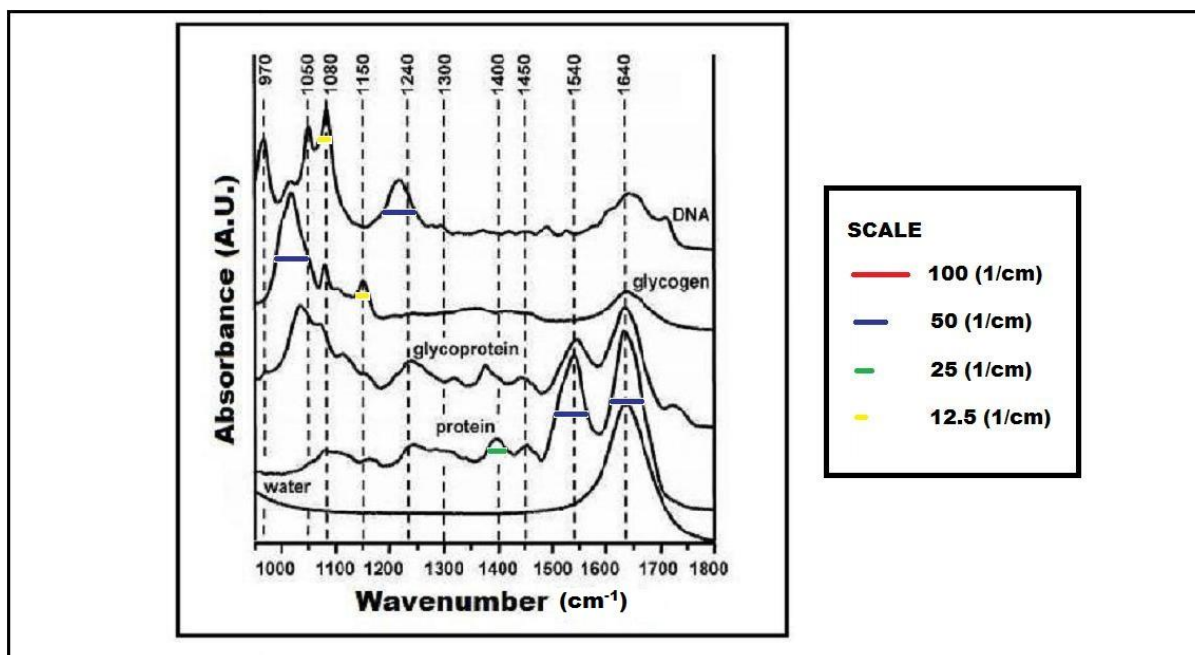


Figure 1. IR Spectra of individual bio molecules; Spectra were acquired in ATR mode from dehydrated films of pure DNA, protein, glycogen and glycoprotein. The approximate full width half maximum (FWHM) of important spectral features have been marked onto the diagram. [Adapted from; Wang, T.D., et al., Detection of Endogenous Biomolecules in Barrett's Esophagus by Fourier Transform Infrared Spectroscopy. PNAS, 2007. 104(40): p. 15864-15869.]

5.1.2 - Spatial Resolution of the FTIR Spectrometer

Measurements with a FTIR spectrometer at high spatial resolution (diffraction limited) are required for the analysis of heterogeneous (such as biological) samples (Figure 2) and may be critical for the application of IR spectroscopy to the diagnosis of disease[3]. For these reasons it is desirable to achieve the highest possible (diffraction limited) spatial resolution with reasonable (>10) signal-to-noise ratios without resorting to prohibitively long data acquisition times. Unfortunately the low signal-to-noise ratios at high spatial resolutions are due to the low irradiance (Wm^{-2}) reaching the detector from a conventional thermal source and are an intrinsic limitation of FTIR spectrometers (using optical apertures). Another trade off is field of view; for a given number of data points (spectra) high spatial resolution will decrease the field of view in a quadratic manner (e.g. decreasing spatial resolution by a factor of two decreases field of view by a factor of four). A final important consideration is that when the spatial resolution approaches the wavelength of the interrogating light then diffraction effects become significant. Once the diffraction limit (approximately on the order of the wavelength of the illuminating light, see section 3.9.1 for more details) is reached no further improvement in spatial resolution is obtainable.

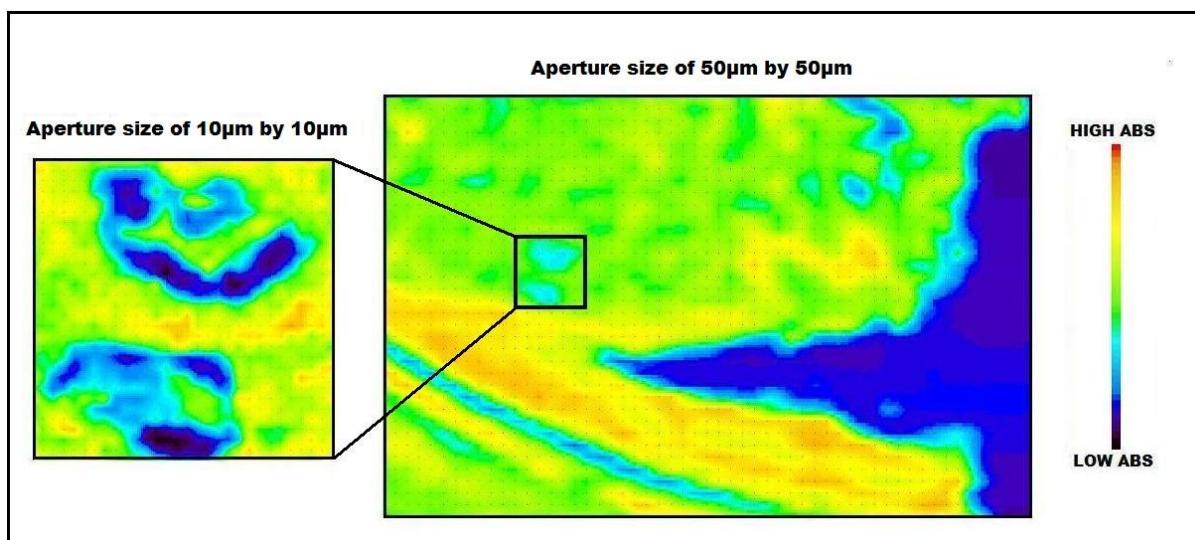


Figure 2. Chemical images (pixel values are the absorbance values at the Amide II peak) of a biological sample collected using a single channel Jasco FTIR spectrometer with different aperture sizes. The larger image on the right was taken using a 50µm aperture size (and a step size of 50µm) and the smaller section (boxed in the picture on right) was taken with a 10µm aperture size (and a step size of 10µm). It can clearly be seen that the image generated using an aperture size of 10µm shows more morphological detail than the image generated using an aperture size of 50µm

5.1.3 - Signal-to-Noise Ratio, Measurement Time, Field of View and Data Set Measurement Time

Once the spectral and spatial resolutions are decided the signal-to-noise ratio and measurement time are the only remaining single-point measurement parameters. Since the measurement time and the signal-to-noise are related (equation 5.0) once one of them is set the other is also set to a specific value. Unfortunately higher signal-to-noise requires a longer measurement time (Figure 3). In Bhargava's book, *Spectrochemical Analysis Using Infrared Multichannel Detectors*[4], the detection and quantification limits for the SNR are given as 3 and 10 respectively.

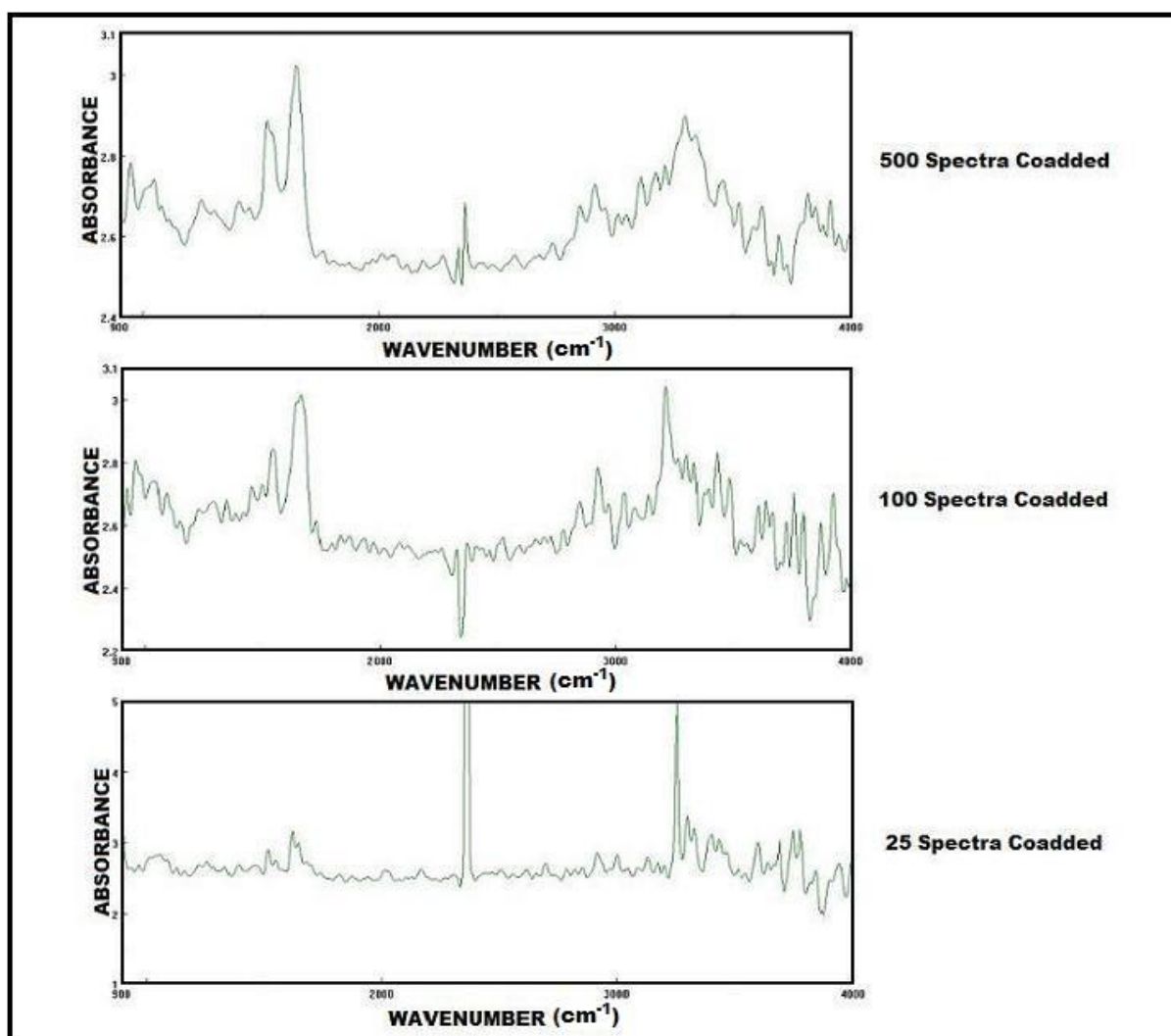


Figure 3. Comparison of different numbers of spectra being co-added (and therefore different measurement times) showing that SNR increases with measurement time. All spectra were collected from a biological sample (human oesophagus) with a single channel FTIR with an aperture size of $10\mu\text{m}$ by $10\mu\text{m}$ and a spectral resolution of 16cm^{-1} .

The limiting factors which will ultimately determine the measurement time (and therefore the signal-to-noise) are the number of pixels in spectral map, N , which is ultimately determined by the field of view (FOV) and the “data set measurement time” (which is the time to collect an entire spectral map which is different from the “measurement time” which is the time taken to collect an individual spectrum). In other words;

$$\text{Data Set Measurement Time} = N \times \text{Measurement Time} \quad (5.4)$$

Data set measurement times are effectively limited to approximately 10 hours (working day). This is an instrument specific limitation since the Jasco microscope detector is liquid nitrogen cooled and cannot be left running unsupervised for more than four hours (therefore overnight operation is not

possible). For example if an area (FOV) of 0.25mm^2 is required with a spatial resolution of $10\mu\text{m}$ by $10\mu\text{m}$ then a 50-by-50 spectral map would be needed which will consist of 2500 pixels. Since the data set must be collected in 10 hours then the measurement time for each pixel is limited to 14.4s. This measurement time would then place an upper limit on the signal-to-noise achievable.

5.2 - Pre-processing of IR Spectra

Once a spectral map is collected the raw spectra will almost certainly require some pre-processing before spectroscopic images are generated and quantitative analysis is performed. Examples of spectral pre-processing include (but are not limited to) spectral subtraction, baseline correction, smoothing and data compression. However special care must be taken at this stage since spectral pre-processing which is not performed properly can introduce artefacts into a spectrum or completely destroy the integrity of the data. In section 5.2 some of these spectral pre-processing methods are described and a more complete discussion of these procedures can be found in Smith's book[1].

5.2.1 - Spectral Smoothing

Spectral smoothing can be applied to noisy spectra to reduce the noise level. However care must be taken not to "over-smooth" a spectrum which may cause a narrow spectral features to be destroyed or neighbouring narrow spectral features may be de-resolved and grow together to become a single spectral feature. Smoothing can be accomplished in a variety of ways; two such methods, the boxcar smoothing algorithm and the Savitsky-Golay smoothing algorithm, will be discussed in sections 5.2.1.1 and 5.2.1.2.

5.2.1.1 - Boxcar Smoothing Algorithm

To perform a boxcar smoothing algorithm first a "smoothing window" is selected; For example consider a smoothing window containing 10 data points (with x and y values) in a spectrum. For the first part of the boxcar smoothing algorithm the y values (such as absorbance or % transmission) of these 10 data are averaged and then the average value is assigned to the middle of the 10 x data points. For the second part of the boxcar smoothing algorithm the smoothing window is then moved along the entire spectrum (one data point at a time) repeating step one at each data point until the entire spectrum has been smoothed. The noise in the original spectrum will be reduced because the fluctuations in the sign of random noise will cancel out when the y values are averaged. The amount of smoothing accomplished will obviously be sensitive to the size of the smoothing window; the more points in the smoothing window the greater the extent of the smoothing.

5.2.1.2 - Savitsky-Golay Smoothing Algorithm

The Savitsky-Golay smoothing algorithm works by fitting a polynomial function to the set of data points in the smoothing window. The higher the degree of the polynomial function used in the Savitsky-Golay smoothing algorithm the lower the amount of smoothing achieved.

5.2.2 - Spectral Subtraction

Spectral subtraction is performed when the individual spectrum of an individual component of a mixture of components is required. As a simple example consider a mixture of components (A and B). If a spectrum (S_{AB}) of the mixture and a spectrum of component B in isolation (S_B) are acquired then the spectrum of component A (S_A) can be extracted. To account for the difference in concentration of component B in isolation (S_B) and within the mixture a subtraction factor, SF, is introduced;

$$S_A = S_{AB} - SF \times S_B \quad (5.5)$$

Very few spectral subtractions will give a perfect result. Problems with a spectral subtraction can be caused by interaction factors in the mixture which may cause spectral features from a particular component in the mixture spectrum to broaden or shift relative to the isolated component spectral features. Spectral subtraction assumes the validity of Beer's law for all the chemical components and all the spectra involved in the subtraction must be measured in units of absorbance.

Spectral subtraction may be useful in the context of analysing biological tissue samples when chemicals used in the tissue processing stages (section 4.1.3), such as paraffin, have not been completely removed from the sample and are interfering with the sample spectrum. Furthermore if the background spectrum is collected without a substrate in the beam path (such as a BaF₂ disk) then the absorbance introduced by the BaF₂ substrate can be corrected for by a spectral subtraction.

5.2.3 - Baseline Correction

The baseline of a spectrum may not be flat for several reasons including, sample scattering, inappropriate choice of background and instrument drift. A spectrum may have a sloping or curved baseline which can be removed by generating a function which matches the shape of the baseline and subtracting it from the sample spectrum. An example of a baseline correction (using a sloping straight line) used on a typical spectrum (aperture size of 50 μm by 50 μm and spectral resolution 4 cm^{-1}) taken from a biological sample (human oesophagus) is shown in Figure 4. Clearly a sloping baseline significantly corrupts the absorbance values of an IR spectrum and the cause of a sloping baseline must be identified and corrected for before quantitative analysis is applied.

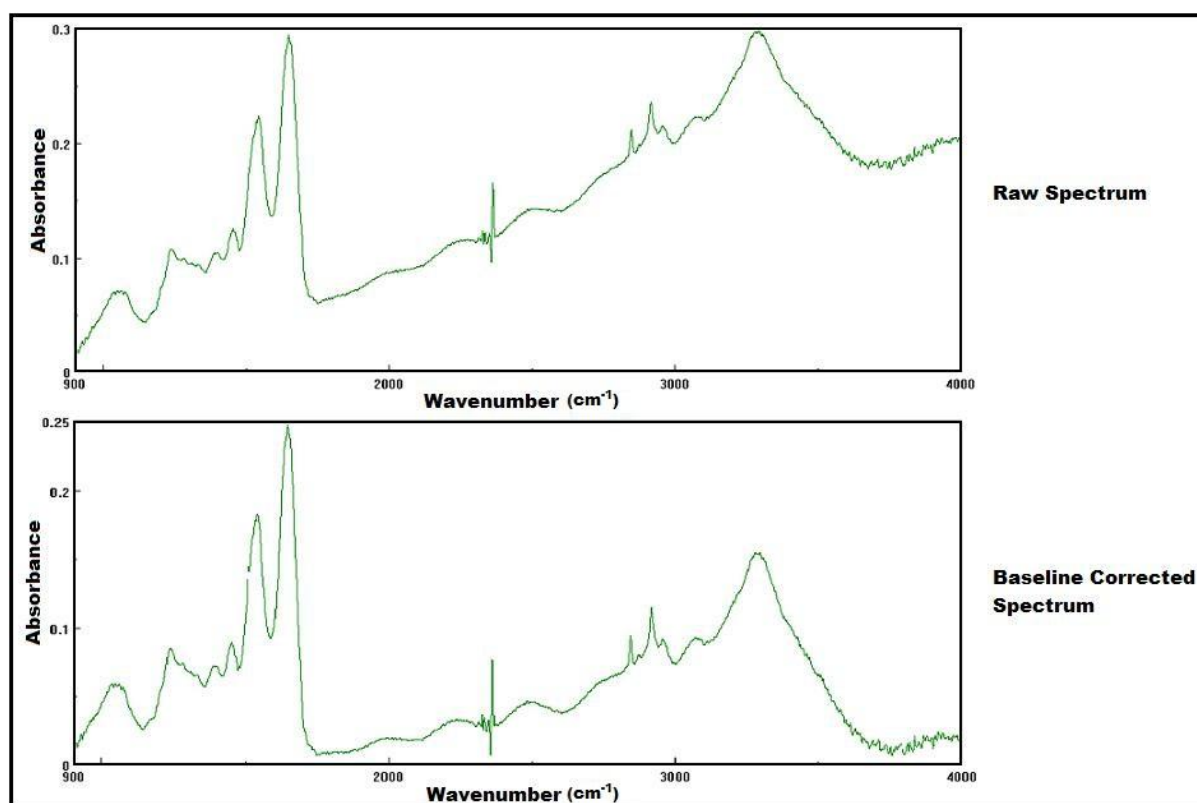


Figure 4. Comparison of a spectrum before and after a baseline correction (one sloping straight line was used as the baseline correction). The spectrum was collected from a biological sample (human oesophagus) at an aperture size of 50 μm by 50 μm and a spectral resolution of 4 cm^{-1} using a single channel FTIR.

5.2.3.1 - Pixel-to-Pixel Baseline Variations

For spectral mapping of biological samples the problem of baseline variations is even more severe than for single point spectra since the baseline correction needed may vary from pixel to pixel. The origin of these pixel-to-pixel baseline variations is the heterogeneous nature of biological samples and is often a function of one or more optically active features in the sample such as boundaries and interfaces between different materials which manifests itself as broad undulations across the baseline[5] (Mie scattering is an example of this phenomena and is discussed in section 2.3.3). A publication by Bu et al[6] describes the problem of pixel-to-pixel baseline variations and mitigates the problem by using fast Fourier transform (FFT) filtering (to remove the low frequency terms) in both the spectral and spatial domains. The method of FFT filtering of spectra is useful since it provides a technique to *non-subjectively* remove baseline fluctuations from spectra which can potentially be applied algorithmically to large spectral maps. Furthermore by also removing high frequency terms from the Fourier transforms of spectra a certain amount of smoothing can also be achieved simultaneously.

5.2.4 - Data Compression

Spectral mapping can accumulate vast amounts of data and a certain amount of data compression (reduction in the number of data points per spectrum) can be useful. A typical 128 by 128 pixel array collecting spectra which consist of 1000 absorbance values each will produce 16,384,000 data points. Using a data resolution of 20 bits this would give a data file size of approximately 328M bits or 40M bytes. Obviously data file sizes will increase with pixel number and spectral resolution generating ever larger data files.

5.2.4.1 - Compression of Spectral Features into a Peak Area or Peak Height

Data compression can be a useful procedure for making data storage and processing more manageable. For example consider the amide II peak at a spectral resolution of 4cm^{-1} . If we suppose that the width of the amide II peak is approximately 50cm^{-1} (Figure 1) then the amide peak will contain at least 13 data points. These 13 data points could be compressed by using them to calculate the area under the amide II peak and using that number in subsequent calculations instead of the original data points. In addition to using the peak area to replace the data points comprising a spectral feature one could also use peak heights measured with respect to some reference point (such as a neighbouring trough). Figure 5 shows the different methods used to compress a spectral feature and extract an absorbance value. Since the process of calculating peak areas reduces random noise they produce more reliable results than peak heights in quantitative analysis.

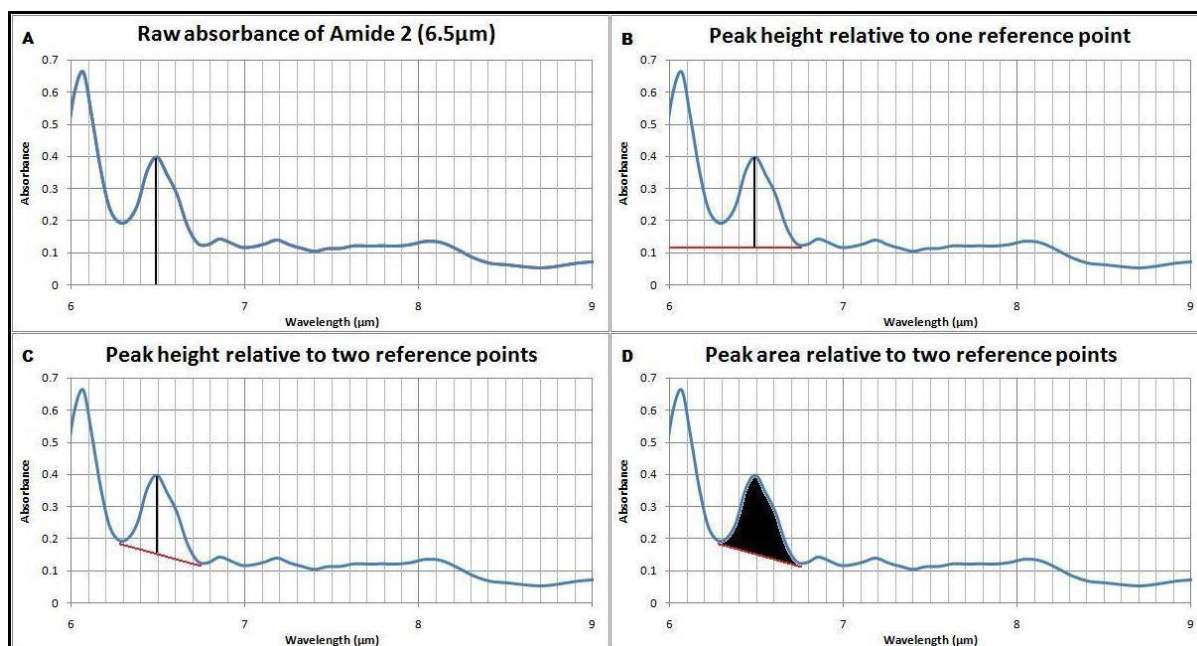


Figure 5. Different methods to compress the data from the amide II peak and extract an absorbance value for quantitative calculations. A) Raw absorbance value B) Absorbance value measured with respect to a neighbouring reference point C) Absorbance value measured with respect to two reference points D) Peak area measured relative to two reference points.

5.2.4.1.1 - Biochemically Significant Spectral Features for Cancer Diagnosis

Data compression has been discussed and the issues regarding the large amount of data present in a typical spectral map have been described. Moreover there may be a lot of superfluous data present in a typical spectrum such as spectral features which have no biochemical significance or spectral features which are strongly correlated with each other. For these reasons it is useful to analyse the biochemical differences between healthy and cancerous tissue and use this information to identify the most important spectral features (which are related to the biochemistry of a sample) which may be used as potential “biomarkers” for the diagnosis of cancer.

The biochemical components of a biological tissue sample were discussed in section 3.3 and shown to be mainly composed of DNA, RNA, proteins, lipids carbohydrates and water. Figure 1 shows the spectral contributions from these biochemical components to a typical biological spectrum. Furthermore a publication by Wong et al discusses the spectroscopic differences between DNA and RNA which has been isolated from cancerous colon cells[7]. Figure 6 is taken from Wong’s paper and shows the IR spectra of adenocarcinoma colon cells, their nuclei and DNA and RNA isolated from them. A comparison between the DNA and RNA spectra suggests some fine (approximate FWHM of 10cm^{-1}) spectral features which can be used to distinguish between DNA and RNA; For example the

spectral feature at 1121cm^{-1} is mainly contributed by RNA and the spectral feature at 1020cm^{-1} is mainly contributed by DNA.

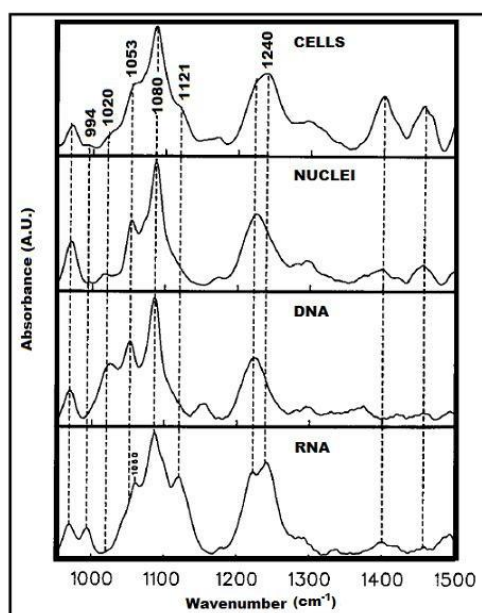


Figure 6. IR spectra of adenocarcinoma colon cells, their nuclei and DNA and RNA isolated from them. A comparison between the DNA and RNA spectra suggests spectral features which can be used to distinguish between DNA and RNA. For example the spectral feature at 1121cm^{-1} is mainly contributed by RNA and the spectral feature at 1020cm^{-1} is mainly contributed by DNA. All spectra have been normalised to the symmetric phosphodiester band. [Wong, P.T., E.D. Papavassiliou, and B. Rigas, Phosphodiester Stretching Bands in the Infrared Spectra of Human Tissues and Cultured Cells. *Applied Spectroscopy*, 1991. 45(9): p. 1563-1567.]

Various publications have described the biochemical differences which occur between healthy and cancerous tissue [2, 7-10]. One important difference is the nuclear-to-cytoplasmic ratio (N/C) which is usually found to be higher in cancerous tissue[8]. The N/C measures the ratio of the size of the nucleus to that of the cytoplasm of a cell and is usually found to be larger for immature cells (since as a cell matures the size of its nucleus generally decreases)[11]. Therefore the increased N/C observed in cancerous tissue may not be a difference in the biochemistry of cancerous tissue per se but rather a consequence of the increased number of immature cells and cell mitosis' in cancerous tissue[12]. It is not clear if there is a combination of spectroscopic features which could be used to estimate the N/C however the phosphodiester groups (1240cm^{-1} and 1080cm^{-1}) have been used to estimate the nucleic acid (both RNA and DNA) content[2, 7].

Another important metric used in spectroscopic studies if cancer is the RNA/DNA ratio [8, 9] which can be measured spectroscopically as $1121\text{cm}^{-1}/1020\text{cm}^{-1}$. However there does seem to be some conflicting evidence regarding whether this ratio should decrease (as claimed by Maziak's publication on oesophagus cancer[8]) or increase (as claimed by Mordechai's publication on cervical

and skin cancer[9]) in cancerous tissue. Since there is increased cell activity in cancerous tissue (more cell divisions) it seems to the author that a biochemical argument based on the increased amount of protein synthesis (and therefore increased amount of translation RNA) would support the case for an increased amount of RNA relative to DNA in cancerous tissue (Figure 7).

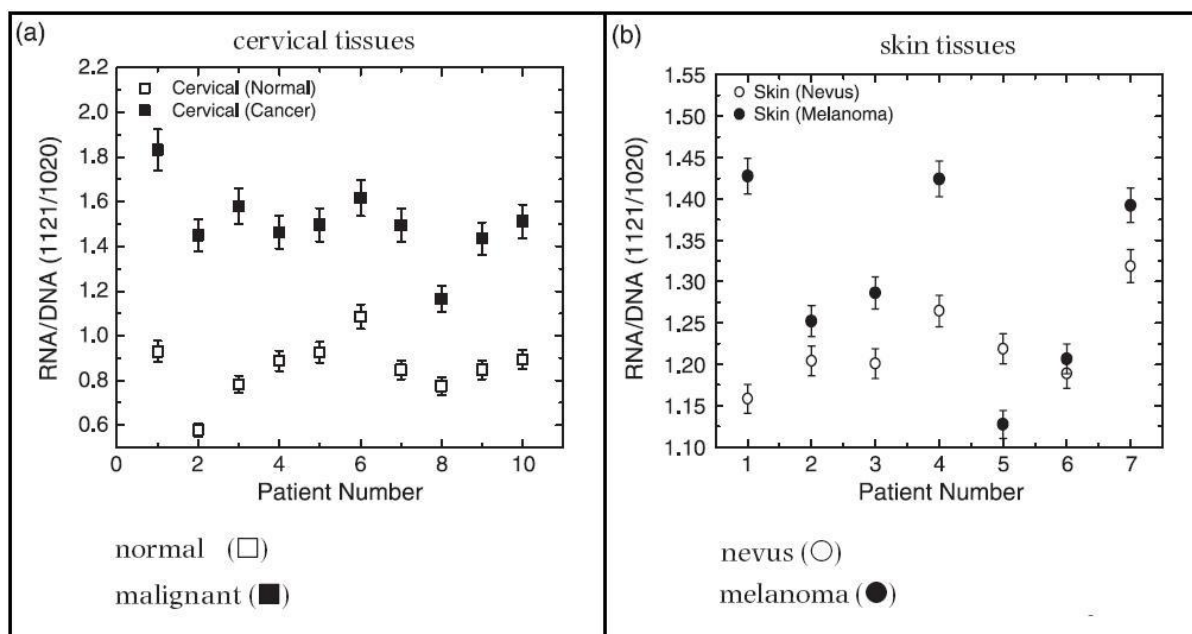


Figure 7. RNA/DNA ratio (as measured by the ratio of 1121cm⁻¹ to 1020cm⁻¹) of a) normal and malignant cervical tissue and b) nevus and melanoma skin tissue. In both cases the relative RNA content was higher than the DNA content (except patient number 5 for skin cancer) possibly indicating a higher amount of transcription in cancerous tissue. [Mordechai, S., et al., Possible Common Biomarkers from FTIR microspectroscopy of Cervical Cancer and Melanoma. *Journal of Microscopy*, 2004. 215(215): p. 86-91.]

The glycogen content (which can be measured using the 1025cm⁻¹ and/or 1150cm⁻¹ spectral features) is usually depleted in cancerous tissue [8, 9] and can therefore be another useful metric for the diagnosis of cancer. However, as Chiriboga et al report[12], the absence of glycogen may be accounted for by biochemical and physiological reasons (such as post-mortem degradation of glycogen and reduced glycogen content due to malnutrition respectively) so spectroscopic interpretations of glycogen content must be made with great care.

5.2.4.2 - Principal Component Analysis

Principal component analysis (PCA) can be used as a method of data compression (when there is some redundancy in the variables describing the data) by defining a set of artificial variables (principal components) that will account for most of the variance in the observed data. In addition to data compression, PCA can also be used to identify the underlying structure of a data set since when

the principal components are interpreted it may be found that they represent the data set in a much smaller number of concepts than the original data variables did.

To illustrate PCA consider a data set N of spectra collected from a particular biological tissue classification. The data variables could be defined as, for example, 10 key spectral feature areas ($x_1, x_2 \dots x_{10}$) extracted from each individual spectrum (Figure 8) (or indeed the data variables could be, in principle, the entire 1000 or so wavenumbers per spectrum).

Variable	x_1	x_2	x_{10}
Name of Spectral Feature	Amide 1	Amide 2	Asymmetric Phosphodiester	Symmetric Phosphodiester	Alcohols and Phenols	Methyl	Methylene	Methyl and Methylene	CH ₂ Bending from Protein	Glycogen
Spectrum 1	x_1^1	x_2^1	x_{10}^1
Spectrum 2	x_1^2	x_2^2	x_{10}^2
.....
Spectrum N	x_1^N	x_2^N	x_{10}^N

Figure 8. Data set N of spectra collected from a particular biological tissue classification. 10 key spectral feature areas have been extracted from each spectrum compressing the data in each spectrum down to 10 variables.

PCA can reduce the 10 data variables into a smaller set of variables (principal components) since there may be “variable redundancy” (variables which are highly correlated so that as one increases so does the other) in the data set. An intuitive feel for variable redundancy can be accomplished by examining the correlations amongst all the 10 data variables of an example data set (255 spectra were collected from healthy (oesophagus) epithelium tissue using a Jasco FTIR spectrometer with a aperture size of 50 μ m by 50 μ m and a spectral resolution of 4cm⁻¹, data was not corrected for pixel-to-pixel baseline variations). A correlation matrix demonstrates the inter-relationship between these 10 key spectral features (Figure 9) by creating x-y plots for every pair of variables (one data point per spectrum). The correlation matrix indicates that there is a strong correlation between the methyl and methylene groups (2960cm⁻¹, 2920cm⁻¹ and 2850cm⁻¹) and a fairly strong correlation between the amide I and II spectral features (1650cm⁻¹ and 1550cm⁻¹). These correlations show that some variable groups seem to hang together and represent a single construct. For example, the

correlation between the amide I and amide II spectral features may indicate that these two variables are representing a broader construct such as the “protein content”.

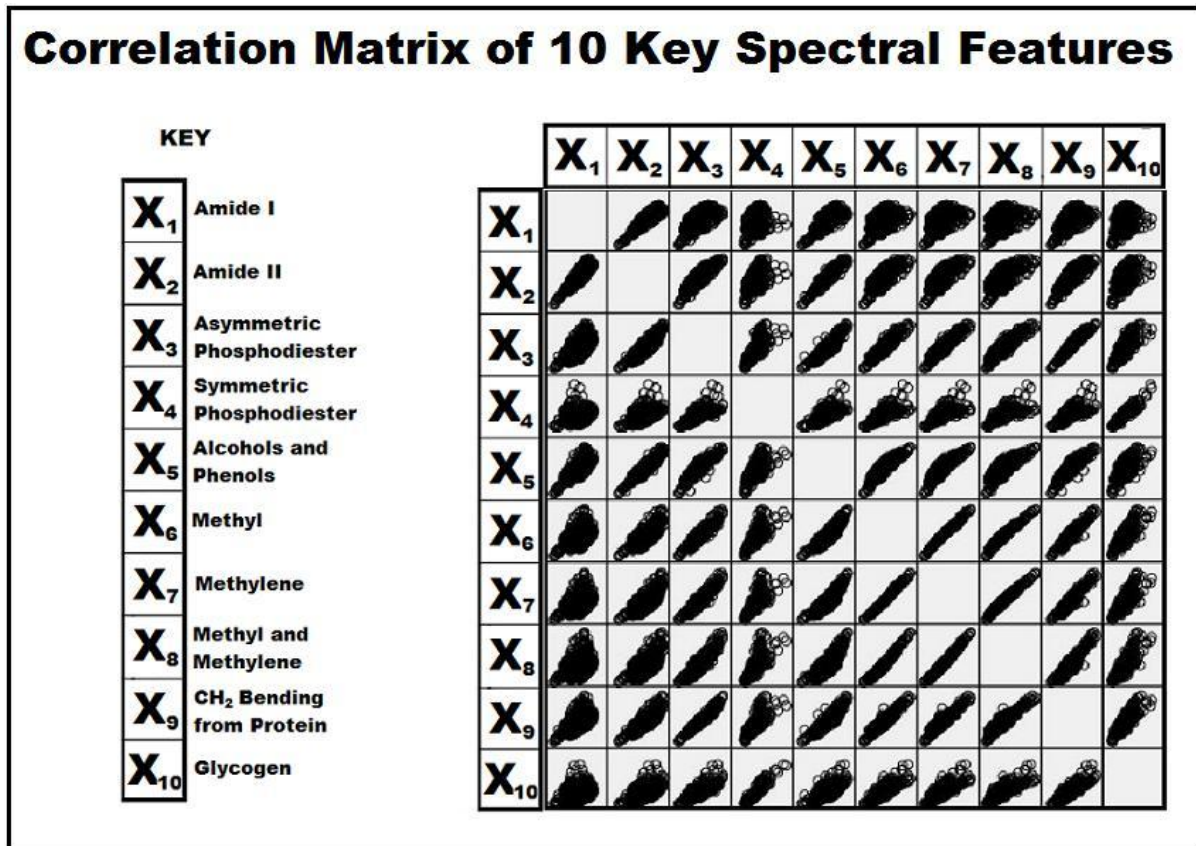


Figure 9. Correlation matrix can be used to identify the correlations between variables. For example variables x6, x7 and x8 are all highly correlated to each other. Data collected from human oesophagus tissue using a single channel Jasco FTIR spectrometer with an aperture size of 50µm by 50µm and a spectral resolution of 4cm⁻¹, data was not corrected for pixel-to-pixel baseline variations.

The principal components generated by a PCA will be a linear combination of optimally-weighted data variables. The principal components (c_k) will have the general form of equation 5.6

$$c_k = b_{k1}x_1 + b_{k2}x_2 \dots \dots \dots + b_{kN}x_N \quad (5.6)$$

Where;

b_{ki} = The weight for variable i for principal component k

For instance, for the 10 spectral feature example, a principal component may exist which relates to the construct “protein content” which would have larger relative weights for the amide variables (x_1 and x_2) and smaller relative weights for those variables which do not pertain to proteins. The weights in a principal component are computed by an algorithm which identifies the weights that are optimally successful in accounting for the variance in the observed data set whilst ensuring that each

principal component is uncorrelated with every other principal component. In general when a PCA is performed there will be N principal components however most of the data variance will be accounted for by the lower order principal components while the higher order principal components contain mostly noise. Therefore the reduction in the dimensionality of the data set by PCA can be effectively achieved by omitting the higher order principal components.

5.3 - Tissue Classification Using IR Spectra

A primary objective of this thesis is to evaluate the prospect of using spectral mapping as an adjunct tool in the tissue classification process which is used for cancer diagnosis (histopathology). The purpose of section 5.3 will be to discuss the statistical techniques used to identify an individual spectrum as belonging to a particular tissue classification.

5.3.1 - Assessment of Tissue Classification Accuracy: Sensitivity and Specificity

Key metrics the medical community uses for the analysis of a new diagnostic tool are the sensitivity and specificity. The sensitivity measures how well a binary test correctly identifies a condition. In the case of cancer diagnosis it will be the probability that a person with cancer is correctly diagnosed as such. The specificity measures how well a binary classification test correctly identifies the negative cases. So it is the probability that a patient without cancer is given the all clear. The cases of a false negative and a false positive are both catastrophic with the treatment not being carried out early enough on ill patients and disruptive treatments being carried out on healthy patients respectively.

A final thought to add here is that in order to calculate reliable sensitivity and specificity data a rigorous gold standard is required to initially classify the tissue. In the case of cancer diagnosis the gold standard is histopathological analysis which has been shown to fall well short of a “perfect gold standard”[13]. Therefore the measured sensitivities and specificities for spectral mapping may be reduced by either the inability of spectral mapping to correctly classify tissue or the incorrect classification of tissue using the “gold standard”!

5.3.2 - Tissue Classification Using Univariate Methods

In certain situations just one or two spectral features can be used to identify a spectrum as belonging to a particular tissue classification. However a univariate approach will obviously not give as robust a classification as a multivariate method can. This is because a multivariate technique can draw upon more biochemical information per spectrum than a univariate method can and will be less sensitive to spectral artefacts and instrument drift. One example of a univariate technique is chemical imaging (discussed in section 2.4.1). Figure 10 shows a chemical image (collected at the

amide I spectral feature) of a human oesophagus tissue sample containing pre-cancerous (high grade) and healthy squamous epithelium tissue (10 μ m by 10 μ m aperture size, 16cm⁻¹ spectral resolution).

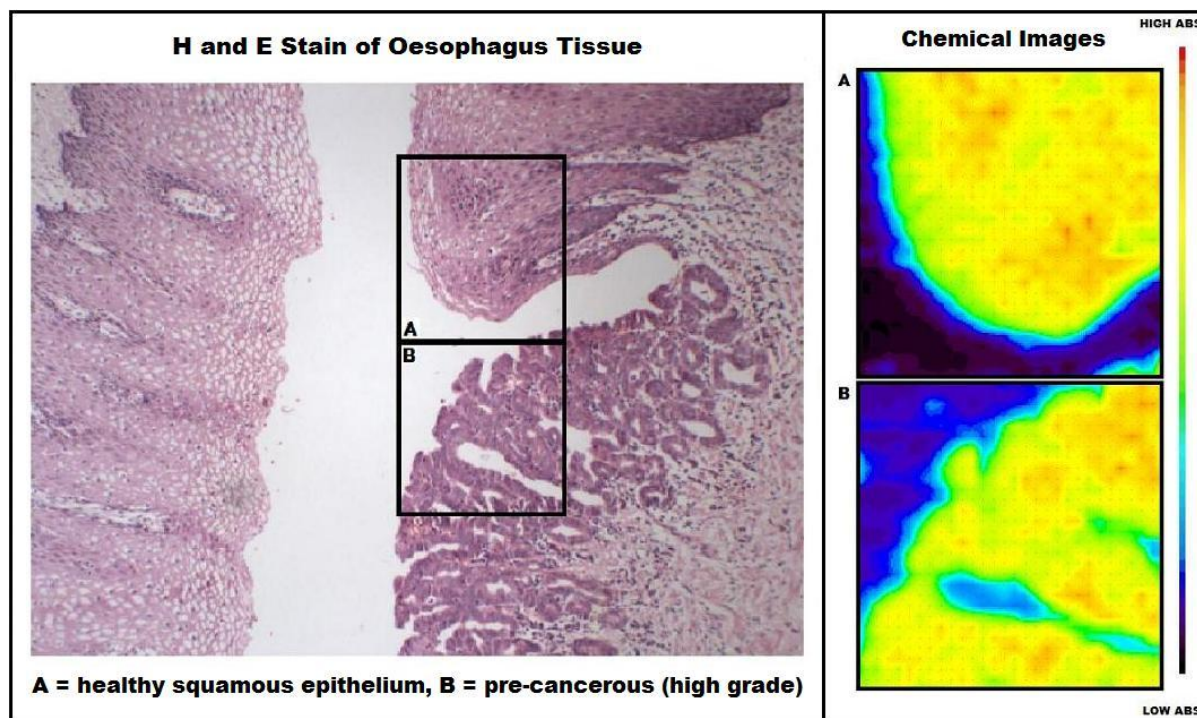


Figure 10. An example of chemical imaging from an oesophagus tissue sample containing both pre-cancerous (high grade) tissue and healthy squamous epithelium tissue. The chemical images were taken with a single channel Jasco FTIR spectrometer at an aperture size of 10 μ m by 10 μ m, a spectral resolution of 16cm⁻¹ and at the amide I peak (1650cm⁻¹). Box A contains healthy squamous epithelium tissue and box B contains the pre-cancerous (high grade) tissue.

5.3.2.1 - The F-Test

The F-test is a useful method for evaluating the ability of a particular spectral feature to discriminate between different tissue classifications. Figure 11 shows an example of how the F value is calculated for a two group system (for example healthy epithelium and cancerous tissue classifications). The F statistic is calculated as follows;

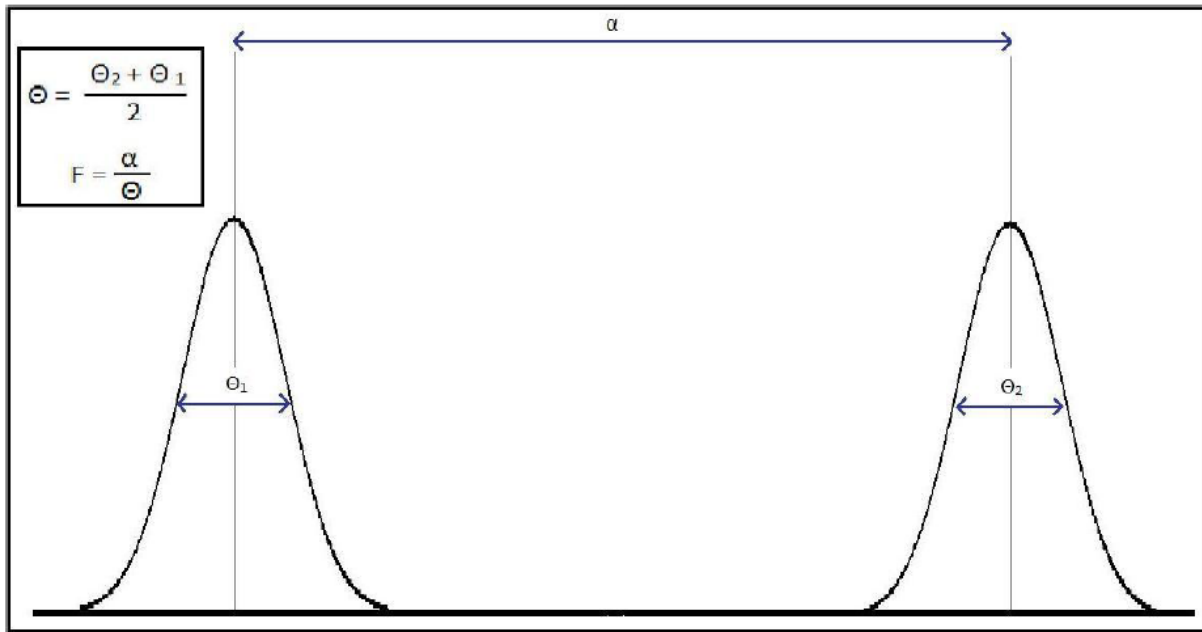


Figure 11. Diagram showing how the F statistic is calculated for a two group F test

$$F = \frac{\alpha}{\theta} \quad (5.7)$$

Where

α = distance between average of spectral feature in group 1 and group 2

$$\theta = \frac{\theta_1 + \theta_2}{2} \quad (5.8)$$

Where;

Θ_1 = standard deviation of spectral feature in group 1

Θ_2 = standard deviation of spectral feature in group 2

Here we see that if the average within-group variability (as represented by the average s.d.) is small relative to the between-group variability (difference in averages) the discrimination is rather good. Conversely if the within-group variability is large and the between-group variability is small we can expect a poor discriminating ability (imagine the normal distributions getting wider and closer together so that their tails are overlapping). The F-value can then be used to provide a metric for deciding which spectral feature has the best discriminating ability in a univariate model; High F-values indicate the best discriminating ability.

5.3.3 - Tissue Classification Using Multivariate Methods

In general the most robust tissue classification methods using spectral mapping will involve a multivariate treatment of the data. A variety of different multivariate statistical methods exist for the analysis of spectral data sets such as artificial neural networks (ANN), cluster analysis and linear discriminant analysis (LDA). Indeed entire software packages are now commercially available (e.g. Cytospec [14]) for the application of multivariate statistical methods to spectral maps and the creation of spectroscopic images. In sections 5.3.3.1 the method of LDA will be described and in section 5.3.3.2 a LDA case study will be performed using spectral data collected from a human oesophagus using the Jasco FTIR spectrometer.

5.3.3.1 - Linear Discriminant Analysis

Linear Discriminant Analysis (LDA) is a multivariate statistical technique where independent variables associated with some entity are used to predict the likelihood that that a particular entity will belong to a particular group. In the case of IR spectroscopy the entity is a spectrum, the independent variables are the absorbance values at particular wavelengths (or combinations thereof), and the groups are the particular tissue classifications (for example cancerous and healthy). Therefore the LDA program uses particular absorbance values (at particular wavelengths) from an individual spectrum to classify it as belonging to cancerous or healthy tissue. The production of a LDA program consists of two stages firstly the training stage and secondly the classification stage. In sections 5.3.3.1.1 - 5.3.3.1.2 a description of a two group (healthy and cancerous) LDA procedure is described.

5.3.3.1.1 - Training Stage (Figure 12)

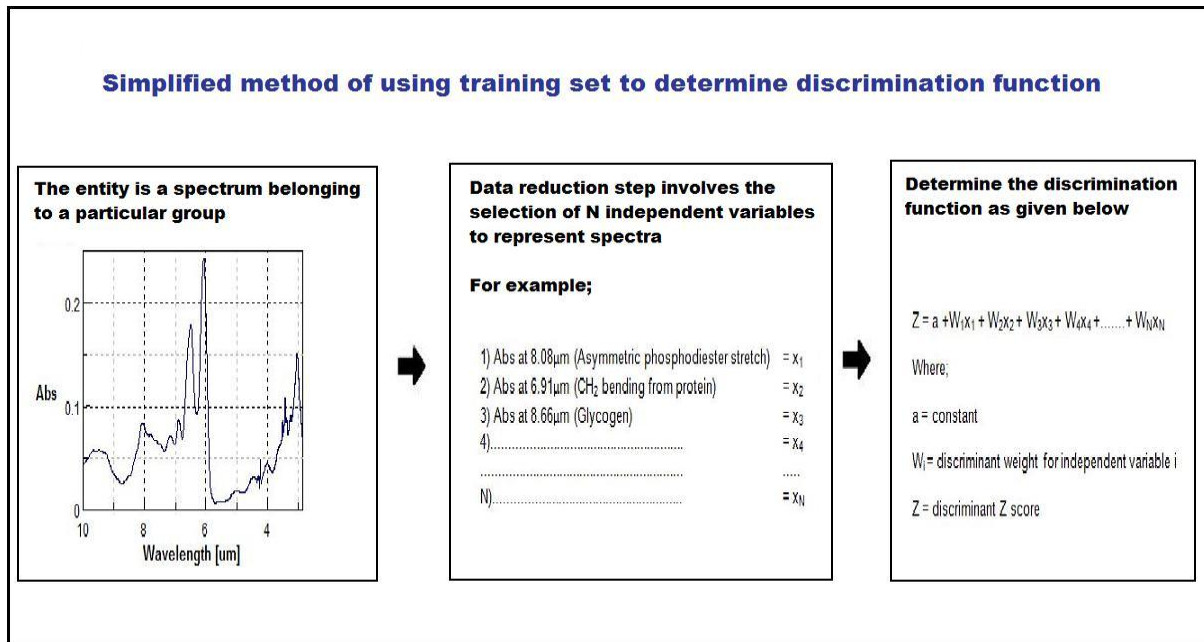


Figure 12. LDA program - training stage example for a two group classification problem

For the training stage several spectra must be gathered which are known to be collected from either healthy or cancerous tissue classifications. Since LDA is a statistical technique the larger this training set the more reliable the classification stage will be. Once the known spectra have been collected the data is reduced from approximately 1000 data points to N independent variables (usually the important spectral features). To create a reliable LDA program it is important to select those independent variables (wavelengths or functions thereof) which provide the best discrimination between tissues. The selection of independent variables is a highly subjective part of the program and care must be taken to ensure the pool of independent variables feed into a LDA program has some physical meaning; garbage in, garbage out. Non subjective methods exist, such as genetic algorithms[15], for the selection of independent variables but were not employed in this thesis. Once N independent variables have been selected the discrimination function (Z) is calculated (for two groups there is one discrimination function and for k groups there are (k-1) discrimination functions). The discriminant function will have the form;

$$Z = a + W_1x_1 + W_2x_2 + \dots + W_Nx_N \quad (5.9)$$

Where;

a = Normalisation constant

W_i = Discriminant weight for independent variable i

The discriminant weights of the discrimination function are determined by maximising the between group variance relative to the within-group variance for each independent variable. For a two group system the discrimination function is then typically normalised (using a constant) to give; $Z < 0$ implies membership of group A, $Z > 0$ implies membership of group B.

5.3.3.1.2 - Classification Stage (Figure 13)

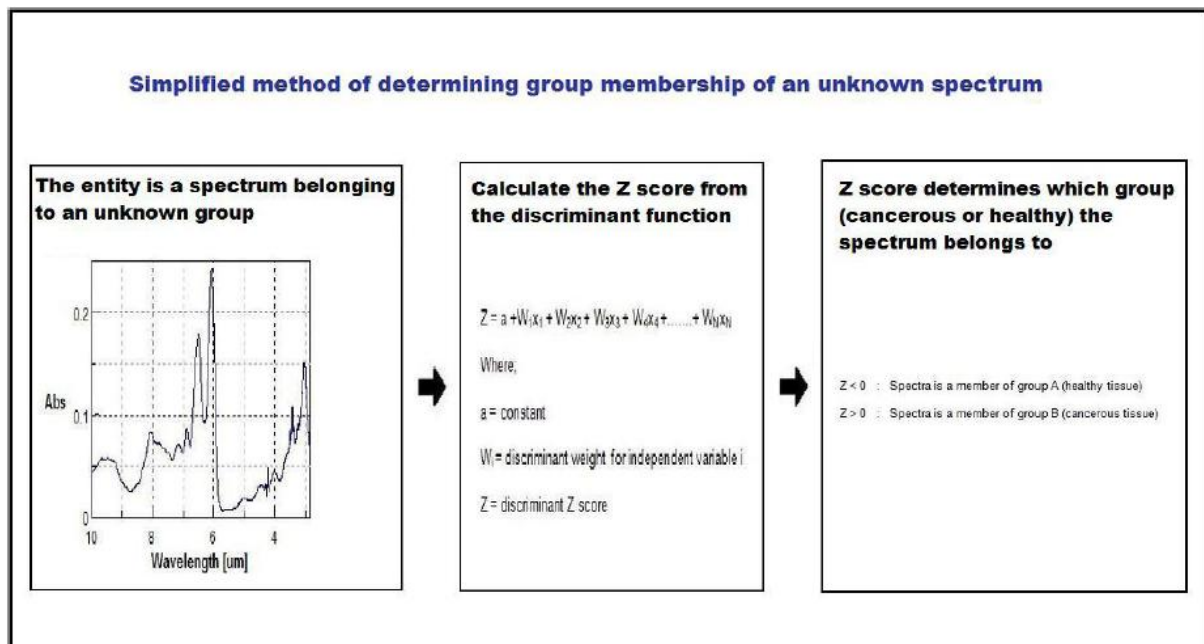


Figure 13. LDA program - classification stage example for a two group classification problem

The discrimination function provides the key to classifying unknown spectra. Given an unknown spectrum its Z score can be calculated by inputting its independent variable values (X_1, X_2, \dots, X_{10}) into the discrimination function. If, for example, the Z score is negative then the spectrum is classified as a member of group A (healthy tissue). By using a second set of known spectra (usually spectra from the original training data omitted from the training stage) the classifying ability of the LDA program can be assessed. If, for instance, the LDA correctly classifies 99% of the second set the LDA program is a robust classifying program, but if the correct classification is 1% the LDA program is an extremely poor classifier.

5.3.3.2 - Case study: Linear Discriminant Analysis

In this section (5.3.3.2) an application of a LDA model to the classification of a spectral data set will be described. However it should be emphasised that this LDA case study is simply to demonstrate the technique of LDA and its results are not significant for several reasons;

- 1) Spectral artefacts such as pixel-to-pixel baseline variations and dispersion artefacts were not corrected for in individual spectra.
- 2) The spectra were only collected from one patient's tissue section (255 epithelium spectra and 426 cancerous spectra).
- 3) The spatial resolution was 50 μ m. Therefore it is likely that many of the spectra are collected from regions which contain more than one tissue classification, particularly around the periphery of a particular tissue classification (for example the spectra collected on the boundary of cancerous and healthy epithelium tissue will have spectral contributions from both tissue classifications).

5.3.3.2.1 - Case study: Development of LDA model

Spectra were collected from two different tissue classifications (cancerous and healthy epithelium tissue). Figure 14 shows the regions on a chemical image (amide I peak height) of a spectral map (aperture size of 50 μ m by 50 μ m, and a spectral resolution of 4cm⁻¹) from which the spectra were taken. In total 681 spectra were extracted, 255 were grouped as healthy epithelium and 426 were grouped as cancer. The mean spectra are shown in Figure 15. Ten biochemically significant variables were selected to be used in the LDA (Figure 16).

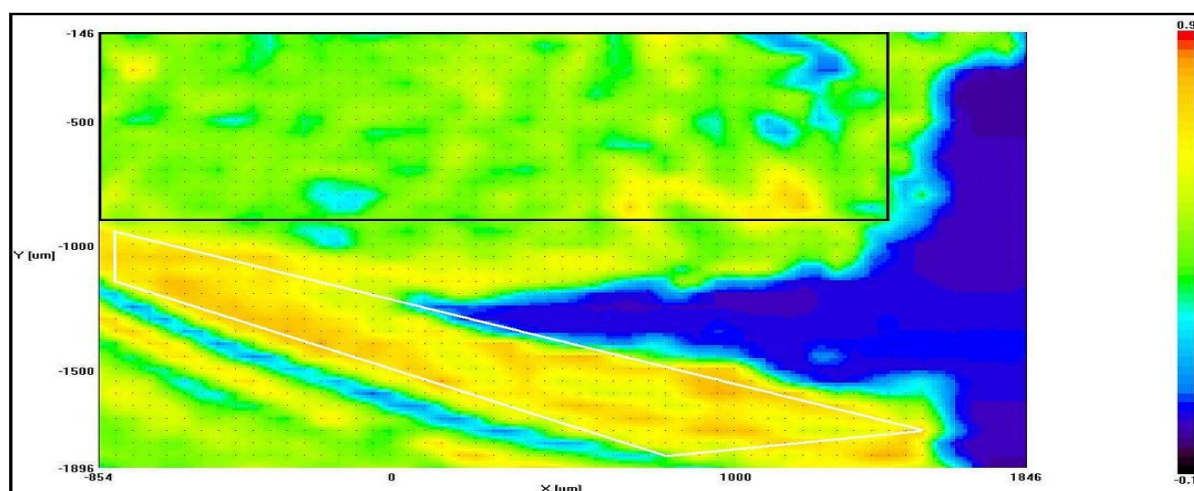


Figure 14. Image showing regions where the spectra were taken from that were used in the LDA. The black region contains spectra from a region classified as cancerous. The white region contains spectra from a region that was classified as healthy epithelium tissue.

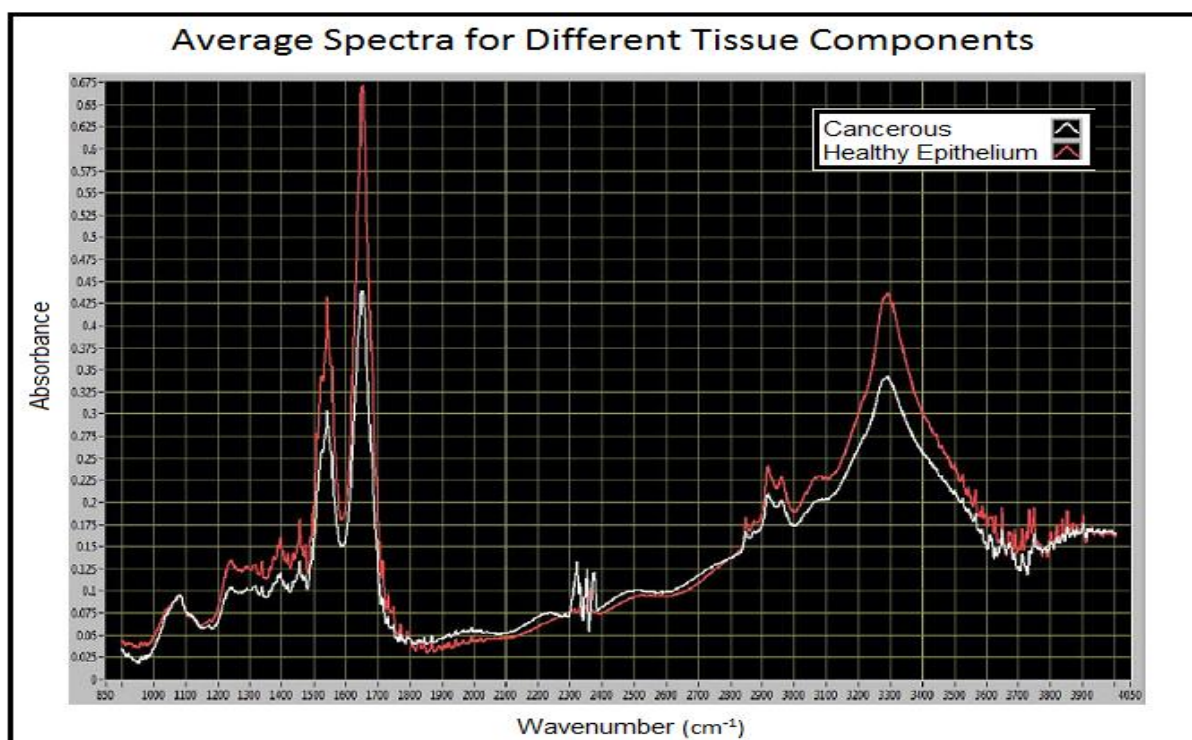


Figure 15. Average spectra collected from two different tissue classifications (cancerous and healthy epithelium tissue). In total 681 spectra were extracted, 255 were grouped as healthy epithelium and 426 were grouped as cancerous. The spectra were collected with a single channel Jasco FTIR spectrometer with an aperture size of 50 μ m by 50 μ m and a spectral resolution of 4 cm^{-1}

Variable	X ₁	X ₂	X ₃	X ₄	X ₅	X ₆	X ₇	X ₈	X ₉	X ₁₀
Name of Spectral Feature	Amide 1	Amide 2	Asymmetric Phospho-diester	Symmetric Phospho-diester	Alcohols and Phenols	Methyl	Methylene	Methyl and Methylene	CH ₂ Bending from Protein	Glycogen
Wavenumber (cm ⁻¹)	1650cm ⁻¹	1550cm ⁻¹	1236cm ⁻¹	1080cm ⁻¹	3300cm ⁻¹	2960cm ⁻¹	2920cm ⁻¹	2850cm ⁻¹	1448cm ⁻¹	1155cm ⁻¹

Figure 16. Ten biochemically significant independent variables selected to be used in the LDA.

The LDA was carried out by a commercial statistics package (SPSS). In order to test the classifying ability of the LDA program the data set was partitioned (randomly) into a training data set and a classification data set. Only 489 spectra (192 healthy epithelium and 297 cancerous) were used to train the model (training stage) and 192 spectra (63 healthy epithelium and 129 cancerous) were omitted to be used for the classification stage to verify the model. The discriminant function generated from the training stage was;

$$Z = -1 + 56x_1 - 211x_2 + 130x_3 - 58x_4 + 58x_5 + 99x_6 + 220x_9 - 51x_{10} \quad (5.10)$$

If;

$Z < 0$ Then spectrum is classified as healthy epithelium

$Z > 0$ Then spectrum is classified as cancerous

Two independent variables (x_7 and x_8) for methyl and methylene have been removed (by SPSS) from the analysis because they are so strongly correlated with a third independent variable (x_6) that they offer no extra discrimination (The correlation between x_6 , x_7 and x_8 can be seen in the correlation matrix in Figure 9 which uses the same data set).

5.3.3.2.2 - Case study: Results of LDA model

Figure 17 shows the results of the LDA. The LDA models ability to correctly classify spectra was tested with both the spectra used in the training stage (192 healthy epithelium and 297 cancerous), and separately, with the spectra omitted from the data set for the classification stage (63 healthy epithelium and 129 cancerous). For the training data the LDA model only one misclassified one spectrum out of 489 spectra (overall 99.8% successful with classification). For the classification data three spectra were incorrectly classified (overall correct classification rate of 98.4%) by the LDA model.

LDA Classification Results					
		C/E	Predicted Group Membership		Total
			Healthy Epithelium	Cancerous	
Spectra used in training stage; 192 = Healthy Epithelium 297 = Cancerous	Count	Epithelium	192	0	192
		Cancer	1	296	297
	%	Epithelium	100.0	.0	100.0
		Cancer	.3	99.7	100.0
Spectra used in classification stage; 63 = Healthy Epithelium 129 = Cancerous	Count	Epithelium	61	2	63
		Cancer	1	128	129
	%	Epithelium	96.8	3.2	100.0
		Cancer	.8	99.2	100.0

Figure 17. Classification results for the LDA model. The LDA model was tested with both the spectra used in the training stage (192 healthy epithelium and 297 cancerous), and separately, with the spectra omitted from the data set for the classification stage (63 healthy epithelium and 129 cancerous). For the training data the LDA model only one misclassified one spectrum out of 489 spectra (overall 99.8% successful with classification). For the classification data three spectra were incorrectly classified (overall correct classification rate of 98.4%) by the LDA model.

5.4 - Practical Protocols for Cancer diagnosis Using Spectral Mapping

The general process for the use of spectral mapping for cancer diagnosis is; the collection of high fidelity spectra, the pre-processing of spectra, and the reliable classification of spectra. In this section the important results gathered in this chapter will be summarised and some of the practical issues associated with applying spectral mapping to cancer diagnosis will be addressed (such as spectral reproducibility and patient-to-patient spectral variations).

Firstly spectral maps will typically have to be collected with measurement parameters that ensure meaningful biochemical information can be extracted from each spectrum. These measurement parameters (discussed in section 5.1) are a spectral resolution of approximately 4cm^{-1} , a (diffraction limited) spatial resolution of approximately $10\mu\text{m}$ and a good SNR (greater than 10 is desirable). Also if spectral mapping is being considered for application in a clinical environment (such as whilst a patient is on the operating table) then the data collection rate would have to be on the order of a few minutes for an entire spectral map. Clearly this combination of measurement parameters using an existing (thermal source) single channel FTIR spectrometer technology is not practical proposition for a clinical environment.

Next each spectrum in the spectral maps will need to be pre-processed to correct for various spectral artefacts such as; pixel-to-pixel baseline variations from sample scattering, spectral features arising from alien components (such as paraffin, CO₂ or water vapour), instrument drift and dispersion artefacts (section 2.3.3). As an aside it may be worth mentioning that once these artefact corrections have been applied the *reproducibility* of a spectrum (after artefact correction) could be tested for by evaluating the variation in the corrected IR spectra (from the same sample region) which have been collected from both different IR spectrometers and from the same IR spectrometer at different times. A corrected sample spectrum that is reproducible will be the same, to within an acceptable error margin, irrespective of when and from what spectrometer it was collected from. The size of this acceptable error margin would depend on the sensitivity to variations in the spectra of the subsequent spectra classification method. To the best of the author's knowledge there has not been any standardised spectral mapping protocols described, or reproducibility studies performed, which address the issue of spectral reproducibility.

Finally, algorithms can be developed to recognise a spectrum as belonging to a particular tissue classification. Univariate (such as the measurement of the asymmetric phosphodiester peak) or bivariate (such as the ratio of an RNA peak to a DNA peak) methods have been employed for the tissue discrimination stage with some success in isolated studies [9]. However multivariate algorithms (such as linear discriminant analysis[15]) would obviously offer a superior discriminating ability and be more sensitive to subtle differences between spectra. A survey of the literature can easily uncover a slew of different multivariate pattern recognition algorithms which have been applied to spectroscopic data sets for the purposes of tissue classification [15, 16]. However it seems to the author that the vast majority of these studies internally validate the performance of their particular classification method by partitioning a *single* data set into a training set and a validation set and then use the latter to validate the classification method (as was done in the case study LDA analysis in section 5.3.3.2). Obviously several independent data sets (ideally from initially unclassified tissue section of samples) would provide a more objective evaluation of the accuracy and robustness of a particular classification method. Studies which have verified their classification method internally (with the same data set used to train their classifier) are actually proof-of-principle studies and clearly more extensive multi-patient / multi-centre studies are required for full clinical acceptance. An *extensive* (which enough samples to be clinically relevant) study which compares the spectral variations between the same tissue classifications from different patients (for example epithelium tissue classifications from different patients) to those spectral variations arising between different tissue classifications would be useful as a first step towards understanding how

spectral mapping can be applied in a clinical setting but, to the best of the author's knowledge, work of this nature not been published.

To summarise the problems identified with the application of spectral mapping to cancer diagnosis are: the FTIR instrumentation is unable to provide high enough quality spectral data on a time scale that is acceptable for cancer diagnostics; non-existent standard protocols for the pre-processing of IR spectra which would ensure spectral reproducibility; robust classification that is statistically significant for multi-patient / multi-centre throughput.

1. Smith, B.C., *Fundamentals of Fourier Transform Infrared Spectroscopy*. 1996: CRC Press.
2. Wang, T.D., et al., *Detection of Endogenous Biomolecules in Barrett's Esophagus by Fourier Transform Infrared Spectroscopy*. PNAS, 2007. **104**(40): p. 15864-15869.
3. Diem, M., et al., *Comparison of Fourier transform Infrared (FTIR) Spectra of Individual Cells Acquired Using Synchrotron and Conventional Sources*. Infrared Physics & Technology, 2004. **45**: p. 331-338.
4. Bhargava, R. and I.W. Levin, *Spectrochemical Analysis Using Infrared Multichannel Detectors*. 2005, Blackwell Publishing. p. 7.
5. Bhargava, R. and I.W. Levin, *Spectrochemical Analysis Using Infrared Multichannel Detectors*. 2005, Blackwell Publishing. p. 92-93.
6. Bu, D., et al., *Enhancement of Infrared Spectral Images for Maximizing Chemical Information by Minimizing Baseline Interferences*. Applied Spectroscopy, 2005. **59**(5): p. 575-583.
7. Wong, P.T., E.D. Papavassiliou, and B. Rigas, *Phosphodiester Stretching Bands in the Infrared Spectra of Human Tissues and Cultured Cells*. Applied Spectroscopy, 1991. **45**(9): p. 1563-1567.
8. Maziak, D.E., et al., *Fourier-Transform Infrared Spectroscopic Study of Characteristic Molecular Structure in Cancer Cells of Oesophagus: An Exploratory Study*. Cancer Detection and Prevention, 2007. **31**(3): p. 244-53.
9. Mordechai, S., et al., *Possible Common Biomarkers from FTIR microspectroscopy of Cervical Cancer and Melanoma*. Journal of Microscopy, 2004. **215**(215): p. 86-91.
10. Sahu, R.K. and S. Mordechai, *Fourier Transform Infrared Spectroscopy in Cancer Detection*. Future Medicine, 2005. **1**(5): p. 635-647.
11. Lasch, P. and J. Kneipp, *Biomedical Vibrational Spectroscopy*. 2008, Wiley-Interscience. p. 144.
12. Chiriboga, L., H. Yee, and M. Diem, *Infrared Spectroscopy of Human Cells and Tissue. Part VI: A Comparative Study of Histopathology and Infrared Microspectroscopy of Normal, Cirrhotic, and Cancerous Liver Tissue*. Applied Spectroscopy, 2000. **54**(1): p. 1-8.
13. Kendall, C., et al., *Vibrational Spectroscopy: A Clinical Tool for Cancer Diagnostics*. The Royal Society of Chemistry, 2009. **134**: p. 1029-1045.
14. Cytospec. Available from: <http://www.cytospec.com/>.
15. Mansfield, J.R., et al., *LDA-Guided Search Engine for the Nonsubjective Analysis of Infrared Microscopic Maps*. Applied Spectroscopy, 1999. **53**(11): p. 1323-1330.
16. McIntosh, L.M., et al., *Analysis and Interpretation of Infrared Microscopic Maps: Visualisation and Classification of Skin Components by Digital Staining and Multivariate Analysis*. Biospectroscopy, 1999. **5**(5): p. 265-275.

6.0 - Analysis of Spectral Maps from the OPG and QCL Imaging Systems

In this chapter the spectral maps generated from the OPG and QCL imaging systems are analysed. For the OPG imaging system it is shown that the image pixel values in units of absorbance will have an approximate uncertainty in the absorbance (δA_{OPG}) of 0.03 which gives a signal to noise ratio of approximately 2 which is too low to provide any numerical information. For the QCL imaging system it is shown that the uncertainty in the absorbance (δA_{QCL}) is 0.002 which gives a signal to noise ratio of approximately 30. The higher SNR of the QCL imaging system (relative to the OPG imaging system) gives it more potential to be used to extract biochemical information from biological samples and used in cancer diagnosis.

6.1 - Analysis of OPG data

In section 6.1 the results from the OPG imaging system are presented. Firstly the method of extracting absorbance data from the OPG imaging instrument is summarised. Secondly a description of the noise associated with the OPG imaging system and methods to estimate the uncertainty in an absorbance measurement are discussed. Next a spectral map generated by the OPG imaging system is compared to a spectral map generated from the Jasco FTIR spectrometer. Finally the best diagnostic data from the OPG imaging system is presented.

6.1.1 - Extracting Absorbance Values from OPG Imaging System Data

Spectral maps generated using the OPG imaging system was collected using the set-up shown in figure 4.32. Several provisions were made to ensure the data collected could be used for quantitative analysis: The beam coherence was destroyed (to remove optical artefacts) by placing a diffuser in the beam path to randomise the phase (section 4.9). The pulse-to-pulse beam intensity variations were mitigated by dividing each image by a reference channel intensity measurement (section 4.10). Spatial inhomogeneities in each OPG pulse were mitigated by averaging over several images. Individual detector disparities in the Cedip IR camera were corrected for using a LNUC (section 4.6.4.1) and a PNUC (section 4.6.4.3). Detector saturation was accounted for by applying the data binning algorithm (section 4.10.4).

The absorbance data collection method (for each wavelength) was as follows;

- 1) A LNUC was set-up on the camera.
- 2) Typically 500 images were collected from the sample and 500 images were collected from the OPG background (section 4.12.2.1). The data collection time for 500 images was

approximately 3 minutes (3 per second). The total (sample and OPG background data sets) data file size was approximately 50MB.

- 3) The resting pixel values (RPVs) from the Cedip IR camera were also measured and deducted from all of the sample and OPG background images (section 4.6.6.1).
- 4) The PNUC was applied to all the OPG background and sample images.
- 5) The sample and OPG background data was passed through the data binning algorithms (saturation and time constant binning algorithms) leaving between 40 and 200 images for each of the sample and the OPG background data sets.
- 6) Each of the remaining individual images (sample and OPG background) were divided by their corresponding reference channel measurements.
- 7) Both the average sample and average OPG background images were calculated resulting in two average images; one sample and one OPG background.
- 8) The absorbance values for the data was calculated using equation 6.1. where x, y are the pixel coordinates of the images

$$A(x, y)_{OPG} = -\log_{10} \left[\frac{\text{sample image}(x, y)}{\text{OPG background image}(x, y)} \right] \quad (6.1)$$

6.1.2 - The Uncertainty of Absorbance Data from the OPG Imaging System

In this section (6.1.2) two alternative methods of estimating the uncertainty (or noise) in the absorbance pixel values obtained from the OPG imaging system will be discussed. Firstly an analysis of the uncertainty in the sample and OPG background images will be described and those uncertainties will be propagated through equation 6.1 to calculate the uncertainty in the absorbance pixel values. Secondly an absorbance measurement using the OPG imaging system will be repeated several times to evaluate the reproducibility of absorbance measurements using the OPG imaging system and to estimate the absorbance uncertainty. In both cases the uncertainty in the absorbance pixel values ($\delta A(x, y)_{OPG}$) is estimated to be approximately 0.03.

6.1.2.1 - Estimation of Absorbance Uncertainty using Error Analysis

In section 4.12.2.2 the total noise present in an image collected with the OPG imaging system was characterised by measuring the pixel uncertainties (equation 4.25) from the OPG background images. It was determined that: firstly the source noise is the primary source of noise in a

measurement made with the OPG imaging system; Secondly, as a rough estimate, the % uncertainty for each pixel value in an OPG background image is 5%.

A similar analysis to section 4.12.2.2 has been performed for an example sample image (500 shots taken at $6.6\mu\text{m}$, the LNUC and PNUC applied, the RPVs were deducted, the data binning algorithms applied and each shot divided by its corresponding reference value). In Figure 1 the mean pixel values for the sample image are shown (original data values 263 to 368 with threshold BPR limiting the pixel range from 77 to 200 replacing 1.2% of the pixels). Figure 2 shows the uncertainty (calculated using equation 4.25) in the pixel values of the sample image (original data values 0.3 to 32.6 with threshold BPR limiting the pixel range from 2.8 to 7.9 replacing 4.4% of the pixels). Figure 3 shows the % uncertainty in pixel values of the sample image (original data values -455% to 69% with threshold BPR limiting the pixel range from 3% to 5.5% replacing 0.6% of the pixels).

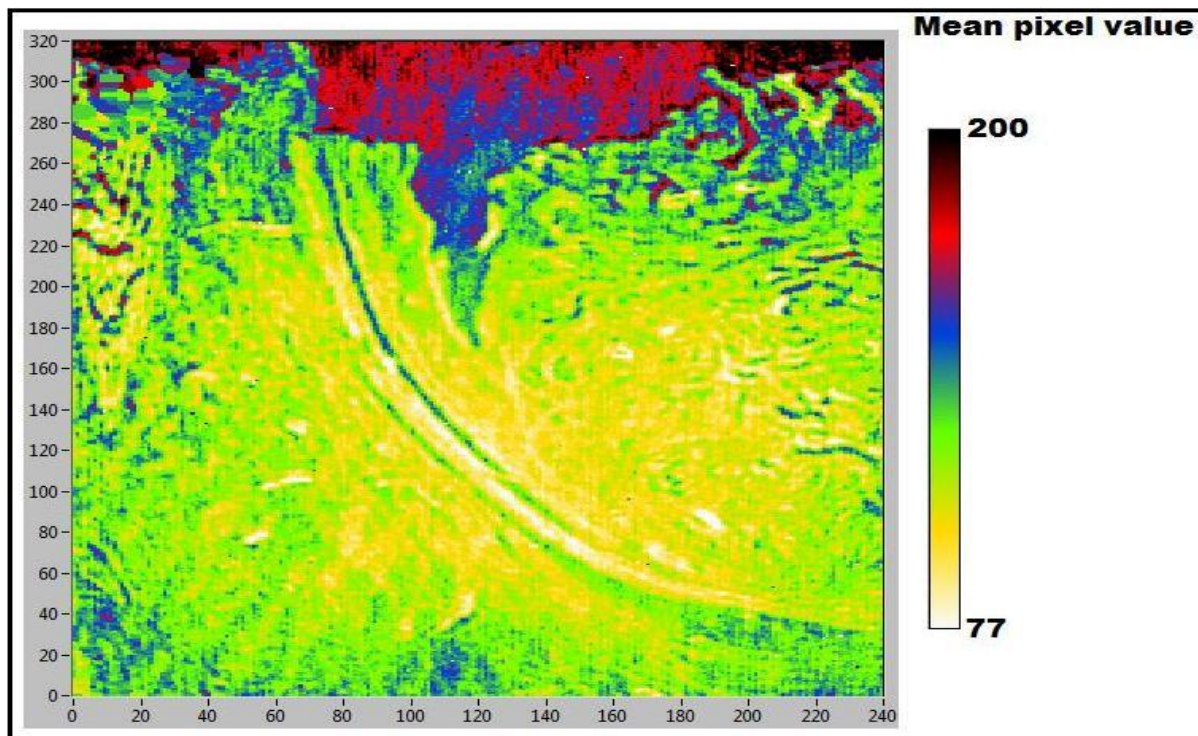


Figure 1. Mean pixel values for a representative sample image taken at $6.6\mu\text{m}$. The original pixel values of the image ranged from 263 to 368 but a threshold BPR was applied which limited the pixel range from 77 to 200 (replacing 1.2% of the pixels).

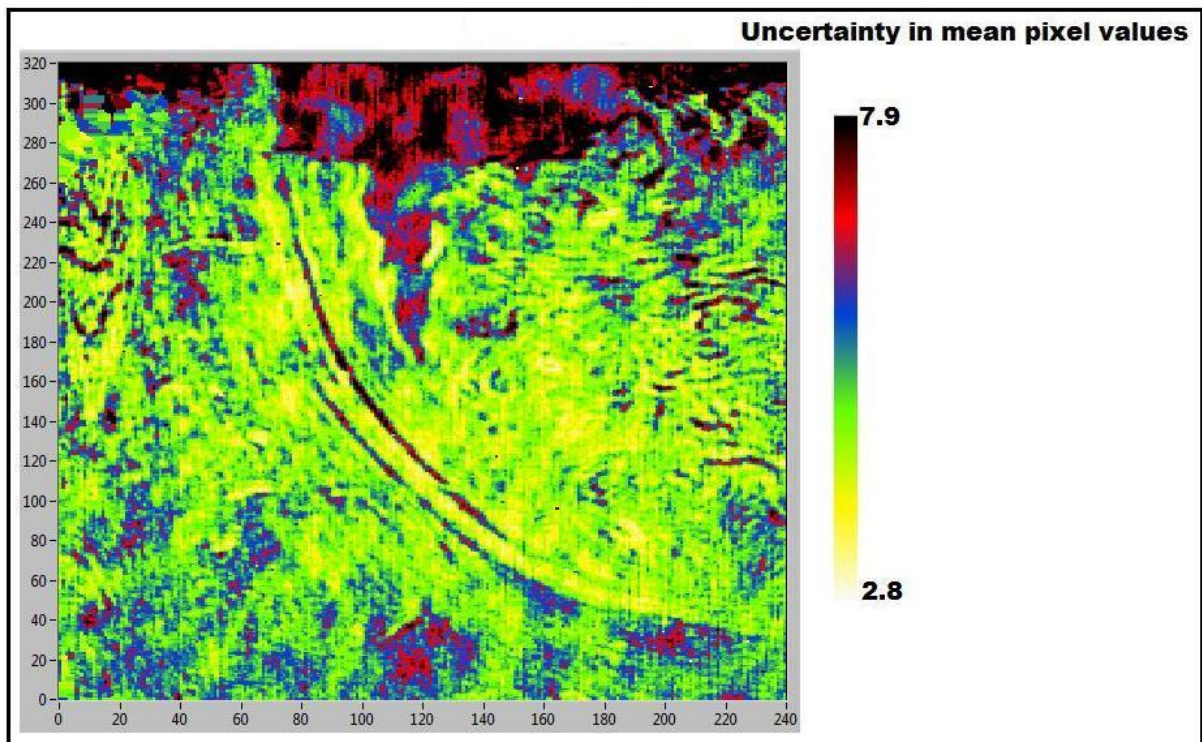


Figure 2. Pixel uncertainty values for representative sample image taken at a wavelength of $6.6\mu\text{m}$. The original had pixel values from 0.3 to 32.6 but with threshold BPR applied the pixel range was limited from 2.8 to 7.9 (replacing 4.4% of the pixels).

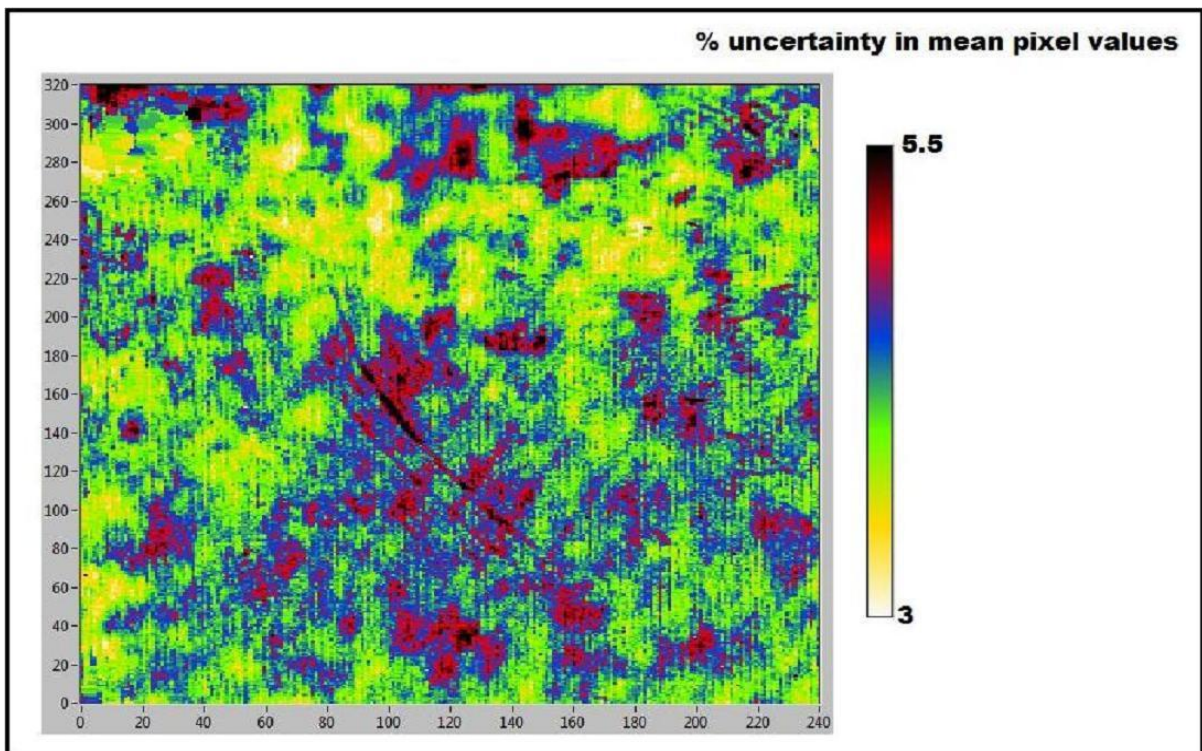


Figure 3. Pixel % uncertainty values for representative sample image taken at $6.6\mu\text{m}$. The original pixel values ranged from -455 to 69 but a threshold BPR was applied limiting range from 3% to 5.5% (replacing 0.6% of the pixels).

From figures 2 and 3 a couple of observations can be made;

- 1) The % uncertainty in the sample pixel values is approximately 5% (same as the OPG background images).
- 2) The pixel uncertainty image (figure 2) provides a contrast mechanism for the sample. This implies that the uncertainty in the pixel values is proportional to the mean pixel value. The physical interpretation of this phenomenon is that the *source noise is proportional to the intensity of the OPG beam*.

Using error analysis the uncertainty in the absorbance pixel values, δA_{OPG} , can be estimated as $\delta A_{\text{OPG}} = 0.03$ (assuming a % uncertainty of 5% in the sample and OPG background pixel values, see appendix 1 for the derivation). Therefore the % uncertainty in the absorbance pixel values will range from approximately 25% to 75% (for absorbance values of 0.12 and 0.04 respectively).

6.1.2.2 - Estimation of Absorbance Uncertainty using Repeated Measurements

An alternative way to estimate the uncertainty in the absorbance pixel values, δA_{OPG} , is to repeat an absorbance measurement several times and compare the measurements. Figure 4 shows the distribution of the measured absorbance values, averaged over the entire array (or image), obtained from 8 repeated measurements at a wavelength of $6.5\mu\text{m}$. Here we see that the absorbance values span 0.09 to 0.17 (range of 0.08) giving an average of 0.12 and a standard error of 0.03. The standard error in this case gives an indication of the uncertainty in the absorbance, therefore $\delta A_{\text{OPG}} \approx 0.03$, which is in agreement with the absorbance uncertainty calculated in section 6.1.2.1 using the error propagation method.

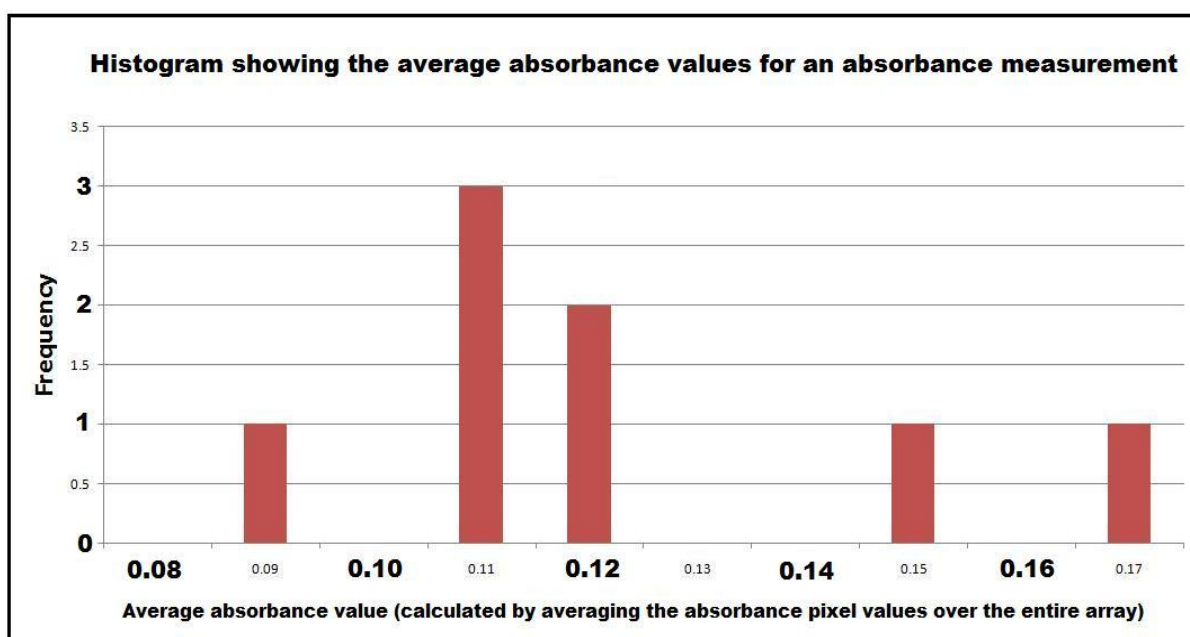


Figure 4. Histogram showing the absorbance value reproducibility from the OPG imaging system. An absorbance measurement was repeated 8 times and the average absorbance value for each measurement (calculated by averaging the absorbance pixel values over the entire array) was determined.

6.1.3 - Comparison of Spectral Maps from OPG Imaging System and Jasco FTIR Spectrometer

In order to evaluate the ability of the OPG imaging system to extract spectroscopic information it is useful to compare a spectral map generated by the OPG imaging system to a spectral map generated by the Jasco FTIR spectrometer. Both of the spectral maps were collected from the *same* tissue section. An H and E stain of the tissue section used to collect the spectral maps from is shown in Figure 5.

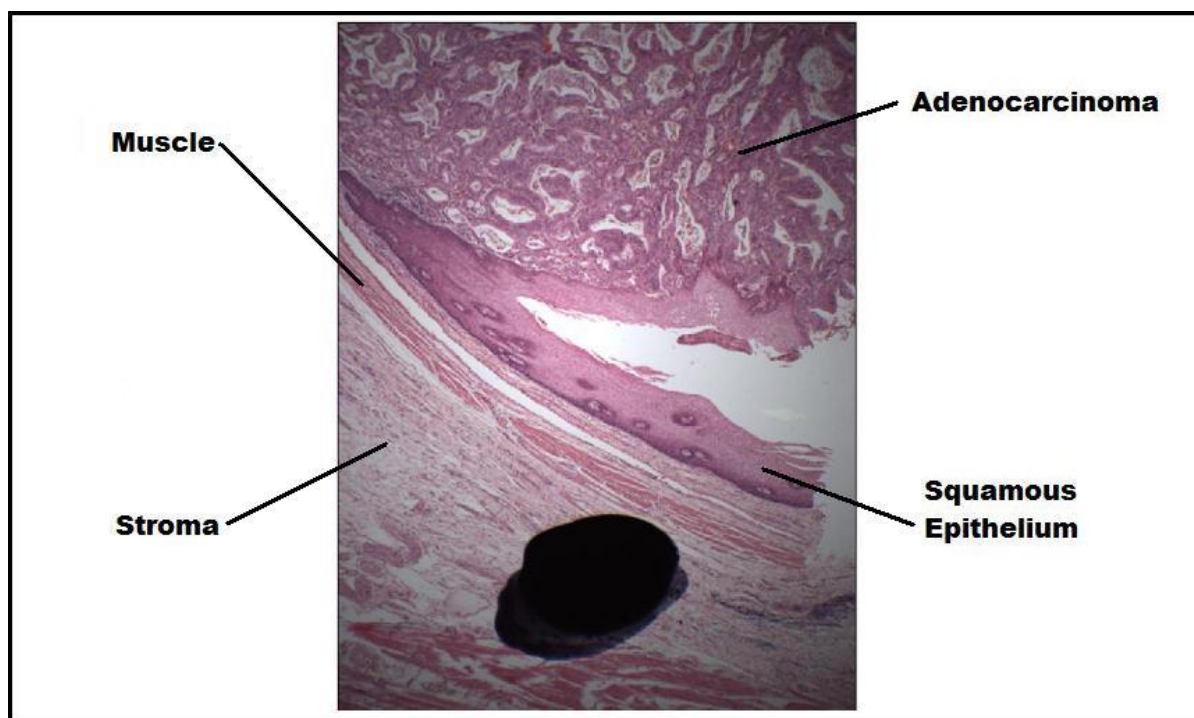


Figure 5. H and E stain of biological tissue (human oesophagus) section which has regions of healthy tissue (squamous epithelium, muscle and stroma) and regions of adenocarcinoma. The black spot is a blot of ink used as a reference point.

Two spectral maps were collected, one using the Jasco FTIR spectrometer (using an aperture size of $50\mu\text{m}$ by $50\mu\text{m}$, a spectral resolution of 4cm^{-1} and a wavelength range from $2.5\mu\text{m}$ to $11.1\mu\text{m}$), and one the using the OPG imaging system (using a pixel limited optical set-up of $15\mu\text{m}$ by $15\mu\text{m}$, a spectral resolution of approximately 20cm^{-1} and a wavelength range of $6.5\mu\text{m}$ to $8.4\mu\text{m}$). The spectral map collected with the single channel FTIR spectrometer took 18 hours to collect (primarily due to use of a single channel detection scheme rather than the use of an array detector) and the image collected with the OPG imaging system took 10 minutes. Two chemical images (using the amide II spectral feature at $6.5\mu\text{m}$) were generated from these spectral maps and are shown in Figure 6.

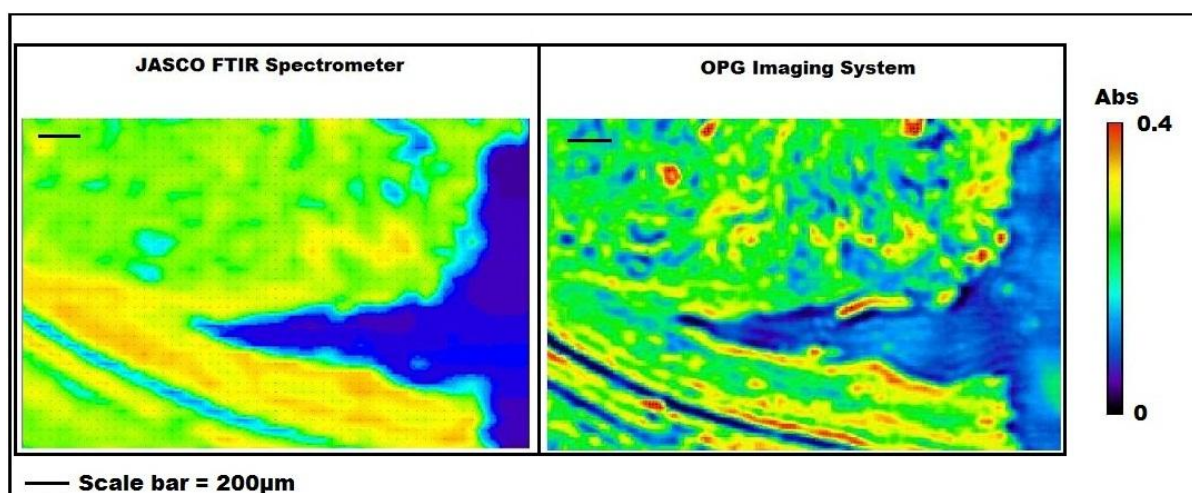


Figure 6. Comparison chemical images from the OPG imaging system and from the Jasco FTIR spectrometer. Both chemical images were collected from the same sample (human oesophagus tissue section with adenocarcinoma and squamous epithelium tissue classifications). The chemical image from the FTIR spectrometer was collected using an aperture size of $50\mu\text{m}$ by $50\mu\text{m}$, a spectral resolution of 4cm^{-1} at the amide II peak ($6.5\mu\text{m}$). The chemical image from the OPG imaging system was collected using a pixel limited optical set-up of $15\mu\text{m}$ by $15\mu\text{m}$, a spectral resolution of approximately 20cm^{-1} at the amide II peak ($6.5\mu\text{m}$).

In order to compare the spectroscopic information collected by the OPG imaging system and the FTIR spectrometer two average spectra were extracted from the region classified as adenocarcinoma tissue (by Bill Otto, a histopathologist at CRUK). Figure 7 shows the regions where the spectra in the spectral maps was collected from. In the case of the spectral map from the FTIR spectrometer 364 spectra were averaged in the region indicated in Figure 7. In the case of the OPG imaging system 3956 spectra were averaged in the region indicated in Figure 7.

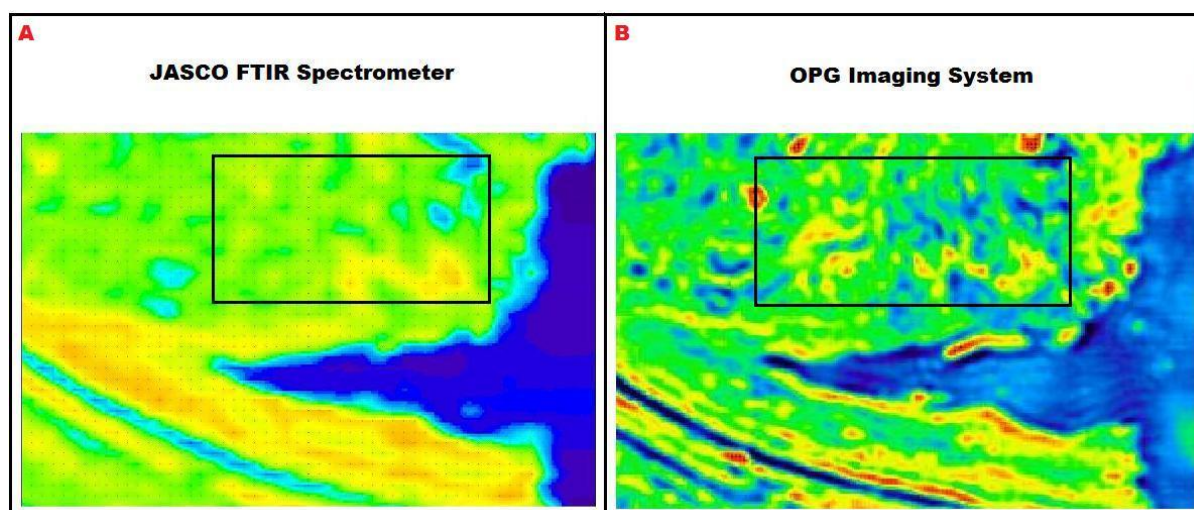


Figure 7. Picture showing regions where adenocarcinoma spectra were collected from in A) The spectral map collected with the Jasco FTIR spectrometer B) The spectral map collected with the OPG imaging system.

Figure 8 compares the spectrum generated from the FTIR spectrometer to the spectrum generated from the OPG imaging system by averaging the spectra collected from the sample regions identified in Figure 7. The error bars associated with an absorbance measurement from the OPG imaging system have also been included to quantify the agreement of these spectra. It can clearly be seen that the size of the uncertainty in the absorbance values (on average around 50% giving a SNR of 2, equation 4.29) makes quantitative analysis using data sets generated by the OPG imaging system, in its current configuration, very challenging.

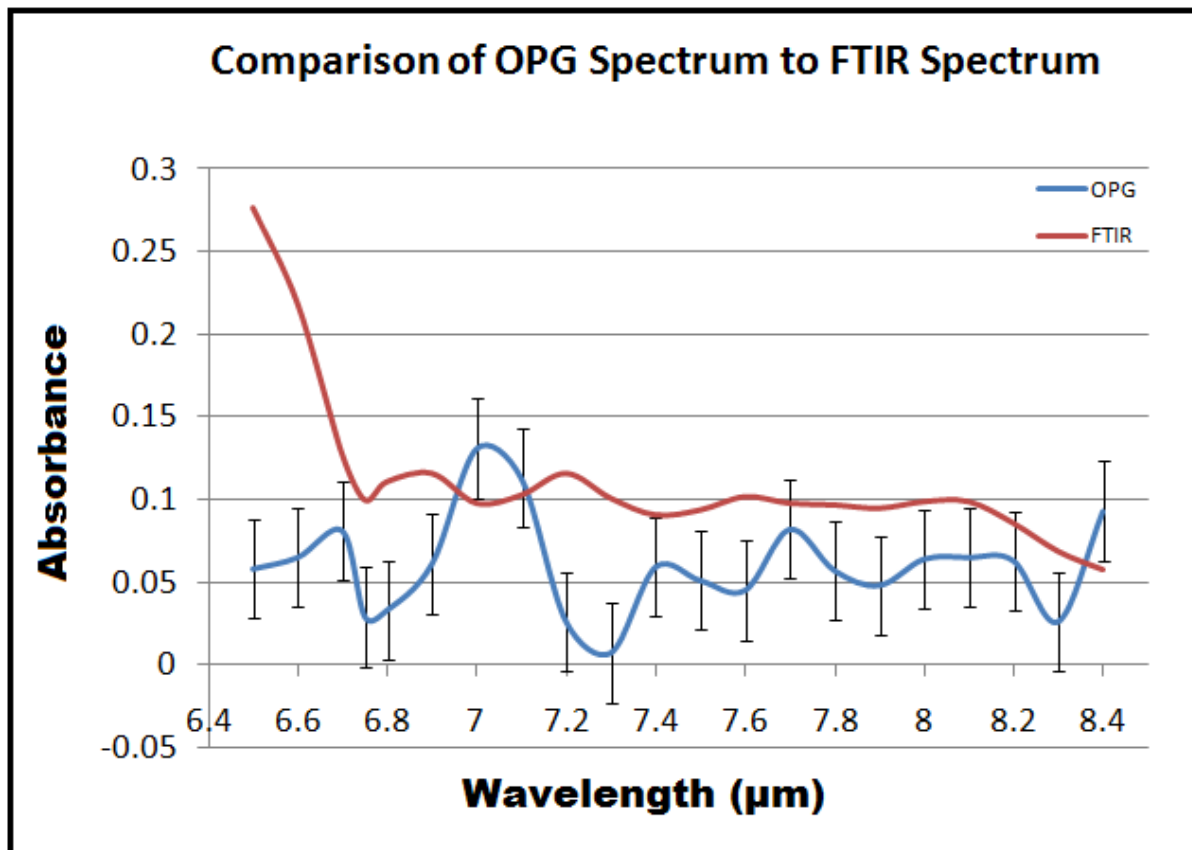


Figure 8. Comparison of OPG Spectrum to FTIR Spectrum. The spectra were both collected from the same sample in a region classified as adenocarcinoma (by Bill Otto, histopathologist at CRUK).

6.1.4 - OPG Imaging System Images and their Application to Cancer Diagnosis

In the previous section (6.1.3) it has been shown that the spectral information collected with the OPG imaging system is of low quality (large uncertainty in absorbance values). The primary cause of the inability of the OPG imaging system to produce high quality spectral data has been identified as the source noise (section 4.12.2.2) caused by the pulse-to-pulse instability of the OPG source. It is the author's observation that, given that the OPG source is an extremely temperamental and

unstable source whose output characteristics have been seen to fluctuate over the course of this research, it is not possible to make a generalisation about OPG sources in *general*. All that can be observed is that the particular OPG source used in these experiments - indeed the particular OPG source used in these experiments at the particular time that these measurements were collected - was not able to be used to generate high quality spectroscopic data. Past studies using this OPG source show some evidence of being able to extract spectroscopic information but have made no detailed analysis of the quality of the spectroscopic information obtained[1]. Therefore the author must conclude that the spectroscopic information collected in the study by Amrania et al was achieved with the OPG source when it was operating in a more stable configuration, or that the result was fortuitous.

The OPG imaging system was used to collect spectral maps from a tissue section (section A) containing healthy tissue (stroma, muscle and squamous epithelium) and adenocarcinoma (figure 5) and a tissue section (section B) containing healthy tissue (squamous) and diseased tissue (low and high grade)(Figure 9).

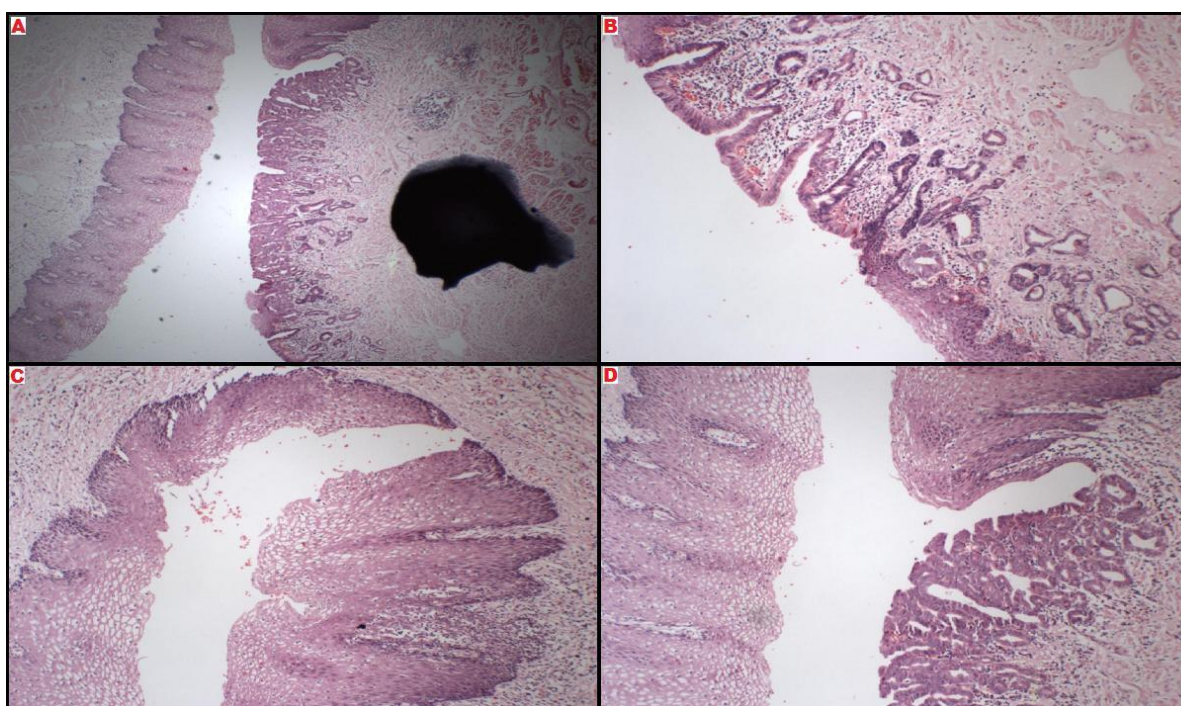


Figure 9. H and E stain of oesophagus tissue - Small sections of the sample at high magnification. A) Squamous and high grade B) Low grade and squamous C) Squamous D) Squamous and high grade

Example chemical images taken with the OPG imaging system (using a pixel limited optical set-up of 15 μ m by 15 μ m) are shown for section A (Figure 10) and section B (Figure 11).The reader should note

that the histopathological images in Figure 9 are indeed from the same sample as shown in the chemical image in Figure 11 but the four histopathological images are just arranged in a slightly confusing way.

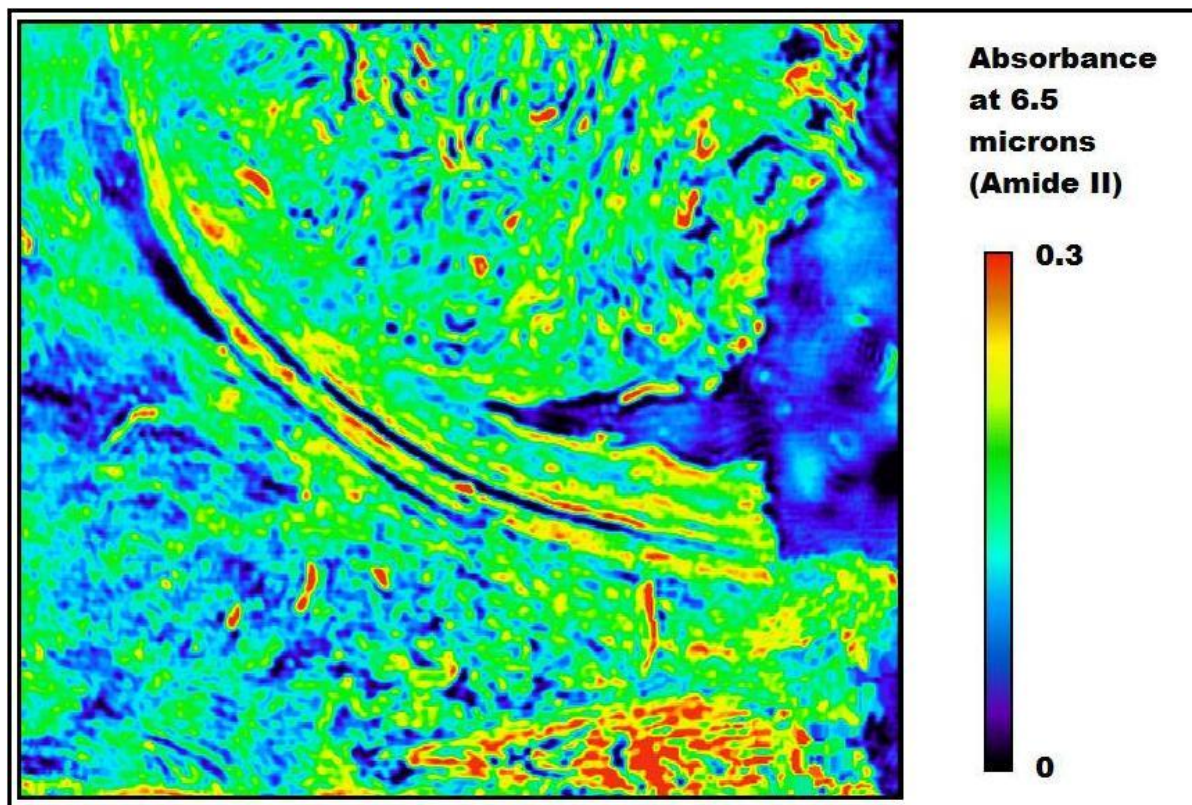


Figure 10. Chemical image taken with the OPG imaging system at 6.6 μ m (amide II) of a sample containing normal and cancerous tissue. The pixels are in units of absorbance. The image has threshold BPR applied limiting the pixel values from 0 to 0.3. The system is pixel limited at 15 μ m by 15 μ m and the field of view of the image is 3.6mm by 4.8mm

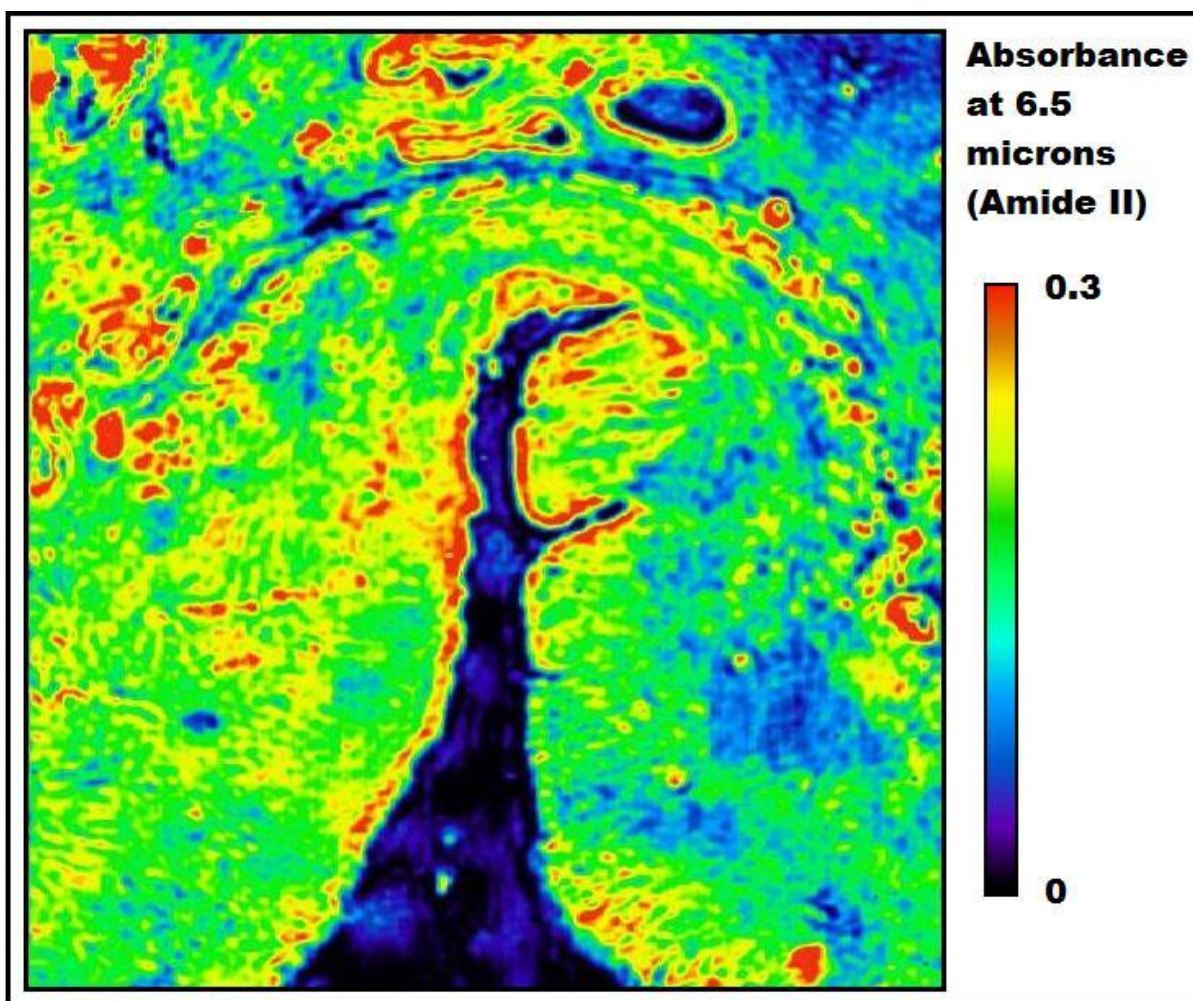


Figure 11. Chemical image taken with the OPG imaging system at 6.6 μ m (amide II) of a sample containing normal, low grade cancerous, and high grade cancerous tissue. The pixels are in units of absorbance. The image has threshold BPR applied limiting the pixel values from 0 to 0.3. The system is pixel limited at 15 μ m by 15 μ m and has a field of view of 3.6mm by 4.8mm.

Figures 10 and 11 demonstrate the capacity for the OPG imaging system to generate chemical images with improved morphological information with respect to the conventional (single channel) FTIR chemical images (as a result of the wide fields of view and high spatial resolution attainable). However the large amount of noise present in the images ($SNR \approx 2$) reduces the reliability of numerical information extracted from these images to unacceptable levels. Furthermore the generation of spectroscopic images (which combine several images) is impractical since the noise problem is compounded. For example to generate a ratio image using two images each with a noise level of 50% would give a ratio image with a noise level of 71%.

6.2 - Analysis of QCL data

In section 6.2 the results from the QCL imaging system are presented. Section 6.2 will proceed in a similar fashion to section 6.1 firstly the method of extracting absorbance data from the QCL imaging

instrument is summarised. Secondly a description of the noise associated with the QCL imaging system and methods to estimate the uncertainty in an absorbance measurement are discussed. Next a spectral map generated by the QCL imaging system is compared to a spectral map generated from the Jasco FTIR spectrometer. Finally the best diagnostic data from the QCL imaging system is presented.

6.2.1 - Extracting Absorbance Values from QCL Imaging System Data

Spectral maps generated using the QCL imaging system was collected using the set-up shown in figure 4.33. To ensure the data collected could be used for quantitative analysis: The beam coherence was destroyed (to remove optical artefacts) by placing a diffuser in the beam path to randomise the phase. Spatial inhomogeneities in each QCL pulse were mitigated by averaging over several images (100). Individual detector disparities in the Cedip IR camera were corrected for using a NLNUC (section 4.6.4.2) and a PNUC (section 4.6.4.3.1). Detector saturation was accounted for by using a 40% attenuation filter (section 4.11). The variable pulse data binning algorithm was applied to reduce the noise contributions from a variable number of pulses reaching the Cedip camera from the QCL (section 4.11.3)

The absorbance data collection method (for each wavelength) was as follows;

- 1) A NLNUC was set-up on the camera.
- 2) Typically 100 images were collected from the sample and 100 images were collected from the QCL background (section 4.13.1.1). The data collection time for 100 images was approximately 1 second (camera set to 100Hz). The total (sample and QCL background data sets) data file size was approximately 10MB.
- 3) The resting pixel values (RPVs) from the Cedip IR camera were also measured and deducted from all of the sample and QCL background images (section 4.6.6.1).
- 4) The PNUC was applied to all the QCL background and sample images.
- 5) The variable pulse data binning algorithm was applied to both the QCL background and sample images
- 6) Both the average sample and average QCL background images were calculated resulting in two average images; one sample and one QCL background.
- 7) The absorbance values for the data were calculated using equation 6.2. where x, y are the pixel coordinates of the images

$$A(x,y)_{QCL} = -\log_{10} \left[\frac{\text{sample image}(x,y)}{QCL \text{ background image}(x,y)} \right] \quad (6.2)$$

6.2.2 - The Uncertainty of Absorbance Data from the QCL Imaging System

As in section 6.1.2 in this section two alternative methods of estimating the uncertainty (or noise) in the absorbance pixel values obtained from the QCL imaging system will be discussed. Firstly it will be assumed that the uncertainty in the sample images is the same as the uncertainty in the background images (this assumption was verified for the OPG imaging system) and error analysis will be used to estimate the uncertainty in the absorbance pixel values from the QCL imaging system. Secondly an absorbance measurement using the QCL imaging system will be repeated several times to evaluate the reproducibility of absorbance measurements using the OPG imaging system and to estimate the absorbance uncertainty. In both cases the uncertainty in the absorbance pixel values ($\delta A(x,y)_{QCL}$) is estimated to be approximately 0.002 – 0.003.

6.2.2.1 - Estimation of Absorbance Uncertainty using Error Analysis

In section 4.13.1.2 the total noise present in an image collected with the QCL imaging system was characterised by measuring the pixel uncertainties (equation 4.25) from the QCL background images. It was determined that, as a rough estimate, the % uncertainty for each pixel value in an OPG background image is 0.3%.

If we assume that the sample images also have a 0.3% uncertainty in their pixel values then, using error analysis (see appendix 1 for a similar derivation), the uncertainty in the absorbance pixel values, δA_{QCL} , can be estimated as $\delta A_{QCL} = 0.002$. Therefore the % uncertainty in the absorbance pixel values will range from approximately 2% to 5% (for absorbance values of 0.12 and 0.04 respectively).

6.2.2.2 - Estimation of Absorbance Uncertainty using Repeated Measurements

An alternative way to estimate the uncertainty in the absorbance pixel values from the QCL imaging system, (δA_{QCL}), is to repeat an absorbance measurement several times and compare the measurements. Figure 12 shows the distribution of the measured absorbance values, averaged over the entire array (or image), obtained from 10 repeated measurements at a wavelength of 8.1 μ m. Here we see that the absorbance values span 0.11 to 0.14 (range of 0.03) giving an average of 0.125 and a standard error of 0.003. The standard error in this case gives an indication of the uncertainty in the absorbance, therefore $\delta A_{OPG} \approx 0.003$, which is slightly higher than the absorbance uncertainty calculated in section 6.2.2.1 using the error propagation method. The discrepancy between the two

absorbance uncertainty values for the QCL imaging system is due to an overestimation of the % uncertainty in the sample and QCL background images for 8.1 μm which is closer to 0.2% than 0.3% (see Figure 55 in chapter 4).

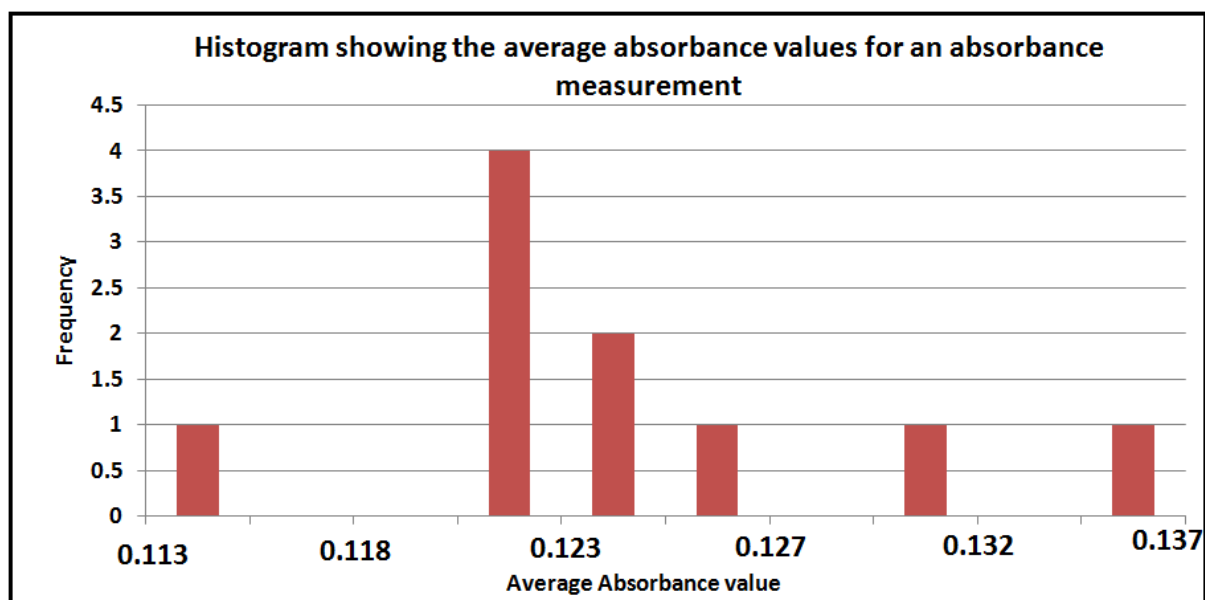


Figure 12. Histogram showing the absorbance value reproducibility from the QCL imaging system. An absorbance measurement was repeated 10 times and the average absorbance value for each measurement (calculated by averaging the absorbance pixel values over the entire array) was determined.

6.2.3 - Comparison of Spectral Maps from QCL Imaging System and Jasco FTIR Spectrometer

In this section a spectral map collected with the QCL imaging system is compared to a spectral map generated by the Jasco FTIR spectrometer. Both of the spectral maps were collected from the *same* tissue section. An H and E stain of the tissue section used to collect the spectral maps from is shown in Figure 5.

Two spectral maps were collected, one using the Jasco FTIR spectrometer (at an aperture size of 50 μm by 50 μm , a spectral resolution of 4 cm^{-1} and a wavelength range from 2.5 μm to 11.1 μm), and one the using the QCL imaging system (25 wavelengths using a pixel limited system of 10 μm by 10 μm and a wavelength range of 6.25 μm to 9.0 μm). Two chemical images (using the amide II spectral feature at 6.5 μm) were generated from these spectral maps and are shown in Figure 13.

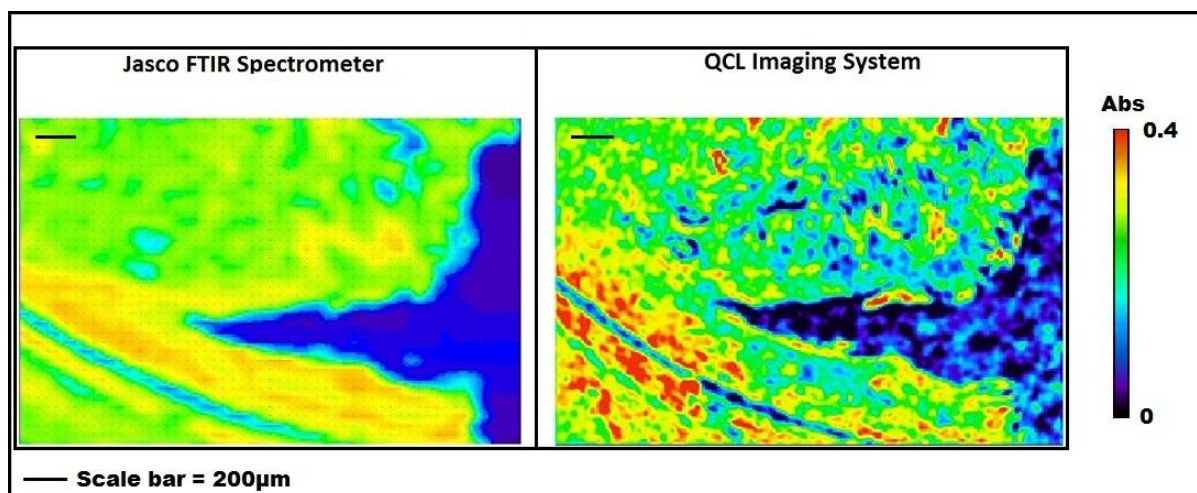


Figure 13. Comparison chemical images from the QCL imaging system and from the Jasco FTIR spectrometer. Both chemical images were collected from the same sample (human oesophagus tissue section with adenocarcinoma and squamous epithelium tissue classifications). The chemical image from the FTIR spectrometer was collected with an aperture size of 50 μm by 50 μm , a spectral resolution of 4 cm^{-1} at the amide II peak (6.5 μm). The chemical image from the QCL imaging system was collected using a pixel limited system of 10 μm by 10 μm at the amide II peak (6.5 μm).

As in section 6.1.3 (where the OPG imaging system is compared to the FTIR) in order to compare the spectroscopic information collected by the QCL imaging system and the FTIR spectrometer two average spectra were extracted from the region classified as adenocarcinoma tissue (by Bill Otto, a histopathologist at CRUK). The same region shown in Figure 7 was used to extract a spectrum from the QCL spectral map and the Jasco FTIR spectrometer spectral map. In the case of the spectral map from the FTIR spectrometer 364 spectra were averaged in the region indicated in Figure 7. In the case of the QCL imaging system 9100 spectra were averaged in the region indicated in Figure 7.

Figure 14 compares the spectrum generated from the FTIR spectrometer to the spectrum generated from the QCL imaging system by averaging the spectra collected from the sample regions identified in Figure 7. The error bars associated with an absorbance measurement from the QCL imaging system have also been included to quantify the agreement of these spectra. Although the two spectra in Figure 14 do not overlap there does seem to be a good agreement between their general shape and it is especially impressive that the amide II peak is very visible in the QCL data. The fact that the two spectra do not overlap may be due to a difference in the collection optics of the two experimental set-ups. Close inspection of the QCL image (in Figure 13) also suggests that there is still an inhomogeneous illumination from the QCL imaging system (evidenced by the structure observed in a spectrally homogenous part of the sample, such as the blue region with no tissue, in the QCL image) possibly caused by speckle effects persisting despite the use of a rotating diffuser.

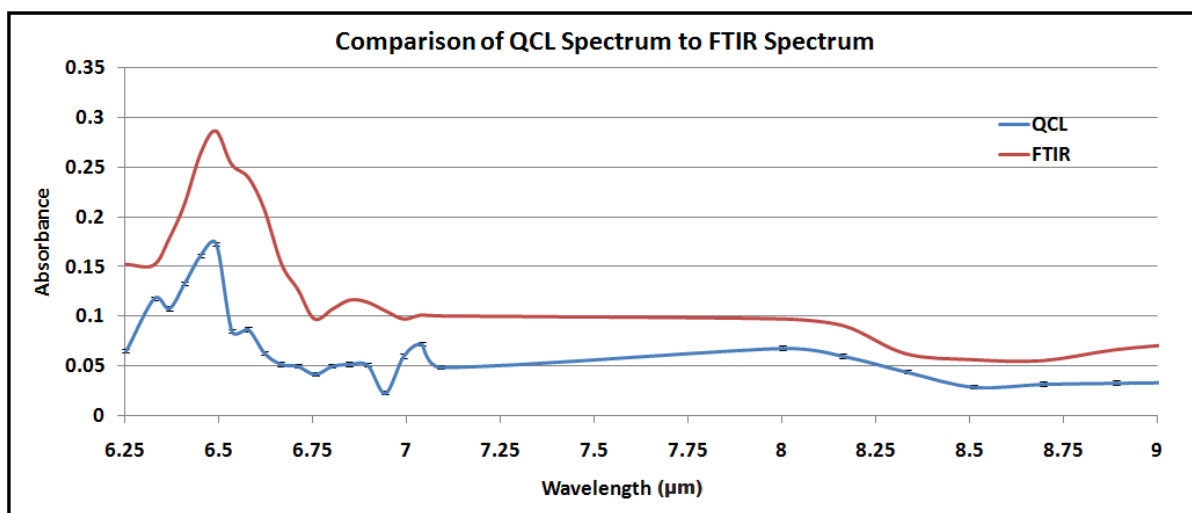


Figure 14. Comparison of QCL Spectrum to FTIR Spectrum. The spectra were both collected from the same sample in a region classified as adenocarcinoma (by Bill Otto, histopathologist at CRUK).

A comparison can also be made of the point spectra (10μm by 10μm sampling size) collected from an adenocarcinoma tissue classification (see Figure 5) from both the Jasco FTIR spectrometer and the QCL imaging system. The comparison will be made by examining chemical images collected from the smaller sampling area shown in Figure 15. Figure 16 shows a comparison of chemical images collected from the Jasco FTIR spectrometer (with an aperture size of 10μm by 10μm) and QCL imaging system (pixel limited at 10μm by 10μm). Figure 17 indicates the positions where point spectra (sampling a region of 10μm by 10μm) were collected from on both the spectral maps.

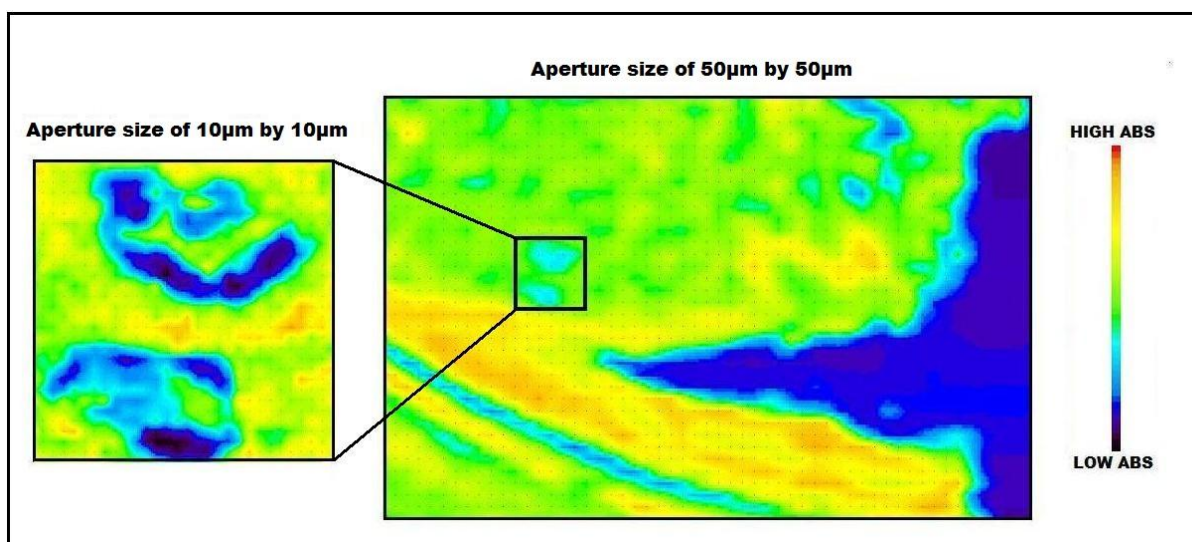


Figure 15. Chemical images (pixel values are the absorbance values at the Amide II peak) of a biological sample collected using a single channel Jasco FTIR spectrometer with different aperture sizes. The larger image on the right was taken using a 50μm aperture size (and a step size of 50μm) and the smaller section (boxed in the picture on right) was taken with a 10μm aperture size (and a step size of 10μm). It can clearly be seen that the image generated using an aperture size of 10μm shows more morphological detail than the image generated using an aperture size of 50μm

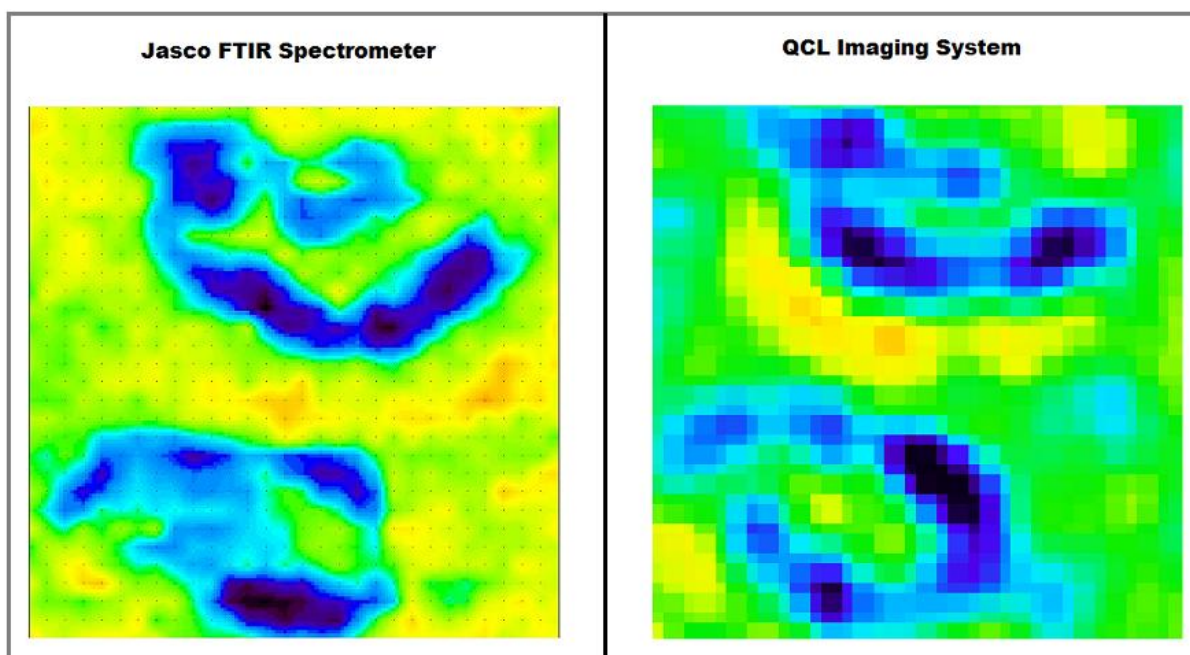


Figure 16. Comparison of chemical images collected using the Jasco FTIR spectrometer (aperture size of $10\mu\text{m}$ by $10\mu\text{m}$) and the QCL imaging system (pixel limited at $10\mu\text{m}$ by $10\mu\text{m}$). The chemical images were collected from the same section of human oesophagus tissue classified as adenocarcinoma by a histopathologist (Bill Otto, CRUK)

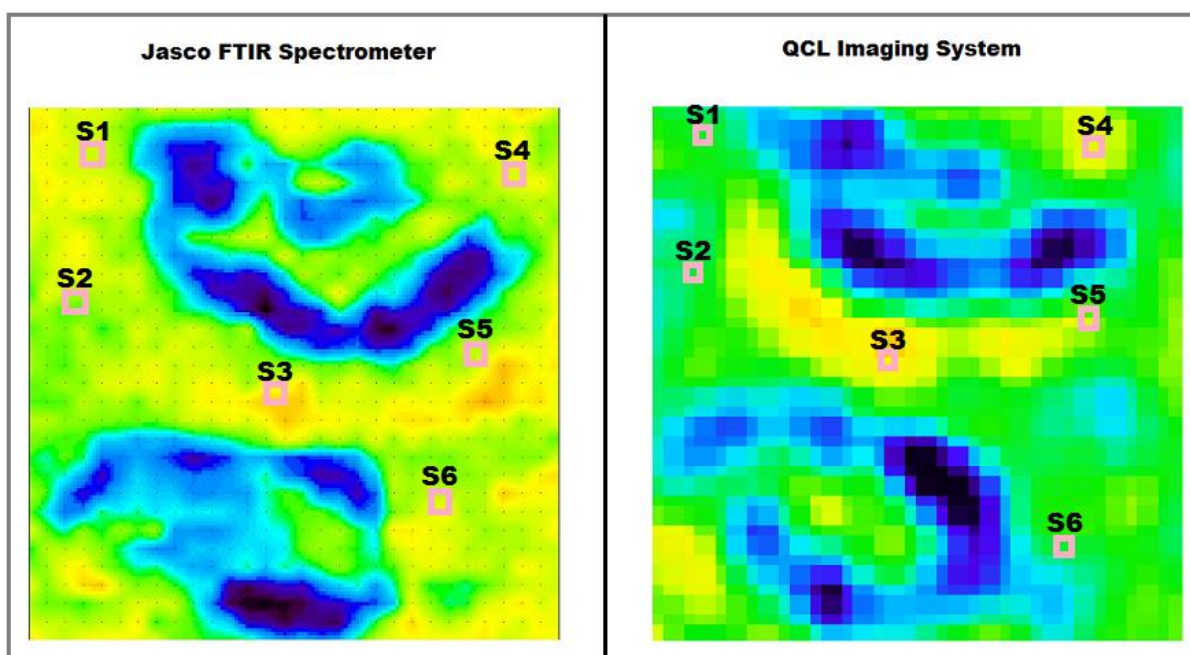


Figure 17. Comparison of chemical images collected using the Jasco FTIR spectrometer (aperture size of $10\mu\text{m}$ by $10\mu\text{m}$) and the QCL imaging system (pixel limited at $10\mu\text{m}$ by $10\mu\text{m}$). The chemical images were collected from the same section of human oesophagus tissue classified as adenocarcinoma by a histopathologist (Bill Otto, CRUK). Point spectra (sampling a region of $10\mu\text{m}$ by $10\mu\text{m}$) were collected from the regions indicated on the chemical images

The point spectra collected from the Jasco FTIR spectrometer spectral map are shown in Figure 18 and the point spectra collected from the QCL imaging system spectral map are shown in Figure 19.

Figures 18 and 19 Demonstrate there is considerable spectral variability between spectra collected from the same tissue classification for both the Jasco FTIR spectrometer and the QCL imaging system. The spectral variability may be caused by noise in the measurements (section 6.2.2), spectral artefacts caused by physical phenomena (such as scattering, detector saturation or, in the case of the QCL imaging system, inhomogeneous illumination), as well as inherent biochemical differences in the sample at different sampling positions. In the case of the point spectra from the FTIR (Figure 18) there does appear to be a sloping baseline which may corrupt the “true” absorbance values. The average spectra (generated by averaging all 6 point spectra from the Jasco FTIR spectrometer and QCL imaging system spectral maps) are shown in Figure 20. In Figure 20 the spectral variability between the point spectra has been quantified by calculating the standard error between the 6 point spectra and representing this spectral variability graphically as error bars.

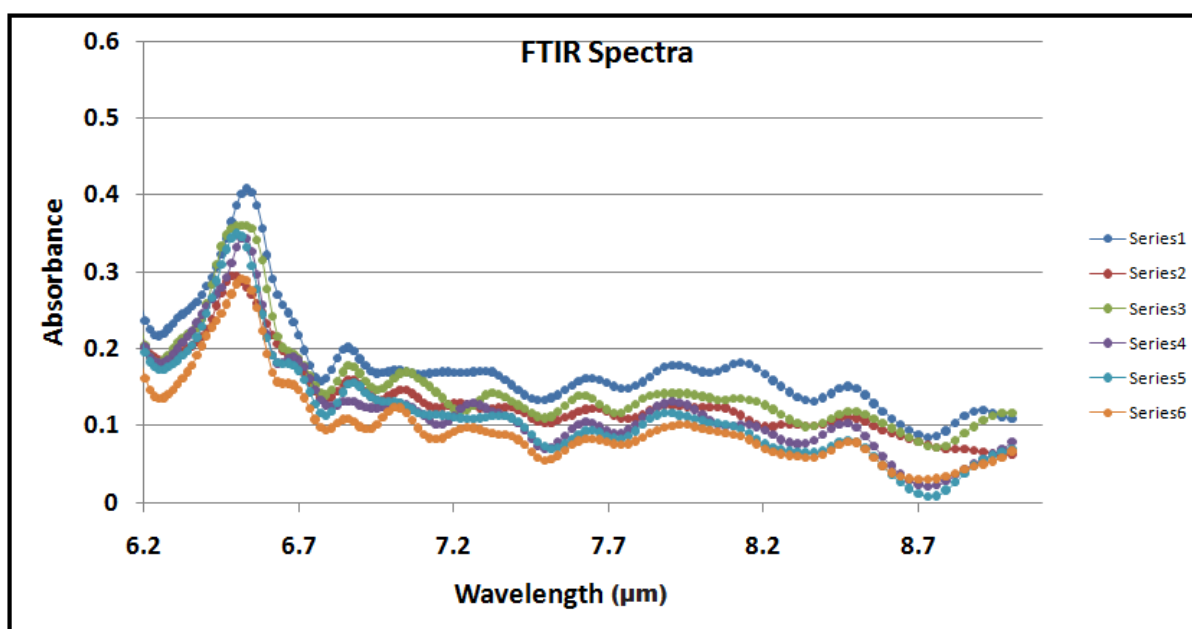


Figure 18. Point spectra collected with the Jasco FTIR spectrometer (spectral resolution of 16cm^{-1}) - S1 to S6 - (each region was 1 pixel with a size of $10\mu\text{m}$ by $10\mu\text{m}$) collected from a part of an oesophagus sample classified as adenocarcinoma tissue.

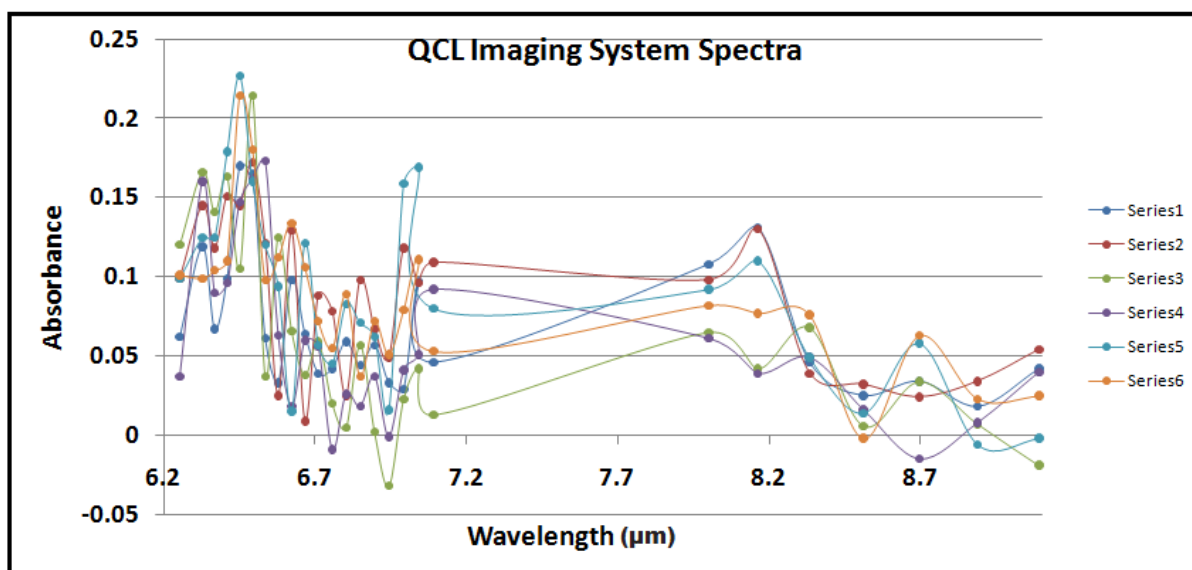


Figure 19. Point spectra collected with the QCL imaging system (spectral resolution of 1cm^{-1}) - S1 to S6 - (each region was 1 pixel with a size of $10\mu\text{m}$ by $10\mu\text{m}$) collected from a part of an oesophagus sample classified as adenocarcinoma tissue.

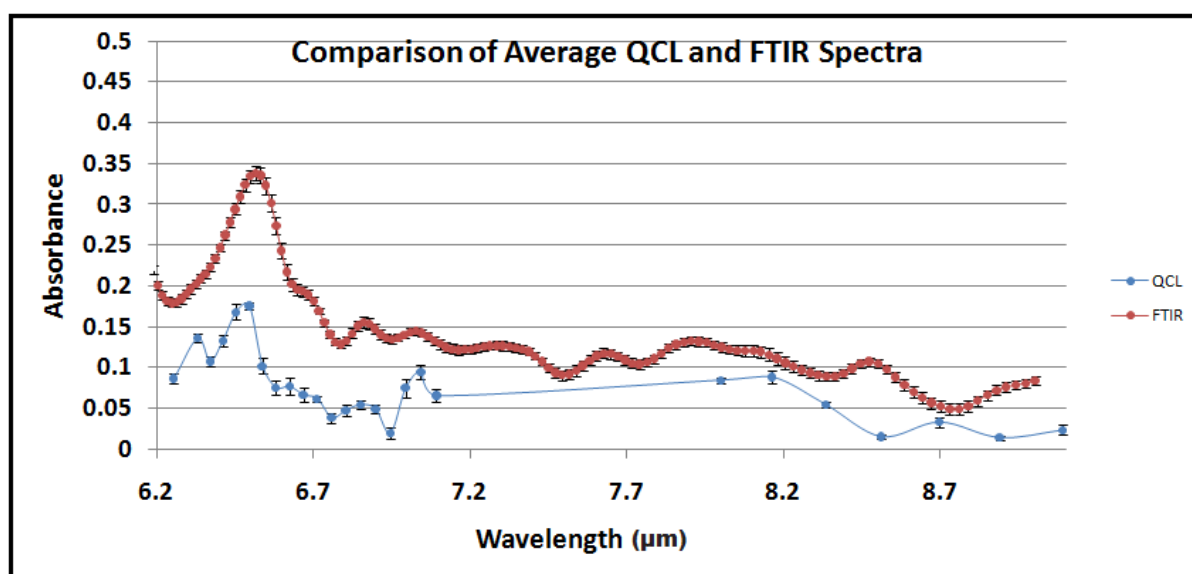


Figure 20. Comparison of average cancerous spectra collected with the Jasco FTIR spectrometer and the QCL imaging system. The average spectra were generated from 6 individual point spectra each collected from a parts of an oesophagus tissue sample classified as adenocarcinoma tissue. Error bars (determined from the standard error of the 6 averaged spectra) have been included to quantify spectral differences.

6.2.4 - QCL Imaging System Images and their Application to Cancer Diagnosis

The QCL imaging system was used to collect a spectral map from a tissue section (section A) containing healthy tissue (stroma, muscle and squamous epithelium) and adenocarcinoma (figure 5). An example chemical image (at $6.5\mu\text{m}$) taken with the QCL imaging system is shown for section A (with a pixel limited system of $10\mu\text{m}$ by $10\mu\text{m}$, Figure 21)

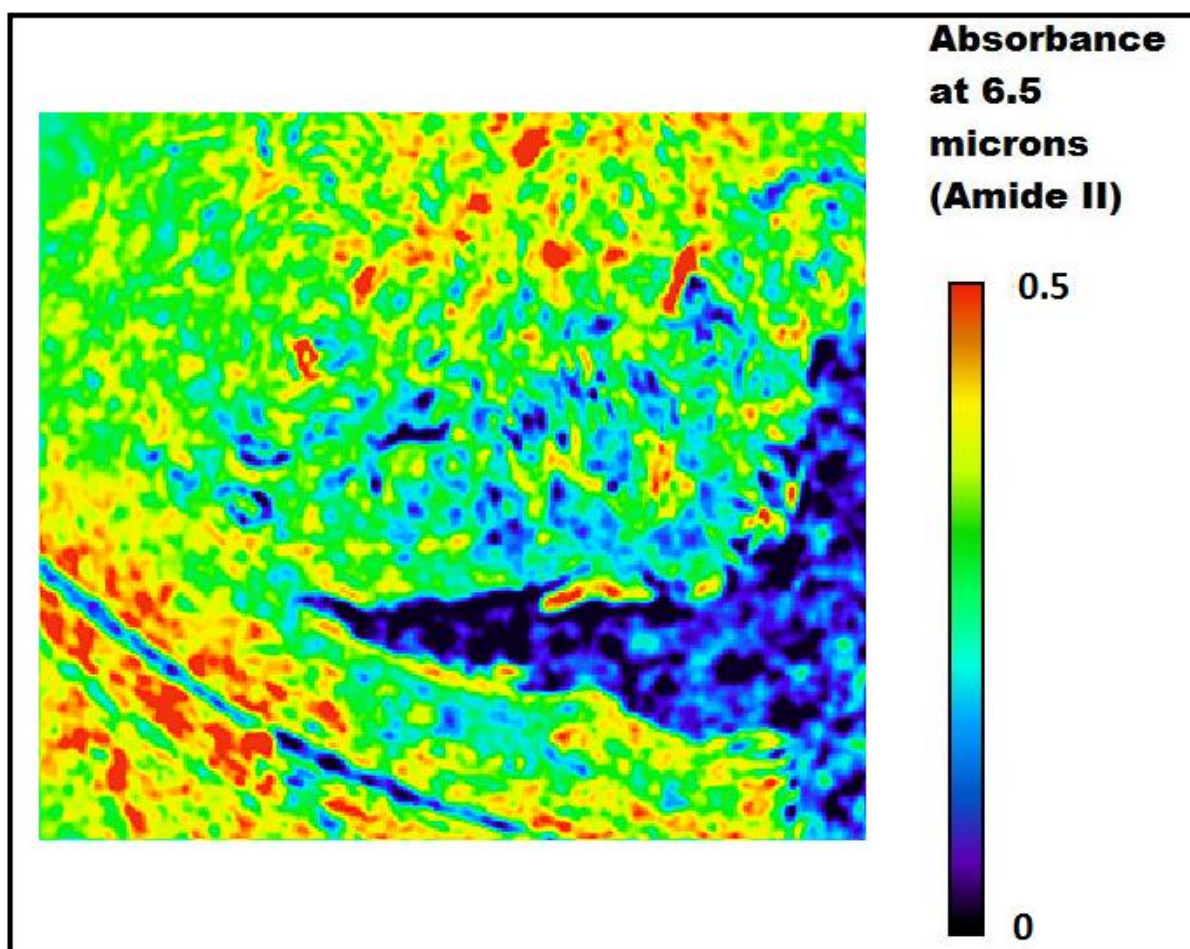


Figure 21. Chemical image taken with the QCL imaging system at 6.5 μ m (amide II) of a sample containing normal and cancerous tissue. The pixels are in units of absorbance. The system is pixel limited at 10 μ m by 10 μ m and has a field of view of 2.4mm by 3.2mm.

Figure 21 demonstrates the QCL imaging system's ability to generate chemical images with improved morphological information compared to the conventional (single channel) FTIR spectrometer chemical images (as a result of the wide fields of view, in this case 1.8mm by 2.75mm, and high spatial resolution attainable). The SNR of this image is approximately 30, which is a significant improvement on the OPG imaging system pictures (SNR of 2) and allows the potential for quantitative analysis. In order to assess the ability of the QCL imaging system to differentiate between the healthy and cancerous parts of a tissue sample, average spectra were collected from the sample regions indicated in Figure 22 (which have been classified by a histopathologist as healthy or cancerous, Fig 5). The individual spectra were collected from the healthy epithelium (labelled E1 to E6 on Fig 22) and cancerous (labelled C1 to C6 on Fig 22) parts of the sample and are shown in Figure 23 and Figure 24 respectively.

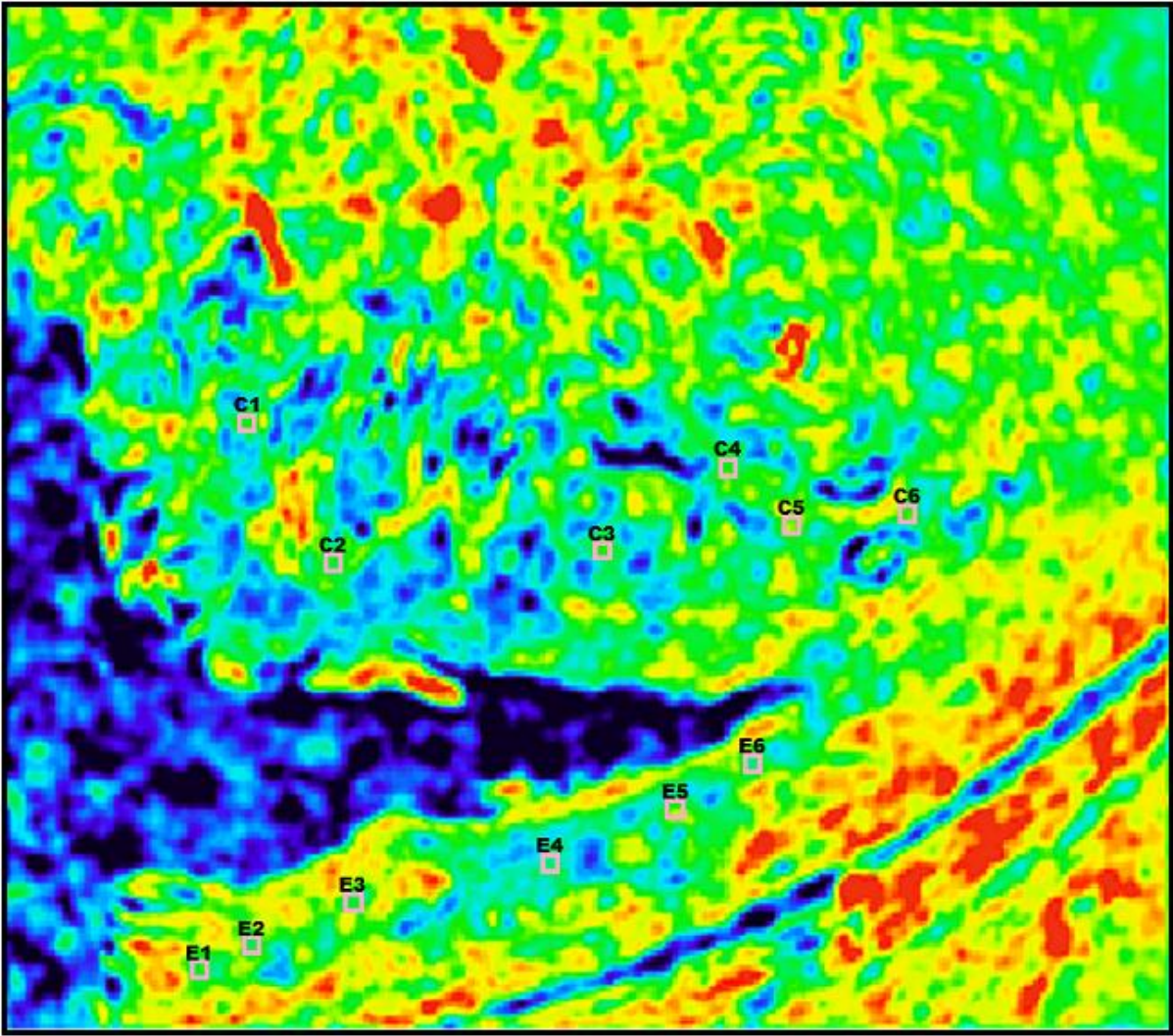


Figure 22. Regions where average spectra were collected from (each region was the average of 25 pixels). C1 to C6 were collected from cancerous parts of the sample (classified as adenocarcinoma). E1 to E6 were collected from healthy parts of the sample (classified as epithelium).

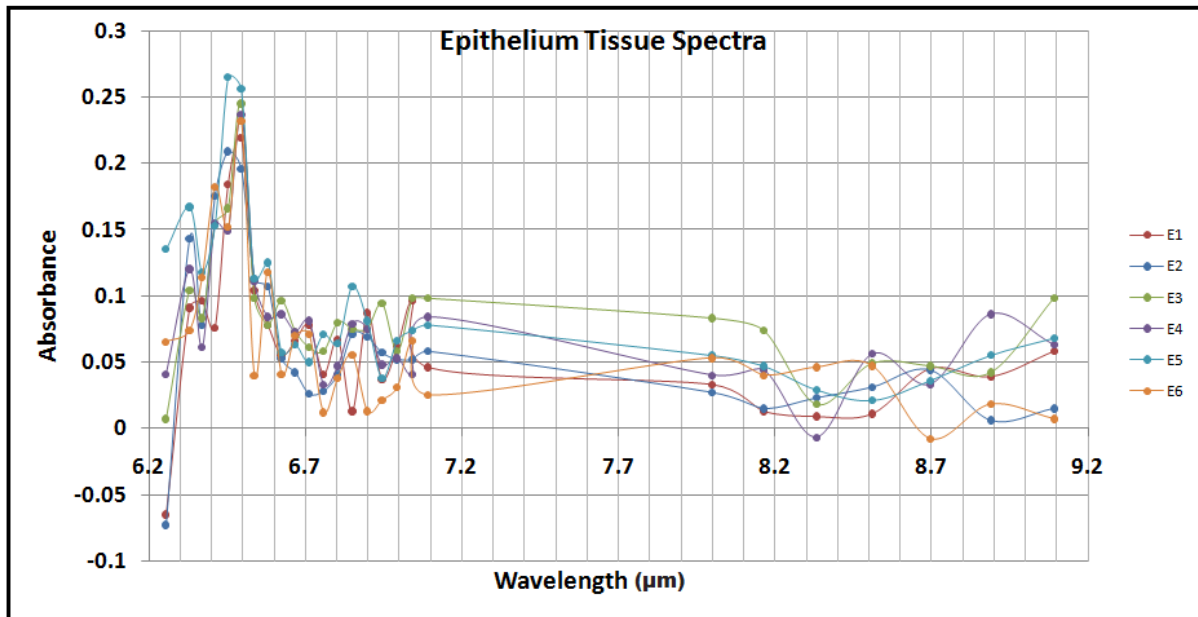


Figure 23. Average spectra - E1 to E6 - (each region was the average of 25 pixels) collected from a part of an oesophagus sample classified as healthy epithelium tissue.

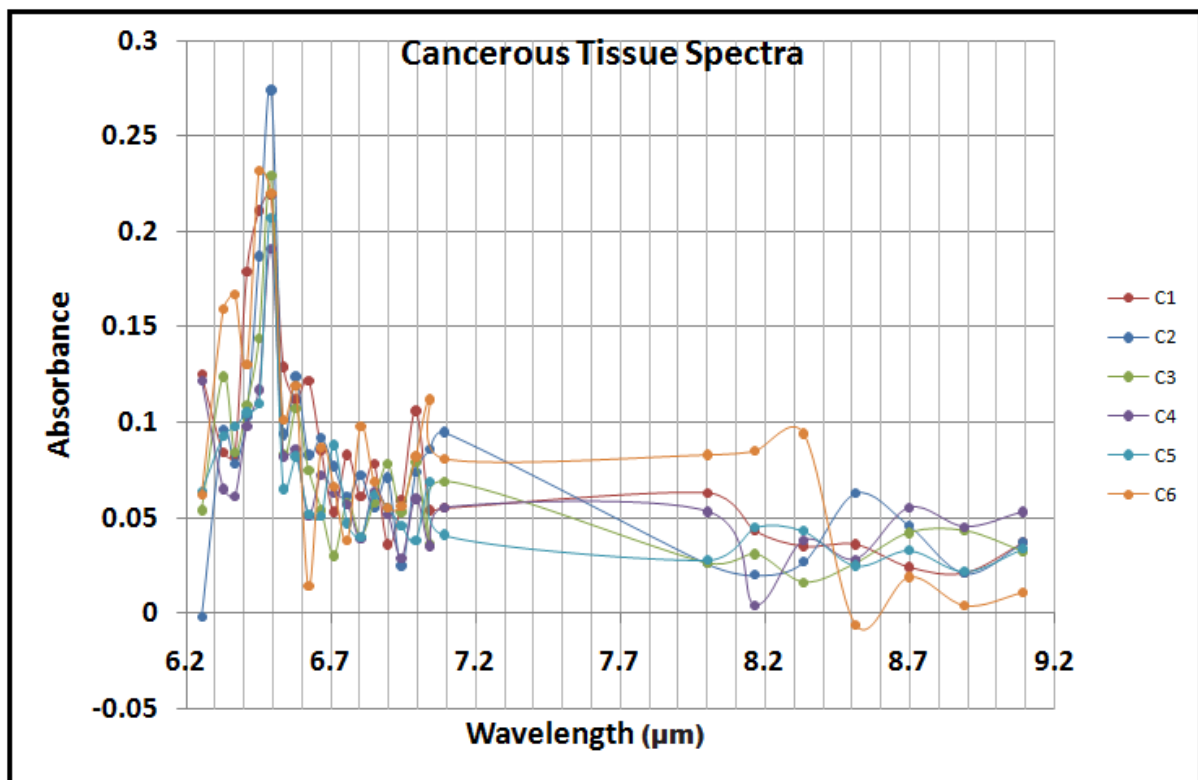


Figure 24. Average spectra - C1 to C6 - (each region was the average of 25 pixels) collected from a part of an oesophagus sample classified as adenocarcinoma tissue.

Figures 23 and 24 demonstrate that there is significant spectral variability amongst spectra collected from the same tissue classification. The spectral variability can be quantified by calculating the standard error (at every wavelength) for the 6 cancerous and 6 healthy spectra which is determined to be, on average, 23% for the healthy tissue and 16% for the cancerous tissue. Figure 25 shows a comparison of the average healthy (epithelium) and cancerous spectra which were generated from the 6 individual spectra shown in Figures 23 and 24. Figure 26 shows a comparison of the average healthy and cancerous spectra again but error bars have been included to quantify the spectral differences. As previously discussed (section 6.2.3) the source of the spectral variability (within the same tissue classifications) may be due to physical phenomena (such as inhomogeneous illumination or detector saturation) and/or natural differences in the biochemistry of the tissue in different parts of the sample. It is probably fair to say that it is difficult to see a clear spectroscopic difference between the different tissue classifications from Figures 25 and 26 and further work would need to be completed - with larger sample sizes as well as multivariate statistical techniques (such as LDA, section 5.3.3.1) - to make any assertions about the QCL imaging systems usefulness as a diagnostic tool for cancer diagnosis.

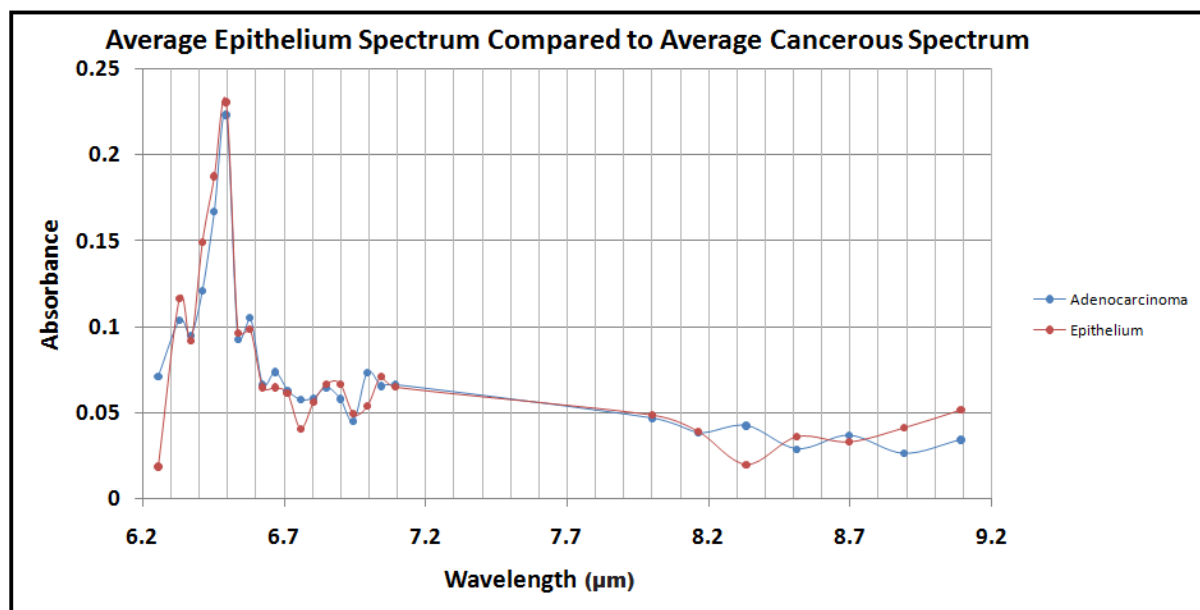


Figure 25. Comparison of average healthy (epithelium) and cancerous spectra. The average spectra were generated from 6 individual spectra each collected from a parts of an oesophagus tissue sample with regions classified as healthy epithelium tissue and adenocarcinoma tissue.

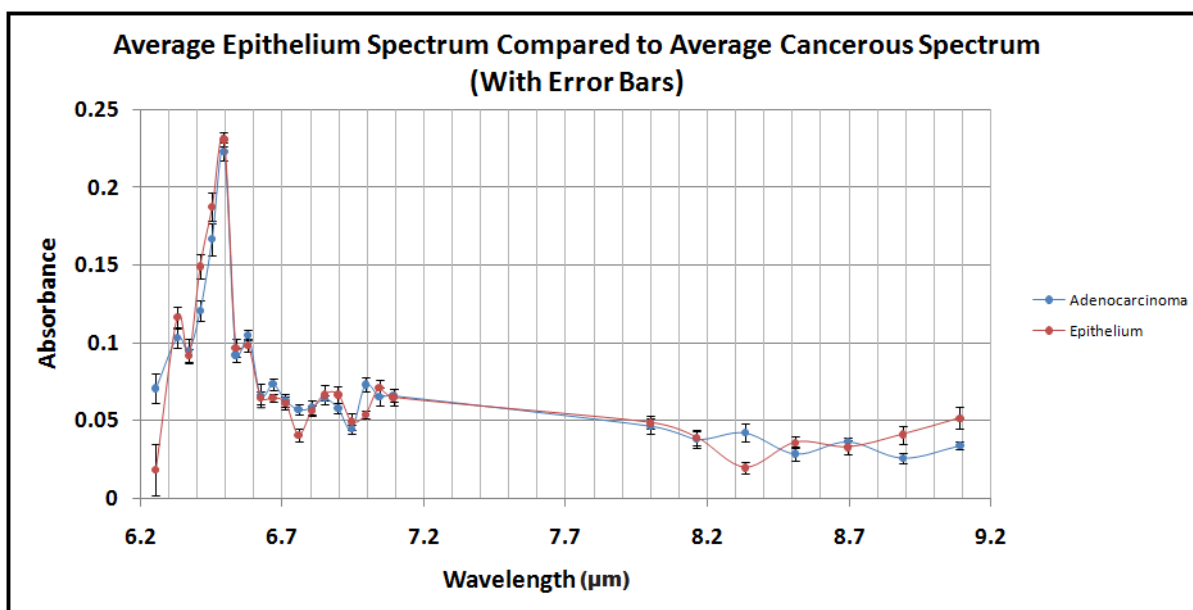


Figure 26. Comparison of average healthy (epithelium) and cancerous spectra. The average spectra were generated from 6 individual spectra each collected from a parts of an oesophagus tissue sample with regions classified as healthy epithelium tissue and adenocarcinoma tissue. Error bars have been included to quantify spectral differences.

1. Amrانيا, H., et al., *Ultrafast Infrared Chemical Imaging of Live Cells*. Chemical Science, 2010. 2: p. 107-111.

7.0 - Conclusion and Suggestions for Further Work

7.1 - Overview of Thesis

In this thesis the inadequacy of conventional histopathological analysis, primarily due to the subjective nature of the diagnosis, to diagnose early stage and pre-cancerous conditions has been discussed. Given the improvement in the chances of a patient making a full recovery when cancerous conditions are detected in their early stages considerable research efforts are being invested into technologies and innovations which have the ability to provide a non-subjective diagnosis. IR spectroscopy has been shown to provide quantitative information regarding the biochemistry of a tissue biopsy which can be used to inform a non-subjective diagnosis of cancer. Moreover, owing to spectacular technological advances, primarily in IR detectors and Information technology, modern FTIR spectrometers can collect large spectral maps, with wide fields of view, high spatial resolutions, in relatively short measurement times which provide morphological and biochemical information. In chapter 5 an analysis of spectral maps from a conventional (single channel) FTIR spectrometer showed that a spectral and spatial resolution of approximately 4cm^{-1} and $10\mu\text{m}$ by $10\mu\text{m}$ (diffraction limited) respectively is sufficient to apply spectral mapping to cancer diagnosis. Furthermore in order for IR spectroscopy to be a practical proposition in a clinical environment the measurement time for a spectral map, with a wide field of view (a few mm^2) and a high SNR (greater than 10 is desirable), needs to be on the order of a minute. Unfortunately conventional (single channel) IR spectrometer instrumentation falls short of being able to provide the desired measurement parameters due to the insufficient brightness of the thermal IR source used in FTIR spectrometers. In this thesis two different IR sources (OPGs and QCLs) have been investigated which are capable, in some instances, of providing a 7 orders of magnitude improvement in diffraction limited power. The coupling of IR laser sources to detector arrays has been shown able to produce diffraction limited chemical images in a couple of seconds with signal to noise characteristics which provide the possibility of extracting biochemical information from a biopsy, and therefore, diagnosing early stage cancerous conditions. Several key issues have been discussed that are associated with the use of high intensity sources to collect spectroscopic images, such as, detector saturation and optical artefacts arising from the source coherence. The usefulness of laser based sources has also been shown not only to be a result of their high brightness but also to depend on their relative intensity noise (RIN). The RIN (or pulse-to-pulse stability) of the OPG has been shown to make the extraction of quantitative data from tissue biopsy, even with sophisticated ratioing procedures, very challenging. Conversely the high stability of the QCL (low RIN) source has been a critical factor which enables the QCL imaging system to extract numerical absorbance data

from tissue biopsies and pave the way for a new method of generating high quality spectroscopic images.

7.2 - Suggestions for Further Work

Looking ahead there are several steps that can be taken to move the work in this thesis forward. It is obvious at this juncture that, for the purposes of collecting spectral maps from tissue biopsies, the QCL source is superior to the OPG source in most respects; it has a broader tuning range, a lower RIN, considerably lower cost, is more robust and less prone to malfunction. Therefore further research efforts should concentrate on refining spectroscopic imaging systems utilising QCLs (or at least other sources with stable outputs) rather than unstable and temperamental OPG sources.

In the short term there are two relatively simple steps which could be implemented to improve the data quality from the QCL imaging system; increasing the data acquisition time and using all reflective optics. In the experiment described in section 6.2.4 100 images were collected (in 1 second) and averaged giving an overall SNR ratio for an image (with absorbance pixel values) of 30. Clearly increasing the measurement time would decrease the noise and increase the SNR of the average images. Generally the noise in an average image generated from N images is proportional to the factor of $1/\sqrt{N}$. Therefore, for example, the noise on the images could be halved by averaging over 400 images (collected in 4 seconds) instead of 100 images. Secondly the use of all reflective optics (such as Cassegrain lenses) instead of refractive elements would allow chemical images to be collected at several wavelengths without adjusting the optics in between wavelengths. In the current QCL imaging system set-up the refocusing of the optics for each wavelength causes subtle changes in the magnification and image position on the detector array for each wavelength. These slight changes in the image at each wavelength make the generation of spectroscopic images (which combine two or more spectral features) extremely difficult with the current experimental configuration.

In the medium term there is still more work that could be done to identify the optimum combination of spectral features for generating spectroscopic images with the most diagnostic value. A preliminary attempt to investigate a combination of spectral features (generated by performing a linear discriminant analysis) that can be used to classify spectra as healthy or cancerous has been described in section 5.3.3.2. However a more complete investigation of this problem would involve the collection of high quality spectra (over a large field of view with diffraction limited spatial resolution) from several samples and the statistical model would allow for several different tissue classifications. This objective would be facilitated by the use of a modern FTIR spectrometer with a

large array detector (such as the Hyperion 3000, Bruker Optics) rather than a single channel FTIR spectrometer. However, it should be emphasised that even a study consisting of “several” samples would only go some way to building confidence in the diagnostic ability of a combination of spectral features. Clearly more extensive multi-patient / multi-centre studies would be necessary for full acceptance by the medical community. Whilst on the subject of IR spectra collected from conventional instrumentation it is also worth observing that the problem of spectral artefacts caused by non-biochemical properties of a sample, such as pixel-to-pixel baseline variations and dispersion artefacts, has not yet been addressed in an entirely satisfactory way in the current literature. Obviously non-subjective methodologies will need to be developed, and applied in a consistent way, so that these (physical) spectral artefacts can be removed and meaningful comparisons of spectra can be made which depend entirely on biochemical differences.

In terms of the QCL imaging system it would be useful to perform small pilot studies with a small number of samples to further examine, and quantify, the diagnostic power of the QCL imaging system. However before this is done it would probably be more constructive to further characterise the detector saturation mechanism discussed in section 4.11.2. At this point it is not entirely clear if the saturation mechanism is caused by the intrinsic quantum nature of the detector array (Moss-Burstein effect), the read out electronics of the camera or some combination of the two. The current solution to the saturation problem - to attenuate the beam - is obviously not ideal since it involves a reduction in the incident power which is the very characteristic which makes laser based sources so useful in the first place. Furthermore synchronisation of the QCL and the IR camera, which may be achieved by closer collaboration with the QCL manufacturer to incorporate an external trigger into the QCL source, would improve the SNR in a given measurement time by eliminating the systematic error arising from a variable number of pulses received by the camera (section 4.11.3) during an integration time.

In the long term in order for IR spectroscopy to be employed as a diagnostic tool (with or without laser sources) larger scale statistically significant studies are needed to demonstrate the efficacy of the technique. For this to happen firstly there must be standardised protocols developed for the entire spectral mapping process; from the processing of tissue biopsies into IR ready samples, to the classification of spectra. Once the methods of biopsy processing, spectra collection, spectral processing and spectral classification have been standardised large inter-centre studies can be carried out to assess the reliability of IR spectroscopy as a tool for cancer diagnosis. Ultimately it is important not to lose sight of the fact that using IR spectroscopy for cancer diagnosis is only useful, in a practical sense, to the medical profession if it can find a commercial application. Whilst there is

considerable enthusiasm and optimism from academics regarding the power of IR spectroscopy to analyse biological samples a succession of nice publications will not be enough to facilitate the transfer of this technology to a clinical environment. The gap between basic science and important practical application can only be closed by the development of low cost, user friendly and reliable instrumentation which can generate high quality diagnostic information. It is our hope that the work described in this thesis, especially regarding the QCL imaging system, is a step in the right direction. Our contribution, along with future joint efforts that define standard methodologies to collect spectroscopic data, quantify reproducibility levels, and the implementation of large scale statistical studies, can help realise the potential of IR spectroscopic imaging as a non-subjective tool for cancer diagnosis.

Appendix 1

Derivation of the Uncertainty of the Absorbance Pixel Values from the OPG Imaging System

$$A = -\log_{10} \left[\frac{\text{sample image}}{\text{OPG background image}} \right] = -\log_{10} X \quad (\text{A.1})$$

Where;

$$X = \left[\frac{\text{sample image}}{\text{OPG background image}} \right] \quad (\text{A.2})$$

The uncertainty in X, δX , is given by

$$\delta X = \left[\frac{\text{sample}}{\text{OPG background}} \right] \sqrt{\left[\frac{\delta(\text{sample})}{\text{sample}} \right]^2 + \left[\frac{\delta(\text{OPG background})}{\text{OPG background}} \right]^2} \quad (\text{A.3})$$

And using the relations;

If;

$$A = -\log_{10}(X) \quad (\text{A.4})$$

Then;

$$\delta A = \frac{1}{\ln(10)} \left[\frac{\delta X}{X} \right] \quad (\text{A.5})$$

Therefore;

$$\delta A = 0.434 \times \sqrt{\left[\frac{\delta(\text{sample})}{\text{sample}} \right]^2 + \left[\frac{\delta(\text{OPG background})}{\text{OPG background}} \right]^2} \quad (\text{A.6})$$

Now if we assume that (see sections 4.12.2.2 and 6.1.2.1)

$$\frac{\delta(\text{sample})}{\text{sample}} = \frac{\delta(\text{OPG background})}{\text{OPG background}} = 0.05 \quad (\text{A.7})$$

$$\sqrt{\left[\frac{\delta(\text{sample})}{\text{sample}} \right]^2 + \left[\frac{\delta(\text{OPG background})}{\text{OPG background}} \right]^2} = 0.0707 \quad (\text{A.8})$$

Therefore;

$$\delta A = 0.03 \quad (\text{A.9})$$

Acknowledgements

I consider this thesis the culmination of my entire academic journey as a student, lasting over ten years, consisting of three degrees, and study at four different institutions. As such I would like to say some thanks to my family and to all those lecturers, teachers and friends I have met along the way.

Firstly Prof C. C. Phillips deserves special thanks for his many excellent suggestions over the past few years, his diligent editing of this thesis, and for giving me the opportunity to undertake this research at Imperial College. Secondly I would like to thank Dr H Amrania who has been a tremendous help and a valued friend throughout the course of my PhD. I am also especially grateful to all my work colleagues past (Dr J Gambari, Dr R Steed, Dr M Matthews) and present (Mr E Yoxall, Mr L Drummond, Mr A Bak, Mr F Murphy, Ms M Yoshida) who have all offered lots of helpful advice and generally lightened the mood in 915 Blackett Laboratory. I would also like to thank Prof Sergei Kazarian and Prof Nick Stone for their editing of my thesis and for agreeing to be examiners for my PhD defence.

I would also like to thank my brother Carl for taking the time to grasp what I am researching, offering me sound advice, and generally taking me outside my box. I would like to thank my brother Lee for his consistently positive outlook on my career choice and for always reminding me of the fantastic opportunities which lay before me. I would also like to thank my brother Chris for showing me the way to “get things done” and relieve the stress of the monumental undertaking of writing a thesis. Most of all however I would like to thank my dear and wonderful parents who have helped me in more ways than I can possibly say and to whom I dedicate this thesis.